Novel roles for CG7379/ING1 in tumour progression.

A study of migration and invasion using *in vivo* and *in vitro* epithelial systems

Thesis submitted for the degree of Doctor of Philosophy

Alexandra Doina Rusu
BEng, MSc

June 2020

The University of Nottingham
School of Life Sciences

Abstract

The ability of cancer cells to invade and metastasize is the hallmark of cancer that sets apart malignant from benign tumours. Approximately 90% of cancer-related deaths can be attributed to cancer's ability to spread. A recent *in vivo* genetic screen that focused on the identification of tumour progression modulators identified CG7379, the fly orthologue of human ING1, as a potential invasion suppressor. ING1 is a type II tumour suppressor gene with well-established roles in transcriptional regulation of genes that control cell proliferation, response to DNA damage, oncogene-induced senescence and apoptosis. Recent work suggests a possible role for ING1 in cancer cell invasion and metastasis; however the underlying molecular mechanism has not been studied thus far.

In the present work, we took a loss-of-function approach to uncover the molecular mechanism employed by CG7379/ING1 to modulate single cell invasion *in vivo* and *in vitro* respectively. Our results show that: i) reduced expression of CG7379 induces invasion and brain metastasis *in vivo* in *Drosophila* and further cooperates with a loss of polarity mutation to intensify the invasive phenotype. Similarly, ING1 knockdown significantly enhances invasion *in vitro* in a human breast cancer model; ii) CG7379 knockdown reduces the junctional localisation of several adherens and septate junction components and severely disrupts cell-cell junction architecture. Similarly, decreased expression of ING1 disrupted E-cadherin distribution at cell-cell junctions *in vitro*, presumably by regulating cytoskeletal dynamics at the transcriptional level; iii) Both CG7379 and ING1 knockdown negatively impact cell proliferation, leading to decreased tumour size and cell accumulation in G0/G1 at 48 hr post-transfection respectively.

Taken together, the results presented in this thesis highlight the complexity of ING1 mediated transcription regulation and suggest that the multiple tumour suppressor effects associated with CG7379 and ING1 are likely to be coordinated at the transcriptome level.

List of publications

RUSU, A. D., CORNHILL, Z. E., CANALES COUTINO, B., CASTELLANOS URIBE, M., LOURDUSAMY, A., MARKUS, Z., MAY, S. T., RAHMAN, R. & GEORGIOU, M. 2020. CG7379/ING1 suppress cancer cell invasion by maintaining cell-cell junction integrity. *bioRxiv*.

CANALES COUTINO, B., CORNHILL, Z. E., COUTO, A., MACK, N. A., **RUSU, A. D.**, NAGARAJAN, U., NGAN FAN, Y., HADJICHARALAMBOUS, M. R., CASTELLANOS URIBE, M., BURROWS, A., LOURDUSAMY, A., MAY, S. T., RAHMAN, R. & GEORGIOU, M. 2020. A genetic analysis of tumour progression in *Drosophila* identifies the cohesin complex as a suppressor of individual and collective cell invasion. *iScience*.

RUSU, A. D. & GEORGIOU, M. 2020. The multifarious regulation of the apical junctional complex. *Open Biology,* 10: 190278.

PATRAS, L., SYLVESTER, B., LUPUT, L., SESARMAN, A., LICARETE, E., PORFIRE, A., MUNTEAN, D., DROTAR, D. M., **RUSU, A. D.** & NAGY, A.-L. 2017. Liposomal prednisolone phosphate potentiates the antitumor activity of liposomal 5-fluorouracil in C26 murine colon carcinoma *in vivo*. *Cancer biology & therapy,* 18**,** 616-626.

JULA, T. C., MUNTEANU, C., **RUSU, A**., & LANG, C. 2016. Long Term Consumption of red Bull and Alcohol can Affect Rat Skeletal Muscle Metabolism. *Studia Universitatis Babes-Bolyai, Biologia*, 61(1), 167-175.

RUSU, A.D., PATRAS, L., BANCIU, M. 2015. Overview on nanoparticulate formulations for 5-Fluorouracil delivery in colorectal cancer treatment. *Studia Universitatis Babes-Bolyai, Biologia*, 60 (2).

Conference contributions

Contributed oral presentation:

RUSU, A. D., CANALES COUTINO, B., CORNHILL, Z. E., COUTO, A., MACK, N. A., RAHMAN, R. & GEORGIOU, M. An *in vivo* loss-of-function analysis of tumour progression identifies CG7379/ING1 as a multifaceted invasion suppressor and a regulator of cell-cell junction integrity. *Gordon Research Seminar on Cell Contact and Adhesion*, 01-02 June 2019, Les Diablerets, Switzerland.

Poster:

RUSU, A. D., CANALES COUTINO, B., CORNHILL, Z. E., COUTO, A., MACK, N. A., RAHMAN, R. & GEORGIOU, M. An *in vivo* loss-of-function analysis of tumour progression identifies CG7379/ING1 as a multifaceted invasion suppressor and a regulator of cell-cell junction integrity. *Gordon Research Conference on Cell Contact and Adhesion*, 02-07 June 2019, Les Diablerets, Switzerland.

RUSU, A. D., CORNHILL, Z. E., CANALES COUTINO, B., RAHMAN, R. & GEORGIOU, M. Loss of ING1 (CG7379) promotes tumour invasion by misregulation of cell-cell adhesion. *BSCB/BSDB Joint Annual Spring Meeting*, 7-10 April 2019, Warwick, UK.

RUSU, A. D., CORNHILL, Z. E., CANALES COUTINO, B., RAHMAN, R. & GEORGIOU, M. Determining the role of CG7379 in malignant invasion. *3rd Midlands Drosophila Meeting*, 19 June 2018, Nottingham, UK.

RUSU, A. D., CORNHILL, Z. E., CANALES COUTINO, B., RAHMAN, R. & GEORGIOU, M. Loss of CG7379 gene promotes cell migration and invasion due to a disruption of cell-cell junction integrity. *Dynamic Cell III: BSCB/Biochemical Society Joint Annual Spring Meeting,* 19-21 March 2018, Manchester, UK.

RUSU, A. D., CORNHILL, Z. E., RAHMAN, R. & GEORGIOU, M. CG7379 and its human orthologue ING1 KD promotes tumour progression in both *in vivo* and *in vitro* models. *2nd Midlands Drosophila Meeting,* 17 May 2017, Leicester, UK.

Statement of originality

The genetic screen project was a large-scale study that took place in the Georgiou laboratory over the course of approximately seven years and involved the hard work of many researchers. The conceptualisation of the *in vivo Drosophila* cancer screen project was performed by Dr Marios Georgiou and the conceptualisation of the *in vitro* testing by Dr Ruman Rahman. The methodology for the screen project was developed by Dr Marios Georgiou, Dr Ruman Rahman, Dr Africa Couto, Dr Natalie Mack and Dr Zoe Cornhill. Similarly, the investigations for the pilot screen were carried out by Dr Africa Couto, Dr Natalie Mack, and Dr Zoe Cornhill. The experiments for the large-scale genetic screen were performed mainly by Dr Africa Couto, Dr Natalie Mack, Dr Zoe Cornhill and Dr Brenda Canales Coutino and the statistical analysis was performed by Dr Anbarasu Lourdusamy. I have participated in many aspects of the main genetic screen, including confocal microscopy.

As the gene studied for my PhD project was one of the first 'hits' picked from the screen project for further characterisation, the investigation of CG7379 was initially performed by Dr Zoe Cornhill. Therefore part of the live imaging (excluding time-lapses) for flies of the following genotypes: *lgl-/-* and *lgl-/-;* CG7379 KD were performed by former group members. Similarly, some of the junction and polarity protein stains (37 animals out of a total of 242 animals) and ING1 and GAPDH primer design for qPCR were performed by Dr Zoe Cornhill. The transwell migration and invasion assays were performed by Dr Brenda Canales Coutino. However, I contributed equally to the optimisation of the assays. Sample processing for the whole-genome transcriptome analysis was performed by Prof Sean May's group at the Nottingham Arabidopsis Stock Centre.

The original work presented in this thesis covers the characterisation of the *Drosophila* gene CG7379 and its human orthologue, the ING1 tumour suppressor. This includes the investigation and characterisation of the transition of a living epithelium towards malignancy when CG7379 expression was knocked down. It also

covers preliminary investigation of human cancer cell behaviour *in vitro* when ING1 expression was knocked down. Data acquisition and analysis presented in the results sections of this thesis were performed by myself, unless stated otherwise.

The figures (Figures 1.5; 1.6; 1.7; 1.8; 1.9) and text from Chapter 1.4.1 (p. 32-42) were reproduced from the review paper 'The multifarious regulation of the apical junctional complex' published earlier this year in Open Biology by myself together with my supervisor, Dr. Marios Georgiou.

The work presented in this thesis has not been previously submitted for a degree or diploma at any other higher education institution. To the best of my knowledge and belief, the thesis contains no material previously published or written by another person except where due references are made.

Acknowledgements

Firstly, I am grateful to my supervisor Dr Marios Georgiou for providing me the opportunity to join his team in 2015 for an internship and for all the assistance with the PhD and scholarship applications. Without his support none of this would have been possible.

I would like to thank both my supervisors: Dr Marios Georgiou and Dr Ruman Rahman for their valuable advice, guidance and constant support throughout my PhD. I would also like to thank all the present and former members of the lab alongside whom I worked during the past four years: Dr Africa Couto, Dr Natalie Mack, Dr Zoe Cornhill, Dr Brenda Canales Coutino, Louisa Taylor and Giuseppe Uras for their patience, help and advice. I would like to send special thanks to our lab technician Zsuzsa Markus for taking care of the fly stocks, the fly food cooking and of health and safety within the lab. I would like to also thank Dr Robert Markus, Seema Rajani, Ian Ward, Dr Chris Gell, Dr Tim Self from the School of Life Sciences Imaging facility for all their help with confocal microscopy; Pam Collier, Dr. Jonathan Rowlinson and Dr Maria Estevez Cebrero for the support with the *in vitro* work and Dr Marcos Castellanos Uribe for the help with the transcriptomics experiment.

I am also grateful for receiving the Vice-Chancellor's Scholarship from University of Nottingham, supplemented by the School of Life Sciences. Without their support this work would not have been possible.

I would also like to thank my parents, my sister and my grandmother for their unconditional support. I acknowledge that me moving further and further away from home could not have been easy for them. Last but not least, I want to thank my partner, Radu, for his unconditional support, for taking care of me during stressful moments and for bringing me back to reality whenever needed.

Contents

Novel roles for CG7379/ING1 in tumour progression. A study of migration and invasion using *in vivo* and *in vitro* epithelial systems

ABBREVIATIONS **15**

CHAPTER 1 – GENERAL INTRODUCTION **20**

1.1 TUMORIGENESIS AS A MULTISTEP PROCESS 21

1.2 MITOTIC SIGNALLING 25

1.2.1 Cell cycle progression in homeostasis *25*

1.2.2 Changes to proliferation signalling encountered in malignancy *29*

1.3 APOPTOTIC SIGNALLING 30

1.3.1 Principles of apoptotic signalling in homeostasis *30*

1.3.2 Changes to apoptotic signalling in cancer *32*

1.4 INVASION AND METASTASIS 33

1.4.1 Epithelial cell adhesion in homeostasis *35*

1.4.1.1 Tight junctions: molecular composition and architecture 36

1.4.1.2 Adherens junctions: molecular composition and architecture 38

1.4.1.3 Molecular nature of cell junction-cytoskeleton interactions 40

1.4.1.4 Molecular mechanisms of protein turnover at cell-cell junctions 42

1.4.2 Epithelial cell polarity *45*

1.4.2.1 Apical Par and Crumbs modules 47

1.4.2.2 The Scribble module 48

1.4.3 Invasion *49*

1.5 *DROSOPHILA MELANOGASTER* AS A MODEL ORGANISM FOR CANCER RESEARCH 50

1.6 RESEARCH AIMS 54

CHAPTER 2 – MATERIALS AND METHODS **55**

2.1 MATERIALS 56

2.1.1 Live stocks *56*

2.1.2 Antibodies *57*

2.1.3 Primers and siRNA *58*

2.1.4 General reagents *59*

2.2 *DROSOPHILA* METHODS 62

2.2.1 Drosophila husbandry *62*

2.2.2 Genetic techniques *63*

2.2.2.1 The galactosidase 4 (GAL4)/upstream activating sequence (UAS) system 65

2.2.2.2 RNA interference mediated knockdown 66

2.2.2.3 The flippase (Flp)/flippase recognition target (FRT) system 67

2.2.2.4 Mosaic analysis with a repressible cell marker 69

2.2.2.5 Meiotic recombination ... 71
2.2.2.6 Genotypes analysed ... 73
2.2.3 Mounting for live imaging ... 74
2.2.4 Dissections ... 75
2.2.4.1 Nota dissections ... 75
2.2.4.2 Brain dissections ... 76
2.2.4.3 Gastrointestinal tract dissections ... 77
2.2.4.4 Ovaries and testes dissections ... 78
2.3 CELL CULTURE METHODS ... 79
2.3.1 Cell storage and maintenance ... 79
2.3.2 Cell counting ... 80
2.3.3 Transient transfection ... 80
2.3.4 Transwell migration and invasion assay ... 81
2.4 MOLECULAR BIOLOGY TECHNIQUES ... 83
2.4.1 Immunohistochemistry ... 83
2.4.2 TdT-Mediated dUTP Nick-End-Labeling ... 84
2.4.3 RNA extraction ... 84
2.4.4 Complementary DNA synthesis ... 85
2.4.5 Quantitative PCR ... 85
2.4.6 Flow cytometry ... 86
2.4.7 Whole-genome transcriptome analysis ... 87
2.5 IMAGING ... 87
2.5.1 Confocal imaging ... 87
2.5.2 Imaging for metastasis detection in flies ... 88
2.6 DATA ANALYSIS ... 88
2.6.1 Relative transcript levels ... 88
2.6.2 Flow cytometry data analysis ... 90
2.6.3 Gene expression data analysis ... 90
2.6.4 Gene ontology term enrichment ... 90
2.6.5 Interaction map ... 91
2.6.6 Image analysis ... 91
2.6.7 General statistics ... 93
CHAPTER 3 – CG7379 KNOCKDOWN PROMOTES INVASION AND METASTASIS ... 94
3.1 INTRODUCTION ... 95
3.1.1 An in vivo genetic screen to identify tumour progression modulators ... 96
3.1.1.1 Development of the tumorigenesis model ... 96
3.1.1.2 The pilot screen ... 98
3.1.1.3 The large-scale genetic screen ... 100
3.1.2 CG7379 ... 103
3.2 RESULTS ... 103

3.2.1. CG7379 knockdown promotes single cell invasion in the living epithelium *103*
3.2.2 Characterisation of the behaviour of invasive cells bearing CG7379 knockdown *114*
3.2.3 CG7379 knockdown alone can induce metastatic behaviour *117*
3.3 DISCUSSION 121

CHAPTER 4 – CG7379 AND ING1 INVOLVEMENT IN CELL-CELL ADHESION 126

4.1 INTRODUCTION 127
4.1.1 Previous research predicts CG7379 role in cell adhesion *127*
4.1.2 Inhibitor of growth (ING) protein family involvement in cancer progression *129*
4.2 RESULTS 133
4.2.1 Evaluation of apoptosis involvement in cell delamination in response to CG7379 knockdown *133*
4.2.2 Ectopic localisation of adherens junction, septate junction and apicobasal polarity constituents in CG7379 knockdown clones *137*
4.2.3 ING1 knockdown promotes invasion in a human adenocarcinoma in vitro model employing similar mechanisms of action as CG7379 ..... *146*
4.2.4 ING1 knockdown severely affects the transcriptome of MCF-7 cells *148*
4.2.5 Assessment of Rho1 impact on CG7379 knockdown induced cell delamination *156*
4.3 DISCUSSION 157
4.3.1 CG7379 regulates cell invasion by modulating apoptosis and cell-cell adhesion *157*
4.3.2 ING1 regulates cell invasion at a transcriptional level *160*
4.3.2.1 ING1 knockdown increases invasion and disrupts adherens junction integrity in MCF-7 cells 160
4.3.2.2 Microarray analysis of genome-wide gene expression reveals a possible role for ING1 in cell-cell adhesion regulation 161
4.3.2.3 Microarray analysis of genome-wide gene expression identifies ING1 as a possible modulator of Rho activity 165

CHAPTER 5 – CG7379 AND ING1 INVOLVEMENT IN CELL PROLIFERATION 168

5.1 INTRODUCTION 169
5.1.1 ING1's involvement in cell growth and cell cycle progression *169*
5.2 RESULTS 172
5.2.1 Clonal analysis of CG7379 knockdown indicates a cell proliferation role for CG7379 during early development of the notum *172*
5.2.2 ING1 expression is putatively required for G1/S transition in MCF-7 cells *174*
5.3 DISCUSSION 179

CHAPTER 6 – DISCUSSION 185

6.1 CG7379/ING1 AS TUMOUR SUPPRESSORS 186
6.2 ING1 MODULATION OF GENE EXPRESSION IS ASSOCIATED WITH HALLMARKS OF CANCER 192
6.3 FUTURE PERSPECTIVES 196

6.4 Conclusions 198

BIBLIOGRAPHY 200

APPENDIXES 227

Appendix 1. CG7379 knockdown phenotypic scores in the large-scale genetic screen 228

Appendix 2. List of differentially expressed genes in response to ING1 knockdown in MCF-7 cells 235

Appendix 3. Biological processes and pathways significantly enriched by ING1 knockdown differentially expressed genes and correlated diseases 273

Appendix 4. List of genetic and physical interactors of cell-cell junction components affected by CG7379 knockdown 296

Appendix 5. Gene and interactions tables for the functionally validated network of differentially expressed genes following ING1 knockdown 302

List of figures

Figure 1.1 Tumour development through clonal selection 22
Figure 1.2 Cell Cycle of a eukaryotic cell 26
Figure 1.3 Apoptotic signalling cascade 30
Figure 1.4 Schematisation of the invasion-metastasis process 34
Figure 1.5 Cell adhesion in mammalian and *Drosophila* epithelial cells 35
Figure 1.6 Molecular composition and architecture of tight junctions and the cytosolic tight junction plague 37
Figure 1.7 Molecular composition and architecture of tricellular tight junctions 38
Figure 1.8 Molecular composition and architecture of adherens junctions 40
Figure 1.9 Molecular mechanism of clathrin mediated cadherin turnover at adherens junctions 45
Figure 1.10 Localization of apicobasal polarity modules in epithelial cells 46
Figure 1.11 *Drosophila* life cycle and development timescale at 25°C 51
Figure 2.1 The GAL4/UAS system 66
Figure 2.2 Molecular mechanism of UAS-RNAi transgene 67
Figure 2.3 The Flp/FRT system 68
Figure 2.4 The MARCM system 71
Figure 2.5 Meiotic recombination experimental design 72
Figure 2.6 Mounting for live imaging 75
Figure 2.7 Dissection of *Drosophila* nota 76
Figure 2.8 Dissection of *Drosophila* brain 77
Figure 2.9 Dissection of *Drosophila* gastrointestinal tract 78
Figure 2.10 Dissection of *Drosophila* reproductive organs 79
Figure 2.11 Schematic of migration/invasion assay protocol 82
Figure 3.1 Homozygote Scribble complex mutant clones 97
Figure 3.2 Example of phenotypes observed during the pilot screen 99
Figure 3.3 Clustering analysis of RNAi lines analysed during the large-scale genetic screen 102
Figure 3.4 Phenotypic effects of CG7379 knockdown on *lgl-/-* clones 105
Figure 3.5 Quantification of protrusion length and the level of invasion induced by CG7379 knockdown 106
Figure 3.6 CG7379 knockdown alone is sufficient to increase invasion 108
Figure 3.7 Cell protrusion aspect following CG7379 knockdown 110
Figure 3.8 Recombination of RNA hairpin and iCasper constructs 113
Figure 3.9 Only a subfraction of the invasive cells undergo anoikis once detached from the clone 114
Figure 3.10 Characterisation of cell behaviour prior to invasion 115
Figure 3.11 Characterisation of invasive cell behaviour 116

FIGURE 3.12 CG7379 KNOCKDOWN INVASIVE CELLS ARE CAPABLE OF EXTRUDING FROM THE EPITHELIAL TISSUE 117
FIGURE 3.13 OPTIMISATION OF AN *IN VIVO* METASTASES DETECTION SYSTEM 119
FIGURE 3.14 INVADING CELLS FROM CG7379 KNOCKDOWN TUMOUR-LIKE TISSUES CAN METASTASIZE TO THE BRAIN 120
FIGURE 4.1 FUNCTIONALLY VALIDATED INTERACTION NETWORK OF INVASION SUPPRESSOR GENES IDENTIFIED IN THE TUMOUR PROGRESSION REGULATORS SCREEN 128
FIGURE 4.2 CG7379/ING1 PROTEIN ALIGNMENT 130
FIGURE 4.3 SCHEMATIC OF SIN3A/HDAC COMPLEX 131
FIGURE 4.4 ONLY A SUBFRACTION OF CG7379 KNOCKDOWN-INDUCED DELAMINATION IS IN RESPONSE TO CASPASE ACTIVATION 134
FIGURE 4.5 P35 OVEREXPRESSION IN *LGL-/-* TUMOURS DOES NOT PHENOCOPY *LGL-/-;*-CG7379 KNOCKDOWN 136
FIGURE 4.6 CG7379 KNOCKDOWN DISRUPTS ADHERENS JUNCTION PROTEIN LOCALISATION 139
FIGURE 4.7 CG7379 KNOCKDOWN DISRUPTS SEPTATE JUNCTION PROTEIN LOCALISATION 142
FIGURE 4.8 APICOBASAL POLARITY DETERMINANTS LOCALISATION IS NOT AFFECTED BY CG7379 KNOCKDOWN 144
FIGURE 4.9 E-CADHERIN OVEREXPRESSION ALONE CANNOT RESCUE CG7379 KNOCKDOWN INDUCED CELL DELAMINATION 145
FIGURE 4.10 ING1 KNOCKDOWN PROMOTES INVASION IN A BREAST ADENOCARCINOMA CELL LINE BY DISRUPTING E-CADHERIN LOCALISATION AT CELL-CELL JUNCTIONS 147
FIGURE 4.11 IDENTIFICATION OF DIFFERENCES IN GENE EXPRESSION INDUCED BY ING1 KNOCKDOWN IN MICROARRAY ANALYSIS OF MCF-7 TRANSCRIPTOME 151
FIGURE 4.12 HIERARCHICAL CLUSTERING OF A SELECTION OF DIFFERENTIALLY EXPRESSED GENES PUTATIVELY ASSOCIATED WITH CELL-CELL JUNCTION STABILITY 152
FIGURE 4.13 GENE ONTOLOGY ENRICHMENT ANALYSIS OF A SELECTION OF DIFFERENTIALLY EXPRESSED GENES PUTATIVELY ASSOCIATED WITH CELL-CELL JUNCTION STABILITY 153
FIGURE 4.14 INTERACTION NETWORK OF A SUBSET OF DIFFERENTIALLY EXPRESSED GENES FOLLOWING ING1 KNOCKDOWN AND ADHERENS JUNCTION COMPONENTS 155
FIGURE 4.15 EXPRESSION OF DOMINANT NEGATIVE RHO1 CANNOT RESCUE CG7379 KNOCKDOWN INDUCED CELL DELAMINATION 156
FIGURE 5.1 CG7379 KNOCKDOWN DECREASES CLONAL COVERAGE 173
FIGURE 5.2 ANALYSIS OF CELL CYCLE DISTRIBUTION FOLLOWING ING1 KNOCKDOWN 176
FIGURE 5.3 ING1 KNOCKDOWN DOES NOT AFFECT APOPTOSIS IN MCF-7 CELLS 178
FIGURE 5.4 SCHEMATIC REPRESENTATION OF ING1 KNOCKDOWN EFFECTS ON CELL CYCLE AND DNA REPLICATION PATHWAYS 181
FIGURE 6.1 PROPOSED MODEL FOR THE ROLE OF ING1 AS TUMOUR SUPPRESSOR 194

List of tables

TABLE 1.1 HALLMARKS OF CANCER 23

TABLE 2.1 LIVE STOCKS 56

TABLE 2.2 PRIMARY AND SECONDARY ANTIBODIES USED FOR IMMUNOFLUORESCENCE 58

TABLE 2.3 PRIMERS AND SIRNAS 59

TABLE 2.4 GENERAL REAGENTS 60

TABLE 2.5 BALANCERS AND GENETIC MARKERS 63

TABLE 2.6 GENETIC CONSTRUCTS 64

TABLE 3.1 PHENOTYPIC EFFECTS OF MOSAIC *LGL-/-*; CG7379 KNOCKDOWN IN *DROSOPHILA* NOTUM 104

TABLE 3.2 AVERAGE INTERMEDIATE PROTRUSION LENGTH AND LEVEL OF INVASION FOLLOWING CG7379 KNOCKDOWN IN *LGL-/-* MUTANT TISSUE 107

TABLE 3.3 AVERAGE LEVEL OF DELAMINATION FROM MOE:GFP LABELLED MOSAIC TISSUES INDUCED ON THE BACK OF THE FRUIT FLY 108

TABLE 3.4 AVERAGE INTERMEDIATE PROTRUSION LENGTH FOLLOWING CG7379 KNOCKDOWN 110

TABLE 3.5 AVERAGE LEVEL OF INVASION FROM MOSAIC TUMOUR-LIKE TISSUES INDUCED IN FLIES CARRYING A CG7379 RNAI—ICASPER RECOMBINATION 113

TABLE 3.6 AVERAGE PROPORTION OF DELAMINATED CELLS UNDERGOING APOPTOSIS 114

TABLE 4.1 AVERAGE LEVELS OF APOPTOSIS WITHIN THE CLONAL TISSUE 134

TABLE 4.2 COMPARISON BETWEEN THE AVERAGE LEVEL OF INVASION INDUCED BY CG7379 KNOCKDOWN AND P35 OVEREXPRESSION 136

TABLE 4.3 MEAN FLUORESCENCE INTENSITY REPRESENTATIVE OF PROTEIN EXPRESSION AT ADHERENS JUNCTIONS AND MEAN PROPORTION OF DISRUPTED JUNCTIONS 139

TABLE 4.4 MEAN FLUORESCENCE INTENSITY REPRESENTATIVE OF PROTEIN EXPRESSION AT SEPTATE JUNCTIONS AND MEAN PROPORTION OF JUNCTIONS WITH A DISRUPTED ARCHITECTURE 142

TABLE 4.5 MEAN FLUORESCENCE INTENSITY REPRESENTATIVE OF APKC LEVELS AT CELL CORTEX 144

TABLE 4.6 AVERAGE NUMBER OF MIGRATORY/ INVASIVE MCF-7 CELLS AND AVERAGE PROPORTION OF DISRUPTED JUNCTIONS 148

TABLE 4.7 SIGNIFICANTLY ENRICHED BIOLOGICAL PROCESSES AND PATHWAYS BY A PANEL OF SELECTED 27 DIFFERENTIALLY EXPRESSED GENES FOLLOWING ING1 KNOCKDOWN 154

TABLE 5.1 AVERAGE SIZE OF MOE:GFP LABELLED CELLS AND CLONAL TISSUE 174

TABLE 5.2 MEAN NUMBER OF MCF-7 CELLS TREATED WITH MOCK SIRNA OR SIRNA AGAINST ING1 THAT GREW IN 48 HR AND THEIR CELL CYCLE DISTRIBUTION EXPRESSED AS PROPORTION OF CELLS IN EACH STAGE OF THE CELL CYCLE 177

Abbreviations

ADD3	Adducin 3
AJ	Adherens Junctions
AKT	Protein Kinase B
ANLN	Anillin Actin Binding Protein
APF	After Puparium Formation
aPKC	Atypical Protein Kinase C
Arp2/3	Actin Related Protein 2/3
BCL-2	B Cell Lymphoma 2
BDSC	Bloomington *Drosophila* Stock Centre
BSA	Bovine Serum Albumin
bTJ	Bicellular Tight Junctions
CCN	Cyclin
Cdc/CDC	Cell Division Cycle
CDK	Cyclin-Dependent Kinases
cDNA	Complementary DNA
cDcp-1	Cleaved *Drosophila* death caspase-1
CHK	Checkpoint Kinase
CKI	Cyclin-Dependent Kinase Inhibitor Protein
Chr	Chromosome
cRNA	Complementary RNA
CTNND1	Catenin Delta 1 (p120)
CXL12	Stromal Cell-Derived Factor 1
Cyo	Curley of Oster
DAPI	4’,6-Diamidino-2-Phenylindole
DAVID	Database for Annotation, Visualization and Integrated Discovery
Dcp	Death Caspase-1
DEG	Differentially Expressed Genes
DGRC	*Drosophila* Genomics Resource Centre
DIAP1	Death-Associated Inhibitor of Apoptosis 1

DIAPH1	Diaphanous Related Formin 1
DIOPT	DRSC Integrative Ortholog Prediction Tool
DSHB	Developmental Studies Hybridoma Bank
Dlg	Disc Large
DMSO	Dimethylsulfoxide
DNA	Deoxyribonucleic Acid
ECM	Extracellular Matrix
ECT2	Epithelial Cell Transforming 2
EGFR	Epidermal Growth Factor Receptor
EMT	Epithelial to Mesenchymal Transition
EPLIN	Epithelial Protein Lost in Neoplasm
ERBB2	Erb-B2 Receptor Tyrosine Kinase 2
ERK	Extracellular Signal Regulated Kinase
ESCRT	Endosomal Sorting Complexes Required for Transport
EXOC5	Exocyst Complex Component 5
FADD	Protein With a Death Domain
FasL	Fas Ligand
FasR	Fas Receptor
FBS	Fetal Bovine Serum
FC	Fold Change
FGF	Fibroblast Growth Factors
Flp	Flippase
FMNL2	Formin Like 2
FOXM1	Forkhead Box M1
FRT	Flippase Recognition Targets
FUCCI	Fluorescent Ubiquitination-based Cell Cycle Indicator
G1	Gap1
G2	Gap2
GAD	Genetic Association Database
GAF	cGMP-Specific Phosphodiesterases, Adenylyl Cyclases, FhlA
GAL	Galactosidase

GAPDH	Glyceraldehyde 3-Phosphate Dehydrogenase
GFP	Green Fluorescent Protein
GLUT1	Glucose Transporter 1
GO	Gene Ontology
GOTERM BP DIRECT	Gene Ontology Hierarchy for Biological Processes
GPNMB	Glycoprotein Nmb
HAT	Histone Acetyltransferase
HDAC	Histone Deacetylase
Hrs	Hepatocyte Growth Factor-Regulated Tyrosine Kinase Substrate
hts	Hu li tai shao
IAP	Inhibitor of Apoptosis
iCas	iCasper
IDEAS	ImageStream Data Analysis and Exploration Software
ING	Inhibitor of Growth
JAK	Janus Kinase
JAM	Junctional Adhesion Molecules
KD	Knockdown
KDM5B	Lysine Demethylase 5B
KIF23	Kinesin Family Member 23
LEF-1	Lymphoid Enhancer Binding Factor 1
Lgl	Lethal Giant Larvae
Lid	Little imaginal discs
M	Mitosis
MAGI	Membrane-Associated Guanylate Kinase Inverted
MARCM	Mosaic Analysis with a Repressible Marker
MCM	Mini-Chromosome Maintenance Complex
MCODE	Molecular Complex Detection
MMP	Metalloproteinase
Moe	Moesin
MPDZ	Multi-PDZ Domain Protein

mRNA	Messenger RNA
MYH10	Myosin Heavy Chain 10
Myo-II	Non-muscle Myosin II
N-WASP	Neural Wiskott-Aldrich Syndrome Protein
NASC	Nottingham Arabidopsis Stock Centre
NGS	Normal Goat Serum
ORC	Origin Recognition Complex
PAS	Per ARNT Sim
PATJ	PALS1-Associated Tight Junction
PBS	Phosphate Buffered Saline
PBST	Phosphate Buffered Saline – Triton-X Solution
PBSt	Phosphate Buffered Saline – Tween 20 Solution
PCNA	Proliferating Cell Nuclear Antigen
PCR	Polymerase Chain Reaction
PFA	Paraformaldehyde
PHD	Plant Homeodomain
PI	Propidium Iodide
PI3K	Phosphoinositide 3 Kinase
Pnr	Pannier
RACGAP1	Rac GTPase Activating Protein 1
RAPGEF2	Rap Guanine Nucleotide Exchange Factor 2
RB/Rb	Retinoblastoma
Rho	Ras Homolog Gene Family
RHOC	Ras Homolog Gene Family, Member C
RISC	RNA Induced Silencing Complex
RNA	Ribonucleic Acid
RNAi	RNA Interference
ROCK	Rho-Associated Protein Kinase
RT	Room Temperature
S	Synthesis
Scrib	Scribble

Shg	Shotgun
siRNA	Small Interfering RNA
SJ	Septate Junctions
STAT	Signal Transducer And Activator Of Transcription
Tcf	Transcription Factor
TGF-β	Transforming Growth Factor Beta
TJ	Tight Junctions
TNF	Tumour Necrosis Factor
TNFR	Tumour Necrosis Factor Receptor
TP53	Tumour Protein 53
TSG	Tumour Suppressor Genes
tTJ	Tricellular Tight Junctions
TUNEL	TdT-Mediated dUTP Nick-End-Labelling
UAS	Upstream Activating Sequence
Ubx	Ultrabithorax
VDRC	Vienna *Drosophila* Stock Centre
VEGF	Vasculature Endothelial Growth Factor
WASF3	WASP Family Member 3
Wnt	Wingless-Related Integration Site
WT	Wild-Type
ZA	Zonula Adherens
ZO	Zonula Occludens

Chapter 1 – General introduction

1.1 Tumorigenesis as a multistep process

Cancer is a group of diseases of over 100 different types of neoplasms, each with its own subtypes (Hanahan and Weinberg, 2000). The vast majority of human cancers are derived from the epithelial tissue and are called carcinomas.

Generally, tumorigenesis is a multistep process that develops over the course of decades through the accumulation of genetic aberrations that affect key biological processes (Farber, 1984; Hanahan and Weinberg, 2000). An exception to the rule are pediatric cancers, which can manifest as early as the first few months of life and are mostly epigenetic (Yiu and Li, 2015).

Genes that are critical for cancer development are split in two main categories: oncogenes and tumour suppressor genes (TSGs). Mutations in either induce similar changes in cells; the key difference being that oncogenes promote tumorigenesis (so are hyperactivated or overexpressed in cancers) whilst TSGs normally function to protect the tissue against tumorigenesis (so they suffer homozygote loss-of-function mutations) (Weinberg, 1994). Genetic lesions can vary in severity, from point mutations, which are rather subtle, to changes in chromosome complement (Hanahan and Weinberg, 2000). Epigenetic changes have an equally important role in tumour progression. Changes in gene expression associated with malignancy often occur as a result of altered chromatin remodelling, histone modifications, protein methylation or aberrant expression of non-coding RNAs (Dawson and Kouzarides, 2012).

Three main stages of tumorigenesis have been described: initiation, promotion and progression (Figure 1.1). The process begins (tumour initiation) with only one cell that suffers at least one driver mutation, usually affecting TSGs (Vincent and Gatenby, 2008). Driver mutations are mutations that confer the cell a selective growth advantage (Vogelstein et al., 2013). The mutant cell will undergo mitosis creating a population of cells that, even though not yet malignant, have a growth advantage over the wild-type cells within a tissue parenchyma. During tumour promotion, this

new population of cells will have to face harsh environmental conditions, either due to external factors or induced by their overgrowth. This will further promote mutagenesis and epigenetic changes (Dawson and Kouzarides, 2012; Vincent and Gatenby, 2008). Many populations of cells may develop at once through this process, but healthy tissue will outgrow many of them. The clones that are best adapted to the dynamic tumour microenvironment will be selected through a Darwinian-like process and will further progress towards malignancy (the tumour progression stage). As a result, the tumour will undergo an exponential growth which leads to an increase of the microenvironment acidity. Tumour cells will adapt and continue to grow whilst the surrounding wild-type tissue will face necrosis. Tumour progression culminates with the malignant cells acquiring migratory and invasive capability and ultimately metastatic properties (Vincent and Gatenby, 2008).

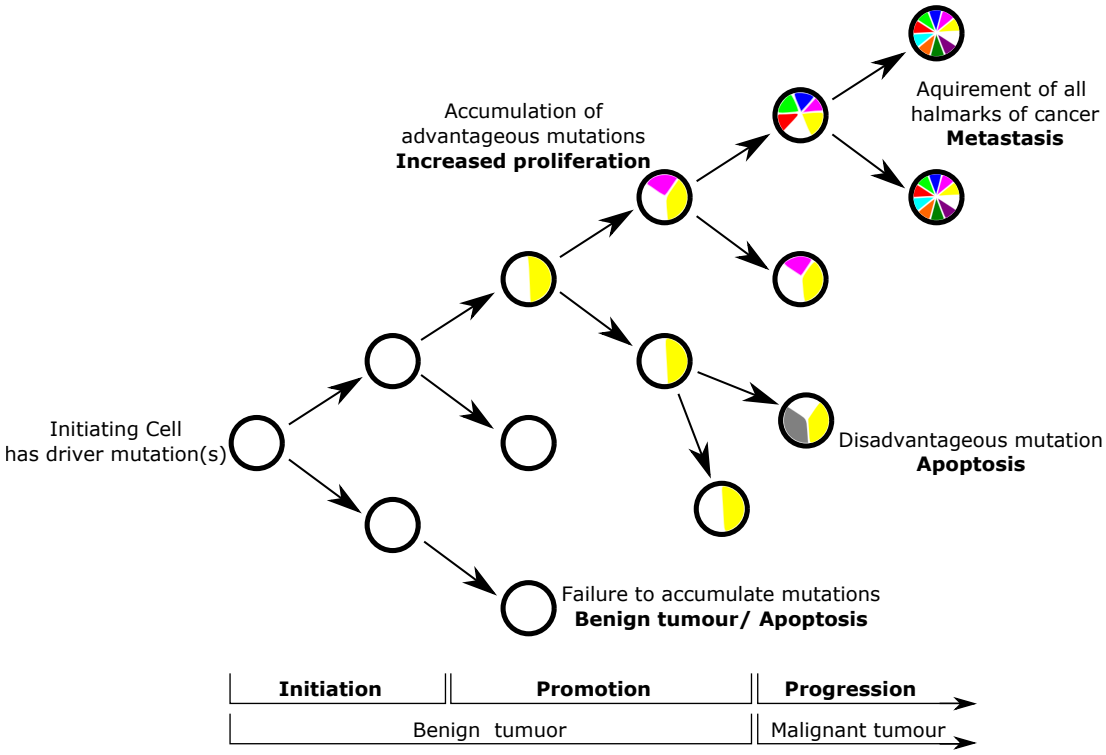


Figure 1.1 Tumour development through clonal selection

Tumour development begins from one cell that acquires one or more mutations that confer growth advantage over other cells from the tissue. Whilst it proliferates, the cell might continue to mutate. Most acquired mutations will not be beneficial, but if enough advantageous mutations accumulate, the cell will form a tumour which, with time, will become malignant. Stages of carcinogenesis as depicted by Farber are indicated at the bottom of the figure. Figure adapted from (Loeb, 2011).

The genetic mutations and epigenetic alterations accumulated by the cells have to alter specific biological processes in order to obtain a sub-clonal advantage and become malignant. Hanahan and Weinberg proposed a model by which cells must acquire eight biological capabilities (Table 1.1), referred to as hallmarks of cancer, each hallmark representing an evolved phenotype. In order to become malignant a cell has to develop all eight hallmarks, irrespective of the order of acquisition. The development of such capabilities is favoured by certain 'enabling characteristics' which almost always characterise the malignant tissue (Hanahan and Weinberg, 2011): cancer cells develop mechanisms that increase the rate of spontaneous mutations and actively recruit inflammatory cells which have immunosuppressive functions, or have the ability to change the tumour microenvironment in a way that further sustains tumorigenesis (Fouad and Aanei, 2017; Hanahan and Weinberg, 2011; Heusinkveld and van der Burg, 2011). Specific aspects of tumour progression which are of particular relevance to this thesis, namely adhesion, polarity, cell division and apoptosis, are described in greater detail in the following chapters (Chapters 1.2 – 1.4).

Table 1.1 Hallmarks of cancer

Hallmark	Description
Sustained proliferative signalling	Tumours are often characterised by overgrowth (Hanahan and Weinberg, 2011). Some of the mechanisms employed by cancer cells to deregulate the proliferative signalling are discussed in Chapter 1.2.
Growth suppression evasion	A series of feedback mechanisms are in place in healthy tissue to ensure that cells do not overrespond to proliferative signalling. As discussed in Chapter 1.2, cancer cells can become insensitive to such signalling (Hanahan and Weinberg, 2011).
Replicative immortality	Cancer cells have been shown to upregulate telomerase expression, which allows the reconstruction of the telomere and enables limitless replicative potential (Hanahan and Weinberg, 2011; Kim et al., 2017).

Hallmark	Description
Hallmarks of cancer - continued	
Apoptosis resistance	Many of the characteristics acquired by cancer cells during tumorigenesis would normally trigger apoptosis. Therefore, cancer cells must develop mechanisms to evade cell death (Hanahan and Weinberg, 2011). These mechanisms are discussed in more detail in Chapter 1.3.
Reprogrammed energy metabolism	In order to meet their high anabolic demands, cancer cells overexpress glucose receptors and glutamine transporters. They can even adopt anaerobic metabolism to overcome hypoxia. Additionally, cancer cells may employ alternative mechanisms to increase amino acid uptake, such as micropinocytosis of extracellular proteins and engulfment or phagocytosis of neighbouring cells (Fouad and Aanei, 2017; Hanahan and Weinberg, 2011).
Immune surveillance evasion	Cancer cells might impair the tumour-antigen detection system by not expressing antigens. Additionally, cancer cells can recruit other types of cells (e.g. regulatory T cells) which exhibit immunosuppressive functions. Moreover, the TGF-β pathway is often misregulated in cancer cells and secreted TGF-β can potentially exercise immunosuppressive functions (Fouad and Aanei, 2017; Hanahan and Weinberg, 2011; Heusinkveld and van der Burg, 2011).
Neo-vascularisation	Tumour cells trigger an 'angiogenic switch' and continuously activate angiogenesis, usually by overexpressing pro-angiogenic factors. In addition, expression of endogenous neovasculature inhibitors can be downregulated. Tumours can also form de-novo vascular networks through a process called vascular mimicry, or they can obtain a blood supply by forcing the existing capillary network to expand (Fouad and Aanei, 2017; Hanahan and Weinberg, 2011).

Hallmark	Description
Hallmarks of cancer - continued	
Invasion and metastasis	The ability of cells to dissociate from the primary tumour and give rise to new tumours at secondary sites is the main characteristic of cancers (Hanahan and Weinberg, 2011). This hallmark is discussed in more detail in Chapter 1.4.

It is worth noting that many of the hallmarks of cancer converge to the same pathways, promoting achievement of several hallmarks at once. For instance, the TSG TP53 has been implicated in cell cycle progression, detection of DNA damage, cell death evasion, replicative immortality, genome instability and energetic metabolism. Similarly, Ras overexpression, TGF-β and Akt signalling seem to be recurrent themes when talking about the hallmarks of cancer (Hanahan and Weinberg, 2011).

1.2 Mitotic signalling

1.2.1 Cell cycle progression in homeostasis

The cell cycle (Figure 1.2) can be divided in two main stages: interphase and mitosis. During interphase the DNA from the cell is duplicated so that during mitosis it can be precisely segregated into two genetically identical daughter cells. Mitosis is closely followed by cytokinesis, the stage during which the mother cell splits into two daughter cells (Cooper, 2000).

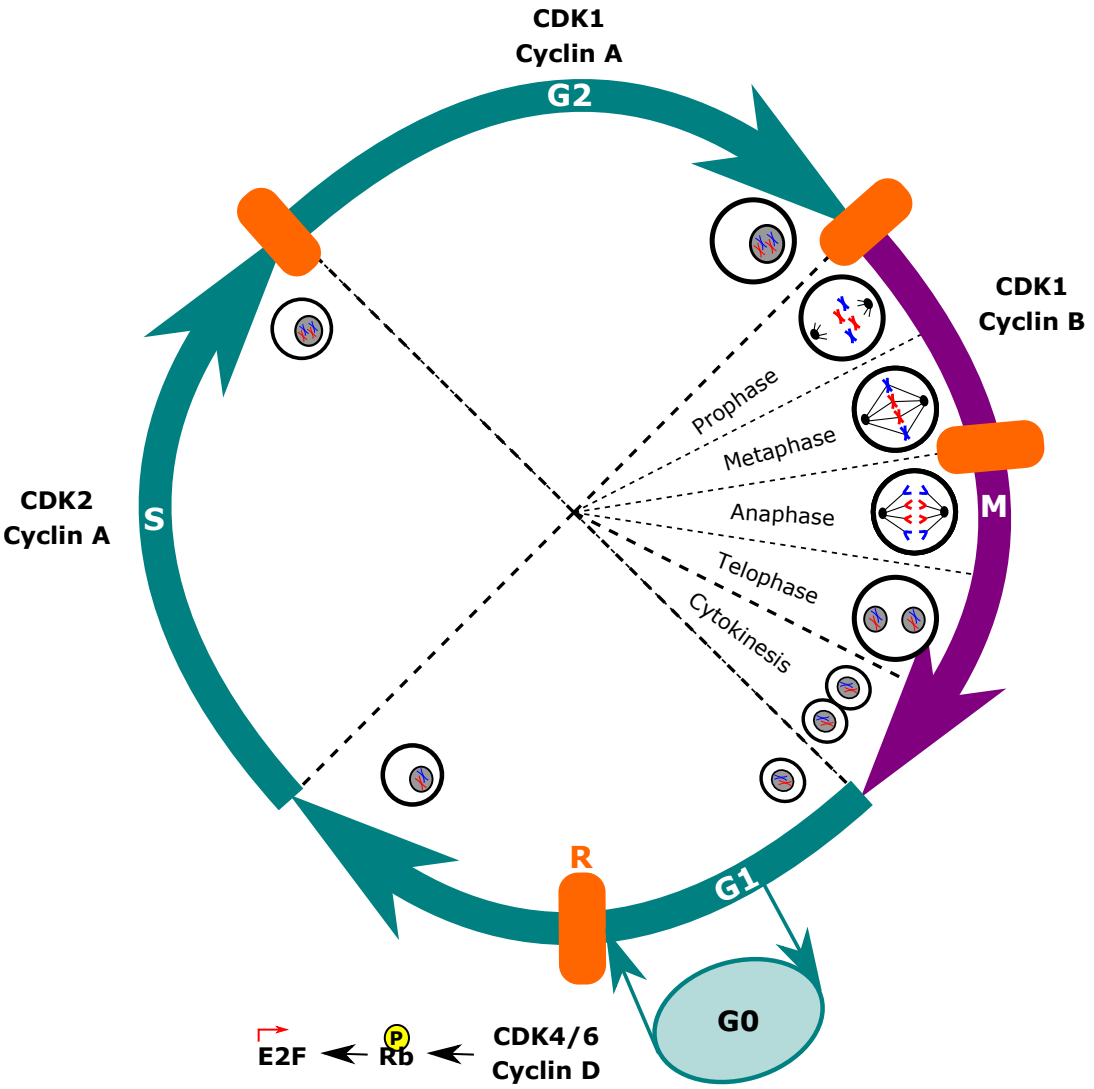


Figure 1.2 Cell Cycle of a eukaryotic cell

A schematic diagram of the cell cycle illustrating interphase (teal) and mitosis (purple), as well as cell cycle checkpoints (orange; R represents the 'restriction point') and the mediators of cell cycle progression (on the side). Cells can enter a quiescent state (G0). Terminally differentiated and senescent cells remain in G0 (cell cycle arrest) unless de-differentiation has occurred, whilst differentiated cells which retain proliferative capacity and transformed cells can re-enter the cell cycle, if signalled to do so. Figure adapted from (Cooper, 2000).

Interphase is the longest part of the cell cycle and can be further divided into three phases: gap 1 (G1) – characterised by cell growth; synthesis (S) – the stage during which the DNA is duplicated and gap 2 (G2) – characterised by intense protein synthesis in preparation for mitosis (Cooper, 2000). Transition from one phase to another is strictly regulated by cyclin-dependent kinases (CDKs) cyclins (CDK activators), and cyclin-dependent kinase inhibitor proteins (CKI) (Otto and Sicinski,

2017). Retinoblastoma proteins (Rb), p53 and Forkhead Box M1 (FOXM1) play a particularly important role in the transcriptional modulation of cell cycle progression (Otto and Sicinski, 2017; Saldivar et al., 2018). Transition through the cell cycle is strictly regulated at four checkpoints: one before the transition into each phase (G1/S, S/G2, G2/M) and one during mitosis (Cooper, 2000).

The 'restriction point' (R) is particularly important for cell cycle progression because once passed, cells commit to completing cell division. In healthy adult tissue, most cells are quiescent (G0), but differentiated cells which retain proliferative capacity and transformed cells can re-enter the cell cycle upon mitogenic stimulation (Otto and Sicinski, 2017). Growth factors, such as the epidermal growth factor receptor (EGFR), can awaken cells from G0 arrest by signalling through a variety of pathways (e.g. extracellular-signal-regulated kinase (ERK) and Phosphoinositide 3 kinase/Protein Kinase B (PI3K—AKT) pathways for EGFR), all of them ultimately impinging on the cyclin—cdk mechanism (Wee and Wang, 2017). G0 arrest is characterised by active (hypophosphorylated) Rb and subsequent impaired E2F transcription (Giacinti and Giordano, 2006). On the other hand, if DNA damage is sensed at the G1/S checkpoint, cell cycle arrest is initiated. In short, checkpoint kinase 1 (chk1) becomes activated and will further activate p53. P53 induces transcription of p21 (a kinase inhibitor) which prevents formation of cyclin E—CDK2 complexes, forcing the cell in G1 arrest (Otto and Sicinski, 2017).

G1/S transition is triggered by cyclin D dependent cdk4/6 activation which in turn triggers Rb hyperphosphorylation (leading to its inactivation) and subsequent release of E2F transcription factors. Concomitantly, active cdk4/6 sequester p21 and p27 (CKI proteins), preventing later inactivation of cdk2. E2F transcription factors drive cyclin E2 transcription. Cyclin E2 activates cdk2, triggering cell cycle progression, DNA replication and centrosome duplication. E2F transcription factors also promote transcription of genes involved in chromosome segregation and chromatin structure, therefore promoting DNA replication. During S phase, cyclin E is degraded allowing CDK2 interaction with newly synthesised cyclin A2. Furthermore, Aurora A localises to the centrosomes and further promotes G1/S transition by stabilizing the N-Myc

proto-oncogene protein, a helix-loop-helix transcription factor (Otto and Sicinski, 2017). At the end of the S phase, the cell should have two copies of each chromosome.

Cdk2 can be inactivated by wee1 driven phosphorylation. When the cell cycle progression is to be resumed, cell division cycle 25 (cdc25) dephosphorylates cdk2 at sites phosphorylated by wee1. At this stage, chk1 can induce temporary S phase arrest in response to DNA damage by phosphorylating and thus inactivating cdc25A (Otto and Sicinski, 2017). Similarly, ATR kinase senses incomplete DNA replication and delays S/G2 transition by repressing CDK1 activity. Once replication is complete, ATR activity declines and S/G2 transition can take place via CDK1 driven FOXM1 phosphorylation (Saldivar et al., 2018).

The G2/M checkpoint is also under the control of chk1, which can induce G2 arrest by inactivating cdc25 proteins. Additionally, chk1 can activate wee1 directly, promoting cdk1 and cdk2 inactivation (Otto and Sicinski, 2017).

During late G2 phase, cdk1 becomes activated by cyclin H—CDK7. Additionally, Aurora A dependent polo like kinase one's (plk1) activation takes place, which drives cdc25C activation and triggers wee1 degradation. Both events ensure activation of cyclin B—cdk1 complexes, which promote G2/M transition (Otto and Sicinski, 2017). Nuclear division takes place in four stages: (i) prophase – chromosomes condense; ii) metaphase – chromosomes position onto the mitotic spindle, forming the 'metaphase plate'; iii) anaphase – replicated chromosomes separate and migrate to opposite ends of the cell; iv) telophase – the nuclear envelope is reassembled and chromosomes decondense (McIntosh and Koonce, 1989). Aurora A modulates centrosome maturation, spindle assembly and orientation and acts in concert with Aurora B, a protein that controls chromosome condensation and orientation. Plk1 triggers chromosome segregation. Additionally, Aurora A and B play important roles in cytokinesis (Otto and Sicinski, 2017). One more checkpoint acts during mitosis, the 'spindle assembly' checkpoint, which monitors chromosome alignment on the

mitotic spindle (Cooper, 2000). Successful completion of M phase results in two identical daughter cells, each of them in interphase.

1.2.2 Changes to proliferation signalling encountered in malignancy

The fundamental trait for tumours is overgrowth. In order to successfully achieve this, cells must sustain proliferative signalling whilst evading growth suppression. In homeostasis, tissues strictly control the production and release of growth factors and possess a number of negative feedback mechanisms that further control the proliferation rate. Cancer cells can employ several strategies to increase proliferation: i) they can overexpress growth factor receptors, becoming hypersensitive to ambient stimuli; ii) they can stimulate growth factor secretion from the healthy cells around the tumour; iii) cancer cells can alter the pathways that control cell cycle progression or iv) they can switch to autocrine stimulation. Normally, in a healthy tissue, one cell type would secret growth factors that stimulate the growth of another cell type (heterotypic signalling). Cancer cells can switch to autocrine signalling by producing the growth factors they are responsive to themselves (Hanahan and Weinberg, 2000; Hanahan and Weinberg, 2011).

Similarly, in homeostasis, cells secrete anti-growth factors. Normally, cells sense changes in their environment and based on that decide whether to proliferate, enter G0 cell-cycle arrest or a postmitotic state. Cancer cells become insensitive to such stimuli, most often by disrupting the Rb and the p53 pathways to avoid the quiescent state and the c-myc pathway, as such avoiding terminal differentiation. Additionally, cancer cells abrogate contact inhibition. Malignant cells can adjust their response to either proliferative or anti-proliferative signals by modulating integrin expression, which further impinges on the cell's adhesive properties (Hanahan and Weinberg, 2000; Hanahan and Weinberg, 2011). Cancer cells, however, do not just enable pro- and block anti- proliferative signals; rather they adopt aberrant biochemical signalling pathways in a context-dependent manner, depending on the tumour setting and the stage of tumorigenesis (Fouad and Aanei, 2017).

1.3 Apoptotic signalling

1.3.1 Principles of apoptotic signalling in homeostasis

Apoptosis has been evolutionarily conserved within eukaryotes as a method of ensuring tissue homeostasis. Two separate mechanisms of apoptosis have been described: the extrinsic and the intrinsic apoptotic programs (Figure 1.3). Both programs act towards triggering a proteolytic cascade of caspases and culminate with cell shrivelling and disassembling followed by consumption of cell debris by phagocytes and neighbouring cells (Nagata, 2018).

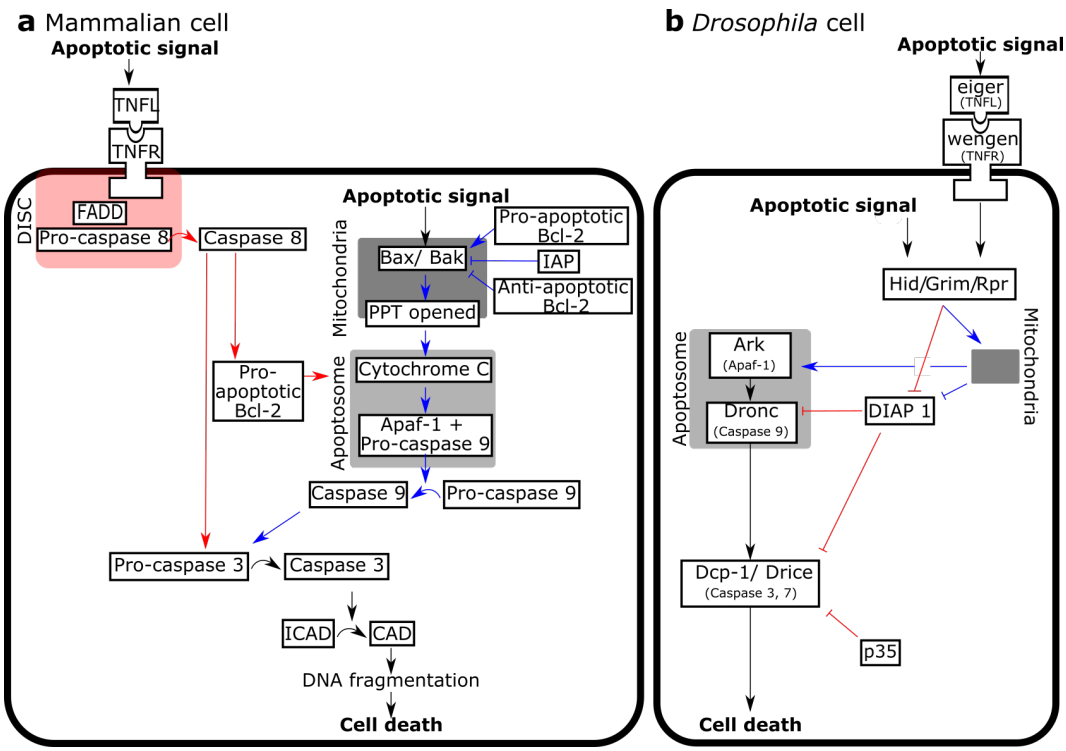


Figure 1.3 Apoptotic signalling cascade

(a) Mammalian cell. Two apoptotic pathways have been described: the mitochondrial pathway that mainly processes intrinsic apoptotic signals, and a death receptor pathway that only processes extrinsic apoptotic signals. Both pathways relay on the activation of a caspase cascade **(b)** *Drosophila* cell. The *Drosophila* apoptotic cascade is reversed: apoptotic signalling is always on and is inhibited by DIAP1 in the absence of apoptotic signals; apoptosis effectors can localise to the mitochondria during apoptosis (in mammals, apoptosis modulators are released from the mitochondria during apoptosis). Blue: mitochondrial pathway. Red: non-mitochondrial pathway. Figure adapted from (Clavier et al., 2016; Marchal et al., 2012; Nagata, 2018; Steller, 2009).

The intrinsic apoptotic pathway (Figure 1.3a, blue) processes apoptotic signals of intracellular origin. This pathway is rigorously regulated by the inhibitor of apoptosis protein family (IAP) which comprises antiapoptotic proteins and the B cell lymphoma2 (Bcl-2) family proteins. Bcl-2 proteins can be both proapoptotic (e.g BH3 proteins Bim, Puma, Bmf, Bid, Noxa, Hrk, Bad and effector molecules Bax, Bak) or antiapoptotic (e.g. Bcl-2, Bcl-xL, Mcl1, A1, Bcl-B). The balance between the pro- and anti- apoptotic members regulates the ionic permeability of the outer mitochondrial membrane: the mitochondrial permeability transition pore opens as a result of Bax/Bak activation. Bax acts under p53 surveillance and is activated in response to stress signals. As a result, cytochrome c, a key regulator of the apoptotic cascade, is released to the cytoplasm triggering the formation of the apoptosome (Apaf-1 and pro-caspase 9) and caspase 9 cleavage. Once activated, caspase 9 initiates the execution pathway by cleaving pro-caspase 3 (Nagata, 2018).

The extrinsic apoptotic machinery (Figure 1.3a, red) relies on the tumour necrosis factor (TNF) proteins. Apoptosis is triggered by a death ligand (e.g. Fas ligand (FasL), TNF-α) that binds to a death receptor from the cell surface (e.g. fas receptor (FasR) or TNFR1/TNFR2 respectively). An associated protein with a death domain (FADD) will then bind the cytoplasmic death domain of the TNFR, which allows for pro-caspases' (e.g. pro-caspase 8 or 10) recruitment. FADD can also recruit c-FLIP (cellular FADD-like IL-1β-converting enzyme), a caspase 8 inhibitor. Pro-caspases, together with the FADD and c-FLIP adaptor molecule and the death receptor form the death inducing signalling complex (DISC). Pro-caspases will then activate through autocatalytic cleavage and, as a consequence, are released into the cytoplasm where they further activate executioner caspases (e.g. pro-caspase 3). An additional extrinsic apoptotic mechanism makes use of the mitochondrial apoptotic pathway. For instance in hepatocytes, the activated caspase 8 cleaves Bid (Bcl-2 protein), triggering cytochrome c release from the mitochondria which will activate the pathway typically used for intrinsic apoptosis (Nagata, 2018).

Active executioner caspases execute apoptosis by cleaving more than 1000 cellular substrates. The apoptotic process culminates with fragmentation of nuclear DNA as

a result of executioner caspases cleaving the inhibitor of caspase-activated DNase (ICAD) and subsequent release of caspase-activated DNase (CAD) (Nagata, 2018).

Drosophila's apoptotic machinery (Figure 1.3b) is similar to the mammalian one described above. Seven caspases are encoded in the fly genome: three initiator caspases (Dronc, Dredd, Strica) and four executioner caspases (Drice, Death caspase 1 (Dcp-1), Decay, Damm). In summary, Ark, the fly homologue of Apaf-1, activates Dronc, the equivalent of caspase 9, which in turn activates the executioner caspase Drice leading to cell death. P35 protein and Death-associated inhibitor of apoptosis 1 (DIAP1) can inhibit the activity of both *Drosophila* executioner caspases. However, some discrepancies are worth noting: i) cells from *Drosophila* experience a chronic activation of Dronc which is compensated by Dronc interaction with DIAP1; ii) apoptosis regulators localise at the mitochondria during apoptosis; iii) cytochrome c signalling might be dispensable for apoptosome formation (Clavier et al., 2016).

1.3.2 Changes to apoptotic signalling in cancer

The harsh conditions developing tumours have to face (e.g. starvation, hypoxia) and many of the traits acquired by the malignant cells, such as DNA damage and hyperactivation of proliferative signalling, would normally induce apoptosis. Therefore, cancer cells must develop mechanisms to evade programmed cell death (Hanahan and Weinberg, 2000). The intrinsic apoptotic machinery seems to be preferentially triggered by tumour progression. Several apoptosis modulators were found to be affected in a variety of human cancers, with more than 50% of cancers relying on functionally inactive tumour protein 53 (TP53, p53). Bcl-2 and IAP overexpression are also common in cancers (Nagata, 2018). Other DNA damage sensors, such as inhibitor of growth one (ING1) for instance, have also been found to be downregulated in tumours (Helbing et al., 1997). Additionally, tumours might decrease expression of proapoptotic factors, decrease membrane receptors for apoptotic ligands, increase expression of negative regulators of apoptosis and/or increase expression of survival signals. On the other hand, tumours might allow

certain levels of necrosis to occur, and will induce necrosis of the surrounding tissue. This is beneficial for tumour progression because when necrotic cells burst, they release pro-proliferative and proinflammatory signals. The later attracts immune inflammatory cells that can be recruited and converted by cancer cells to aid tumour development. Additionally, cancer cells might promote autophagy. Through autophagy, cells break down cellular organelles and use the resulting catabolites as substrate for biosynthesis and energy metabolism. Moreover, some stressed cancer cells might employ autophagy to reach a reversable dormancy state. However, under certain conditions, autophagy can also have an anti-tumorigenic effect (Hanahan and Weinberg, 2000; Hanahan and Weinberg, 2011). Apoptosis resistance should be seen as a trait of tumours rather than individual cancer cells. Some cancer cells are more susceptible to apoptotic stimulation than healthy tissue, hence the success of many anti-cancer therapies (Fouad and Aanei, 2017).

1.4 Invasion and Metastasis

For tumours to become malignant, they must become invasive. After all, the ability to invade surrounding tissues and metastasize are the only abilities that truly set apart neoplasms from benign tumours (Fouad and Aanei, 2017). This requires epithelial cells to take on mesenchymal or amoeboid characteristics (Yilmaz and Christofori, 2010). However, in order to form a secondary tumour at a secondary site, cells must undergo the opposite process and regain their epithelial characteristics. Each of these processes relies on a cell's ability to manipulate its adhesive state. It is therefore of no surprise to find that the same collection of proteins that regulate cell-cell junctions (regulators of adhesion, polarity, the cytoskeleton and trafficking) are also implicated in cancer and metastasis (Bruner and Derksen, 2018; Lu et al., 2018; Mack and Georgiou, 2014; Martin and Jiang, 2009; Rusu and Georgiou, 2020).

From a mechanistic point of view, metastasis can be described as a five step process (Figure 1.4): i) cells sprout from the primary tumour (either individually or as a group) and invade the surrounding tissue, ii) they then enter the blood or lymphatic circulation (intravasation), iii) to later escape (extravasation) iv) and form

micrometastatic lesions at a secondary site v) which will later develop into macroscopic tumours (colonisation). Micrometastasis (Figure 1.4c) must adapt to the new environment in order to begin colonisation. This is believed to be a difficult process as cancer cells lack the support of the stroma that the primary tumour has (Fouad and Aanei, 2017). However, more recent research suggests that cancer cells might be able to prime the metastatic site before their arrival (Peinado et al., 2017). Once successful colonisation has been achieved, cancer cells may further disseminate (Hanahan and Weinberg, 2011).

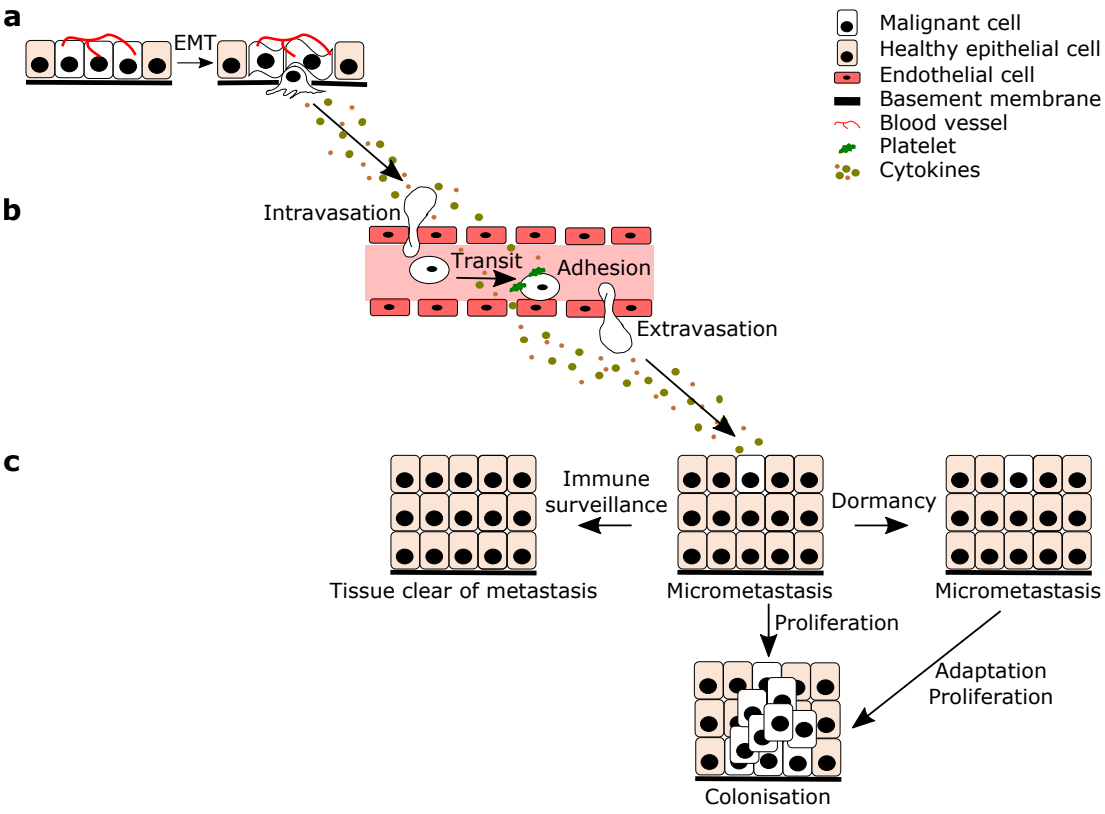


Figure 1.4 Schematisation of the invasion-metastasis process

(a) Invasion. Tumour cells break from the tissue and cross the basal lamina. They may adopt different types of motility: mesenchymal (represented here), ameboid or collective. **(b)** Tumour cells make use of the sanguine and lymphatic circulation to travel long distances. Association with blood cells improves tumour cells survival and ability to escape the blood stream. **(c)** Once tumour cells reach a new tissue, they can face three fates: If they cannot adapt to the new environment, invasive cells die or enter a dormant state, from which they can awake even decades later; if they can adapt, the invasive cells colonise the new tissue. It is believed that tumour cells also send signals (cytokines) to prepare the pre-metastatic niche to help colonisation. Figure adapted from (Gómez-Cuadrado et al., 2017).

1.4.1 Epithelial cell adhesion in homeostasis

Epithelial cells form highly organised polarised sheets with characteristic cell morphologies and tissue architecture. Cell-cell adhesion and intercellular communication are prerequisites of such cohesive sheets of cells, and cell connectivity is mediated through several junctional assemblies, namely: desmosomes, adherens, tight and gap junctions (Figure 1.5). Adhesive contacts between cells and the extracellular matrix are maintained by focal adhesions and hemidesmosomes on the basal membrane. These cell-cell junctions form signalling hubs that not only mediate cell-cell adhesion, but impact multiple aspects of cell behaviour, helping to coordinate epithelial cell shape, polarity and function. This chapter will focus on the tight and adherens junctions.

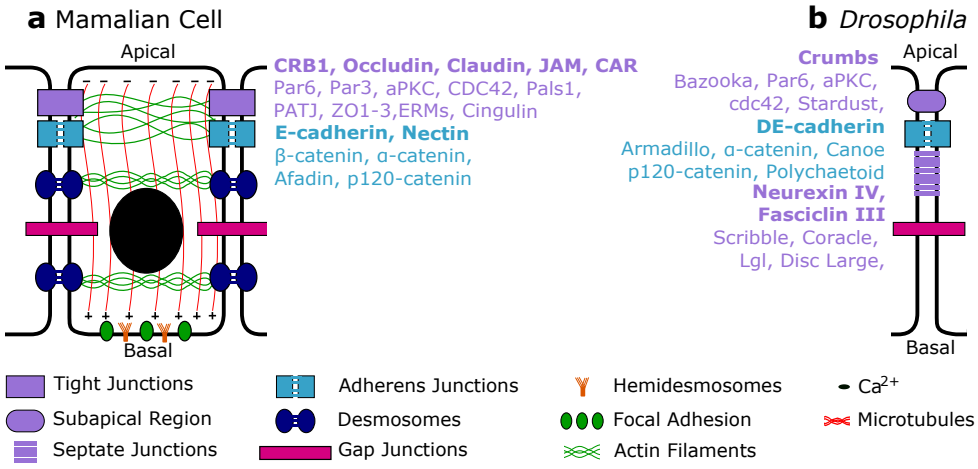


Figure 1.5 Cell adhesion in mammalian and *Drosophila* epithelial cells

(a) Mammalian epithelial cell. Communication and adhesion between neighbouring epithelial cells are ensured through the correct apicobasal localisation of multiple intercellular junctions. In vertebrates, tight junctions occupy the most apical part of the membrane, followed by adherens junctions, desmosomes and gap junctions. Adhesive contacts between cells and the extracellular matrix are maintained by focal adhesions and hemidesmosomes on the basal membrane. Both cell junctions and focal adhesions are tightly linked to the cytoskeleton through microtubules, actin filaments and microfilaments, forming an intricate and complex network that supports cell signalling. **(b)** Cell adhesion in *Drosophila* epithelial cells. Invertebrate epithelial cells possess adherens junctions that are located apical to the septate junctions, the invertebrate functional orthologue of tight junctions. Homologues of mammalian tight junction proteins can also be found in the subapical region of the *Drosophila* cell, a distinct membrane region apical to the ZA. Molecular differences are highlighted on the image. Bold text represents transmembrane proteins. Reproduced from (Rusu and Georgiou, 2020).

1.4.1.1 Tight junctions: molecular composition and architecture

Tight junctions (TJ) encircle epithelial cells at the most apical side of the lateral membrane (Figure 1.5a) where they form the zonula occludens (ZO), a belt like structure of tight connectivity between adjacent cells. TJs act as a paracellular diffusion barrier (or gate) for ions and solutes, and as a fence for proteins that localise at, or in close proximity to, the apicolateral membrane, thus preventing the mixing of apical and basolateral determinants. Additionally, through their linkage to the cytoskeleton, they also act as mechanotransducers, forming signalling platforms that can alter gene expression (Balda and Matter, 2009; Hatte et al., 2018; Matter and Balda, 2003; Zihni et al., 2014). TJ biochemical composition (Figure 1.6) includes both transmembrane components, junctional adhesion molecules (JAMs) and numerous complexes of cytosolic adaptors and regulatory proteins, known as the TJ plaque.

Claudins, occludin, tricellulin and marvelD3 have been identified as constituents of TJ strands (Furuse et al., 1993; Ikenouchi et al., 2005; Raleigh et al., 2010). Claudins are the major determinant of paracellular permeability (Günzel and Yu, 2013) and have been shown to be sufficient for TJ nucleation (Furuse et al., 1998). Claudins are able to recruit the zonula occludens scaffolding proteins (ZO-1, -2, -3), whose interaction is required for TJ formation (Umeda et al., 2006).

The cytosolic TJ plaque comprises scaffold and cytoskeletal proteins. This organised network of proteins confers a signalling platform by interlinking TJ components with cytoskeletal proteins and regulators, signalling components (e.g. phosphatases, kinases) and proteins with dual membrane-nuclear localisation. Therefore, TJs can regulate vital processes for epithelial architecture such as cell proliferation, invasion and gene expression (Balda and Matter, 2008; 2016; Bauer et al., 2010). ZO-1 plays a critical role in tissue organisation being able to interact with ZO-2, ZO-3, occludin, claudin, α-actinin, kinases, phosphatases and transcription factors (Bauer et al., 2010; Fanning, 2001; Fanning et al., 1998; Fanning et al., 2007; Katsuno et al., 2008; Matter and Balda, 2007; Umeda et al., 2006; Wittchen et al., 1999). Other scaffold proteins that contribute to the TJ signalling platform are ZO-2, -3, cingulin, the

membrane-associated guanylate kinase inverted (MAGI) proteins, PALS1-associated tight junction (PATJ), paracingulin and multi-PDZ domain protein (MPDZ) (Van Itallie and Anderson, 2014; Zihni et al., 2016).

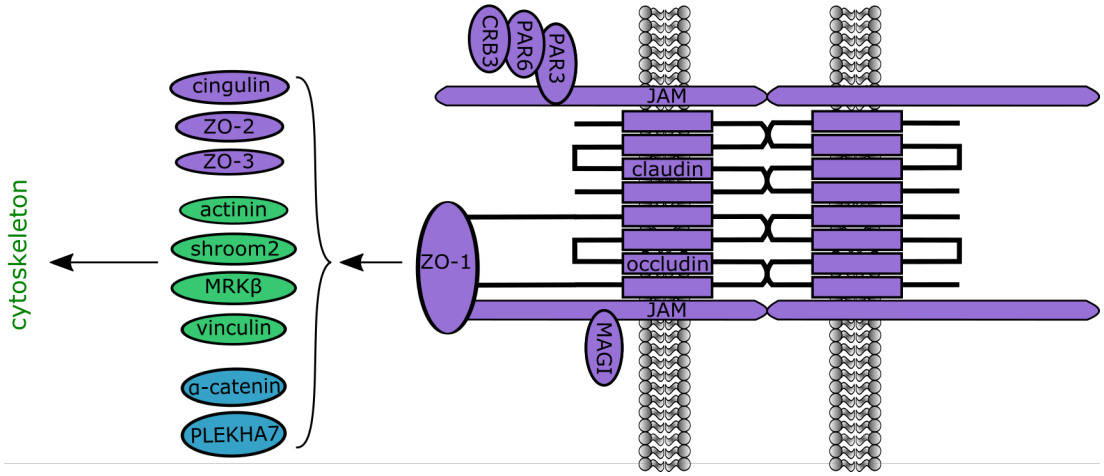


Figure 1.6 Molecular composition and architecture of tight junctions and the cytosolic tight junction plague

Claudins, occludins and JAMs form channel like structures between cells allowing the transport of ions and other molecules. The cytosolic region of TJ transmembrane proteins interacts with polarity complexes through Par3, highlighting their role in the establishment of the apicobasal polarity. A series of scaffolding proteins localised at TJs (cytoplasmic plague) connect to the cytoskeleton. The most remarkable scaffolding protein is ZO-1, which can form complexes with various cytoskeleton linkers and/or modulators such as actinin, Shroom2, MRKβ, vinculin. Through its interactions with vinculin, afadin and α-catenin, ZO-1 confers a link between AJs and TJs. Actin and actin interactors are represented in green, AJs components in teal and tight junction components in purple. Figure reproduced from (Rusu and Georgiou, 2020).

Within a sheet of cells, the vast majority of junctions that form are between two neighbouring cells. However, tricellular contacts can also form and these contacts require several specialised junctional architectures (Figure 1.7). At tricellular contacts, TJ strands from neighbouring cells attach and turn basally, forming the central sealing element (Staehelin, 1973). Both tricellulin and angulin preferentially localise at tricellular TJs (tTJs).

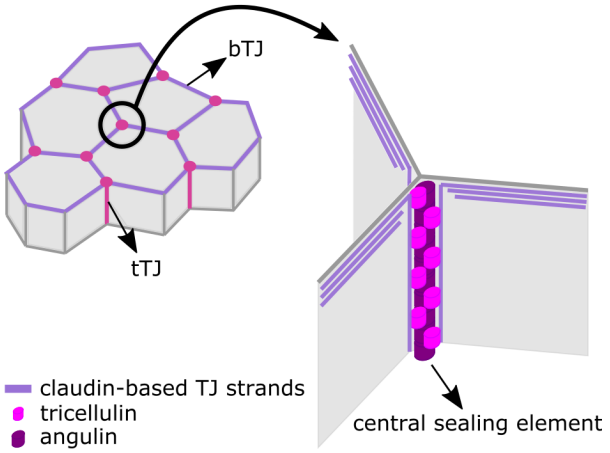


Figure 1.7 Molecular composition and architecture of tricellular tight junctions

Tricellular TJs are enriched in tricellulin and angulin in addition to the already presented TJ components. TJ strands from neighbouring cells attach and turn basally, forming the central sealing element. Figure reproduced from (Rusu and Georgiou, 2020).

Although TJs are vertebrate specific, septate junctions (SJs) function as the main occluding junctions in invertebrates (Figure 1.5b). SJs are thought to be analogous to TJs from a functional point of view, but they differ in numerous ways, including in both their molecular composition and in their location on the lateral membrane (Matter and Balda, 2003).

1.4.1.2 Adherens junctions: molecular composition and architecture

Adherens junctions (AJs) are strong anchoring junctions that form the zonula adherens (ZA), just basal to the ZO in vertebrates. Together with TJs and desmosomes, AJs define the apical junctional complex (Figure 1.5) (Farquhar and Palade, 1963). Just as with TJs, AJs are composed of membrane spanning adhesion molecules with extracellular domains which form intercellular connections with neighbouring cells, and with intracellular domains which associate with various cytoplasmic scaffolding and signalling complexes, forming a cytoplasmic signalling plaque (Figure 1.8) (Mack and Georgiou, 2014).

AJs are extremely important for tissue morphogenesis, homeostasis, and plasticity. They not only mediate cell adhesion, but also cytoskeletal dynamics, intracellular signalling and transcription regulation (mainly through β-catenin). This places AJs at the core of cellular processes such as cell recognition, cell division, polarisation and motility (Baum and Georgiou, 2011; Farge, 2003; Nishimura and Takeichi, 2009; Okada et al., 2007; Whitehead et al., 2008; Yonemura, 2011).

From a structural point of view, the AJ consists of a mosaic of independent cadherin and nectin clusters, linked together and coordinated by actin filaments (Figure 1.8) (Indra et al., 2013). Additionally, in a mature junction, the cadherin-catenin complex and nectins interact with adhesion molecules from the TJ (Indra et al., 2013).

Cadherin clusters are the major components of the AJ and consist of cadherin-catenin multi-protein complexes. Type I classic cadherins are at the core of these complexes. The extracellular domains of cadherins from adjoining cells form dimers through Ca^{2+} dependent homophilic interactions and therefore physically connect neighbouring cells (Gumbiner et al., 1988). Intracellularly, E-cadherin binds to p120-catenin (p120) and β-catenin (Meng and Takeichi, 2009). P120-catenin–E-cadherin interactions stabilize the complex at the cell surface (Ishiyama et al., 2010). In addition, p120 regulates the RhoA and Rac1 RhoGTPases (Anastasiadis, 2007; Yanagisawa et al., 2008) The E-cadherin–β-catenin interaction is important for three reasons: i) it recruits α-catenin to the AJ; ii) it aids in the transduction of signals from the cell-cell junction to the nucleus (Farge, 2003; Gladden et al., 2010; Okada et al., 2007; Whitehead et al., 2008); iii) it modulates canonical Wnt signalling by preventing β-catenin interaction with transcription factor/lymphoid enhancer binding factor 1 (Tcf/LEF-1) (Gottardi et al., 2001; Orsulic et al., 1999). Less well studied members of the cadherin-catenin junctional complex include vinculin and epithelial protein lost in neoplasm (EPLIN).

Nectins are ubiquitously expressed Ca^{2+} independent immunoglobulin-like transmembrane adhesive receptors. Nectins link to cadherin complexes and the cytoskeleton by binding afadin, which in turn interacts with α-catenin and the actin

cytoskeleton (Takai et al., 2008). By interacting with integrins, the nectin-afadin complex also instigates a link between cell-cell and cell-matrix adhesion systems (Takai et al., 2008).

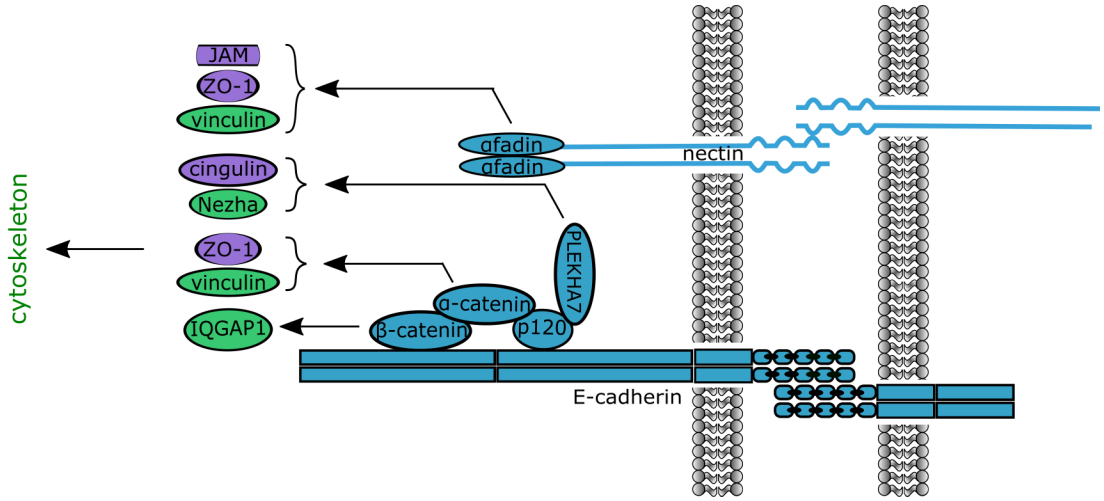


Figure 1.8 Molecular composition and architecture of adherens junctions

Type I cadherins, here represented by E-cadherin, are the main component of adherens junctions. The cytosolic region of E-cadherin binds p120 and β-catenin, which further recruits α-catenin, which binds F-actin. P120-catenin further recruits PLEKHA7 which binds Nezha, ensuring a link to the microtubule cytoskeleton. Nectin-nectin interactions also take place between neighbouring cells. In the cytosol, nectin forms a complex with afadin through which it links to the actin network and the cadherin clusters. Actin and actin interactors are represented in green, AJs components in teal and tight junction components in purple. Figure reproduced from (Rusu and Georgiou, 2020).

1.4.1.3 Molecular nature of cell junction-cytoskeleton interactions

Both AJs and TJs are tightly linked to the cytoskeleton through actin and microtubule filaments (Figure 1.5). The resulting network links the intercellular junctions to virtually all compartments of the cell, forming a complex signalling platform able to transduce both adhesive and mechanical signals from the membrane into the cell, and back again. These signals can drive junction reorganisation.

AJ stability relies on the actomyosin cytoskeleton. Several studies have shown that actin or myosin depletion can disrupt cadherin-based cell-cell adhesion, suggesting the existence of a complex interplay between the AJ and cytoskeletal components

(Liang et al., 2015; Miyake et al., 2006; Sawyer et al., 2009; Shewan et al., 2005; Smutny et al., 2010; Vaezi et al., 2002; Verma et al., 2012). The link to actomyosin strengthens adhesion by stabilising E-cadherin and promoting cadherin clustering (Lecuit and Yap, 2015). One molecular component of the cytoskeleton essential for junction integrity is non-muscle myosin II (Myo-II), which has two isoforms present at cell-cell junctions in mammalian epithelial cells: Myo-IIA and Myo-IIB. It has been shown that depletion of either can perturb E-cadherin distribution at junctions (Smutny et al., 2010).

Multiple lines of evidence show that α-catenin binds actin filaments indirectly through vinculin and EPLIN (Abe and Takeichi, 2008; Watabe-Uchida et al., 1998; Yonemura et al., 2010). Additionally, α-catenin conformation can be modified by force: α-catenin can switch from a 'closed' to an 'open' conformation that allows for the simultaneous binding of β-catenin and F-actin. The tension needed to switch to an 'open' conformation is driven by actomyosin contraction (Ishiyama et al., 2013). It is however important to note that there are many additional ways in which AJs can be linked to the actin cytoskeleton. For example, E-cadherin directly interacts with the motor Myosin VI, which is involved in processes such as clathrin-mediated endocytosis and cell migration (Buss et al., 2004; Mangold et al., 2012).

For TJs, the most important cytoskeletal linkers are the ZO proteins. ZO-1, ZO-2 and occludin link directly with F-actin (Fanning et al., 1998; Van Itallie et al., 2016; Wittchen et al., 1999). ZO-1 also interacts with Shroom2 and MRCKβ, both regulators of Myo-II activity (Etournay et al., 2007; Huo et al., 2011). Additionally, cingulin was shown to interact with both myosin and F-actin (Cordenonsi et al., 1999; D'atri and Citi, 2001).

The actin cytoskeleton is a highly dynamic structure (Yamada et al., 2005) and therefore filament turnover and actin assembly must take place at the ZA in order to ensure cytoskeleton integrity. Indeed, several actin regulators, such as actin related protein 2/3 (Arp2/3), neural Wiskott-Aldrich syndrome protein (N-WASP), cortactin and formins are recruited to the AJs, which confer cadherin clusters the ability to

actively build actin filaments (Kovacs et al., 2011; Lecuit and Yap, 2015; Wu et al., 2014). In turn, both Arp2/3 and N-WASP are required for AJ and TJ assembly and proper organisation (Ivanov et al., 2005; Kovacs et al., 2011).

AJ assembly and homeostasis also depends on microtubule integrity (Meng et al., 2008; Stehbens et al., 2006). Microtubules, tethered to the AJ via dynein, provide a track for the kinesin-dependent delivery of the junctional components necessary for junction formation (Ligon and Holzbaur, 2007). PLEKHA7 links AJs to microtubules by simultaneously binding p120-catenin and Nezha (a microtubule minus end binding protein) (Meng et al., 2008). Nezha further interacts with KIFC3 to promote ZA formation (Meng et al., 2008). Other linkers that could potentially tether microtubules to the AJ include IQGAP1. It is however highly likely that microtubule and actin dynamics at the ZA are interlinked (Kaverina et al., 2002; Ligon and Holzbaur, 2007; Ligon et al., 2001; Mary et al., 2002).

1.4.1.4 Molecular mechanisms of protein turnover at cell-cell junctions

Cell junctions are highly dynamic structures that continually form and disassemble; an attribute that is essential to preserve epithelial integrity. This inherent junctional plasticity is required to accommodate changes in internal and external mechanical forces over time, and to maintain tissue homeostasis in stable epithelia (Baum and Georgiou, 2011).

Several proteins localised at the apical junctional complex are internalised through clathrin, caveolin or dynamin mediated endocytosis. E-cadherin turnover at the AJ (Figure 1.9) has been most heavily researched, but other junctional proteins, such as α-catenin, β-catenin, ZO-1, Fasciclin III, Crumbs, Pals1, Par3 and claudins undergo similar dynamic recycling (de Madrid et al., 2015; Gehne et al., 2017; Georgiou et al., 2008; Harris and Tepass, 2008; Wells et al., 2006; Wong et al., 2010).

Clathrin-mediated endocytosis can be dissected into five stages: nucleation, cargo selection, clathrin coat assembly, vesicle scission, and clathrin uncoating (McMahon

and Boucrot, 2011). Nucleation (Figure 1.9b) involves the formation of a membrane invagination, which then recruits the adapter protein AP2 (Figure 1.9c), which can then bind other cargo-specific adaptor proteins, thereby mediating cargo selection (Henne et al., 2010). Once detached from the plasma membrane, following vesicle scission (Figure 1.9d), hepatocyte growth factor-regulated tyrosine kinase substrate/endosomal sorting complexes required for transport (Hrs/ESCRT) mediated sorting processes target the protein either for recycling or for degradation (Palacios et al., 2005) (Figure 1.9e); the vesicles make use of the microtubule and actin networks to travel back to the junction or towards lysosomes depending on the fate decided for the cargo (West and Harris, 2016). Fate is determined pre-internalisation by modifications to protein structure (Figure 1.9a).

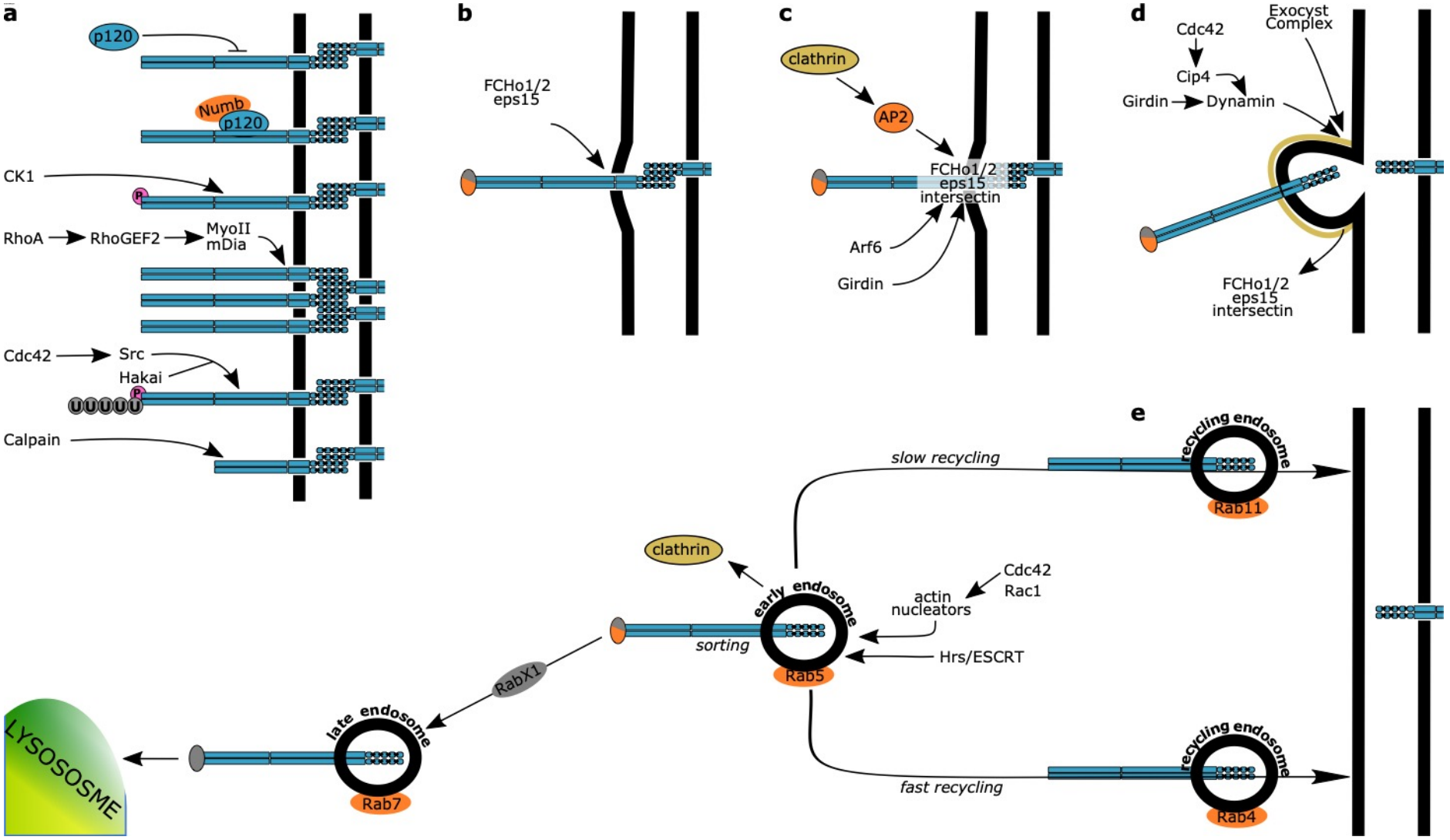

a
p120
Numb
p120
CK1
P
RhoA
RhoGEF2
MyoII
mDia
Cdc42
Src
Hakai
P
Ub Ub Ub Ub Ub
Calpain
b
FCHo1/2
eps15
c
clathrin
AP2
FCHo1/2
eps15
intersectin
Arf6
Girdin
d
Cdc42
Exocyst
Complex
Cip4
Girdin
Dynamin
FCHo1/2
eps15
intersectin
e
recycling endosome
slow recycling
Rab11
clathrin
Cdc42
Rac1
actin
nucleators
early endosome
sorting
Hrs/ESCRT
Rab5
RabX1
late endosome
Rab7
LYSOSOSME
recycling endosome
fast recycling
Rab4

Figure 1.9 Molecular mechanism of clathrin mediated cadherin turnover at adherens junctions

(a) Labelling. Several mechanisms are in place for labelling cadherins for endocytosis: p120 detachment from AJs (Nanes et al., 2012); numb interaction with p120 at cell adhesion sites (Sato et al., 2011); CK1 mediated E-cadherin phosphorylation (Dupre-Crochet et al., 2007); lateral clustering of E-cadherin induced by RhoGEF2 activated Myo-II and mDia (Levayer et al., 2011). The label can also pre-determine fate after internalisation: Cdc42 activated Src kinase can phosphorylate E-cadherin promoting its ubiquitylation by the E3 ubiquitin-ligase Hakai (Fujita et al., 2002; Shen et al., 2008); calpain can cleave the C-terminal domain of VE-cadherin cytoplasmic tail, labelling the protein for degradation (Su and Kowalczyk, 2016). **(b)** Nucleation. F-BAR containing proteins detect and bind slight curvatures in the cell membrane, which triggers the assembly of a nucleation module (Henne et al., 2010). **(c)** Cargo selection and clathrin coat assembly. The nucleation module recruits AP2 to the nucleation site, where it will further recruit clathrin and cargo specific adaptor proteins (e.g. girdin) (Henne et al., 2010). **(d)** Vesicle scission. The endocytic machinery forms a pit around the tagged protein, as F-BAR proteins are excluded from the endocytic site (Henne et al., 2010). Girdin activated dynamin in collaboration with Cip4 and sec10 (a component of the exocyst complex) mediate the scission of the pit from the membrane, forming the early endosomes (Langevin et al., 2005; Leibfried et al., 2008; Weng et al., 2014). **(e)** Clathrin uncoating and cargo fate. Once internalised, clathrin disassembles from the endocytic vesicles (Palacios et al., 2005). Early endosomes associate with Rab5 and recruit Rac1, Cdc42 and actin nucleators on their surface to modulate cytoskeleton dynamics and facilitate transport. Hrs/ESCRT mediated sorting processes take place: cadherins can either be moved to recycling endosomes associated with Rab11/Rab4 for slow/fast recycling back to the membrane; or can be transported in a RabX1 dependent way to late endosomes associated with Rab7 (Fujita et al., 2002; Palacios et al., 2005; Shen et al., 2008; Su and Kowalczyk, 2016; Woichansky et al., 2016). Figure reproduced from (Rusu and Georgiou, 2020).

1.4.2 Epithelial cell polarity

Cells have the ability to asymmetrically distribute macromolecules (proteins, lipids, carbohydrates, RNA) alongside the plasma membrane and within the cytoplasm (Cao et al., 2015). Virtually, all eukaryotic tissues are polarized. The plasma membrane of epithelial cells is polarized in three distinct domains, apical, lateral and basal, each of them being characterized by specific protein complexes (Baum and Georgiou, 2011; Rodriguez-Boulan and Macara, 2014). There are three different types of polarization: i) apicobasal polarity, found in epithelial sheets that act as barriers; ii) planar cell polarity, found in epithelial cells, perpendicular to the apicobasal axis; iii) front-rear polarity, characteristic to migratory cells and cells undergoing asymmetric division.

The apicobasal polarity, characteristic to epithelial cells, defines both the structural and the functional polarity of the cell and is crucial for many biological processes including cell differentiation, division and migration. Regulation of apicobasal polarity is ensured by several proteins that cluster in three polarity modules (Figure 1.10) ubiquitously expressed across species (Cao et al., 2015).

The basolateral domain is characterized by the Scribble and Yurt-Coracle modules. The apical domain is characterized by the presence of Crumbs module, Scribble's antagonist, whilst the Par module localizes to the apicolateral domain (Baum and Georgiou, 2011; Rodriguez-Boulan and Macara, 2014).

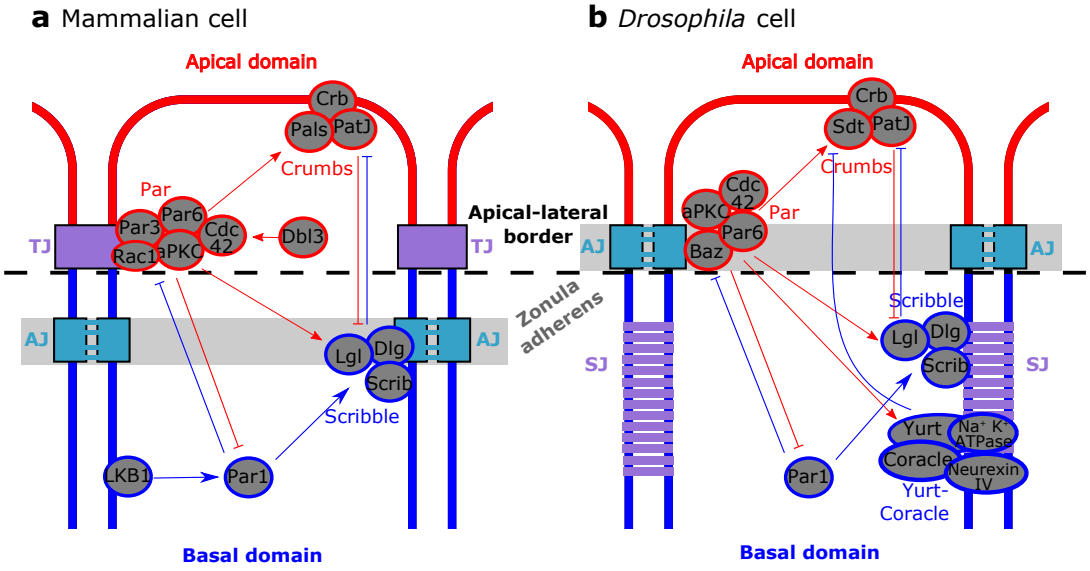


Figure 1.10 Localization of apicobasal polarity modules in epithelial cells

(a) Mammalian and **(b)** *Drosophila* cells regulate apicobasal polarity in a very similar way at molecular level. The main distinction is given by the differential localisation of AJ in relation to TJ and SJ respectively. The apical and basolateral domains are determined by interactions between the same molecular players: the Crumbs and Par modules, restricted to the apical domain and the Scribble module localised to the basolateral domain. Interactions between the atypical protein kinase C (aPKC), Cdc42 and Par1 restrict complexes to their domains by phosphorylating crb, lgl and Par3 (baz) respectively. Additionally, in the *Drosophila* cell, the Yurt-Coracle module acts towards the establishment of the baso-lateral identity. Discs denote proteins and arrows interactions between polarity modules. Baso-lateral players are represented in blue and components with apical localisation in red. Figure adapted from (Campanale et al., 2017; Mack and Georgiou, 2014).

Polarity modules are involved not only in cell polarity maintenance but also in cytoskeletal organisation, organelle rearrangements, vesicular trafficking and cell-cell junction coordination. The integrity of polarity modules is important for the maintenance of the apical-junctional complex (Rodriguez-Boulan and Macara, 2014). Cellular junctions also contribute to the correct positioning of polarity modules. Additionally, in epithelial cells the microtubule skeleton is also polarised on the apicobasal axis, microtubules being oriented with the minus end apically. Nezha (Patronin in *Drosophila*) and ACF7 (shot) are particularly important in this sense. Microtubules aid cell polarisation by controlling the intracellular transport and the positioning of the organelles (Khanal et al., 2016; Noordstra et al., 2016).

The apicobasal polarity is generated and maintained through several mutual exclusion interactions between components of different polarity modules (Figure 1.10). PAR1, and aPKC play key roles in this process. Par1 is localised basally and excludes apical proteins, such as Par3, from the basolateral domain. Conversely, aPKC has an apical localisation and mediates phosphorylation of PAR1 and lgl restricting their localisation to the basolateral domain. For instance, Par5 binds to Par1 phosphorylated Par3 and relocates it to the apical domain. The Par3—Par5 complex dissociates into the cytoplasm allowing for Par3 dephosphorylation and Par3 interaction with aPKC and Par6. It has been proposed that aPKC-mediated phosphorylation of Par3 would further promote Par3 interactions with the Crumbs—Pals1 module (Rodriguez-Boulan and Macara, 2014).

1.4.2.1 Apical Par and Crumbs modules

Both Par and Crumbs modules play an important role in the establishment of apical polarity through interactions at TJ and AJ levels respectively and by restricting the Scribble module to the basolateral domain (Rodriguez-Boulan and Macara, 2014).

The Par module is ubiquitously expressed. The core of the Par module is composed of interactions between Par3 (bazooka (baz) in *Drosophila*), Par6, aPKC and the Rho-GTPase cdc42. During epithelial morphogenesis Par1, Par4 and Par5 also play an

important role (Rodriguez-Boulan and Macara, 2014). Par3/baz bind adhesion proteins at the most apical junctional structure: at TJ in vertebrates (Rodriguez-Boulan and Macara, 2014) or AJ in *Drosophila* (Mack and Georgiou, 2014). Par3/baz will then recruit Par6, which in turn will recruit the atypical protein kinase C (aPKC). The kinase activity of aPKC is modulated by Par6, who also recruits substrates for aPKC. Consequently, aPKC phosporylates target proteins therefore maintaining polarity through feedback loops and mutual exclusion interactions. Furthermore, Par6—Cdc42 interactions ensure the apical localisation of the Par polarity module (Rodriguez-Boulan and Macara, 2014).

The Crumbs module is specific to epithelial tissues. It forms feedback loops with the Par complex in order to maintain the basolateral localisation of scribble. It also plays a role in aPKC upregulation and apicolateral localisation trough interactions between crumbs and Par6, which restrict in turn Par3 and Par6 interactions (Rodriguez-Boulan and Macara, 2014).

1.4.2.2 The Scribble module

The basolateral localized complex Scribble consists of three TSGs: lethal giant larvae (*lgl*), discs large (*dlg*) and scribble (*scrib*) (Royer and Lu, 2011). Both *scrib* and *dlg* localise to the lateral membrane (Rodriguez-Boulan and Macara, 2014). Scrib specifically regulates positioning of AJs and restriction of the apical determinants from the basolateral cellular domain by inhibiting Par complex lateral localisation through antagonistic interactions. In addition, lgl localisation at the basolateral domain is restricted by aPKC phosphorylation. Lgl also prevents Par6 localisation to the cell cortex. Par3 basolateral localisation is inhibited by scrib—Par1 interactions (Assémat et al., 2008). Additionally, lgl influences the actin cytoskeleton and regulates exocytosis, a crucial process for the maintenance of the apical, lateral and basal domains (Cao et al., 2015). Lgl can also interact with other non-polarity proteins and subsequently act in Hippo, Wingless-related integration site (Wnt) and Notch signalling, being therefore involved in the regulation of several biological processes, such as cell cycle progression and apoptosis (Cao et al., 2015).

1.4.3 Invasion

Cancer cells may employ different types of invasion, each with its own characteristics and advantages. Invasive cells very often display migration plasticity, as they can switch between the different types of movement based on the stiffness of the ECM, the density of the collagen network and the proximity of blood vessels (Gligorijevic et al., 2014; Talkenberger et al., 2017; Weigelin et al., 2012).

The most studied process with regards to cell invasion is epithelial to mesenchymal transition (EMT). EMT refers to the ability of a cell to downregulate expression of epithelial markers, such as E-cadherin, and concomitantly increase expression of mesenchymal markers, e.g. N-cadherin. As a consequence, cell polarity changes from apicobasal to front rear polarity and cell-cell adhesion is substantially diminished. As a result, cells can break from the tissue (Figure 1.4a). Various extracellular (e.g. growth factors) and intracellular (e.g. micro RNAs) stimuli can trigger EMT, and several signalling pathways have been implicated in the induction or promotion of EMT (Wnt, Notch, Hedgehog, JAK-STAT, AP-1, NF-kB, Hippo). However, at a mechanistic level EMT is controlled by a handful of transcription factors, most commonly affected in cancer being ZEB, Snail, Twist and p53 (Diepenbruck and Christofori, 2016). Mesenchymal-like invasive cells are characterised by an elongated cell morphology, long actin-rich protrusions, high adhesivity to the extracellular matrix (ECM) and a relatively slow velocity around 0.2 μm/min (Clark and Vignjevic, 2015; Talkenberger et al., 2017). Also, a need for proteases to degrade the ECM (either self-produced or supplied by the tumour microenvironment) has been highlighted (Hanahan and Weinberg, 2011). More recently, EMT was shown to be a plastic process that can be (and is) reverted during colonisation (Tsai et al., 2012).

Ameboid invasive cells are characterised by a rounded, easily deformable cell shape, low adherence to the ECM and relatively high invasion speeds (Talkenberger et al., 2017). This type of movement has also been termed ‘path-finding’ because amoeboid cells squeeze through the pores of the ECM (Clark and Vignjevic, 2015; Talkenberger et al., 2017). Three different variants of amoeboid-like movement have been

described so far: i) very fast movement, characterised by migration speed of up to 10 μm/min and velocity of up to 5 μm/min *in vitro*, extension of short, thin protrusions and a fast-changing morphology; ii) a chaotic, somewhat slower movement characterised by the blebbing morphology of the invading cells; iii) a slow movement, characterised by a low velocity about 0.1 μm/min, extension of short protrusions and some proteolytic activity (Clark and Vignjevic, 2015). Amoeboid movement is powered by Myo-II driven cytoskeleton contractions and is therefore under the control of Rho GTPases and their effector ROCK (Lawson and Ridley, 2017).

Malignant cells can also invade collectively. Cell cluster movement is directed in a similar mode to individual cell invasion: by making use of actomyosin flows and protrusions. Similarly, collective invasion is characterised by a front-rear polarised state of the clone. What sets collective invasion apart is that invasive cells retain epithelial characteristics such as maintenance of cell-cell contact, by expressing cell-cell junction proteins. This helps cells coordinate their movement (Diepenbruck and Christofori, 2016; Theveneau and Linker, 2017).

The movement of invasive cells is often directed towards increased concentrations of chemoatractants such as nutrients (chemotaxis) or towards increased substrate adhesion (haptotaxis). In the absence of chemotactic or chemoattractant gradients, invasive cells display a rather random movement (chemokinesis) (Rikitake and Takai, 2011).

1.5 *Drosophila melanogaster* as a model organism for cancer research

Drosophila is a well-established model for genetic studies and, during the last few decades, has become an increasingly popular model for the study of tumour progression. Observations from *Drosophila* made great contributions towards the understanding of fundamental processes involved in the development of cancer (Enomoto et al., 2018).

Fruit flies have a life cycle of only ten days (Figure 1.11), which allows for complex genetic experiments to be carried out. An important characteristic of the *Drosophila* genome is the low redundancy: only one or very few genes code for members of the same protein class. Moreover, the genome of *Drosophila* has been fully sequenced and it shows high conservation with the human genome (Adams et al., 2000). For instance, more than 60% of the genes involved in cancer progression have high homology *Drosophila* correspondents. Many of the molecular signalling pathways that regulate cell biology are also well conserved between flies and humans (Potter et al., 2000). This makes the fruit fly a reliable model for the study of human diseases.

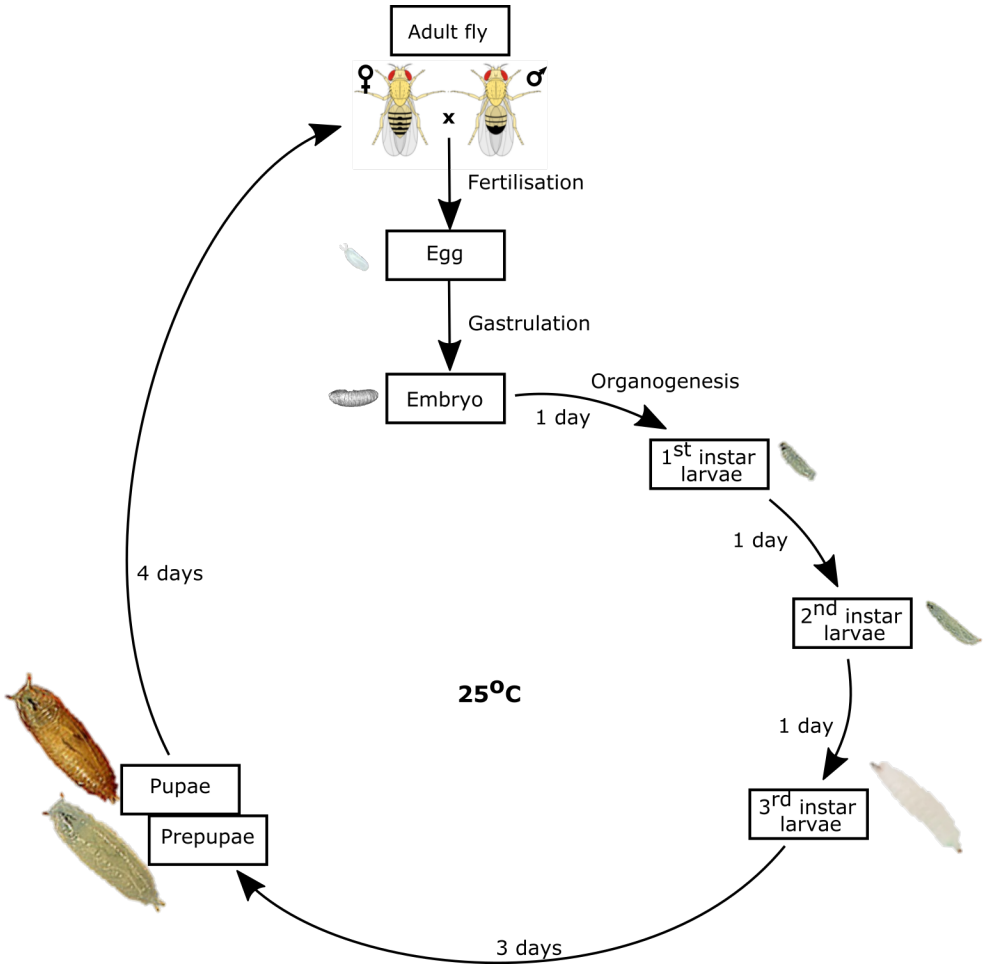


Figure 1.11 *Drosophila* life cycle and development timescale at 25°C

The diagram shows the stages of *Drosophila* development throughout the life cycle. Associated timeframe corresponds to fly development at 25°C.

One advantage of using *Drosophila* as a model organism is the availability of a vast array of genetic tools. For instance, transposable elements, endogenously present in flies, are commonly used for the insertion of transgenes, such as interference RNA (RNAi) (Dietzl et al., 2007; Robertson et al., 1988). Insertions can also be directed to specific loci by using different vectors (Horn and Handler, 2005). Site specific mutagenesis using CRISPR-CAS has also been successfully implemented in *Drosophila* (Gratz et al., 2013). However, the most important tool for the study of tumour progression in *Drosophila* is by far the mosaic technique (Chapter 2.2.2.4) (Enomoto et al., 2018).

By employing the mosaic technique, several traits of tumour progression can be replicated *in vivo* in a timely manner. Multiple mutations/transgenes can be simultaneously expressed in cells mimicking 'clonal evolution'. Moreover, cell populations carrying different mutations can be simultaneously expressed in the same tissue (tumour heterogenicity) and they will develop in close contact and in constant communication with the healthy tissue and local microenvironment. Even haemocytes have been reported to be recruited to the tumour like induced tissues in a similar way to tumour-associated macrophages in humans (Enomoto et al., 2018). Moreover, tracheogenesis has been reported in response to hypoxia in flies in a similar way to angiogenesis in mammalian tumours (Grifoni et al., 2015). Fly and mammalian epithelia are highly similar in terms of tissue architecture. They are both characterised by apicobasal polarity, regular cell shape and tight adhesivity. Therefore, epithelial architecture can be fruitfully studied in the fly in order to gain insight into tumorigenesis mechanisms (Baum and Georgiou, 2011; Rodriguez-Boulan and Macara, 2014).

Drosophila melanogaster has also been used as a model for the study of metastasis. Two approaches have been described. The first model is based on allograft experiments. Injection of neoplastic brain tumours into the abdomen of adult flies led to the formation of micrometastasis in the ovariole, proving that tumours are able to metastasize in *Drosophila* as in order to reach the ovariole, tumour cells had to actively pass through continuous layers of basal membrane and muscle cells

(Beaucher et al., 2007). Another approach to the study of metastasis in flies relies on clonal induction of tumour-like tissue using the MARCM system: the success of the metastatic process is determined by the formation of clones outside the tissue in which they were originally induced (Campbell et al., 2019).

As with any other model system, there are some limitations on the study of tumour progression in flies. The process of metastasis in *Drosophila* is somewhat different to mammalian metastasis, as flies display an open circulatory system. The internal organs of the fly are suffused in a fluid (haemolymph) that in many ways accounts for blood, lymph and interstitial fluid found in vertebrates (Rotstein and Paululat, 2016). Whilst circulating tumour cells can be identified in *Drosophila* (Campbell et al., 2019), the lack of vasculature means that tumour cells do not have to undergo processes such as intravasation and extravasation that characterise metastatic processes in human cancers (Miles et al., 2011). The tracheal system from flies accounts for some of the roles of the circulatory system from mammals such as oxygen (and possibly growth factors) supply (Grifoni et al., 2015). However, tracheogenesis in flies, although similar to angiogenesis, is still a different process which might employ in part different molecular mechanisms. Furthermore, the low redundancy of the genome, whilst a huge advantage from a methodological point of view, might run the risk of oversimplifying some of the molecular mechanisms involved in tumourigenesis. It is therefore crucial that data obtained from *Drosophila* studies is interpreted with caution and that further studies are performed in human cells and/or mammalian models to test the results obtained from *Drosophila* research.

1.6 Research Aims

Cancer research has progressed greatly over the past two decades. Due to advances in genome and transcriptome sequencing techniques we now know many of the genes involved in cancer progression. Recent advances in the field revealed a crucial role for epigenetic regulation in tumour progression, but many of the transcription regulators associated with cancer are incompletely characterised. Tumorigenesis is a very complex process. Therefore, before trying to develop drugs that target certain genes or proteins, we should have a clear understanding of all the processes that they modulate.

In order to address this problem, a large-scale *in vivo* genetic screen for tumour progression modulators was performed in *Drosophila* in the Georgiou laboratory. From this screen, CG7379 was identified as a modulator of cell invasion. Inhibitor of growth 1 (ING1), the human orthologue of CG7379, received a lot of attention from the cancer research community about two decades ago, however, its role in invasion and metastasis has been discovered only more recently and has not been properly investigated. Therefore, the overall aim of my PhD was to characterise the invasive behaviour induced by decreased CG7379/ING1 expression and explore the relationship between ING1's involvement in transcription regulation and its presumed ability to regulate cell invasion.

The specific aims of this project are:

I. Examine how loss of CG7379 leads to invasion and metastasis *in vivo* by investigating the molecular mechanism underlying this phenotype.
II. Asses the ability of CG7379 KD invasive cells to colonise other tissues and form macrometastases.
III. Examine whether CG7379's mechanisms of action have been evolutionarily conserved
IV. Examine the effect of CG7379 and ING1 knockdown on cell proliferation

Chapter 2 – Materials and Methods

2.1 Materials

2.1.1 Live stocks

Table 2.1 lists the genotypes and source of origin for the live stocks used for the experiments presented in this thesis. Most fly stocks were previously created in the Georgiou lab. Some were bought commercially from the Bloomington *Drosophila* Stock Centre (BDSC, USA), *Drosophila* Genomics resource centre (DGRC, Japan) or from Vienna *Drosophila* Stock Centre (VDRC, Austria). One stock was received from Dr Natalia Bulgakova from University of Sheffield. Only one cell line was used for the experiments presented in this thesis, namely MCF-7, a breast adenocarcinoma cell line derived from a metastatic site. The MCF-7 cells were received from Prof. Anna Grabowska (Faculty of Medicine & Health Sciences, University of Nottingham).

Table 2.1 Live stocks

Genotype	Source
Drosophila stocks	
w, Ubx-Flp; lgl^4,FRT40A/CyoGFP; Pnr-GAL4, UAS-Moe:GFP/TM6b	Georgiou Lab.
w, Ubx-Flp; FRT40A/CyoGFP; Pnr-GAL4, UAS-Moe:GFP/TM6b	Georgiou Lab.
w; tub-GAL80, FRT40A; MKRS/TM6b	Georgiou Lab.
w, Ubx-Flp; IF/CyoGFP; Pnr-GAL4, UAS-Moe:GFP/TM6b	Georgiou Lab.
w, Ubx-Flp, tub-GAL80, FRT19A; ;; MKRS/TM6b	Georgiou Lab.
w, Ubx-Flp, tub-GAL80, FRT19A; IF/CyoGFP; ;;	Georgiou Lab.
w, Ubx-Flp, tub-GAL80, FRT19A; IF/CyoGFP; MKRS/TM6b	Georgiou Lab.
w, hs-Flp, tubGAL80, FRT9-2/FM7, KrGFP ; ;; MKRS/TM6b	Georgiou Lab.
w, Ubx-Flp; IF/CyoGFP; MKRS/TM6B	Georgiou Lab.
w, Ubx-Flp; IF/CyoGFP; Pnr-GAL4, UAS-Moe:GFP/TM6b	Georgiou Lab.
w, Ubx-Flp, Dlg, FRT19A/FM7, Kr-GFP; ;; MKRS/TM6b	Georgiou Lab.
w; Tomato-Ecad; ;;	Bulgakova Lab.
w; Ubi-shg:GFP; ;;	DGRC

Genotype	Source
Drosophila stocks – continued	
w; mCherry-Ecad; ;;	Bloomington
w; UAS-Rho1.N19/CyO; ;;	Bloomington
y, w, FRT19A; ;; ;;	Bloomington
w; Sco/CyO; UAS-iCasper/TM6b	Bloomington
w; ;; UAS-Ras.V12	Bloomington
y, w; ;; ry, UAS-RNAi:14430	Bloomington
w; ;; UAS-RNAi:27988	VDRC
w; ;; UAS-RNAi:27989	VDRC
Cell stocks	
MCF-7	Grabowska Lab.

2.1.2 Antibodies

Table 2.2 lists the primary and secondary antibodies used for the experiments presented in this thesis and their source of origin. Most primary antibodies used for staining fly tissues were acquisitioned from the Developmental Studies Hybridoma Bank (DSHB), although antibodies from Santa Cruz, New England Biolabs, Molecular probes and Roche were also used in some instances. The anti-bazooka and anti-crumbs antibodies were received from Prof. Andreas Wodarz and Prof. Elisabeth Knust respectively. Antibodies against human E-cadherin were acquired from Abcam. Secondary antibodies were acquisitioned from Molecular probes.

Table 2.2 Primary and secondary antibodies used for immunofluorescence

Antibody	Dilution (IF)	Supplier
Primary antibodies		
Rat anti-E-cadherin (DCAD2)	1:100	DSHB
Mouse anti-armadillo (N27A1)	1:100	DSHB
Rat anti-α-catenin (DCAT-1)	1:100	DSHB
Mouse anti-Fasciclin III (7G10)	1:400	DSHB
Mouse anti-coracle (C566.9)	1:100	DSHB
Mouse anti-disc Large (4F3)	1:100	DSHB
Rabbit anti-PKCζ (sc-216-G)	1:50	Santa Cruz
Rabbit anti-bazooka	1:1000	Prof. Andreas Wodarz
Rat anti-crumbs	1:1000	Prof. Elisabeth Knust
Mouse anti-PH3 (Ser10) (6G3)	1:500	Cell signalling
Rabbit anti-cleaved Dcp-1 (Asp216)	1:100	New England Biolabs
Mouse anti-GFP	1:1000	Roche
Rabbit anti-GFP	1:1000	Molecular Probes
Mouse anti-E-cadherin (ab1416)	1:100	Abcam
Secondary antibodies		
Alexa Fluor ® 647 goat anti-mouse	1:300	Molecular Probes
Alexa Fluor ® 647 goat anti-rabbit	1:300	Molecular Probes
Alexa Fluor ® 647 goat anti-rat	1:300	Molecular Probes
Alexa Fluor ® 488 goat anti-mouse	1:300	Molecular Probes
Alexa Fluor ® 488 goat anti-rabbit	1:300	Molecular Probes

2.1.3 Primers and siRNA

All primers used for quantitative polymerase chain reaction (qPCR) and small interfering RNAs (siRNA) used for gene knockdown during optimisation procedures, experiments and validation of results are listed in Table 2.3. All oligonucleotides were ordered desalted and dried from various suppliers, also listed in Table 2.3.

Table 2.3 Primers and siRNAs

Target	Oligo sequence	Supplier
Primers for qPCR		
GAPDH	Fw: ATGTTCGTCATGGGTGTGAA	TherrmoFisher
	Rv: GTCTTCTGGGTGGCAGTGAT	Scientific
RHOC	Fw: AGCGGAAGCCCCACCAT	Sigma-Aldrich
	Rv: GTCCACCTCAATGTCCGCAA	
DIAPH1	Fw: CGACGGCGGCAAATCTAAGAA	Sigma-Aldrich
	Rv: ATTCAGGTTCATATTCCAGCAGCA	
ECT2	Fw: GCAAGAGTGGTTCTGGGGAA	Sigma-Aldrich
	Rv: TTGCGATTGCTGTTAGGGGT	
ING1	Fw: TACTGTCTGTGCAACCAGGT	Eurofins
	Rv: TTCTCCAGGGCTTTGTCCAT	
siRNAs for transfection		
ING1	AGAGAGGGCUUACAACAGG	Dharmacon
	CGAGAAGACCAUGGACAAA	
	CCACGUACUGUCUGUGCAA	
	GCGUGGGGCUCAAUCAUAA	
Cyclophilin B	GGAAAGACUGUUCCAAAAA	Dharmacon
Non-targeting	UGGUUUACAUGUCGCUAA	Dharmacon

2.1.4 General reagents

All other reagents used for optimisation procedures, experiments or stock maintenance for either *in vivo* or *in vitro* experiments are listed in Table 2.4 in alphabetical order.

Table 2.4 General reagents

Reagent	Supplier
50x TAE buffer	GeneFlow
5x siRNA buffer	Dharmacon
Accumax	Scientific Laboratory Supplies
Agar pure powder	TherrmoFisher Scientific
ApopTag® Red In Situ Apoptosis Detection Kit	Merck
Bovine serum albumin (BSA)	Sigma
Chloroform	Sigma
Clarion Assay, human	TherrmoFisher Scientific
Cornmeal	ASDA
Cover slip 22mmx22mm (0.13x0.17mm)	TherrmoFisher Scientific
Cover slip 22mmx50mm (0.13x0.17mm)	TherrmoFisher Scientific
CyQuant Cell Proliferation Assay Kit	TherrmoFisher Scientific
4',6-diamidino-2-phenylindole (DAPI)	TherrmoFisher Scientific
Diethyl pyrocarbonate	TherrmoFisher Scientific
Dharmafect1 Transfection Reagent	Dharmacon
Dimethyl sulfoxide (DMSO)	TherrmoFisher Scientific
dNTP Mix	TherrmoFisher Scientific
DNase I	Invitrogen
Dried yeast	DCL yeast
Ethanol	Sigma
Fetal Bovine Serum (FBS)	TherrmoFisher Scientific
Fluorogel mounting medium	Source Bioscience UK
GeneChip Hybridization, Wash, Stain kit	TherrmoFisher Scientific
GeneChip WT PLUS Reagent Kit	TherrmoFisher Scientific
GeneJET; RNA cleanup and concentration kit	TherrmoFisher Scientific
Glycerol	Sigma
Glycogen	Sigma
Golden syrup	ASDA
Hanks Balanced Salt Solution (HBSS)	TherrmoFisher Scientific

Reagent	Supplier
General reagents - continued	
iQ SYBR Master Mix	BioRad
Isopropyl alcohol	Sigma
L-Glutamine	TherrmoFisher Scientific
Matrigel basement membrane	Scientific Laboratory Supplies
Microscope slide plain	TherrmoFisher Scientific
Millicell Hanging Cell Culture Insert (x48)	TherrmoFisher Scientific
Nail varnish	ASDA
Normal Goat Serum (NGS)	Abcam
Oil 10S VOLTALEF	VWR
Paraformaldehyde (PFA)	TherrmoFisher Scientific
Phosphate Buffered Saline (PBS)	Sigma
Propidium Iodide (PI)	Sigma
Propionic acid	Sigma
Proteinase K	TherrmoFisher Scientific
RevertAid Reverse Transcriptase	TherrmoFisher Scientific
RiboLock RNase Inhibitor	TherrmoFisher Scientific
RNase	Stratech Scientific LTD
RPMI-1640 medium, modified without L-glutamine and phenol red	Sigma
Shandon Kwik-Diff stain kit	TherrmoFisher Scientific
Taq polymerase	TherrmoFisher Scientific
Triton X-100	Sigma
TRIzol Reagent	Life Technologies
Trypsin	TherrmoFisher Scientific
Tween 20	Sigma
Water, DNase, RNase-FREE	MP Biomedicals UK

2.2 *Drosophila* methods

2.2.1 *Drosophila* husbandry

Flies were raised in disposable plastic vials on standard cornmeal medium. The food was prepared following the Bloomington *Drosophila* Stock Centre recipe (ingredients: water, golden syrup, yeast, soya flour, cornmeal, agar and propionic acid). Dry yeast was added on top of the food for crosses. Stocks were routinely raised at 18^{o}C, where the life cycle of the fly is approximately 20 days (Dillon et al., 2007). Fresh flies were transferred into new vials (flipping) every 21 days to maintain the stocks and evade mould/mite infestation. Expanding stocks and crosses were kept at 25^{o}C, where fly development takes approximately 10 days (Dillon et al., 2007). Flipping was done twice a week to maximise progeny.

For manipulation and observation purposes, flies were anesthetised using CO2 porous polyethylene gas diffusers. Observations were performed using Leica M60 microscopes or a Leica MZ10F fluorescence microscope. For crosses set up flies were sexed based on the appearance of the anal plates and virgin females were collected twice a day: every 16 hr if kept at 18^{o}C and every 8 hr if kept at 25^{o}C, as females do not accept male mates for 10-12 hr after eclosion (Sullivan et al., 2000). Balancer chromosomes were used to supress meiotic recombination and genetic markers to track progeny genotype through genetic crosses. Balancer chromosomes are often associated with genetic markers. A complete list of balancers and genetic markers used during experiments and their associated phenotypes can be found in Table 2.5.

Table 2.5 Balancers and genetic markers

Name	Chr.*	Type	Phenotype
Cyo (Curley of Oster)	2	Balancer	Curly wings.
CyoGFP	2	Balancer	Curly wings; GFP expression in the abdomen.
FM7 (ln(1)FM7)	1	Balancer	Kidney-shaped eyes.
TM6b (ln(3LR)TM6)	3	Balancer	Short, fat body and extra macrochaetae on the humeral callus.
MKRS	3	Marker	Stubble bristles.
IF (Kr^{If-1})	2	Marker	Irregular facets: the eyes of the fly are reduced in size and the ommatidia in the eyes are fused/ irregularly distributed.
Sco (Scutoid)	2	Marker	Loss of bristles on the humeral callus.
w (mini white)	1	Marker	White eyes.

* Chr. = Chromosome

2.2.2 Genetic techniques

Flies carrying a variety of genetic constructs (Table 2.6) were used for the experiments presented in this thesis. Although the majority of fly stocks used were developed in our lab, commercially available flies carrying transgene insertions were used for the generation of these stocks. Transgenes were inserted into the fly genome by making use of so called P-elements, which are transposons naturally expressed in *Drosophila* (Dietzl et al., 2007; Rubin and Spradling, 1983). Insertional mutagenesis relies on microinjection of the modified transposons together with a marker mutation into *Drosophila* embryos. The success of the integration is then assessed based on the fly phenotype. Most often, the mutation inserted with the transposon would rescue the mini white mutation carried by the host flies (Silicheva et al., 2009).

Table 2.6 Genetic constructs

Construct	Abbreviation	Function
P{GawB}pnr[MD237]	pnr-GAL4	GAL4 activity is driven in the central region of the notum by the pannier promoter.
P{tubP-GAL80}	tub-GAL80	Ubiquitously driven GAL80 expression under the tubulin promoter represses GAL4 activity.
P{neoFRT}19A P{neoFRT}40A	FRT	Sites of flippase induced post-mitotic recombination (Flippase Recognition Target). Sites at: Chr X 19A2, X: 19910870..19910870 Chr 2 40A3, 2L:21794705..21794705
P{Ubx-flp}	Ubx-flp	Flippase expression in the pattern of the Ubx gene.
P{Ubi-p63E-shg.GFP}3	Ubi-shg:GFP	Ubiquitous expression of GFP tagged E-cadherin (at the C-terminal end) under the Ubiquitin-63E promoter.
{Ecad-TolTomato}	Tomato-Ecad	Expresses tomato-tagged E-cadherin under the control of native shg regulatory sequences.
TI{TI}shg[mCherry]	mCherry-Ecad	Expresses mCherry-tagged E-cadherin under the control of native shg regulatory sequences.
P{UAS-GMA}	UAS-Moe:GFP	Expression of GFP tagged actin-binding domain of Moesin under the control of UAS.

Construct	Abbreviation	Function
Genetic constructs - continued		
P{w[+mC]=UAS-p35.H}BH3	UAS-p35	P35 expression, under UAS control, blocks apoptosis.
P{UAS-Rho1.N19}	UAS-Rho1.N19	Expression of dominant negative Rho1 under UAS control.
P{UAS-Ras85D.V12}TL1	UAS-ras.V12	Expression of constitutively active Ras under UAS control.
P{UAS-lhRNAi}	UAS-RNAi	Expression of various RNAi constructs against CG7379 under UAS control.
PBac{UAS-iCasper-noGFP-T2A-HO1}	UAS-iCasper	Expresses a caspase reporter under UAS control that emits infrared fluorescence upon caspase cleavage.
$l(2)gl^4$	*lgl-/-* or lgl^4	Loss-of-function mutant allele. Induces cell polarity defects.

Drosophila experiments presented in this thesis made use of sophisticated genetic techniques in order to induce tumour-like tissues on the epithelium from the back of the fruit fly. The employed techniques are discussed in detail in the following sections (Chapters 2.2.2.1 – 2.2.2.4).

2.2.2.1 The galactosidase 4 (GAL4)/upstream activating sequence (UAS) system

The galactosidase 4 (GAL4)/upstream activating sequence (UAS) system is a dual-component system that enables transgene expression under strict spatial and temporal control. GAL4, first identified in *Saccharomyces cerevisiae* as a transcription activator, recognizes and binds a UAS enhancer element driving expression of downstream genes (Brand and Perrimon, 1993). GAL4 can be engineered under the control of different promoters, driving therefore tissue specific expression of

targeted genes (Figure 2.1). The *pannier* (*pnr*) promoter, which restricts expression of GAL4 and subsequently controlled genes to the central region of the dorsal thorax epithelium of *Drosophila* (Heitzler et al., 1996), was used for the experiments presented in this thesis. The UAS-tagged genes used for the experiments presented here include a combination of fluorescent reporters, mutated genes and RNAi lines (Table 2.6) that allows for the observation and analysis of many different phenotypes.

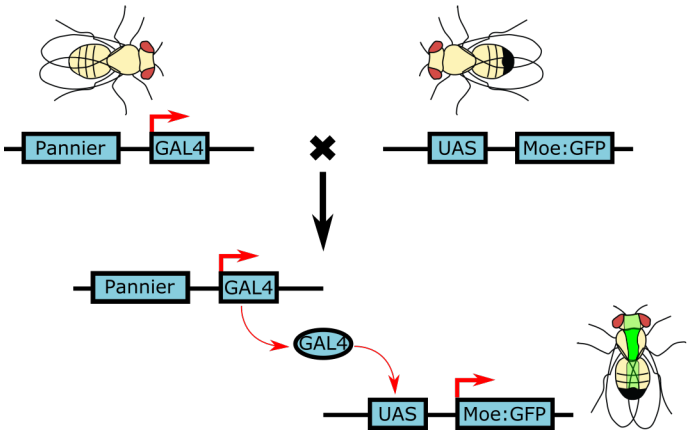


Figure 2.1 The GAL4/UAS system

If flies engineered to express GAL4 are crossed with flies carrying a transgene insertion under UAS control, the progeny will express both the GAL4 and the UAS-tagged construct which activates tissue specific expression of the gene of interest. The tissue specificity is dictated by the promoter used (in this example pannier drives GFP expression to the notum). Figure adapted from (Brand and Perrimon, 1993).

2.2.2.2 RNA interference mediated knockdown

Transgenes expressed under the UAS/GAL4 system often include RNA interference (RNAi). Basically, short fragments from genes of interest are cloned as inverted repeats and are inserted using P-elements into the fly genome. Expression of a transgenic RNAi hairpin results in reduced expression of the target gene and therefore, *in vivo* targeted RNAi expression is an incredibly useful tool for loss-of-function analysis (Dietzl et al., 2007).

At a molecular level, double-stranded RNA (dsRNA) hairpins are cleaved by dicer into small interfering RNA (siRNA) of about 20 nucleotides. Those are transported to the RNA induced silencing complex (RISC) in order to be unwound to small single stranded RNA fragments. Further on, the anti-sense strand binds with high specificity to target messenger RNA (mRNA) due to perfect complementarity resulting in mRNA degradation and loss of function (Okamura et al., 2008) (Figure 2.2).

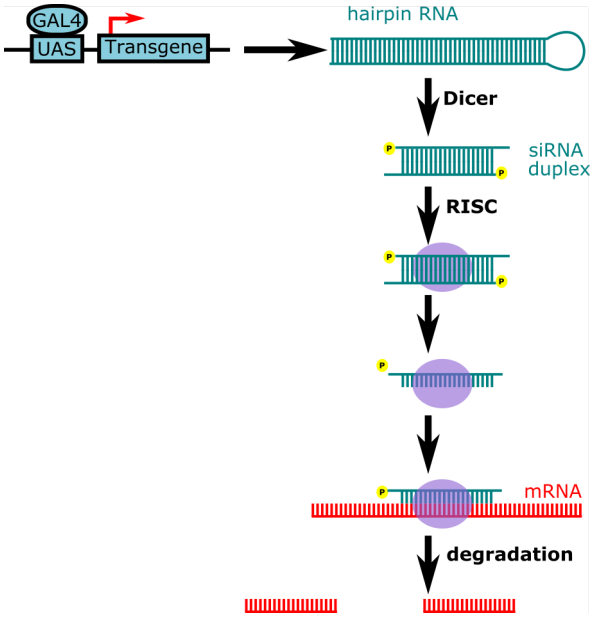


Figure 2.2 Molecular mechanism of UAS-RNAi transgene

UAS-RNAi transgenes can be expressed in a tissue specific manner using the GAL4/UAS system. Dicer and RISC process the dsRNA hairpins transcribed as a result of GAL4 activity, generating siRNA. The strand complementary to the target endogenous mRNA then binds the mRNA resulting in mRNA degradation and subsequent gene silencing. Figure adapted from (Kim, 2003).

2.2.2.3 The flippase (Flp)/flippase recognition target (FRT) system

Flp/FRT is a yeast site-directed recombination system which has been implemented in *Drosophila* with the aim to manipulate expression of specific genes. In short, during the G2 phase of the cell cycle the flippase enzyme (Flp) induces mitotic recombination between two identical flippase recognition targets (FRT) found at identical sites on the chromosome of a heterozygous parent cell (Figure 2.3). Two different daughter cells, each homozygous for one of the expressed alleles, are generated (Theodosiou

and Xu, 1998). In our experiments, Flp expression was placed under the control of the tissue specific promoter Ultrabithorax (Ubx), therefore restricting the recombination process to the dorsal thorax of the fly (Bienz and Tremml, 1988). FRT19A and FRT40A were used to drive recombination on the first and second chromosome respectively (Table 2.1).

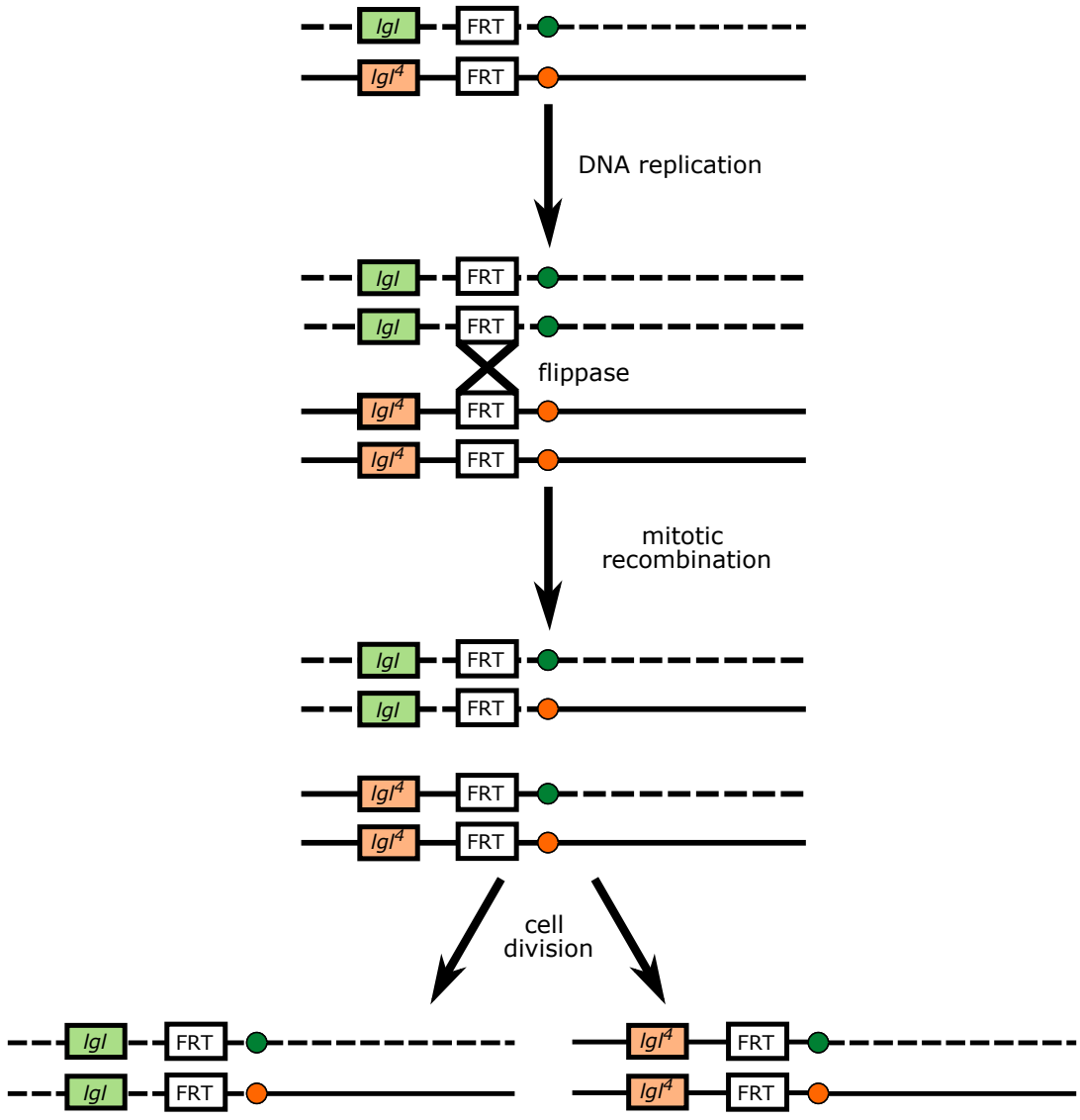


Figure 2.3 The Flp/FRT system

A heterozygous parental cell for lethal giant larvae (*lgl*), with identical FRT sites on both chromosome arms undergoes replication. During G2 Flp expression induces mitotic recombination between identical FRT sites on homologous chromosome arms. Subsequently, mitosis takes place and chromosome segregation results in two different daughter cells: one homozygous for the wild-type *lgl* allele (left hand side) and one homozygous for the mutant lgl^4 allele (right hand side). Figure adapted from (Theodosiou and Xu, 1998).

2.2.2.4 Mosaic analysis with a repressible cell marker

Mosaic analysis with a repressible marker (MARCM) is a genetic technique that combines the Flp/FRT and UAS/Gal4 systems with the aim of creating mosaic tissues in flies, which present both mutant and wild-type (WT) cells. The MARCM system introduces the use of a repressor for the GAL4/UAS system, namely GAL80. The presence of even one copy of the GAL80 in the genome of a cell will repress expression of any GAL4 controlled genes. When a cell that is heterozygote for GAL80, expresses GAL4, UAS transgene(s), flippase and appropriate FRT sites undergoes mitosis, it generates a cell homozygote for GAL80 and one that does not have any GAL80 copies in its genome. Similar to the parent cell, the cell homozygote for GAL80 will repress GAL4 expression, whilst the other one will express the gene(s) of interest as dictated by the GAL4 promoter (Lee and Luo, 1999; 2001). Additional mutations can be introduced to the system paired to GAL80 and their expression would be synchronised with GAL4 driven transgene expression. Several combinations of different FRTs, UAS-transgenes and fluorescent proteins were used for the experiments presented in this thesis as highlighted in Chapter 2.2.2.6. One such example is presented in detail in Figure 2.4.

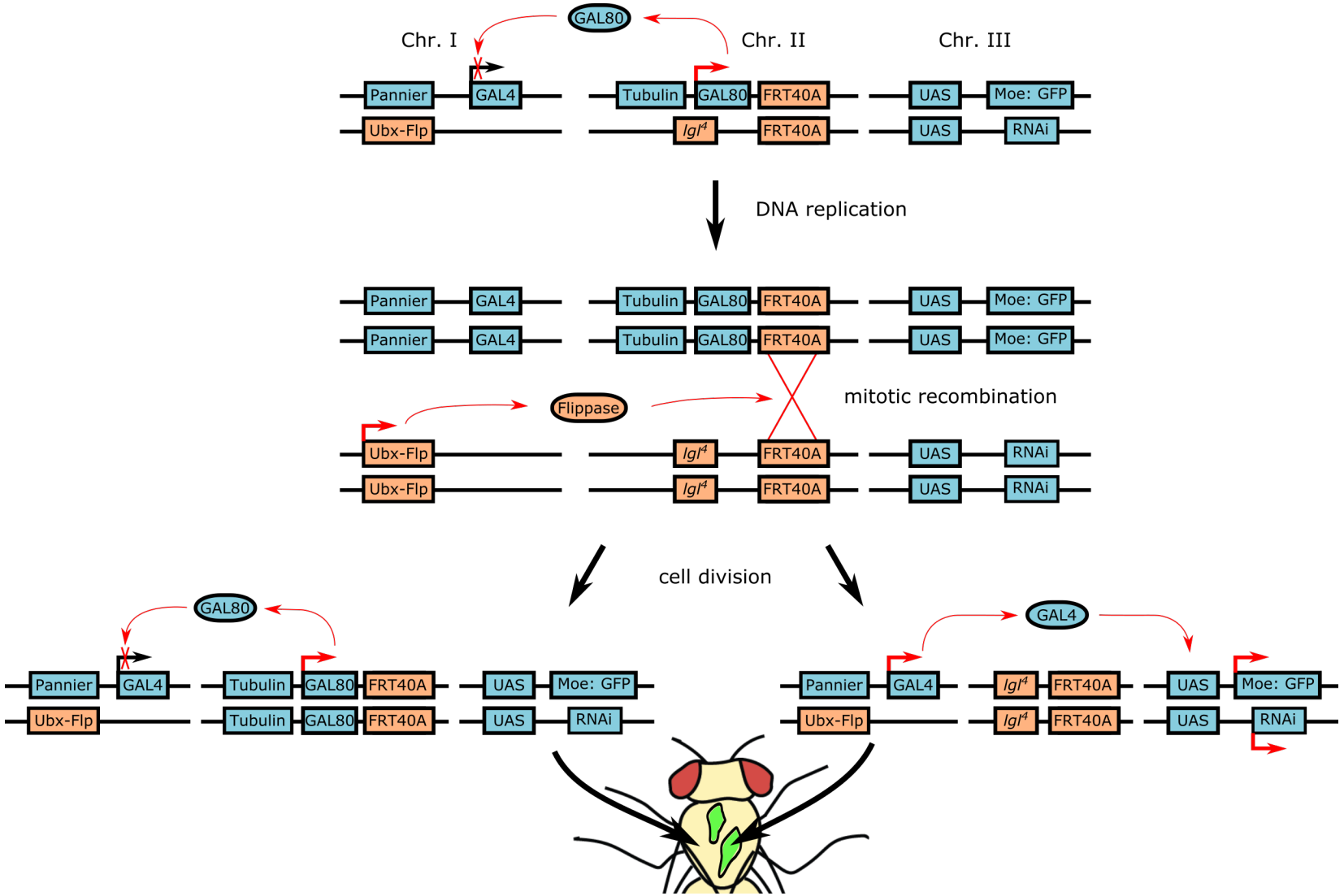

GAL80
Chr. I
Chr. II
Chr. III
Pannier
GAL4
Ubx-Flp
Tubulin
GAL80
FRT40A
lgl4
FRT40A
UAS
Moe: GFP
UAS
RNAi
DNA replication
Pannier
GAL4
Pannier
GAL4
Tubulin
GAL80
FRT40A
Tubulin
GAL80
FRT40A
UAS
Moe: GFP
UAS
Moe: GFP
Flippase
mitotic recombination
Ubx-Flp
Ubx-Flp
lgl4
FRT40A
lgl4
FRT40A
UAS
RNAi
UAS
RNAi
cell division
GAL80
Pannier
GAL4
Ubx-Flp
Tubulin
GAL80
FRT40A
Tubulin
GAL80
FRT40A
UAS
Moe: GFP
UAS
RNAi
GAL4
Pannier
GAL4
Ubx-Flp
lgl4
FRT40A
lgl4
FRT40A
UAS
Moe: GFP
UAS
RNAi

Figure 2.4 The MARCM system

In this example the first chromosome contains sequences coding for GAL4 and for flippase. GAL4 expression is restricted to the mid-notum of the fly by using the pannier promoter, and flippase expression is restricted to the dorsal thorax by using the Ultrabithorax promoter. Expression of the GAL80 repressor of the UAS/GAL4 system is linked with FRT40A on the second chromosome, under the tubulin promoter, which drives ubiquitous expression. On the opposite chromosome, a null allele for *lgl* was expressed linked to another FRT40A. The UAS-tagged genes are expressed on the 3rd chromosome and consist of a fluorescently labelled protein (Moe:GFP) and an RNAi hairpin. During G2, flippase expression drives mitotic recombination between the two FRT40A and following mitosis two different daughter cells are generated: one homozygote for GAL80 (left hand side) and one homozygote for the *lgl* mutation (right hand side). Therefore, only cells bearing the *lgl* mutation and all *lgl-/-* cells will express the RNAi and will be fluorescently labelled because they would have lost the expression of the GAL80 repressor. All other cells will repress GAL4 expression due to GAL80 expression and would have lost the *lgl* mutation, being therefore phenotypically WT.

2.2.2.5 Meiotic recombination

During meiotic prophase I, exchange of genetic material between homologue chromosomes can occur through a process named crossing-over or meiotic recombination. In *Drosophila*, this process only occurs in females (with the exception of the 4th chromosome, which is exempt from recombination in both males and females) and is usually prevented through the use of balancer chromosomes. The crossing-over phenomenon can however be useful when trying to manipulate the *Drosophila* genome, as it allows for the recombination of genes from different fly stocks onto one chromosome (Figure 2.5) *(Roote and Prokop, 2013)*. Crossing-over is a random process, but the probability of the event can be estimated based on the gene's position on the physical and genetic maps of the *Drosophila* genome *(Fiston-Lavier et al., 2010).* The frequency with which two genes will undergo a single chromosomal crossover during meiosis, also known as recombination frequency, is equal to the number of map units between the two genes on a chromosomal map (centimorgan, cM), and maxes out at 50%. The further apart two genes are, the more likely they are to recombine. In practice, females that are heterozygote for the two genes of interest are crossed to males carrying a balancer and a dominant marker on the same chromosome as the genes of interest.

Recombination will occur at random in the female gametes and therefore each individual from the progeny is the result of an independent recombination event. Further on, stocks are created from individual progeny flies. The amount of progeny needed to obtain at least one successful recombination can be calculated with the desired probability (usually 95%) by using Mather's formula, Eq. (2.1):

$$amount\ of\ progeny = \frac{\log(1 - probability)}{\log(1 - recombination\ frequency)} \tag{2.1}$$

The number of stocks created is usually double the amount of progeny calculated. Each stock should then be individually tested for the expression of each of the genes of interest. Only recombinants will express both mutations (Greenspan, 1997).

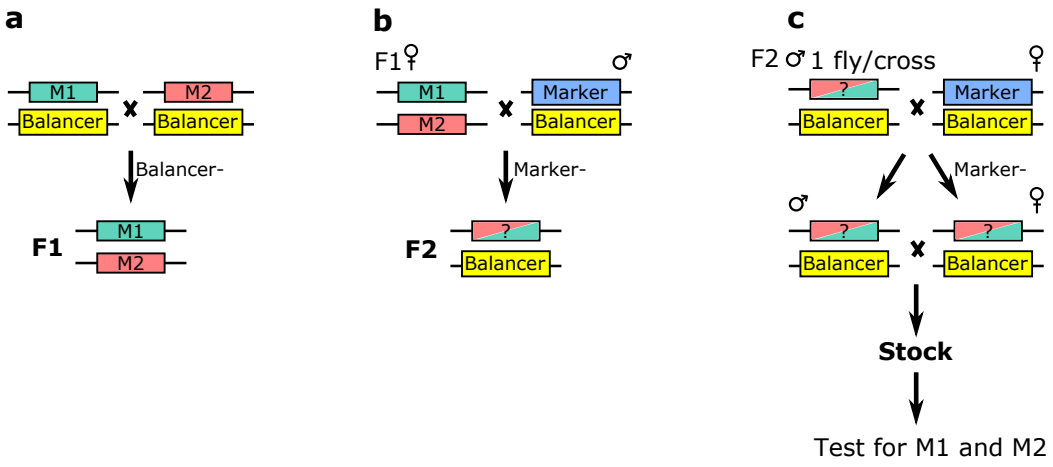


Figure 2.5 Meiotic recombination experimental design

a. *Drosophila* stocks carrying each a different mutation on the same chromosome are crossed together. **b.** Virgin F1 heterozygote females (for the two mutations) are crossed to heterozygote males carrying a balancer and a dominant marker mutation on the same chromosome as the genes of interest. **c.** Individual F2 males are crossed back to balancer/marker virgin females in order to generate a stock of balanced putative recombination lines. Each stock would have to be thoroughly tested for the presences of the two mutations of interest. Figure adapted from (Greenspan, 1997).

Several genes had to be recombined to make the experiments presented in this thesis possible, however most recombination experiments were previously performed and stocks readily available for experimental use were created (Table 2.1). The only recombination performed by myself aimed to express UAS-RNAi against CG7379 and the UAS-iCasper construct on the same chromosome (Chapter 3.2.1).

2.2.2.6 Genotypes analysed

Wild-type GFP labelled clones (WT):

w, Ubx-Flp/+; FRT40A/tubGAL80, FRT40A; PnrGal4, UAS-Moe:GFP/MKRS

CG7379 knockdown GFP labelled clones in WT tissue (CG7379 KD):

w, Ubx-Flp/+; FRT40A/tubGAL80, FRT40A; PnrGal4, UAS-Moe:GFP/UAS-RNAi

***Ras* overexpressing GFP labelled clones in WT tissue (*Ras^{V12}*):**

w, Ubx-Flp/+; FRT40A/tubGAL80, FRT40A; PnrGal4, UAS-Moe:GFP/UAS-Ras.V12

CG7379 knockdown GFP labelled clones in epithelial tissue with ubiquitous E-cadherin overexpression (*shg_{ubq}*; CG7379 KD):

w, Ubx-Flp, tub-GAL80, FRT19A/FRT19A; Ubi-shg:GFP/+; PnrGal4, UAS-Moe:GFP/ UAS-RNAi

CG7379 knockdown GFP labelled clones expressing a dominant negative mutation for Rho1 (*$Rho1^{N19}$*; CG7379 KD):

w, Ubx-Flp, tub-GAL80, FRT19A/FRT19A; UAS-Rho1.N19/+; PnrGal4, UAS-Moe:GFP/ UAS-RNAi

Wild-type GFP labelled clones with fluorescently labelled (far-red) apoptotic cells:

w, Ubx-Flp/+; FRT40A/tubGAL80, FRT40A; PnrGal4, UAS-Moe:GFP/UAS-iCasper

CG7379 knockdown GFP labelled clones with fluorescently labelled (far-red) apoptotic cells:

w, Ubx-Flp/+; FRT40A/tubGAL80, FRT40A; PnrGal4, UAS-Moe:GFP/UAS-RNAi, UAS-iCasper

GFP labelled *lgl* mutant clones (*lgl-/-*):

w, Ubx-Flp/+; lgl^4, FRT40A/tub-GAL80, FRT40A; PnrGal4, UAS-Moe:GFP/+

CG7379 knockdown GFP labelled clones mutant for *lgl* (*lgl-/-*; CG7379KD):

w, Ubx-Flp/+; lgl^4, FRT40A/tub-GAL80, FRT40A; PnrGal4, UAS-Moe:GFP/UAS-RNAi

Apoptosis defective GFP labelled clones mutant for *lgl* (*lgl-/-*; *p35*):

w, Ubx-Flp/+; lgl^4, FRT40A/tub-GAL80, FRT40A; PnrGal4, UAS-Moe:GFP/UAS-p35

GFP labelled *lgl* mutant clones with fluorescently labelled (far-red) apoptotic cells:

w, Ubx-Flp/+; lgl^4, FRT40A/tub-GAL80, FRT40A; PnrGal4, UAS-Moe:GFP/UAS-iCasper

CG7379 knockdown GFP labelled clones mutant for *lgl* with fluorescently labelled (far-red) apoptotic cells:

w, Ubx-Flp/+; lgl^4, FRT40A/tub-GAL80, FRT40A; PnrGal4, UAS-Moe:GFP/UAS-RNAi, UAS-iCasper

2.2.3 Mounting for live imaging

For live imaging, pupae 20-24 hr after puparium formation (APF) were immobilised ventral side down onto microscope slides using double sided sticky tape. Using tungsten forceps, one third of the pupal case was peeled off starting from the head of the pupa, exposing the notum. Using clear nail varnish, a bridge like structure was then created by stacking five 22x22 mm coverslips 0.13-0.17 mm thick on each side of the slide. The

entire structure was covered with a 22x50 mm coverslip greased with a thin layer of 10S voltalef injection oil. A schematic of the resulting structure is shown in Figure 2.6.

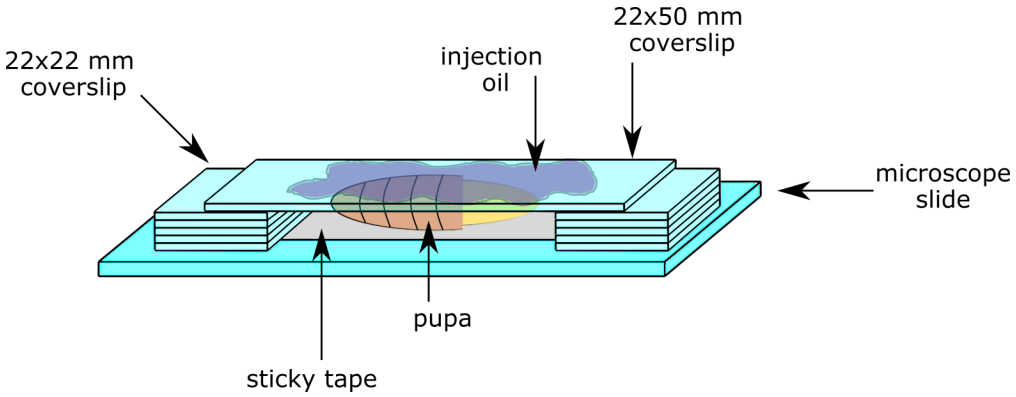


Figure 2.6 Mounting for live imaging

2.2.4 Dissections

2.2.4.1 Nota dissections

The dorsal thorax of 20-24 hr old pupae was dissected following the protocol described by Jauffred and Bellaiche as illustrated in

Figure 2.7 Figure 2.7 (Jauffred and Bellaiche, 2012). Pupae were pinned, dorsal side down, in a silicon dish and covered with ice cold PBS. The pupal casing was then removed using tungsten forceps and the head and abdomen of the pupae were excised using dissection scissors. Internal organs were removed by flushing the opened pupae with PBS. The trachea was then cut out and the sides of the notum excised using dissection scissors, leaving the middle strip of the notum where Pnr-GAL4 drives UAS transgene expression.

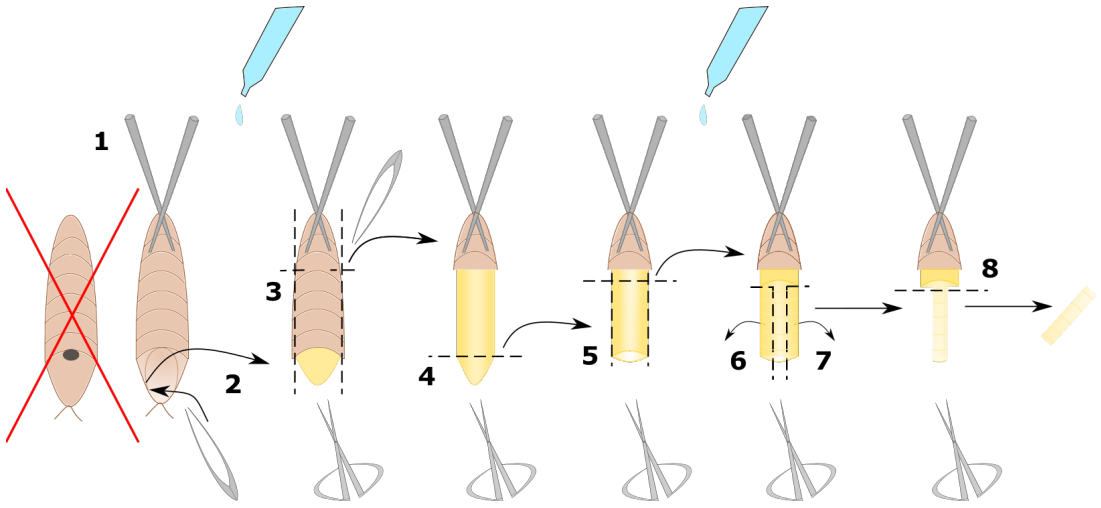


Figure 2.7 Dissection of *Drosophila* nota

1. The pupae was pinned dorsal side down in a silicon dish. The pins were inserted in the posterior side of the pupae. Cold PBS was then added until the pupae was submerged **2.** The puparium above the head was removed using tungsten forceps. **3.** Using dissection scissors, two cuts were made in the pupal case along the side of the pupal body. Two small incisions were made on top of the puparium, perpendicular to each cut. The pupal case was then carefully removed using tungsten forceps. **4.** The head of the pupae was cut off from above the eye globes. **5.** The ventral side of the pupal thorax and abdomen were next removed by making two cuts along the right and left sides of the pupal body and one incision across the ventral side of the body, towards the posterior end of the pupae. Using a Pasteur pipette, the open body was then flushed with PBS to remove all inner organs. **6-7.** The lateral regions of the remaining tissue were then excised, keeping the central region of the notum where Pnr-GAL4 drives transgene expression. **8.** The final step was the detachment of the notum from the posterior part of the pupae.

2.2.4.2 Brain dissections

The brains of adult flies were dissected following the protocol described by Wu and Luo as illustrated in Figure 2.8 (Wu and Luo, 2006). Flies were anaesthetised using CO_2 and were then moved in a glass dish containing 95% ethanol for 30 seconds. Following a PBS wash, flies were moved into a rubber dish plate filled with ice cold PBS. The head of the fly was removed from the body. Using tungsten forceps, the head of the fly was carefully cracked in two starting from where the gastrointestinal tract (GI) meats the brain and

following an imaginary line in between the eyes. The brain was then pulled out and the air sacks and any foregut residues were carefully removed.

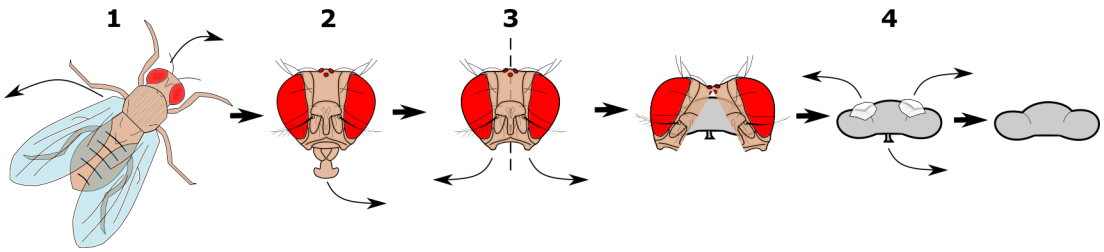


Figure 2.8 Dissection of *Drosophila* brain

1. The head of the fruit fly was removed using two tungsten forceps by pulling the head and the body of the fly in opposite directions. **2.** The proboscis was then removed from the head using a pulling motion. **3.** Using two tungsten forceps, the head of the fly was split open following an imaginary line starting from the orifice created during proboscis removal. **4.** The air sacks and residues of the foregut were carefully removed from the brain.

2.2.4.3 Gastrointestinal tract dissections

The gastrointestinal tracts of adult flies were dissected following the protocol described by Micchelli as illustraed in Figure 2.9 (Micchelli, 2014). Flies anaesthetised using CO_2 were placed in 95% ethanol for 30 seconds, they were then rinsed with PBS and moved into a rubber dish plate filled with ice cold PBS. The head, legs and wings were then carefully detached from the body using tungsten forceps. A small, superficial incision was made in the abdominal cuticle between the 8^{th} and the 9^{th} tergites revealing the midgut and the reproductive tracts. These organs were then separated from the abdominal wall by disrupting the fine tracheal strands. The abdominal cuticle was then disconnected from the thorax at the narrow waist and the reproductive tract from the gastrointestinal tract. Finally, the muscle and cuticle of the thorax surrounding the gastrointestinal tract were then removed by tearing the thorax between the remaining stumps of cuticle where the legs were attached.

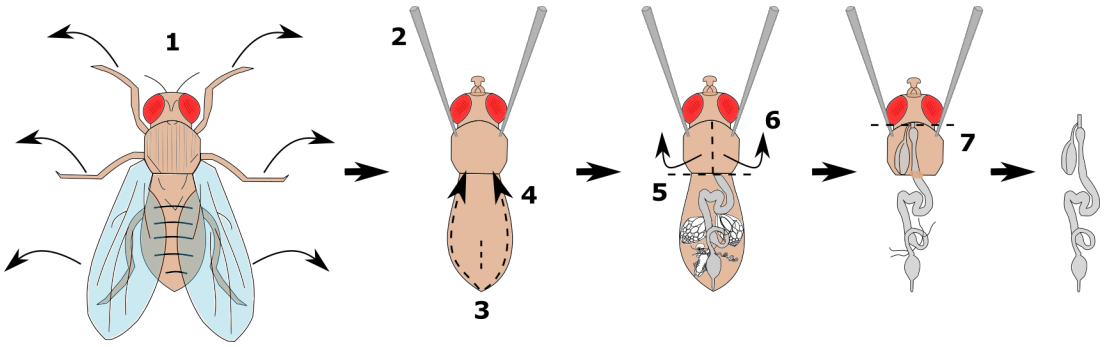


Figure 2.9 Dissection of *Drosophila* gastrointestinal tract

1. The limbs and wings of the fruit fly were detached from the body. **2.** The fly was securely fastened in a silicon dish ventral side up, by inserting a minute pin on each side of the thorax. **3.** Using the forceps, a superficial incision was created on the posterior side of the abdominal cuticle. **4.** The abdominal epithelium was then striped away by pulling each side of the abdomen anteriorly, revealing the internal organs. **5.** The abdominal cuticle was disconnected from the thorax. **6.** Working anteriorly, the muscles and cuticle of the thorax were separated between the remaining stumps of cuticle where the legs were attached. **6.** The thoracic cuticle was then disconnected from the head and the foregut was pinched just anterior to the cardia.

2.2.4.4 Ovaries and testes dissections

The reproductive tract was either dissected together with the gastrointestinal tract as described in Chapter 2.2.4.3, or by following the protocol described by Henderson as illustrated in Figure 2.10 (Henderson, 2004). For the second option, the external genitalia of CO_2 anesthetised and ethanol treated flies placed in ice cold PBS, was pulled away from the rest of the body using tungsten forceps. Due to this motion, the abdomen tore apart revealing the inner organs. The ovaries or testes were then separated from the midgut.

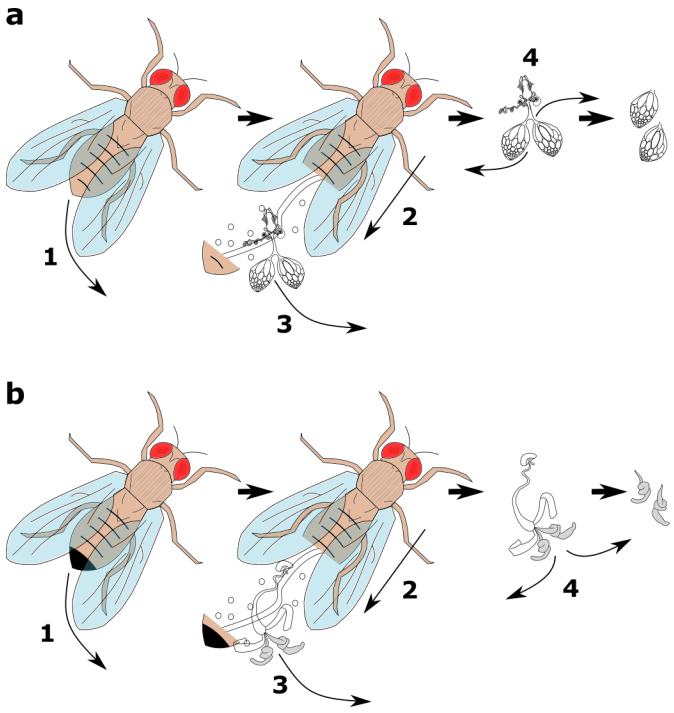


Figure 2.10 Dissection of *Drosophila* reproductive organs

a. Ovaries dissection **b.** Testes dissection **1.** Using a pair of tungsten forceps, the fly was grasped between the thorax and the abdomen. The terminal part of the abdomen was pulled using another pair of forceps, releasing the internal organs from the cavity. **2.** If the internal organs were not released in step 1, the abdomen of the fly was carefully squeezed. **3.** Female/male reproductive apparatus was detached from the other organs and teased away from the debris. **4.** Ovaries/testes were set apart from the rest of the reproductive system.

2.3 Cell culture methods

2.3.1 Cell storage and maintenance

MCF-7 human breast carcinoma cells were cultured in RPMI medium without phenol red (Invitrogen) supplemented with 2 mM L-glutamine and 10% FBS and grown in T75 culture flasks at 37^{o}C in a 5% CO2 atmosphere. Cells were routinely passaged when 70%-90% confluent: growth medium was removed, cells were washed in PBS and detached by incubation with a solution of 1% Trypsin in PBS for 5 minutes at 37^{o}C. Pre-warmed growth medium was then added to deactivate the trypsin and the desired

numbers of cells were seeded into new flasks containing appropriate amount of pre-warmed media.

For storage, cells were pelleted by centrifuging for five minutes at 800 rpm following detachment and re-suspended in freezing medium (90% FBS, 10% DMSO), transferred to cryovials and stored at -80^{o}C in a Mr Frosty freezing container for at least 24 hr. For long term storage tubes were transferred to liquid nitrogen.

2.3.2 Cell counting

To count cells, 10 µl of cell suspension was applied to a haemocytometer BS 748 (Hawksley, UK). Cells were counted in all four squares in the corners and the square in the middle of the haemocytometer. As the final volume of each square is 100 nl, Eq. (2.2) was used to approximate the concentration of cells in suspension:

$$Cells/ml = \frac{total\ number\ of\ counted\ cells}{5}\ x\ 10^4 \tag{2.2}$$

2.3.3 Transient transfection

Gene expression was knocked down using siRNA. The day before performing the transfection, 30x10^4 cells were seeded/well of a 6-well plate and were incubated at 37^{o}C with 5% CO2 until 50-60% confluent. Transfection media containing DharmaFect1 transfection reagent and ON-TARGET plus SMARTpool siRNA against ING1 was then added. Cells were then incubated at 37^{o}C with 5% CO2 for 48 hr prior to downstream applications (ING1 half-life was estimated to be ~15 hr (Garate et al., 2008)). ON-TARGETplus Non-targeting siRNA was used as a negative control. Additionally, Cyclophilin B siGLO, which allows for visualisation of siRNA incorporation to the nuclei, was used for transfection optimisation together with qRT-PCR analysis of gene

expression at 24, 48 and 72 hr post-transfection. Nucleotide sequences of siRNAs used can be found in Table 2.3.

2.3.4 Transwell migration and invasion assay

A schematic representation of the transwell migration and invasion assay is presented in Figure 2.11. Forty-eight hours after siRNA transfection, 500 μl of $5x10^4$ cells/ml cell suspension of MCF-7 cells treated with siRNA against ING1 or non-targeting siRNA were harvested and plated at appropriate density in 8 μm pore 24 well plate hanging inserts (Millipore). For invasion assays the inserts were covered with 100 μl of 1 mg/ml extracellular matrix (Corning). A solution of 0.5% BSA was used for cell plating and 10% FBS was used in RPMI media as a chemoattractant underneath the inserts. Following a 48 hours incubation at 37^{o}C in 5% CO_2 atmosphere, invading cells were detached from the bottom of the inserts using accumax cell detachment solution (Merk Millipore) and incubated for 15 minutes in CyQuant GR dye (Thermo Fisher Scientific) 1:75 dye to 4x lysis buffer. The dye causes fluorescence enhancement upon binding to cellular nucleic acids. Therefore, the fluorescence intensity of the cell suspension is directly proportional with the number of invading cells. Fluorescence intensity was measured using 480/520 nm filters and optimal gain on a BMG fluorescent plate reader. The number of invading cells was calculated based on a standard curve for cell concentrations ranging 0 to 10^6 cells/ml of un-treated MCF-7 cells lysed as for the invasion assay protocol. For image acquisition of the migrating/invading cells, inserts were stained using Shandon Kwik-Diff stain kit (TherrmoFisher scientific) following the manufacturer's instructions. Images were acquired using a 10x/0.3 NA objective on a Zeiss Axioplan/Axiophot brightfield microscope.

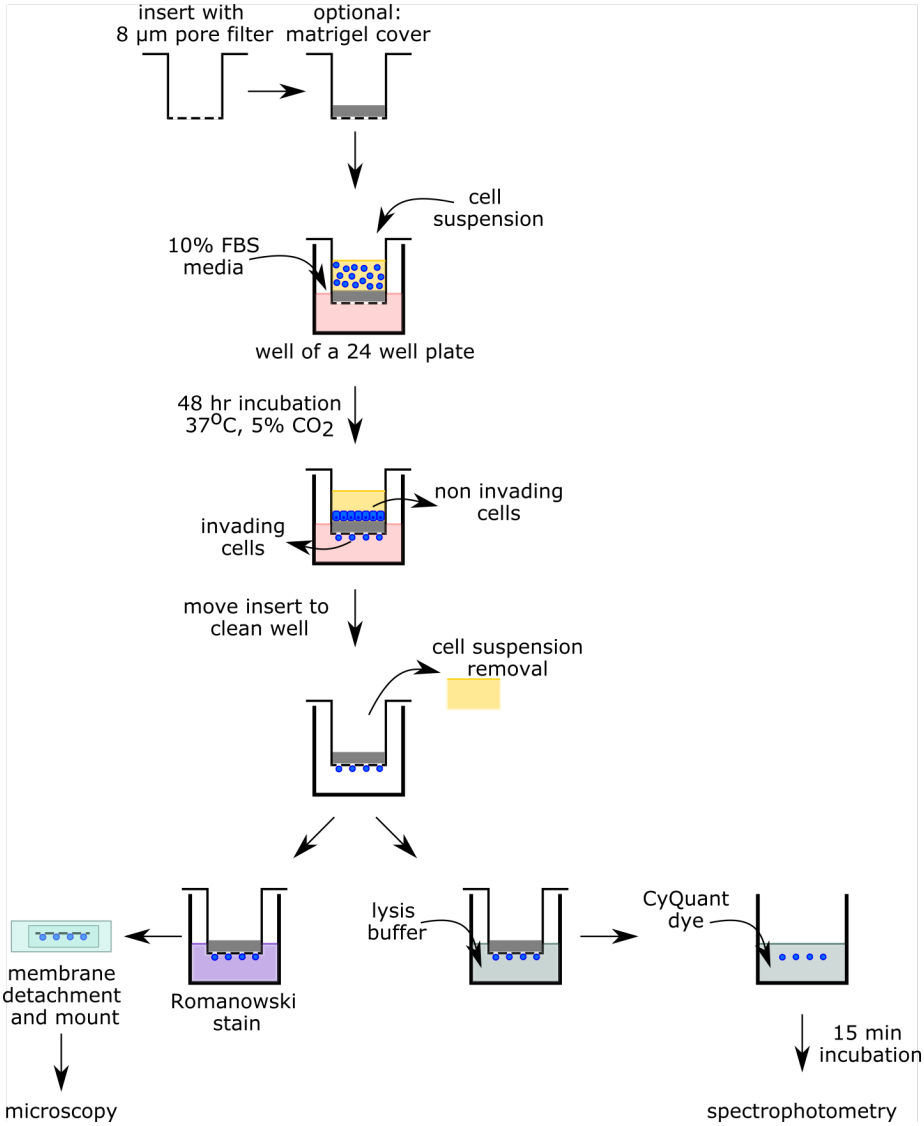


Figure 2.11 Schematic of migration/invasion assay protocol

Schematic representation of the Boyden chamber technique used for transwell migration and invasion assays. Figure adapted from Merck Millipore website (MERCK, 2020).

2.4 Molecular biology techniques

2.4.1 Immunohistochemistry

Dissected tissues and cells cultured on coverslips were fixed in 4% PFA at room temperature (RT) for 20 or 30 minutes respectively, followed by three rounds of 0.1% PBS-Triton X (PBST) rinses. For cultured cells an additional permeabilization step was performed using 0.2% PBST for 30 min at RT. The samples were then blocked for an hour at RT in blocking solution (0.2% BSA and 5% NGS in 0.1% PBST for Drosophila tissue or 3% BSA in 0.1% PBST for MCF-7 cells) and incubated in primary antibody solution overnight at 8^{o}C. The following day, samples were rinsed three times with PBST and incubated with secondary antibody and DAPI (300 nM) for an hour at RT. Antibody solutions were prepared in block. Dilutions used can be found in Table 2.2.

Following three more PBST washes, *Drosophila* notum and MCF-7 cells were mounted on microscope slides using GeneTex FluoroGel mounting media (Source Bioscience UK). Samples were left to set overnight at 8^{o}C or for 2 hr at RT before imaging.

Following the final three PBST washes, *Drosophila* brains were placed in a solution of 10% Glycerol and 90% PBS and were then mounted on custom made microscope slides. Using clear nail varnish, a bridge like structure was created by stacking one 22x22 mm coverslips 0.13-0.17mm thick on each side of the slide, approximately 0.5 cm apart. *Drosophila* brains were placed in between the coverslips and the entire structure was covered with a 22x50 mm coverslip. A solution of 10% Glycerol and 90% PBS was then carefully pipetted underneath the long coverslip until the gap between the two small coverslips was filled. The entire structure was sealed using clear nail varnish. Samples were left to set at RT for approximately three hours, until the nail varnish has dried and were imaged the same day.

2.4.2 TdT-Mediated dUTP Nick-End-Labeling

The ApopTag® Red In Situ Apoptosis Detection Kit (S7165, Merck Millipore) was used to label apoptotic cells using Laura A. Johnston lab protocol (Wells and Johnston, 2012). In short, dissected nota were fixed in 4% PFA for 20 minutes at RT. Following three 0.1% PBS-Tween (PBSt) washes, tissues were incubated in a pre-cooled ethanol/PBS (2:1) solution for 5 min at -20°C. Following two more 0.1% PBSt washes, tissues were incubated in 10 mM Sodium Citrate pH 6.0 for 30 min at 70°C and rinsed three times with 0.1% PBSt. Tissues were then incubated for 10 minutes at RT in the equilibration buffer provided with the kit, then with the TdT enzyme (diluted 30% v/v in reaction buffer) for 1 hour at 37^{o}C. The reaction was stopped by incubating the samples with the Stop/Wash solution provided in the kit for 10 minutes at RT, followed by three 0.1% PBSt washes. For staining, a 30 minutes RT incubation with anti-dig rhodamine was performed (20% antibody, 50% PBSt, 25% blocking solution provided with the kit, 5% NGS). Following four 0.1% PBSt washes, tissues were incubated with DAPI (3 μM) for 3 minutes at RT. After three more 0.1% PBSt washes, samples were mounted on microscope slides using GeneTex FluoroGel mounting media (Source Bioscience UK) and were left to set overnight at 8^{o}C or for 2 hr at RT before imaging.

2.4.3 RNA extraction

Total cellular RNA was extracted from un-transfected cells, cells with ING1 knockdown and cells transfected with ON-TARGETplus Non-targeting Control siRNAs (Dharmacon) using TRIzol (Thermo Fisher Scientific) following the manufacturer's instructions. In short, cells were pelleted, then homogenised and incubated in TRIzol for 10 minutes at RT. A phenol-chloroform phase separation was performed by chloroform addition and appropriate centrifugation. The aqueous layer containing RNA was then isolated and treated with isopropanol for 10 minutes at RT. Precipitated RNA was washed with 75% ethanol, air dried and resuspended in nuclease free water through a 15 minutes

incubation at 55°C. The RNA solution was then concentrated and purified using the GeneJET RNA cleanup and concentration kit (K0842, TherrmoFisher Scientific). DNase treatment was then performed using Thermo Scientific™ RNase-free DNase I to eliminate any traces of genomic DNA. The concentration of RNA was measured by spectrophotometry using a Nanodrop2000 and the purity of the RNA samples was assessed by calculating the 260 nm:280 nm (RNA:protein) and 260 nm:230 nm (RNA:other contaminants, e.g. salts, phenol, EDTA, non-ionic detergents) ratios.

2.4.4 Complementary DNA synthesis

Complementary DNA (cDNA) was synthetized from extracted total RNA using RevertAid First Strand cDNA Synthesis Kit (k1621, TherrmoFisher Scientific) following the manufacturer's instructions. In short, 2 μg RNA were mixed with 1 μl OligoDT and nuclease free water to a final volume of 12 μl and were incubated 5 minutes at 65°C followed by a 1 minute incubation on ice to ensure efficient primer annealing. Further on 4 μl reaction buffer, 1 μl RNase inhibitor (Ribolock), 2 μl 10 mM dNTP and 1 μl reverse transcriptase (RevertAid) were added to the mix and samples were incubated at 42°C for 60 minutes for DNA polymerisation followed by enzyme inactivation at 70°C for 10 minutes. Negative controls lacking reverse transcriptase were prepared in parallel for each sample.

2.4.5 Quantitative PCR

Quantitative real-time PCR (qPCR) was performed to determine transfection efficiency by measuring relative ING1 mRNA levels. Similarly, relative expression of Ras homolog gene family, member C (RHOC), Diaphanous Related Formin 1 (DIAPH1) and Epithelial Cell Transforming 2 (ECT2) following ING1 KD was also determined by qPCR. A C1000 thermal cycler CFX96 RT system was used. Samples were prepared using gene-specific primers (Table 2.3) for the target genes or the house keeping gene: glyceraldehyde-3-

phosphate dehydrogenase (GAPDH) and were labelled using IQ SYBR Green qPCR Master Mix (BioRad). Primer specificity and efficiency were first determined by standard and melting curve analyses.

2.4.6 Flow cytometry

MCF-7 cells treated with siRNA against ING1 or non-targeting siRNA were collected 48 hr post transfection. For cell cycle analysis samples were processed following the protocol described by Pozarowski and Darzynkiewicz (Pozarowski and Darzynkiewicz, 2004). In short, cells were washed in PBS and fixed in 70% ethanol by incubating on ice overnight. Following a PBS wash, cells were incubated in propidium iodide (PI) staining solution (10 µg/mL PI and 100 µg/mL DNase-free RNase A in 0.1% PBST) for 30 minutes at RT. Samples were then transferred to a FC500 flow cytometer for cell fluorescence measurements. Maximum excitation of PI bound to DNA is at 536 nm, and emission is at 617 nm. Therefore, the blue light line laser was used for excitation of PI fluorescence, and emission was measured using the long-pass 600 nm filter.

For the analysis of apoptosis, the staining protocol suggested by Filby et al. (Filby et al., 2011) was followed. Cells were washed in 2% FBS, fixed in 2% PFA for 45 minutes at RT and permeabilised in 0.1% PBST for 10 minutes at RT, followed by a PI staining solution incubation for 30 minutes at RT. Samples were then processed using an ImageStreamX MkII machine. PI excitation was done using the 488 nm laser and emission was measured using 610/20 nm filter. Images were acquired for the bright field and PI channel using 40x magnification. Samples were acquired with a BF area lower limit of 35 μm^2 to eliminate debris.

2.4.7 Whole-genome transcriptome analysis

Whole-genome transcriptome analysis of transfected and un-transfected (both untreated and treated with non-targeting siRNA) MCF-7 cells was conducted at the Nottingham Arabidopsis Stock Centre (NASC). The RNA concentration and quality was assessed using the Agilent 2100 Bioanalyzer (Agilent Technlogies Inc., Palo Alto, CA) and the RNA 600 Nano Kit (Caliper Life Sciences, Mountain View, CA). Samples with a minimum RNA concentration of 100 ng/µl and RNA Integrity Number (RIN) ≥ 8 were used for gene expression analysis. Single stranded complementary DNA was prepared from 200 ng of total RNA as per the GeneChipTM WT PLUS Reagent Kit (Applied Biosystems and Affymetrix). Total RNA was first converted to cDNA, followed by in vivo transcription to make complementary RNA (cRNA). Single stranded cDNA was synthesized, end labelled and hybridized for 16 hr at 45℃ to Clariom™ S Assay arrays (Thermo Fisher Scientific).

2.5 Imaging

2.5.1 Confocal imaging

Live imaging was performed with either a Leica TCS SP2 (×40/1.25 NA oil objective), a Zeiss LSM880C (x40/1.30 NA oil Ph3 M27 oil objective) or a Zeiss Exciter (Plan-Apochromat x40/1.30 NA oil objective) inverted confocal microscope. Samples were excited with a 458 nm laser, and signal was collected at 500–600 nm. Z-stacks were acquired with a 0.35 µm pixel size and frame averaging of two shots using 1 µm z-sectioning. For time-lapses, z-series were acquired every 3 minutes for 2 hours.

Images from fixed samples were acquired on a Zeiss LSM880 inverted confocal microscope using a x40/1.30 NA oil Ph3 M27 objective. Emission signals were collected sequential as follows: 500-540 nm following 488 nm excitation; 650-700 nm following

633 nm excitation; 562-590 nm following 543 nm excitation and 414-508 nm following 405 nm excitation. Z-stacks were acquired with a 0.17 μm pixel size for samples stained for junction/polarity proteins in *Drosophila* tissue and 0.35 μm pixel size for MCF-7 cells, using 0.5 μm z-sectioning and frame averaging of two shots for all instances. For samples stained for apoptosis in *Drosophila* tissue images were acquired with 0.35 μm pixel size and 1 μm z-sectioning. *Drosophila* brain images were acquired using a x20/0.5 NA Ph2 M27 air objective, 0.7 μm pixel size and 3 μm z-sectioning.

2.5.2 Imaging for metastasis detection in flies

Metastases in adult flies were detected by analysing flies in a dark environment under a Leica MZ10F fluorescence microscope equipped with a blue led lamp and a green acetate filter. Flies were anesthetised using a CO_2 porous polyethylene gas diffuser, submerged in ethanol for 30 seconds, rinsed with PBS and transferred in a rubber dish. A drop of immersion oil was added on top of the fly, which was then investigated for GFP expression. Further on, flies were re-submerged in ethanol to wash the oil and were dissected as described in Chapter 2.2.4. Dissected organs were transferred in a solution of 90% glycerol 10% PBS and were analysed for GFP expression patterns. Magnification up to 6.3x was used. Representative images were acquired using a QIClick colour camera for fluorescence and brightfield imaging (MediaCybernetics) and QCapture Pro image acquisition software for full camera control. Exposure time used was 10-20s for GFP image acquisition.

2.6 Data analysis

2.6.1 Relative transcript levels

Relative transcript levels were calculated relative to expression levels of the house keeping gene GAPDH, using the efficiency calibrated model. This method, described by

Pfaffl (Pfaffl, 2001), is a more generalised representation of the $2^{-\Delta\Delta C_T}$ method (also known as the comparative C_T or fold change (FC) method) and accounts for the polymerase efficiency. Standard curves were first performed for the primers to be used (Table 2.3), and the efficiency of the amplification was calculated following Eq. (2.3). The relative transcript levels were then calculated using Eq. (2.4)-(2.7).

$$E = -1 + 10^{\frac{-1}{slope}} \tag{2.3}$$

$$mean\ C_T = average\ C_T\ readings \tag{2.4}$$

$$\Delta C_T\ = mean\ C_T\ (target\ gene) - mean\ C_T\ (house\ keeping\ gene) \tag{2.5}$$

$$E^{\Delta C_T}\ = \frac{E_{\text{house keeping gene}}^{\text{mean } C_T \text{ (house keeping gene)}}}{E_{\text{target gene}}^{\text{mean } C_T \text{ (target gene)}}} \tag{2.6}$$

$$FC\ = \frac{E^{\Delta C_T\ (treatment\ group)}}{E^{\Delta C_T\ (control\ group)}} \tag{2.7}$$

To compare results from qPCR to the ones from the microarray, an extra step was introduced to convert qPCR FC to the same format as the FC from the microarray experiment. As described by Schmittgen and Livak (Schmittgen and Livak, 2008), qPCR FC<1 were further processed using Eq. (2.8).

$$adjusted\ FC = \frac{-1}{FC}. \tag{2.8}$$

2.6.2 Flow cytometry data analysis

Cell cycle distribution was assessed by applying the Michael H. Fox algorithm, using Kaluza Analysis 2.1 Software (Beckman Coulter). Apoptosis detection was performed using ImageStream Data Analysis and Exploration Software (IDEAS 6.2) and was guided by the apoptosis wizard.

2.6.3 Gene expression data analysis

Gene expression data was analysed using Partek Genomics Suite 6.6 software (Partek Incorporated). The raw CEL files were normalized using the RMA background correction with quantile normalization, log base 2 transformation and mean probe-set summarization with adjustment for GC content. Differentially expressed genes (DEG) were identified by one-way ANOVA analysis. Two sets of controls were used: untreated cells and cells treated with non-targeting (mock) siRNA. Comparisons were performed as follows: untreated cells vs. mock siRNA; untreated cells vs. ING1 KD and mock siRNA vs. ING1 KD. Genes were considered differentially expressed between two groups of treatment if they showed a p-value ≤0.01 with FDR ≤0.05 and fold-change >1.5 or <-1.5.

2.6.4 Gene ontology term enrichment

Differentially expressed genes (DEG) following ING1 KD were analysed for gene ontology (GO) biological process and pathway enrichment, using Database for Annotation, Visualization and Integrated Discovery (DAVID) Bioinformatics Resources 6.8 (Huang et al., 2007). Functional annotation was performed with EASE score 0.1 and a minimum number of three genes for the corresponding term used as thresholds. Bonferroni correction was applied. The following databases were used: Gene Ontology Hierarchy for Biological Processes (GOTERM BP DIRECT), Kyoto Encyclopedia of Genes and Genomes (KEGG), Genetic Association Database (GAD).

2.6.5 Interaction map

The GeneMANIA plug-in for the Cytoscape software (Shannon et al.; Warde-Farley et al., 2010) was used to generate an interaction network between selected genes which were miss-regulated by the ING1 knockdown and genes that are coding adherens junction proteins. The interaction network was generated based on the GO molecular function of the selected genes, by integrating publicly available data and using 10 max resultant attributes and 20 max resultant genes. The derived network reflects genetic and physical interactions between these genes.

2.6.6 Image analysis

Fiji (imageJ) software was used to analyse images (Schindelin et al., 2012). In addition to standard Fiji processing options, the manual tracking Fiji plugin for the 3D tracking of individual invading cell trajectories, developed by Dr Fabrice Cordelières (French National Center for Scientific Research) was used (Cordeliéres).

The clonal surface was determined based on the Moe:GFP labelling. The total area of GFP positive tissue was automatically measured based on a pre-established threshold. The threshold was manually adjusted for each image to best reflect GFP signal. GFP positive cells were counted in a 25 μm square and the total number of clonal cells was estimated based on the clonal area.

Invading cells were identified based on their characteristic round shape and based on their ability to migrate away from the clone within the tissue plane and/or extrude basally from the dorsal epithelium. All invading cells from the field of view were counted and the number of invading cells was expressed as a percentage of the estimated number of GFP labelled cells within the field of view. Pre-invasive (polarised) cells were identified based on their characteristic accumulation of moesin towards one end of the

cell (actin-rich spot), and the amount of pre-invasive cells was expressed as percentage pre-invasive cells/total number of labelled cells.

Similarly, all/ pre-invasive apoptotic clonal cells labelled with anti-cDCP1 or anti-digoxigenin antibodies were counted within the field of view and compared to the total number of GFP positive cells/ pre-invasive cells detected within the same field of view. All apoptotic invasive cells labelled with the fluorescent caspase reporter were counted within the field of view and the percentage of apoptotic invading cells out of the total number of invading cells was then calculated. However, in order to obtain an optimal signal to noise ratio for the iCasper construct some changes were implemented to the image acquisition protocol: the image resolution and the number of frame averaging were increased (0.17 μm pixels, four averages/ frame) and the imaged area was decreased (the centre of the notum was always imaged). Given these circumstances, the percentage of invading cells that could be calculated from the iCasper images is not necessarily representative for each genotype. In order to account for this, the average percentage of apoptotic invading cells estimated based on the average percentage of apoptotic invasive cells determined using the iCasper images was compared to the percentage invading cells previously calculated in the cell delamination experiment.

The total distance an invading cell travelled was measured by summing up the distances travelled by the cell every three minutes within a 30 minutes timeframe. The final travelled distance was calculated as a function of the position of the cell right before delamination and the position the cell reached at the 30 minutes timepoint following delamination. Velocity was calculated as a distance per time ratio based on the final distance travelled by the cell.

Intermediate and basal protrusion length was manually measured using the freehand line tool, following the protrusion shape from the base of the cell to the tip of the protrusion.

The level of fluorescence intensity at cell-cell interface was measured by drawing a line alongside each cell junction using the line tool and averaging the fluorescence intensities detected alongside that line. Intact cell junctions were randomly peaked within the clonal and WT tissue. A minimum of 65 junctions were analysed for each tissue. Cells at the boundary between the clonal and the WT tissue were excluded from analysis. The percentage of defective junctions was calculated as the ratio of missing and/or fragmented cell junctions identified per total number of junctions analysed.

2.6.7 General statistics

Prism (GraphPad) software was used to generate graphs and carry out most statistical analysis. The appropriate statistical test to determine significance was selected based on initial assessment of data distribution. For comparison of two data sets, Student's *t*-test was applied if data was normally distributed and Mann-Whitney U test otherwise. Multiple sample comparison was performed using ANOVA for normally distributed data or Kruskal-Wallis H test for data that did not show a normal distribution. Mean (normal distribution) or median (non-normal distribution) were graphically represented as appropriate. Significance is shown on graphs as follows: $p<0.05$*, $p<0.01$**, $p<0.001$***, $p<0.0001$****.

For the evaluation of the correlation between two data sets, Pearson's (for normally distributed data) or Sperman's correlation coefficients (r) were calculated. The correlation coefficient measures the strength of the association between two variables. A coefficient of -1 or 1 would correspond to a perfectly linear relationship, whilst an r value of 0 denotes no relationship. Generally, r values above 0.7 or below -0.7 are suggestive of a high positive or negative correlation respectively (Mukaka, 2012). The statistical significance of the correlation was also considered. Student's *t*-test was performed in parallel. Only results showing a p-value greater than 0.5 and an r value of ±0.7 were considered to denote a strong correlation between the tested parameters.

Chapter 3 – CG7379 knockdown promotes invasion and metastasis

3.1 Introduction

Tumorigenesis is a complex multistep process that develops over decades and requires several genes and subsequently pathways to be dysregulated. Solid tumours have on average 2-8 driving mutations and 30-60 passenger mutations, and this number can further increase with aging (Vogelstein et al., 2013). Whilst large-scale genomic analysis studies laid the groundwork for cancer research, identifying most if not all driver genes and a plethora of passenger mutations (Vogelstein et al., 2013), the understanding of the whole tumour progression picture is far from being complete. Although more cancer-related mutations have yet to be detected, we now have enough data to guide in parallel the development of more targeted and effective research approaches (Vogelstein et al., 2013). Many oncogenes and tumour suppressor genes have been characterised so far, but the role of many more has yet to be determined. Even the characterisation of some of the well-known tumour suppressor genes is somewhat incomplete with new roles and mechanisms of actions still emerging (e.g. ING1, the tumour suppressor gene investigated within this thesis).

One ambitious study conducted in the Georgiou lab aimed to address this problem through a loss-of-function large-scale genetic screen. In this study, the cell morphology and behaviour were thoroughly characterised in a living epithelium (the dorsal thorax of the *Drosophila* pupa) following individual RNA interference mediated knockdown (KD) of 497 uncharacterised genes that have been found to be mutated or down-regulated in different epithelial cancers (Canales Coutiño et al., 2020).

3.1.1 An *in vivo* genetic screen to identify tumour progression modulators

3.1.1.1 Development of the tumorigenesis model

This study adapted the *in vivo* model previously described by Georgiou and Baum to better fit tumorigenesis characterisation (Georgiou et al., 2008). The MARCM technique was combined with a null mutation for a polarity gene and with RNA interference in order to create tumour-like tissues of specific genotypes on the back of the living fly. This tissue was chosen as it can be imaged using non-invasive techniques (Chapter 2.2.3). The null mutation for the polarity gene (background mutation) was used as a base for the knockdowns in order to mimic the multistep process of tumorigenesis and to allow for identification of both enhancers and suppressors of tumour progression, invasion and metastases. The tumour-like tissues (clones) were specifically labelled using Moe:GFP, which allowed for the analysis of tissue morphology and behaviour in high spatial and temporal resolution. This construct is considered to be 'relatively nondisruptive' (Edwards et al., 1997) and has been extensively used for cell labelling in *Drosophila*. Therefore, the first step of the project was to establish a background mutation.

Loss-of-function mutations of either of the Scribble polarity complex genes promotes cell transformation in the epithelium. The resulting tissue exhibits many traits of malignant mammalian tumours: defective polarity and differentiation, over-proliferation, aberrant cell architecture and invasive behaviour (Bilder and Perrimon, 2000; Humbert et al., 2008). Clonal analysis of *scrib* null mutants in highly proliferative epithelium such as the imaginal discs in *Drosophila* larvae highlighted that mutant cells are kept in check by the co-existing wild-type cells through cell competition (*scrib* null cells did not over-proliferate and eventually died through apoptosis) (Chen et al., 2012). However, expression of constitutively active *ras* in tissue lacking expression of either *scrib, dlg or lgl* in the larval imaginal discs led to the formation of metastasis to the ventral nerve chord (Pagliarini and Xu, 2003). Moreover, *lgl* null brain tumours grafted onto the

abdomen of *Drosophila* metastasised to the ovaries of the fly (Beaucher et al., 2007). In addition, the mammalian orthologues of *scrib*, *dlg* and *lgl* are also established tumour suppressors (Humbert et al., 2003).

The three members of the Scribble basolateral polarity complex were therefore considered for the use as a background mutation. When *dlg* and *scrib* were used to generate homozygous mutant clones in the nota of the fly, the resulting tumours were very small in comparison to wild-type (WT) clones, rendering the identification of potential tumour suppressors in the screen rather impossible (Figure 3.1c-e). *Lgl* homozygote clones in contrast, showed only a moderate reduction in clonal size (Figure 3.1b,e). In addition, subtle, but significant increases in cell delamination and multilayering were observed, making it ideal to use as a background mutation in the screen.

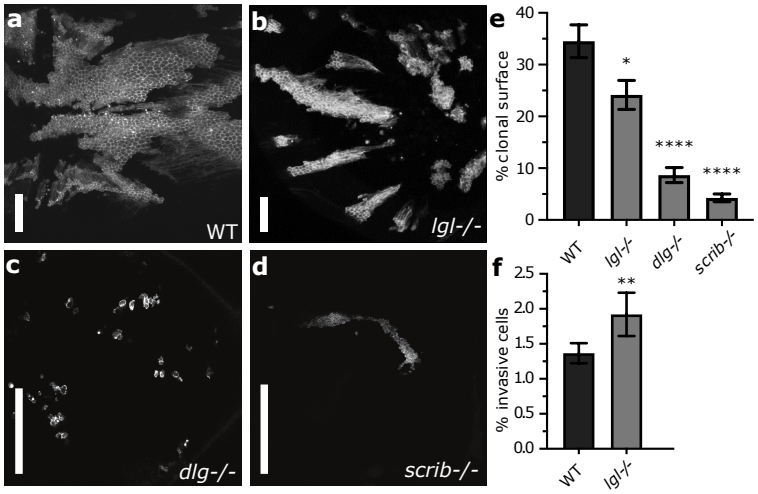


Figure 3.1 Homozygote Scribble complex mutant clones

(a-d) Moe:GFP labelled clonal tissue in the dorsal thorax epithelium of live *Drosophila* pupae. GFP labelled tissue is either WT (a) or homozygous mutant for tumour suppressor genes *lgl* (b), *dlg* (c) or *scrib* (d). **(e)** Quantification of the average clonal surface. n=10 WT; 18 *lg-/-l*; 14 *dlg-/-*; 13 *scrib-/-* animals **(f)** Quantification of the average number of delaminating clonal cells. *Lgl* mutant clones are similar in size with WT clones and show a significant increase in cell delaminaion. n=30 (WT); 41 (*lgl*). Unpaired Student's *t*-test (e) and Kuskal-Wallis test (f) were performed to determine statistical significance. Error bars represent ±s.e.m; *p<0.05; **p<0.01. Scale bar: 50 μm. Figure reproduced from (Canales Coutiño et al., 2020).

3.1.1.2 The pilot screen

Fifty well characterised cancer modulators were investigated in relation to the *lgl-/-* mutation as part of a pilot screen. These included various oncogenes, tumour suppressor genes, matrix metalloproteinases and regulators of cell morphogenesis. The aims of this experiment were to: i) verify if the system was working properly and if so; ii) to develop a scoring system that would allow assessment of tumorigenic properties of non-previously characterised genes to be investigated in the large-scale screen. Expected phenotypes such as increased proliferation leading to tissue overgrowth upon Tsc1 RNAi expression (Potter et al., 2001); increased invasion following pTEN KD (Tamura et al., 1999); increased multilayering as a consequence of pak KD (Aguilar-Aragon et al., 2018); abnormal cell morphology as a result of E-cadherin KD (Tepass et al., 1996) or abnormal cell division (including blebbing) as a result of moe RNAi expression (Kunda et al., 2008) (moe RNAi does not targe Moe:GFP, as the fluorescent construct encodes only the C-terminal tail of the Moe protein (Edwards et al., 1997)) were observed (Figure 3.2). Additionally, negative controls, consisting of genes that under normal circumstances are not expressed in the notum, failed to significantly change the *lgl-/-*phenotype, further confirming that the newly developed *in vivo* cancer model would allow for identification of tumour modulators. Therefore, by simultaneously expressing a homozygous *lgl-/-* null mutation and an RNAi construct specifically within Moe:GFP labelled tissue (Figure 2.4), a detailed study of cell structure and dynamics in cancer progression can be performed.

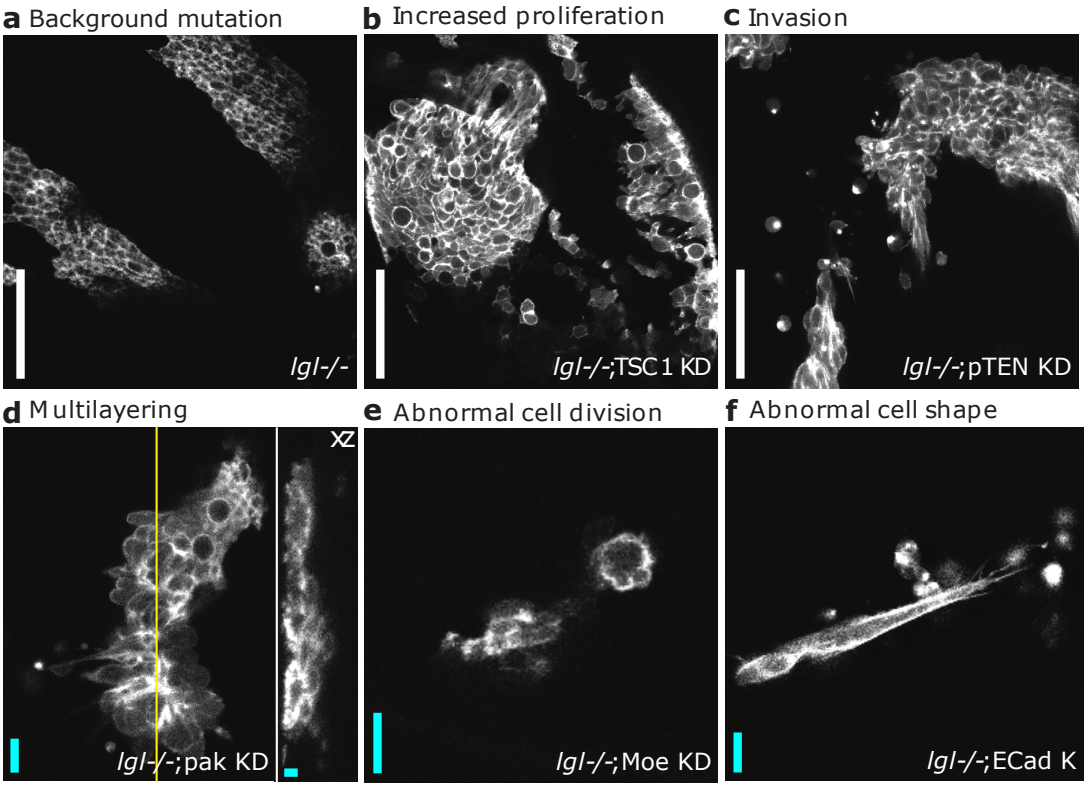


Figure 3.2 Example of phenotypes observed during the pilot screen

Moe:GFP labelled clones generated on the back of the fruit fly during the pilot study. All clonal tissues are homozygote for *lgl-/-* and (b-f) express RNAi lines targeting well characterised tumour suppressors. **(a)** Baseline phenotype given by the expression of the background mutation alone, **(b)** Tissue overgrowth, **(c)** Increased invasion, **(d)** Multilayering, **(e)** Abnormal cell division highlighted by blebbing cell membrane, **(f)** Elongated cell shape. White scale bar: 50μm, cyan scale bar: 10 μm. Figure reproduced from (Canales Coutiño et al., 2020).

Another essential step was to create a database of known malignant phenotypes and to set up a scoring procedure which would allow for an objective analysis of the phenotypes generated. The Moe:GFP labelling of the mutant tissue offers detailed information about cell shape by enabling visualisation of the actin rich structures of the cell such as the cytoskeleton or accessory components, e.g. protrusions. Extensive study and characterisation of the cell behaviour and morphology observed within the pilot screen led to the identification of 32 different cancer-related phenotypes (Appendix 1). Those phenotypes were qualitatively scored in relation to the background mutation used (*lgl-/-* alone). Thresholds were set to identify significant changes to the *lgl* mutant

phenotypes. For most categories an enhancement of the *lgl-/-* phenotype was reflected in a positive score up to a maximum of +2, whilst an inhibition would receive a negative score down to a minimum of -3 depending on the severity of the phenotype. Some binary categories (where 0 denotes no change and 1 denotes an enhancement of the baseline phenotype) were also included. In this way a systematic semi-quantitative scoring of tumour behaviour for every imaged animal became possible (Appendix 1). Of note here is that downregulating expression of one gene may affect several phenotypes. For instance, TSC1 KD (Figure 3.2b) simultaneously affected the polarisation of the cytoskeleton in both clonal and invading cells, increased the clone size and the overall clonal coverage, increased basal protrusion length and decreased the apex size. Each RNAi line was therefore independently scored for each phenotype.

3.1.1.3 The large-scale genetic screen

The large-scale genetic screen aimed to give a brief characterisation of the behaviour of 497 uncharacterised genes that have been found to be mutated in different epithelial cancers. In order to minimise the occurrence of false positives when searching for tumour modulators in the described system, two RNAi lines were independently used for the KD of each gene throughout the entire experiment wherever possible. Five animals were analysed for each RNAi line, and for data analysis purposes each RNAi line was treated separately. To reduce the subjectivity of the developed scoring system, each image was blindly analysed by two independent scientists, with the average scores providing a less biased representation of the studied phenotypes.

In 87.5% of the cases, the two RNAi lines used against the same gene gave statistically similar phenotypes confirming that the phenotypes observed were due to a loss of gene expression and not off target effects. Moreover, a quality control was performed for a selection of four phenotypes: clonal tissue, invading cells, basal protrusions and cell apex area. Randomly selected genes for each of these categories were analysed using

quantitative measurements. A strong correlation was observed between the quantitative and the qualitative scores (Spearman correlation test, r^2=0.91-0.97), validating therefore the scoring system. Next, the distribution of the average scores for each phenotypic category was determined. The RNAi lines that were assigned a score above or below the interquartile range (IQR) from the median score during the phenotypic analysis stage were considered to significantly modulate tumour progression in this system.

Hierarchical clustering of all 754 RNAi lines analysed across the 32 studied phenotypes was then performed (Figure 3.3a). Ten phenotypic clusters of genes sharing similar overall phenotypes were identified. Genes encompass within one cluster are likely to share similar molecular functions. To further distinguish genes that affect a certain cellular process consensus clustering was performed (Figure 3.3b). Three distinct category clusters were identified: actin cytoskeleton regulation, invasion and multilayering, and cell proliferation and cell and tissue morphology. Genes that were shown to modulate one aspect of cell behaviour/ morphology in one category have a high probability to affect the other phenotypes from the same cluster.

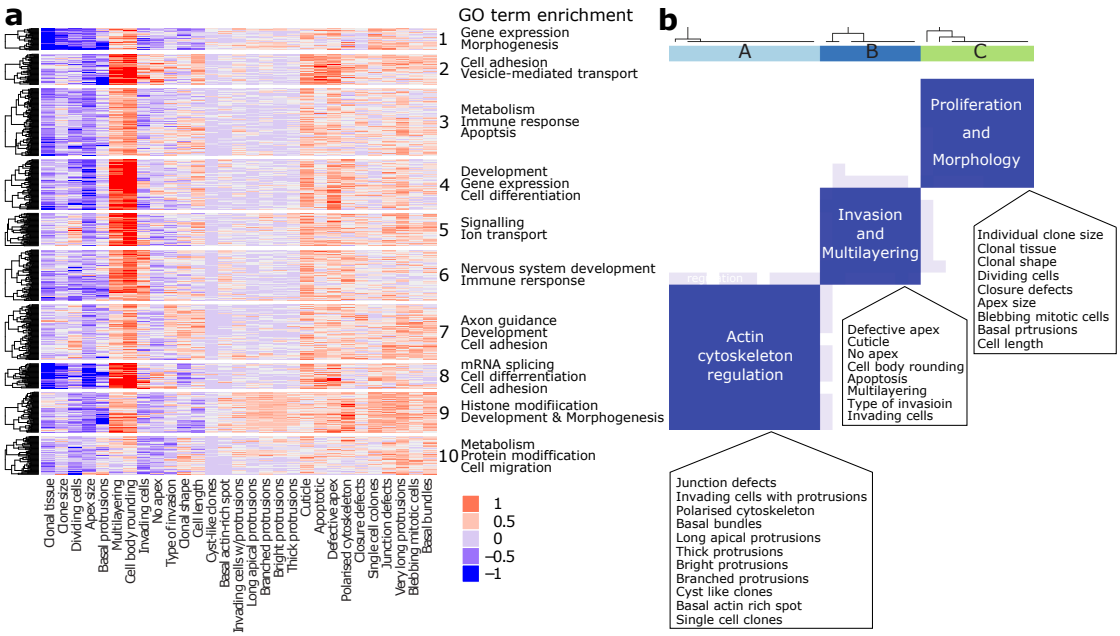


Figure 3.3 Clustering analysis of RNAi lines analysed during the large-scale genetic screen

(a) Supervised hierarchical clustering based on Euclidean distance for the 754 RNAi lines across the 32 cancer-related phenotypic categories was performed to identify phenotypic clusters (Row=RNAi line; Column=phenotypic category; map colours=average phenotype scores). The optimal number of clusters was determined *a priori*. The biological significance of each cluster was assessed by GO enrichment analysis. Relevant GO categories for each cluster are shown on the right-hand side. **(b)** Consensus clustering of the phenotypic categories analysed during the screen identifies three phenotypic subgroups. The blue shading represents consensus values between pairs of phenotypes. Phenotypes that always occur in the same cluster display high consensus, represented in the map by dark shades of blue. From (Canales Coutiño et al., 2020).

This method identified, amongst others, 119 RNAi lines that when downregulated enhance tumour invasion. Several GO biological processes were statistically enriched with the invasion hits: cell adhesion, biosynthetic process, calcium ion transport, regulation of transcription, axon guidance, histone modifications and chromatin remodelling. Some of these correlations were expected based on the existing literature (e.g. cell adhesion), whilst others are more novel (e.g. histone and chromatin remodelling), opening up a whole new research path to follow. One such novel invasion enhancer identified in the screen is the CG7379 gene that is predicted to play a role in histone and chromatin remodelling.

3.1.2 CG7379

The *Drosophila* CG7379 gene is located on the right arm of chromosome 3. Spanning 1930 bp, it encodes a 433 amino acids long polypeptide (Attrill et al., 2015). CG7379 has only one isoform which is ubiquitously expressed at low to moderately high levels in *Drosophila* throughout all developmental stages (Gelbart and Emmert, 2013) and has been identified as a p53 interactor (Lunardi et al., 2010). As a component of the SIN3A protein complex (Spain et al., 2010), CG7379 is predicted to be involved in histone regulation (Gaudet et al., 2011).

Although CG7379 is largely uncharacterised in *Drosophila*, it has been picked up in numerous screens, focusing on diverse biological functions, including Notch pathway regulation, muscle morphogenesis, adiposity regulation, and airway morphogenesis (Baumbach et al., 2014; Hosono et al., 2015; Mummery-Widmer et al., 2009; Saj et al., 2010; Schnorrer et al., 2010).

3.2 Results

3.2.1. CG7379 knockdown promotes single cell invasion in the living epithelium

The loss-of-function genetic screen previously performed in our laboratory led to the identification of CG7379 as a putative tumour suppressor. Between the two RNAi lines used in the screen to KD CG7379 expression (27988 and 27989), CG7379 KD was identified as a hit for eight of the 32 investigated phenotypes (Table 3.1; Appendix 1). When knocked down in *lgl-/-* mutant clones within the living epithelium from the nota of *Drosophila* pupae, CG7379 promoted tumour progression by enhancing invasion (Figure 3.4d). Additionally, CG7379 KD in cooperation with *lgl-/-* lead to the emergence of invading cells with protrusions, basal bundles or thick/bright/branched protrusions

(Figure 3.4c), increased apical/intermediate protrusion length (Figure 3.4a) and decreased basal protrusion length (Figure 3.4b lower panels). A description of each phenotype as well as the average scores for the two RNAi line used to KD CG7379 can be found in Appendix 1.

Table 3.1 Phenotypic effects of mosaic *lgl-/-*; CG7379 knockdown in *Drosophila* notum

Phenotypical category	Enhancement	Inhibition
Invading cells	27988	✗
Invading cells with protrusions	27988	✗
Basal bundles	27989	✗
Long apical/intermediate protrusions	27988 & 27989	✗
Thick protrusion	27989	✗
Bright protrusions	27988 & 27989	✗
Branched protrusions	27988	✗
Basal protrusions	✗	27988 & 27989

Further on, more animals carrying the KD were analysed as in the screen to evaluate the consistency of the phenotypes. Three different RNAi lines (27988, n=7; 27989, n=6; 14430, n=11) were tested to ensure the specificity of the phenotype to the KD, especially since in the screen not both RNAi lines used were picked as 'hits' for all phenotypes. As shown in Figure 3.4, CG7379 KD performed using any of the three RNAi lines led to the manifestation of most phenotypes identified in the screen. However, during this extensive investigation we failed to identify any 'bright protrusions' or invasive cells with protrusions. Moreover, the basal protrusions appeared to show an unusual variability in size rather than being generally shorter: whilst some of the cells lacking CG7379 expression showed a clear reduction in protrusion length (Figure 3.4b lower panels), others appeared to have developed longer protrusions than their *lgl-/-* counterparts (Figure 3.4b upper panels). Furthermore, it is important to stress that phenotypes such as thick/branched protrusion and basal bundles, although consistently seen across

animals bearing CG7379 KD clones, did not account for the majority of the basal protrusions.

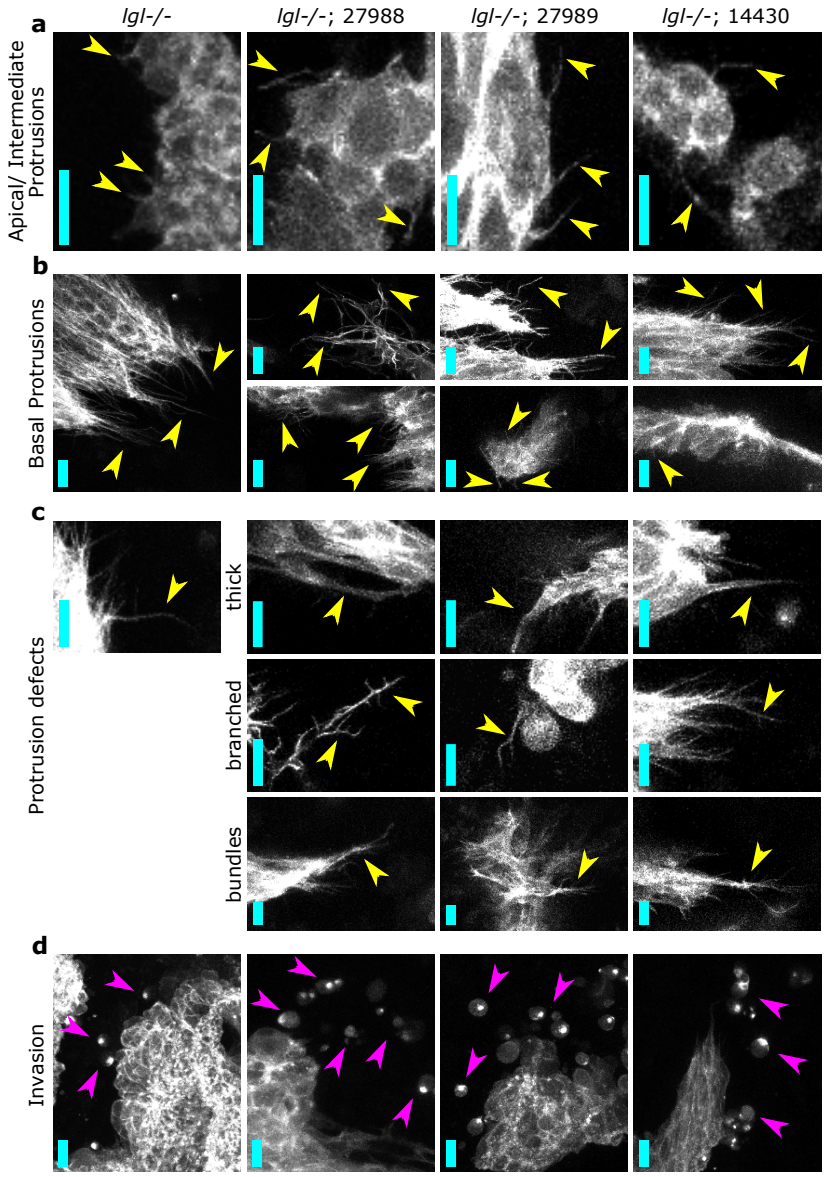


Figure 3.4 Phenotypic effects of CG7379 knockdown on *lgl-/-* clones

Example images for the categories for which CG7379 KD was identified as a 'hit' in the genetic screen. Images represent z-stack projections of relevant slices **(a)** intermediate slices showing intermediate level protrusions; **(b)** bottom of the stack showing basal protrusions; **(c)** example of a typical protrusion from *lgl-/-* clones and examples of protrusion defects sometimes identified following CG7379 KD **(d)** Z projection of entire stack showing invading cells. Cyan scale bar: 10 μm. Yellow arrowhead points towards relevant cell protrusions. Magenta arrowhead points towards invasive cells.

To determine whether the observed phenotypes were indeed of statistical significance, we further measured the level of invasion and the length of protrusions in *lgl-/-;* CG7379 KD clones which we compared to *lgl-/-* clones. When expressed in combination with the *lgl-/-* mutation, all three RNAi lines significantly increased cell delamination (Table 3.2, Figure 3.5c). Similarly, the use of either of the three RNAi lines lead to a significant increase in the intermediate protrusion length (Table 3.2, Figure 3.5a). The length of basal protrusions in contrast, did not exhibit any significant changes following CG7379 KD (Figure 3.5b), however the *lgl-/-* mutation increased the length of basal protrusions in comparison to WT Moe:GFP labelled clones (WT: 6.9±0.5 μm, *lgl-/-*: 8.5±0.3 μm, p=0.0156). As suggested earlier, this may be attributable to the huge variability observed in basal protrusion length (Table 3.2). Taken together, we consider that CG7379 might have the potential to modulate actin behaviour.

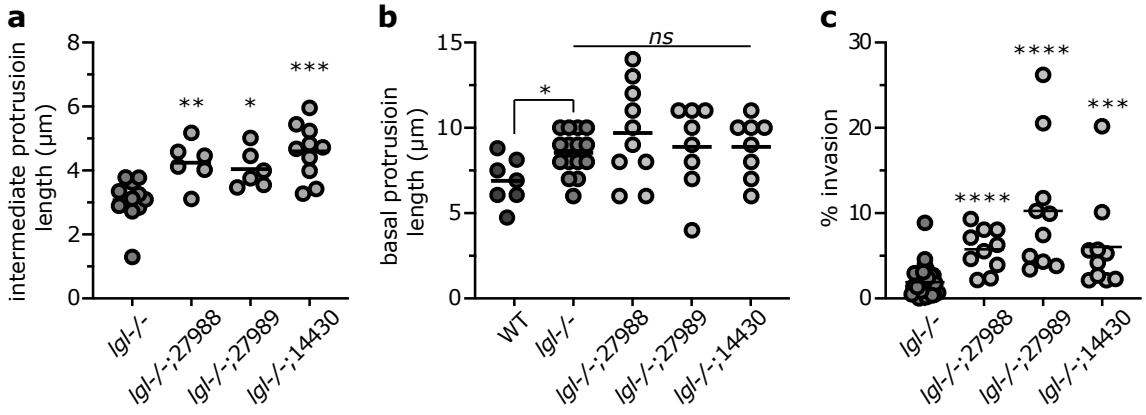


Figure 3.5 Quantification of protrusion length and the level of invasion induced by CG7379 knockdown

(a) Quantification of intermediate protrusion length: n≥ 13 protrusions per animal from 11 *lgl-/-*; 6 *lgl-/-;* 27988; 6 *lgl-/-;* 27989 and 10 *lgl-/-;* 14430 animals respectively **(b)** Quantification of basal protrusion length: n≥ 28 protrusions per animal from 7 WT; 15 *lgl-/-*; 10 *lgl-/-;* 27988; 9 *lgl-/-;* 27989 and 9 *lgl-/-;* 14430 animals respectively **(c)** Quantification of invasion represented as percentage invading cells out of total clonal coverage: n≥ 10 animals/genotype. Unpaired Student's *t*-test (a, b) or Mann-Whitney U test (c) were performed to determine statistical significance, * p<0.05; **p<0.01; ***p<0.001; ****p<0.0001.

Table 3.2 Average intermediate protrusion length and level of invasion following CG7379 knockdown in *lgl-/-* mutant tissue

	lgl-/-	*lgl-/-*;27988	*lgl-/-*; 27989	*lgl-/-*;14430
Intermediate protrusions (μm)	3.1±0.2	4.3±0.3	4±0.2	4.6±0.3
Basal protrusions (μm)	8.5±0.3	9.7±0.9	8.9±0.9	8.9±0.6
Invasion (%)	1.9±0.3	5.8±0.8	10.3±2.4	6±1.7

Given that neither CG7379, nor its human orthologue ING1 have been thoroughly investigated in relation to their effect on cell invasion, a further characterization of their role in the invasive behaviour of tumour cells could cast some light on the proposed metastasis preventing roles that ING1 might possess.

It was important to first determine whether the invasive phenotype was a consequence of a co-operation between the simultaneous loss of CG7379 and *lgl*, or if CG7379 KD alone would be sufficient to promote invasion. Using the MARCM technique (Chapter 2.2.2.4) CG7379 was knocked down specifically in otherwise wild-type Moe:GFP expressing tissue on the back epithelium of *Drosophila*. The clones generated using this approach appeared relatively normal in terms of epithelial organization as unlike their *lgl-/-*; CG7379 KD counterparts they did not display multilayered structures. However, invading cells were still detectable beneath the epithelium (Figure 3.6d). When quantified as a percentage of the total number of tumour-like cells in the notum, this increase in invasion proved to be statistically significant in comparison to the appropriate WT or *lgl-/-* control clones, irrespective of the RNAi line used (Table 3.3). However, the phenotype was clearly exacerbated by the *lgl* mutation, as shown by the significant enhancement of the invasive potential of *lgl-/-,* CG7379 KD cells in comparison to those featuring only the KD (p= 0.0055; compare Figure 3.6b and d).

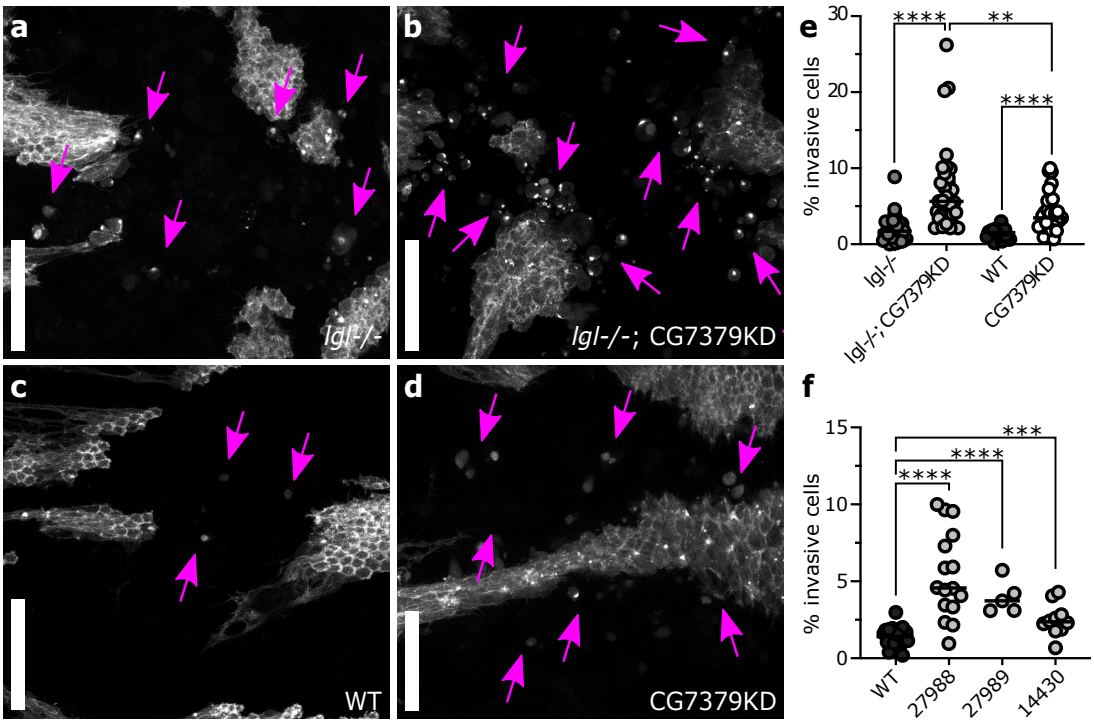


Figure 3.6 CG7379 knockdown alone is sufficient to increase invasion

(a-d) Examples of invasive mutant clones labelled with Moe:GFP, genotype: *lgl-/-*; CG7379 KD (b) and CG7379 KD (d) in comparison to the appropriate control clones, genotype: *lgl-/-* (a) and WT (c). Sample images of Z projection from the apex to the base of the clones. Scale bar: 50 μm **(e)** Quantification of invasion represented as percentage invading cells out of total number of labelled cells. n=21 WT; 32 *lgl-/-*; 31 CG7379 KD; and 31 *lgl-/-*; CG7379 KD animals. Kruskal-Wallis test was performed to determine statistical significance. **(f)** Quantification of invasion/RNAi. n=16 RNAi 27988; 5 RNAi 27989; 10 RNAi 14430 animals. Unpaired Student's *t*-test was performed to determine statistical significance. **p<0.01; ***p<0.001; ****p<0.0001.

Table 3.3 Average level of delamination from Moe:GFP labelled mosaic tissues induced on the back of the fruit fly

WT	CG7379KD	*lgl-/-*	*lgl-/-;* CG7379KD
1.4±0.1%	4.1±0.5%	1.9±0.3%	7.4±1%
	27988	27989	14430
	5.4±0.7%	4.0±0.5%	2.5±0.3%

Similarly, CG7379 KD in WT tissue significantly increased the length of intermediate protrusions, irrespective of the RNAi line used (Table 3.4, Figure 3.7a-c). The phenotype was further amplified by the *lgl-/-* mutation as *lgl-/-*; CG7379 KD cells exhibit significantly longer intermediate protrusions than CG7379 KD cells (p=0.0007). Moreover, protrusion defects such as thick or branched protrusions (Figure 3.7f-f'') were seen more often than in WT Moe:GFP labelled clones. Similar to cells from *lgl-/-*; CG7379 KD clones, cells from CG7379 KD clones often formed basal bundles (Figure 3.7f) as opposed to cells from Moe:GFP labelled WT clones (Figure 3.7e). Together with the fact that all these phenotypes were consistently observed across three different RNAi lines targeting CG7379 (Figure 3.6f, Figure 3.7d), this indicates that the invasion and protrusion related phenotypes observed in the screen following CG7379 KD in *lgl* defective tissue are indeed a consequence of diminished expression levels of CG7379 deeming this gene interesting for a more thorough characterisation. For practical reasons, only the two RNAi lines that gave the most striking results (27988, 27989) were further used for all experiments performed.

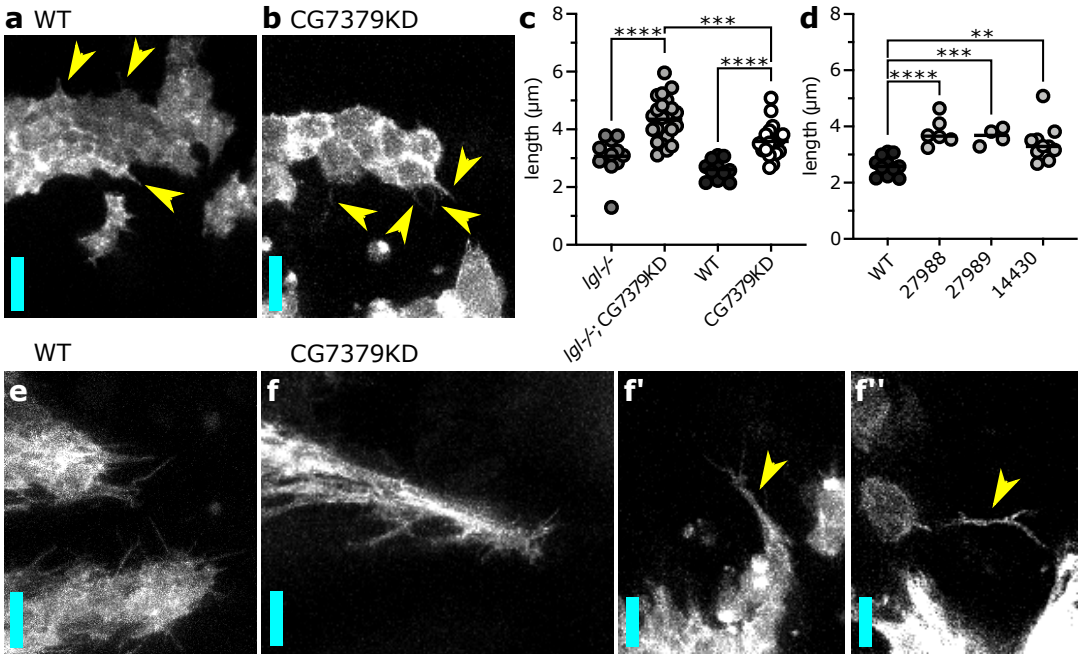


Figure 3.7 Cell protrusion aspect following CG7379 knockdown

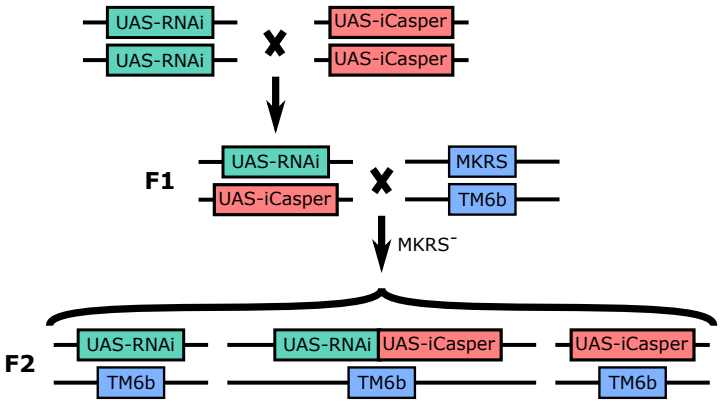
(a,b) Examples of intermediate protrusions in WT (a) and CG7379 KD (b) Moe:GFP labelled clones. **(c)** Quantification of intermediate protrusion length. n≥ 13 protrusions/animal from 11 WT; 11 *lgl-/-*; 20 CG7379 KD and 22 *lgl-/-*; CG7379 KD animals. One-way ANOVA was performed to determine statistical significance. **(d)** Quantification of intermediate protrusion length/RNAi. n≥ 13 protrusions/animal from 11 WT; 6 RNAi 27988; 4 RNAi 27989 and 10 RNAi 14430 animals. Unpaired Student's *t*-test was performed to determine statistical significance. **p<0.01; ***p<0.001; ****p<0.0001. **(e)** Representative example of basal protrusion aspect in WT Moe:GFP labelled clones. **(f-f'')** Examples of protrusion defects induced by CG7379 KD in Moe:GFP labelled clones: basal bundles (f), thick protrusion (f'), branched protrusion (f''). Cyan scale bar: 10 µm. Yellow arrowheads point towards relevant protrusions.

Table 3.4 Average intermediate protrusion length following CG7379 knockdown

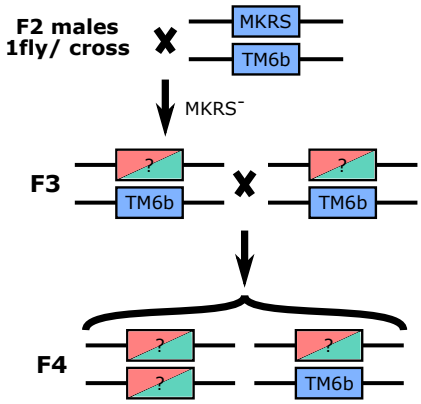
WT	CG7379KD	*lgl-/-*	*lgl-/-;* CG7379KD
2.6±0.1 µm	3.6±0.1 µm	3.1±0.2 µm	4.3±0.2 µm
	27988	27989	14430
	3.8±0.2 µm	3.7±0.1 µm	3.4±0.2 µm

The viability of the invasive cells was next assessed using the *in vivo* caspase sensor, iCasper (To et al., 2015). This sensor was derived from a genetically engineered infrared fluorescent protein and contains a caspase cleavage sequence. Active executioner caspases trigger a conformational change of the iCasper construct which leads to fluorescence emission in the infrared spectrum (680-800 nm) under red light excitation at 630 nm. The iCasper construct is inserted onto the 3rd chromosome of the *Drosophila* genome. Since the commercially available RNAi lines we used to knockdown CG7379 expression are also inserted onto the 3rd chromosome, iCasper and 27988 or 27989 RNAi lines were recombined (Figure 3.8). Flies that are homozygote for either an RNAi construct against CG7379 or the caspase sensor were crossed together to generate female flies that are heterozygote for the two constructs. The virgin females were then crossed to TM6b/MKRS males in order to prevent further crossing-over and stabilize the putatively recombinant lines that were created. In the second generation of progeny, each individual is the result of an independent recombination event and as such, single animals have to be tested for the presence of the recombination. For practical reasons, single males were used. Given that the position of neither one of the RNAi constructs on the chromosome was known, the optimal number of offspring that should have been screened to identify a recombinant could not be calculated. In order to increase the chances of such an event to occur, 50 stocks were created from individual flies from F2 for each RNAi line used. Successful recombination was assessed based on the phenotype of the animals as follows i) the presence of the iCasper construct was shown by fluorescence on the far-red channel; ii) significant increase in invasion in comparison to WT clones denoted the presence of the RNAi line (Table 3.5).

a Meiotic recombination



b Stock creation



c Testing

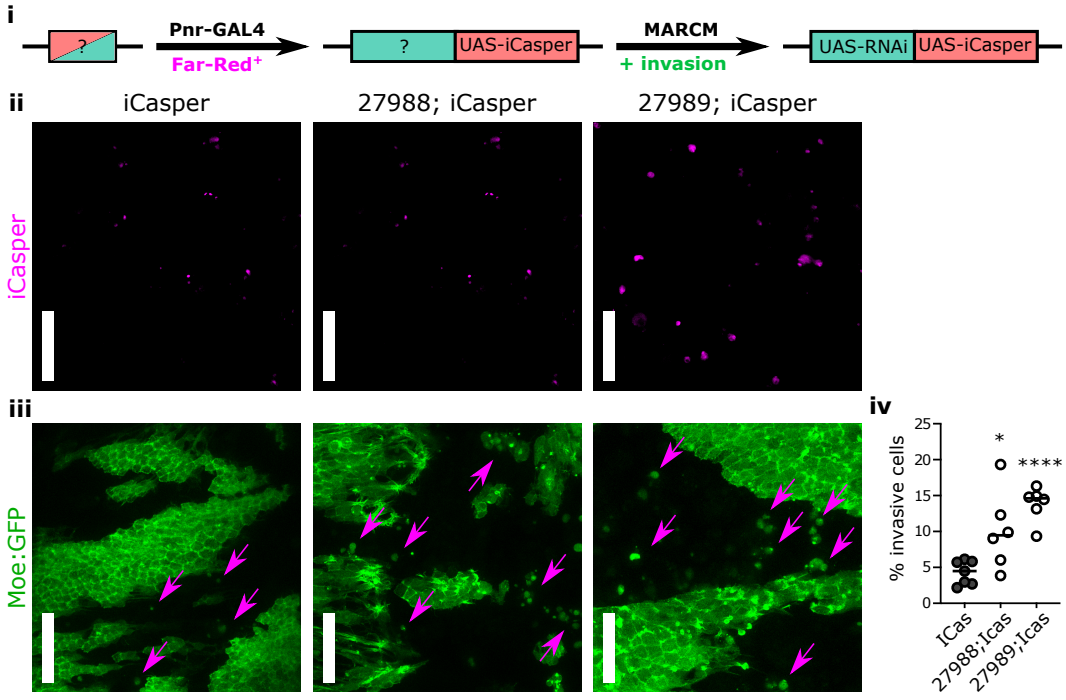


Figure 3.8 Recombination of RNA hairpin and iCasper constructs

UAS-RNAi lines against CG7379 were recombined with the caspase reporter iCasper on the 3rd chromosome to allow for live labelling of apoptotic cells in tissues exhibiting reduced CG7379 expression. **(a)** First, flies that were homozygote for an UAS-RNAi transgene were crossed with flies that were homozygote for UAS-iCasper. Females from the first generation of progeny were crossed with males carrying the TM6b balancer and the MKRS marker. **(b)** Stocks were created from individual males from the second-generation progeny. **(c)** The success of the recombination was tested by inducing Moe:GFP labelled clones on the back of the fruit fly as described in **(i)**. Pnr-GAL4 drives expression of all UAS-transgenes present in the genome of the fly and therefore animals positive for both constructs of interest should concomitantly fluoresce on the far-red channel as a result of caspase activation and present an invasive phenotype as a result of CG7379 KD. **(ii)** Representative images of the iCasper construct in recombinant flies. Animals that carry the iCasper construct fluoresce on the far-red channel. Flies expressing iCasper but no RNAi were used as positive control. **(iii)** Representative images of the GFP channel for the animals showed in (b). Note the increased invasion in recombinant flies as compared to flies expressing iCasper but no RNAi quantified in **(iv)**. Images represent GFP and far-red Z projections of entire z-stacks. Scale bar: 50 μm. Unpaired Student's *t*-test was performed to determine statistical significance. *p<0.05; ****p<0.0001; n= 7 (iCasper); 6 (RNAi; iCasper).

Table 3.5 Average level of invasion from mosaic tumour-like tissues induced in flies carrying a CG7379 RNAi—Icasper recombination

ICas	27988; Icas	27989; Icas
4.3±0.6%	10±2.2%	13.8±1%

As previously shown, not many cells invade from the WT clones and approximately 40% of them appear to be apoptotic, as they tested positive for iCasper, while significantly less apoptosis was detected in the invasive cells from CG7379 KD clones (Table 3.6, p=0.0009). A similar trend (although not significant) was observed following CG7379 KD in *lgl* mutant tissue. *Lgl-/-* alone did not have a significant impact on cell viability. This taken together with the increase in invasion led to a 4.6-fold increase in the amount of viable invasive cells following CG7379 KD in WT animals (p<0.0001) and a 3.7-fold increase when using the *lgl-/-* background mutation (p<0.0001; Figure 3.9).

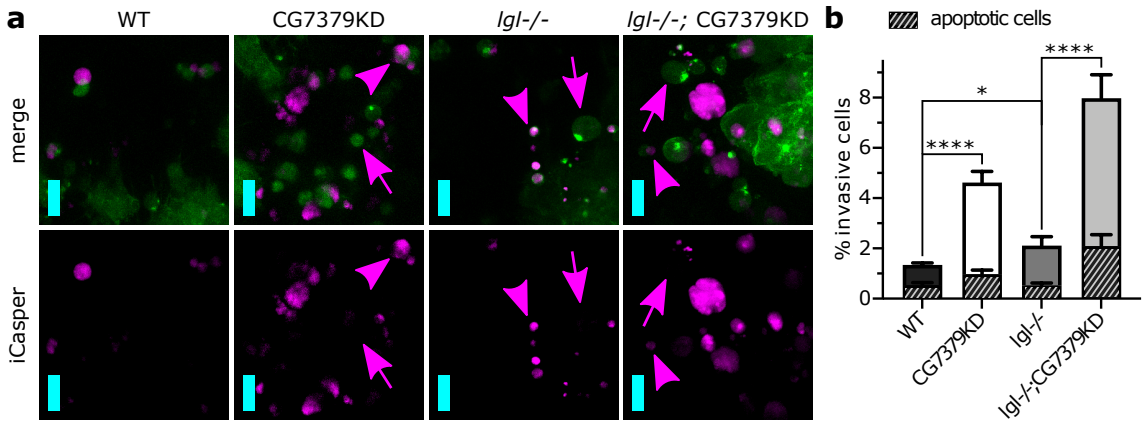


Figure 3.9 Only a subfraction of the invasive cells undergo anoikis once detached from the clone

(a) Example images of apoptotic (arrowhead) and non-apoptotic (arrow) invasive cells. iCasper (magenta) and Moe:GFP (green) labelled mutant clones (genotypes specified above panels). Images represent Z projections of entire z-stack. Scale bar: 10μm **(b)** Quantification of (a). Apoptotic cells (striped pattern) are iCasper positive and represent only a small subfraction of the total number of invading cells. Significance on the graph refers to viable invasive cells. n=400 (WT); 791 (CG7379KD); 346 (*lgl-/-*) and 485 (*lgl-/-;* CG7379KD) cells across 20 animals/genotype. Kruskall-Wallis test was performed to determine statistical significance. *p<0.05; ****p<0.0001.

Table 3.6 Average proportion of delaminated cells undergoing apoptosis

WT	CG7379KD	*lgl-/-*	*lgl-/-;* CG7379KD
36.5±3.4%	21.4±1.9%	30±2.8%	26±2.5%

3.2.2 Characterisation of the behaviour of invasive cells bearing CG7379 knockdown

Further on, tumours and WT clones were followed over time in an attempt to characterise the behaviour of the invasive cells. We noticed that prior to delamination, cells round up and show actin accumulation towards one end of the cell in the form of a bright GFP spot (Figure 3.10). A correlation between this actin polarization in pre-invasive cells and invasion was observed in all four genotypes investigated.

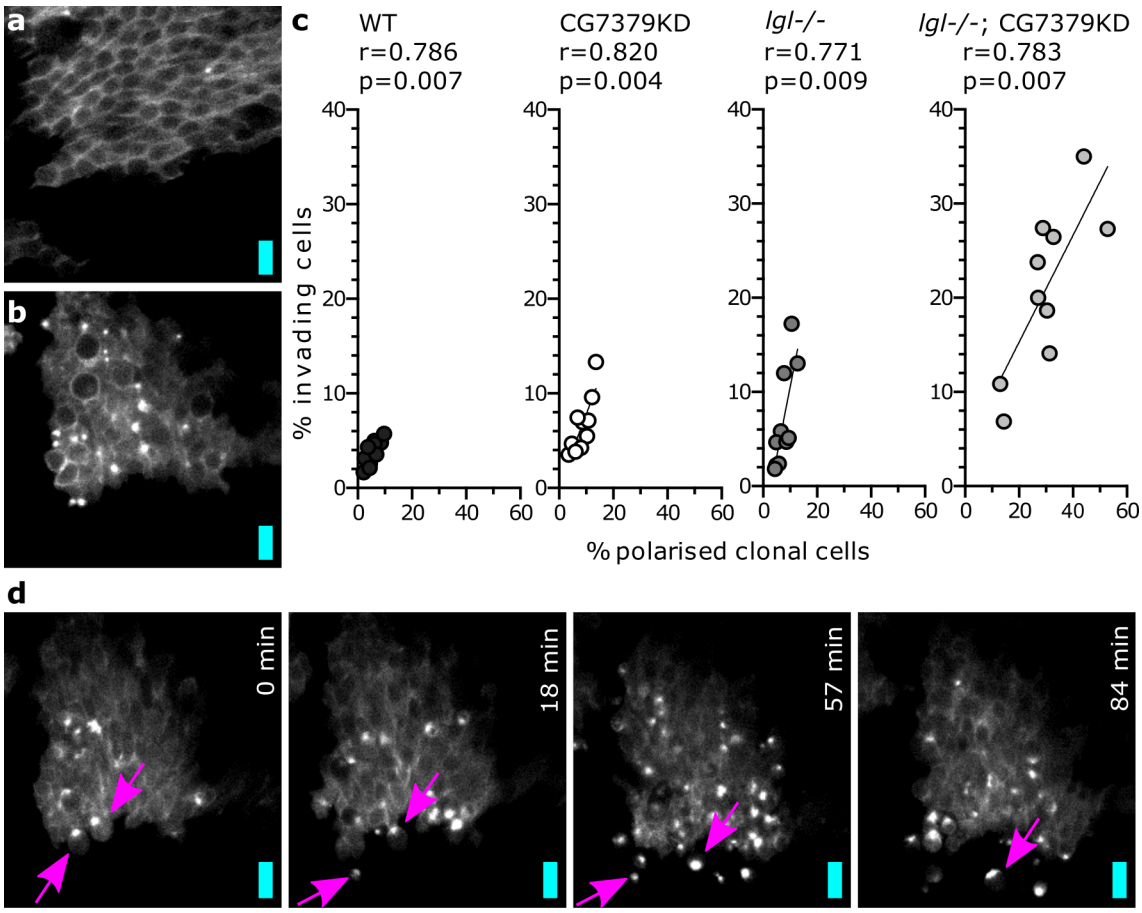


Figure 3.10 Characterisation of cell behaviour prior to invasion

(a,b) Example of non-invasive (a) and highly invasive (b) Moe:GFP labelled mutant tissue from the same animal (genotype: CG7379 KD) **(c)** Graphic representation of the correlation noticed between actin polarisation and invasion. Pearson's or Spearman's correlation tests were performed based on the data distribution. The two parameters show high (and significant) correlation, irrespective of whether the mutant clones were rarely invasive or highly invasive. n=10 animals/ genotype **(d)** Arrows point towards two pre-invasive cells that round up and form a characteristic actin-rich spot at one side of the cell prior to invasion (0 mins). The cells then detach from the mutant clone and migrate away (18-84 mins). Images show representative z-slices from time-lapses. Scale bar: 10 μm.

Single cell tracking was next performed in order to assess the directionality and velocity (the speed with which a cell moves in a particular direction) of the invading cells. The trajectory of each cell was measured every three minutes from the moment it detached from the clone for a total of 30 minutes and the total number of micrometres travelled was documented (total travelled distance in Figure 3.11a). Additionally, the distance the

cell would have travelled if following a straight line was also documented (final travelled distance in Figure 3.11a). The movement of an invading cell would be considered directional if the two parameters would not be significantly different. After analysing the trajectories of 20 cells from a minimum of five animals/genotype, significant differences between the total and final distance travelled were registered for all genotypes (Figure 3.11b). Invasion did not become directional following CG7379 KD, nor as a consequence of double CG7379 and *lgl* loss. Similarly, invading cells did not show significant changes in migration velocity (Figure 3.11c).

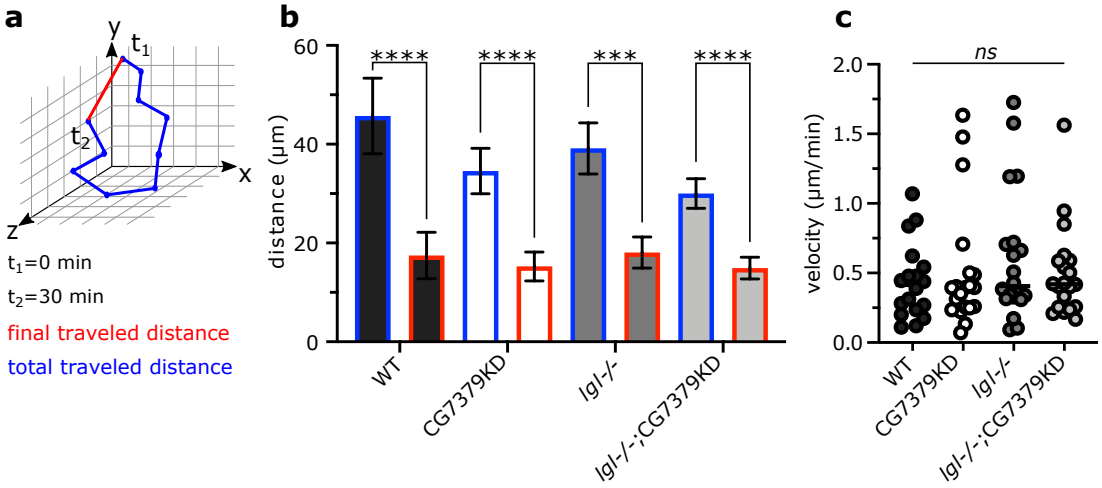


Figure 3.11 Characterisation of invasive cell behaviour

(a) Schematic representation of the two trajectories measured for each invading cell in order to determine directionality. The total travelled distance follows the trajectory of the cell movement whilst the final travelled distance measures the distance that the cell would have travelled if moving in a straight line. **(b)** Quantification of total (blue) and final (red) travelled distance from CG7379 KD and *lgl-/-*; CG7379 KD compared to WT and *lgl-/-* cells respectively. If invasion is directional, the two parameters would be expected to be similar for a given phenotype. Mann-Whitney U test was performed to determine statistical significance. **(c)** Quantification of invasion velocity. Kruskal-Wallis test was performed to determine statistical significance. ***p<0.001, ****p<0.0001

3.2.3 CG7379 knockdown alone can induce metastatic behaviour

The ability of delaminated cells to extrude from the epithelial tissue, invade towards other organs and induce metastasis was next assessed. Invading cells that localise well below the epithelial sheet and therefore must have broken through the cellular matrix were observed as early as 27-28 hr APF (Figure 3.12).

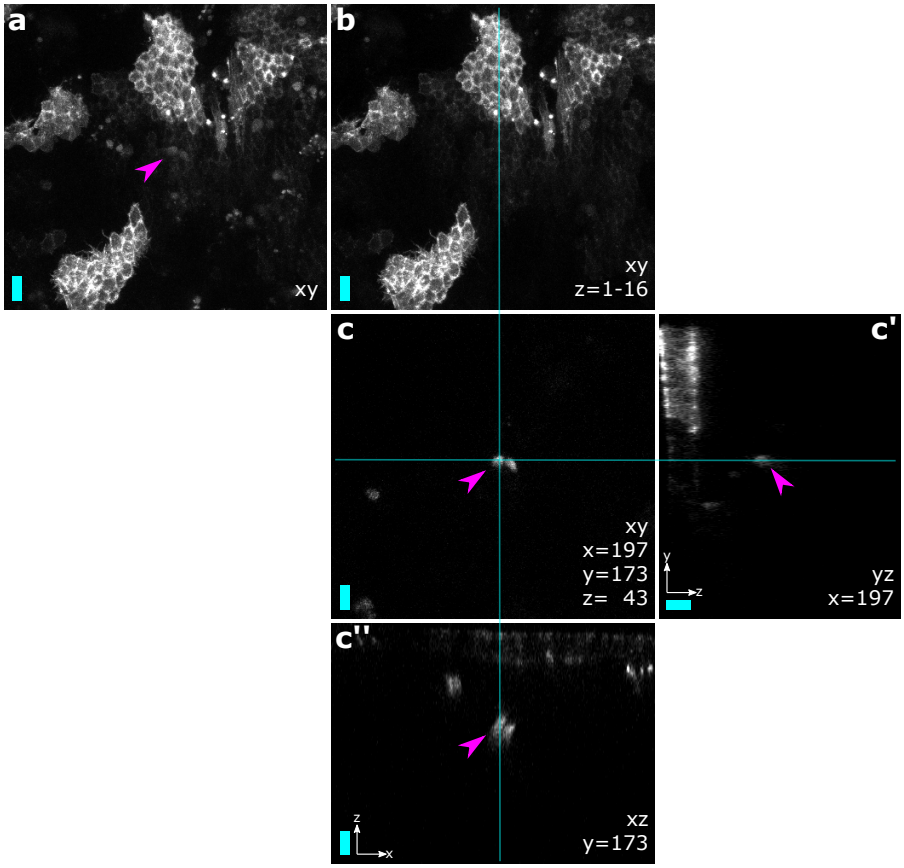


Figure 3.12 CG7379 knockdown invasive cells are capable of extruding from the epithelial tissue

(a) Z max intensity projection of the back of a 28 hr old *Drosophila* pupae carrying Moe:GFP labelled CG7379 KD clones in the notum (z-stack: 98 μm) **(b)** Z max intensity projection of the CG7379 KD clones spanning 16μm on the Z plane **(c)** Basally delaminated cell from one of the Moe:GFP labelled CG7379 KD clones located 25 μm underneath the epithelial sheet. The position of the invading cell is indicated in the figure. **(c')** YZ orthogonal view projection of the invasive cell in (c). **(c'')** XZ orthogonal view projection of the invasive cell in (c). Magenta arrowheads point towards the invasive cell. Cyan lines highlight the plane of projection. Scale bars: 10 μm.

However, no signs of metastasis were noticed in pupae up to 54 hr APF. As metastasis is a process that develops over a rather long period of time, adult flies were used for this experiment instead. First, flies 0, 5 and 10-day-old were analysed to determine the best time to look for metastasis. WT clones were used as a negative control and clones overexpressing *Ras* (*Ras*^{V12}) as a positive control. Flies were analysed using a Leica MZ10F fluorescence microscope. Any GFP expression outside the back of the head and the medial domain of the thorax and abdomen should be the result of metastasis, as Moe:GFP was specifically expressed within this tissue by using the *pnr* promoter (Calleja et al., 2000) (see chapter 2.2.2.4). However, flies with WT clones were also investigated and any tissues, apart from the notum, that expressed GFP in WT flies were discarded from the analysis. Flies were first visually inspected under blue light for GFP expression patterns and then the brain, ovaries/testis and the gastrointestinal tract were dissected and separately analysed. WT flies 0, 5, and 10-day-old did not show any GFP expression pattern in any of these tissues. Animals carrying *lgl-/-* clones in the notum often did not survive up to the adult stage and therefore the ability of *lgl-/-* alone or in combination with Ras^{V12}/ CG7379 KD to induce metastasis could not be assessed in adult flies.

Ras^{V12} clones showed the ability to metastasize in all tissues analysed (Figure 3.13a-f) across the three time frames, however the five days timepoint seemed to be optimal for analysis as gastrointestinal and brain metastases occurred at a higher frequency than in adults younger than 24 hours. Moreover, all tissues investigated showed an increase in their metastatic potential in comparison to 10-day-old flies (Figure 3.13h). To further assess the accuracy of this *in vivo* metastasis detection system brains from WT and *Ras*^{V12} flies were stained for GFP and visualised using confocal microscopy (Figure 3.13g-g''). As expected, WT brains were clear of metastasis (n=11) and all brains from flies with *Ras*^{V12} that appeared fluorescent when inspected with the dissection microscope were positive for GFP expression (n=7).

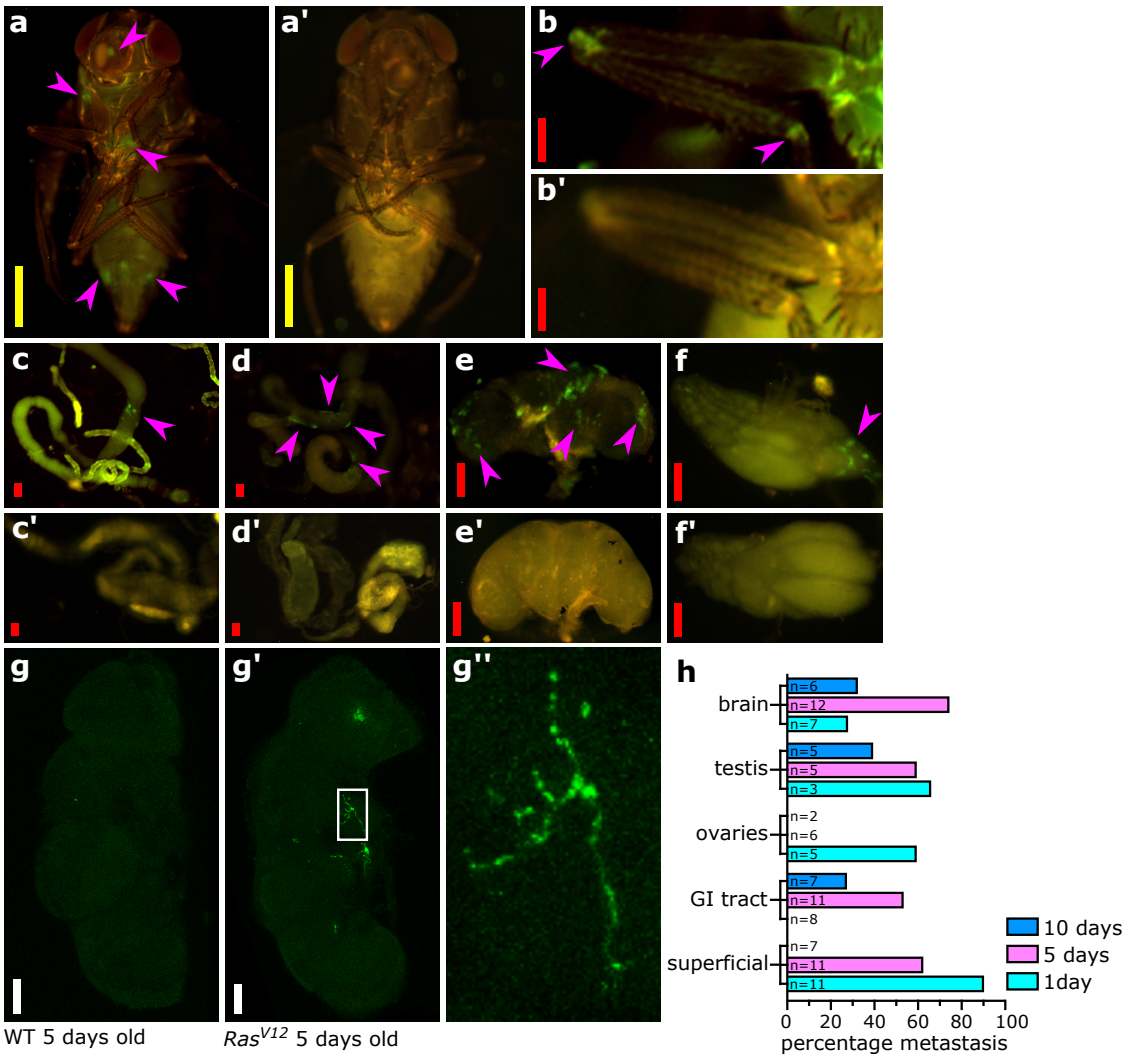


Figure 3.13 Optimisation of an *in vivo* metastases detection system

(a-f) Flies with *Ras* overexpression specifically induced in Moe:GFP labelled clonal tissues under *pnr* control. *Ras*^{v12} tumours were able to metastasize to distal organs such as the midgut (c), testes (d), brain (e) and ovaries (f). Metastases were also noticed in more superficial tissues: proboscis, katepisternum, abdomen (a), mesocoxa, mesotrochanter (b). Magenta arrowheads point towards metastatic overgrowths. **(a'-f')** Corresponding tissues for (a-f) from flies expressing Moe:GFP labelled WT clones under *pnr* control. **(g, g')** Confocal images of brains dissected from 5 day-old WT (g) or *Ras*^{V12} (g') flies. The white rectangle in (g') marks the area zoomed in panel **(g'')**. Images represent max intensity Z projections of confocal z-stacks. Scale bar: white 50 μm, red 100 μm, yellow 500 μm, cyan 10 μm. **(h)** Quantification of metastatic instances in 0, 5 and 10-day-old flies featuring *Ras*^{V12} clones. Length of each bar equals the total number of tissues investigated. Stripped pattern on the graph and percentages on the side denote metastatic instances recorded in each group.

Further on, 5-day-old flies bearing clones with CG7379 KD on their nota were visually inspected and dissected. Brain metastasis were observed in 16.7% of flies featuring CG7379 KD clones induced using the 27988 RNAi line (Figure 3.14). No other tissues apart from the brain seemed to be affected. No metastases were detected when the 27989 RNAi line was used for gene KD. Thirty brains from 5-day-old flies featuring wild-type Moe:GFP labelled clones on their nota were analysed in parallel. No GFP expression was detected.

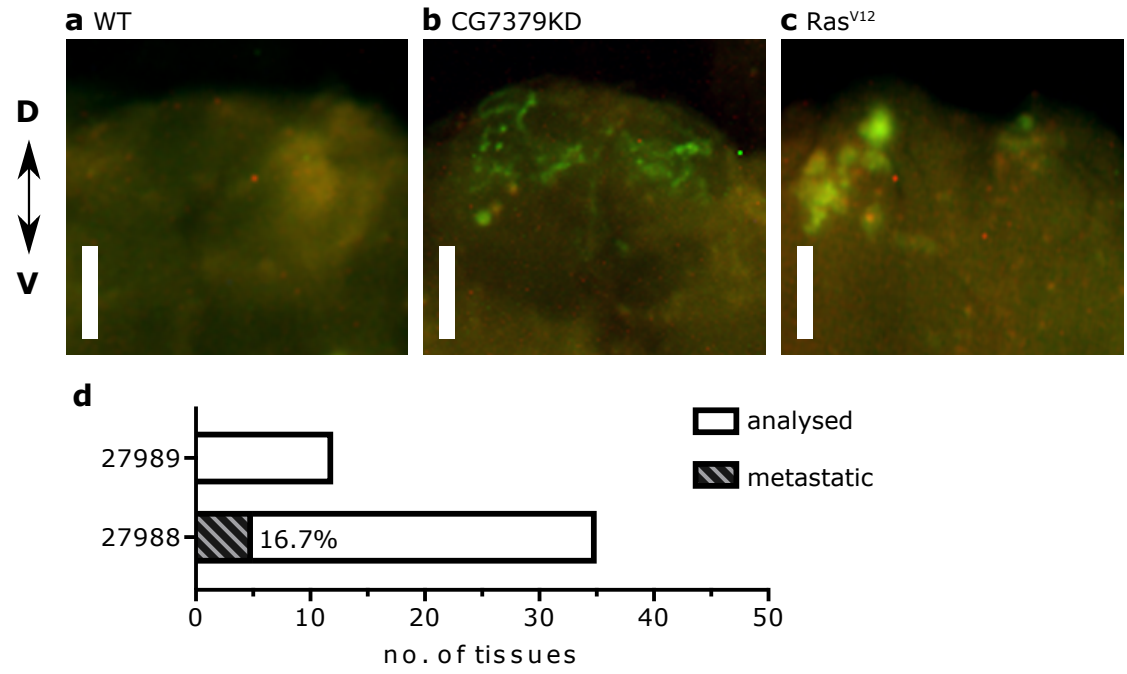


Figure 3.14 Invading cells from CG7379 knockdown tumour-like tissues can metastasize to the brain

Example images of WT **(a)**, CG7379 KD **(b)** and *Ras*^{V12} **(c)** brains from 5-day-old flies (anterior view of the central brain). **(d)** Quantification of brain metastasis (striped pattern) occurrence as a consequence of CG7379 KD. n=35 (27988 RNAi); 12 (27989 RNAi) brains. Scale bar: 50 μm.

3.3 Discussion

The *in vivo* model for epithelial cancer developed in our laboratory is a powerful model for the study of tumour progression. First of all, it allows us to phenocopy the neoplastic tumour development whilst having complete control over the genotype of the tumour-like tissue. Such tissues can then be studied in great detail, based on the Moe:GFP labelling. More importantly, by having complete control over the genotype of the tumour it is possible to single out and precisely study the role of only one gene. This is nearly impossible in most cancer models due to tumour heterogeneity and complexity. Secondly, by using the MARCM technique mosaic tissues are created where the tumours are surrounded by wild-type tissue with which they maintain natural interactions. This makes the system particularly suitable for the study of invasion as the complex interactions required between invading cells and stroma are maintained, unlike in most *in vitro* models.

One of the most invasive genotypes from the screen was *lgl-/-;* CG7379 KD which produced a fourfold increase in cell delamination. The increased invasion observed could be directly attributed to the loss of CG7379 expression, or there could be a cooperative effect between CG7379 KD and the *lgl* mutation. To address this, Moe:GFP labelled CG7379 KD clones without the *lgl* mutation were generated. A significant reduction in the number of invading cells found beneath the epithelium was noticed, when compared to *lgl-/-*; CG7379 KD mutant clones; however there was also a significant increase in invasion when compared to wild-type, or *lgl* mutant clones (Figure 3.6). It therefore appears that although loss of CG7379 function promotes epithelial cell delamination, there is a strong cooperative effect when this loss is accompanied by a loss of *lgl* function.

It has been previously shown that cells from the notum of the fly can delaminate basally and then undergo a process similar to anoikis (Marinari et al., 2012). Invading cells were imaged for up to two hours without observing any obvious signs of cell death, whilst

Marinari, et al. noticed apoptosis ten minutes after delamination. Moreover, the invasion patterns observed in our experiments are phenotypically different than those described by Marinari as cells delaminate irrespective of their localization in the epithelium as opposed to preferentially from the midline. In addition, no signs of tissue overcrowding (the driver force for cell extrusion as described by Marinari) were noticed as the CG7379 KD clones appeared relatively normal, forming an organised monolayered epithelium. However, *lgl-/-* and *lgl-/-;* CG7379 KD tumours are multilayered. To specifically test for the viability of invading cells we used the genetically encoded caspase reporter iCasper. Activation of this construct was previously reported to reflect induction of apoptosis. Moreover, the fluorescent signal has been shown to label all stages of apoptosis starting from cell rounding and persisting even after phagocytosis of the apoptotic cell (To et al., 2015). WT, *lgl-/-,* CG7379 KD and *lgl-/-;* CG7379 KD clones from 20-24 hr APF pupae were tested for live apoptosis. Most invading cells were viable at the time of analysis. Moreover, CG7379 KD significantly decreased apoptosis of invasive cells which is in line with the ability of ING1, CG7379 human orthologue, to modulate apoptotic processes (Bose et al., 2014; Garkavtsev et al., 1998; Helbing et al., 1997; Russell et al., 2006). This together with the fact that we have imaged invading cells for up to two hours after detachment without observing morphological traits of cell death strongly suggests that invading cells do not undergo immediate cell death. However, further experiments should consider following invasive cells expressing the caspase sensor as they delaminate and then for an hour post-invasion to ensure that caspase activation does not occur in response to loss of cell-cell contact.

Dynamic remodelling of the actin cytoskeleton is essential for cell motility and migration regardless of the cell type or invasion mechanism employed by the cell. The actin polarization at one edge of the cell and actin-myosin contractions are responsible for directing the movement and generating the force required for migration in both normal and pathological conditions (Lucas et al., 2013; Vignjevic and Montagnac, 2008; Yamazaki et al., 2005). Actin structures, similar to those observed by us to correlate with

invasiveness of the clonal tissue (actin-rich spots and occasional membrane blebbing) have previously been reported and associated with invasion in both *Drosophila* and human tissues (Kaltschmidt et al., 2002; Yamazaki et al., 2005). Whilst invasive cells from the Moe:GFP labelled clones appear to have an amoeboid like motility displaying a rounded morphology and high velocity (average velocity: 0.5±0.04 μm/min, Figure 3.11c), their movement appears to be rather chaotic resembling chemokinesis (Clark and Vignjevic, 2015; Rikitake and Takai, 2011). The rounding of the invasive cells together with the lack of lamellipodia are suggestive of low polarity and adhesiveness to the substratum (Fok et al., 2006) and is consistent with the behaviour of invasive tumour cells studied in other systems and could be indicative of Rho—ROCK (ras homolog gene family – Rho-associated protein kinase) activity leading to actomyosin contractility (Poincloux et al., 2011; Wilkinson et al., 2005). The type of migration adopted by invasive cells is determined by the mechanical and biochemical properties of the extracellular matrix (Hartman et al., 2017). The morphology of cells invading through a 3D Matrigel matrix have been shown to be characterised by a rounded shape as well (Hakkinen et al., 2010), which could explain the consistency in delaminated cell morphology and behaviour across all phenotypes investigated in this study.

Additionally, CG7379 itself appears to be able to modulate the behaviour of the actin cytoskeleton as CG7379 KD clones displayed a range of protrusion defects. A gradient of Rac activity, from maximal expression levels basally to no expression apically, has been previously shown to determine cell protrusion formation, morphology and dynamics. Based on this model, higher levels of Rac expression are associated with an increase in the number and length of the protrusions and favours filopodia over lamellipodia formation (Couto et al., 2017). As previously described (Georgiou and Baum, 2010), WT cells in our model displayed short apical protrusions, intermediate protrusions and longer, mostly filopodia like, basal protrusions reflecting a balanced Rac gradient (Couto et al., 2017). Also in accordance with the literature (Couto et al., 2017), *lgl-/-* clones seemed to display fewer intermediate protrusions and significantly longer basal

protrusions reflective of a steepened gradient of Rac activity. Cells bearing CG7379 KD displayed long intermediate protrusions that could reflect an alteration of the Rac gradient. To test this hypothesis, single cell clones defective for CG7379 expression should be induced in the notum. This would allow for quantification of the number of intermediate protrusions/cell and for a detailed analysis of protrusion form and dynamics.

CG7379 KD did not have a significant effect on the invasion velocity nor directionality irrespective of the KD background. Despite this, some of the invasive cells from CG7379 KD clones were able to cross the basal membrane (Figure 3.12) and metastasize the brain (Figure 3.14). Both Rho and Rac signalling are crucial for successful invasion and metastasis as it relies on a strict equilibrium between Rac and Rho expression, with cells needing to be able to switch between the two modes of signalling (Deakin and Turner, 2010).

As expected, invasive cells from wild-type Moe:GFP clones are not able to metastasize from the notum to distal tissues. It was previously shown that *Ras* overexpression in combination with mutation in either one of the polarity genes from the Scribble complex induces metastasis in *Drosophila* larvae (Miles et al., 2011; Pagliarini and Xu, 2003). Clones expressing *lgl-/-; Ras*^{V12} were first induced in our system to be used as positive controls, but this combination was lethal at pupal stages, as previously described in the literature (Pagliarini and Xu, 2003). Previously published data shows that *Ras* overexpression on its own can only induce benign tumours in *Drosophila* larvae (Pagliarini and Xu, 2003), however the effect of prolonged hyperactivation of *Ras* covering successive developmental stages was not assessed. Therefore, in our study the effect of *Ras* mosaic overexpression induced starting from embryonic stages (Artero et al., 1992; Natzle and McCarthy, 1984) and amplified during pupation by aging the animals at 29^{o}C was assessed during adulthood. Consistent with previous publications *Ras*^{V12} cells did not spread to other organs during larval and early pupation stages,

however metastases were identified in adult flies. The pattern of cell dissemination from *Ras*^{V12} clones and the time that took for macrometastases to form are in line with a recently published study where cells from Apc-Ras-Sna mutant clones induced in the gut of 2 to 5-day-old adult flies were shown to disseminate to the abdomen, thorax, head, legs, ovaries and the brain within two weeks of induction (Campbell et al., 2019). From all the ages tested, 5-day-old flies appeared to be the best suited for the study of metastasis as they presented metastasis in the gastrointestinal tract and doubled the frequency of brain metastasis in comparison to 0 and 10-day-old flies. This is important as in humans the brain and the liver are preferential metastasis sites for epithelial cancers (Arvelo et al., 2016). Moreover, more metastases were recorded in 5 vs. 10-day-old flies for all tissues. This could be a consequence of immune system activation in response to *Ras* overexpression (Hauling et al., 2014).

Mosaic expression of the 27988 RNAi line against CG7379, but not 27989, in the notum lead to the formation of brain metastases in 5-day-old flies (Figure 3.14). This could be a consequence of the decreased sample size when using the 27989 RNAi or might reflect a more efficient KD when using the 27988 RNAi line as opposed to 27989. The ability of cells lacking CG7379 to induce metastasis is in accord with a study performed on its human orthologue that highlights the ability of ING1 overexpression to reduce the metastatic potential of breast cancer in mice (Thakur et al., 2014).

Chapter 4 – CG7379 and ING1 involvement in cell-cell adhesion

4.1 Introduction

4.1.1 Previous research predicts CG7379 role in cell adhesion

By bringing together phenotypic categories likely to affect the same cellular process, consensus clustering performed in the screen (Canales Coutiño et al., 2020; Canales Coutiño, 2019) led to the identification of 119 RNAi lines that are likely to modulate invasion in cancer progression. A functionally validated network of those genes was then generated by integrating publicly available data from DroID (www.droidb.org, version 2018_08), Flybase (version FB2018_03) and BioGRID (version 3.5.165). Only genetic and physical interactions validated by experimental data were introduced in the network and the only 'linker genes' allowed were those that linked 'hit' genes by no more than one interaction. The resulting network consists of a total of 140 genes linked by 321 interactions. Ninety-nine of these genes have not been previously associated with malignant invasive behaviour, nine of which are completely uncharacterised (Figure 4.1).

Complexes of highly interconnected nodes were then identified using the Molecular Complex Detection (MCODE) algorithm. Such clusters usually denote molecular complexes and signalling cascades. Some of these clusters are rich in proteins which are associated with cancer invasion (e.g. cluster 1, cytoskeleton organisation; cluster 6, adhesion); whilst others are rich in proteins that have not yet been linked to cancer invasion (e.g. cluster 4; cluster 7). Accordingly, GO term analysis of the network identified enrichment of processes that are likely to be essential for cell invasion (e.g. adhesion, cytoskeletal remodelling) together with some more intriguing ones such as axon guidance or gene expression.

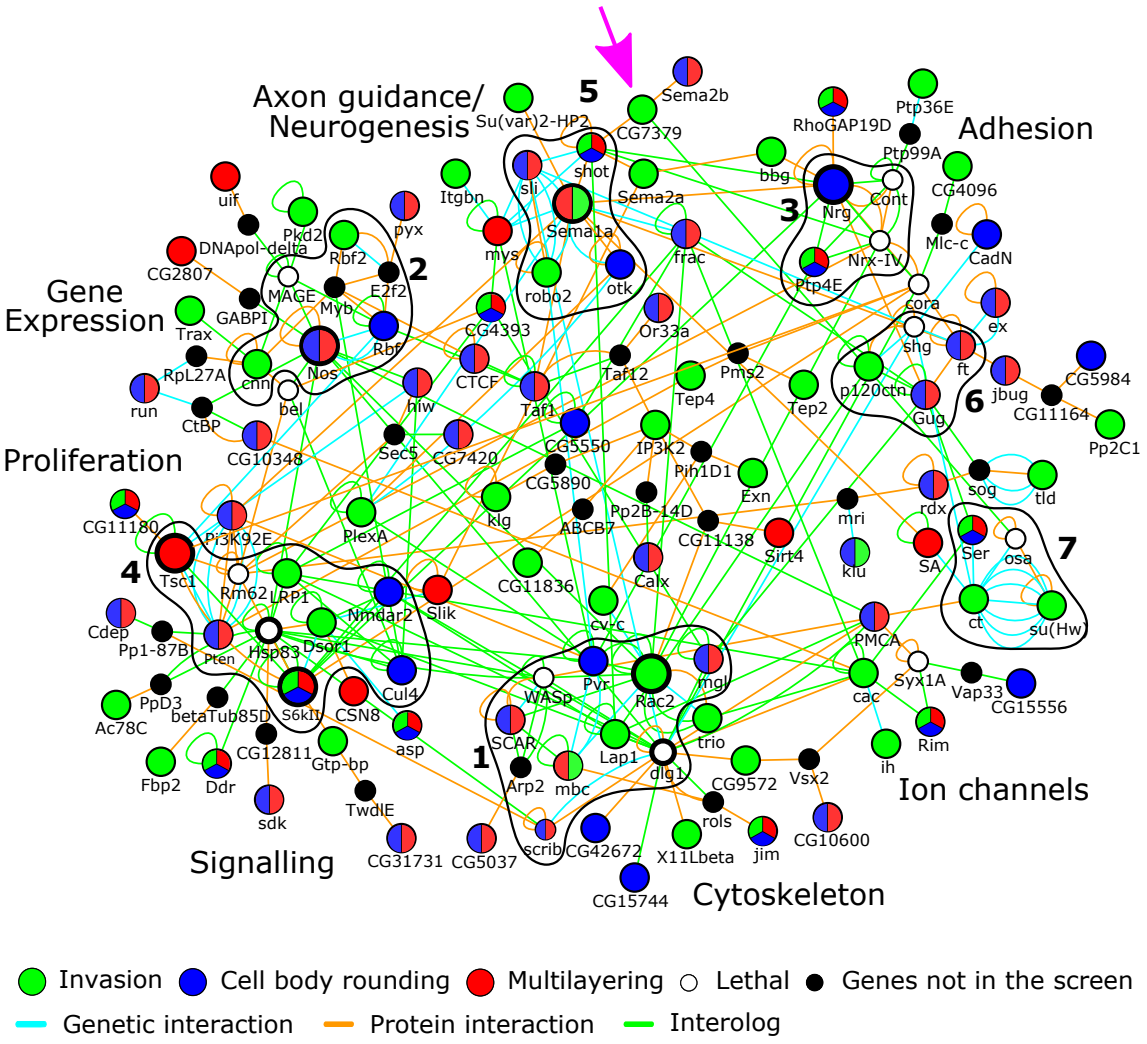


Figure 4.1 Functionally validated interaction network of invasion suppressor genes identified in the tumour progression regulators screen

Genetic (cyan), protein (orange) and interolog (green) interactions between 'hit' genes for the following categories: 'invasion' (green), 'cell body rounding' (blue) and/or 'multilayering' (red) in the large-scale genetic screen previously performed in our laboratory. Lethal genes from the screen (white) and linker genes (black) were also included. MCODE clusters of highly interconnected nodes are outlined in black. Enriched GO terms are indicated on the side. Lines represent interactions, nodes represent genes (multicoloured=hit for more than one category; bold=hub gene). Magenta arrow highlights CG7379, the gene of interest for this study. Network reproduced from (Canales Coutiño et al., 2020).

Network analysis can be a powerful tool to use to select genes of interest (Chen et al., 2009). The network developed as part of the screen consists of a complex net of interactions that brings together well-characterised invasion modulators, e.g. E-cadherin, p120-catenin (Jeanes et al., 2008; Peglion and Etienne-Manneville, 2013), and genes that were not previously associated with cancer cell invasion, highlighting potential unknown functions. An example in this sense is CG7379; predicted to be involved in chromatin remodelling (Gaudet et al., 2011), it was detected by the screen as an invasion suppressor. Furthermore, the interaction network identifies CG7379 as a potential cell adhesion regulator which interacts with p120-catenin – a component of adherens junctions (Ishiyama et al., 2010), shot – a cytoskeletal linker molecule (Grevengoed and Peifer, 2003) and semaphorin 2b – previously implicated in the regulation of cell-matrix adhesion (Meltzer et al., 2016). Additionally, CG7379 has been involved in the maintenance of epithelial integrity in the tubes that make up the fly tracheal system (Hosono et al., 2015).

4.1.2 Inhibitor of growth (ING) protein family involvement in cancer progression

DRSC Integrative Ortholog Prediction Tool (DIOPT) from Harvard Medical School (Hu et al., 2016) predicts high homology between ING1 and CG7379 and moderate homology between CG7379 and ING2-5. According to DIOPT, CG7379 and ING1 show 28% identity and 41% similarity. A very strong identity of 77% has been identified between ING1 and CG7379 within the conserved plant homeodomain (PHD) smart domain (Figure 4.2), which is responsible for binding lysine 4-tri-methylated histone H3 (H3K4me3). CG7379 and ING1 also show homology within the amino terminal histone binding domain, which is responsible for binding unmodified H3 tails (Chruscicki et al., 2010). Similar to CG7379, ING1 was identified as part of the Sin3 complex (Kuzmichev et al., 2002) and functional association between ING1 and p53 has been repeatedly reported (Russell et al., 2006),

suggesting that CG7379 and ING1 may be functionally similar in *Drosophila* and human respectively.

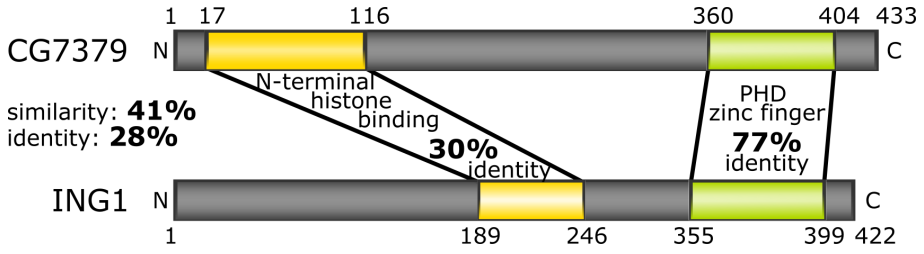


Figure 4.2 CG7379/ING1 protein alignment

Drosophila G7379 shows strong homology with the human ING1 protein (DIOPT score 11). Both histone binding domains characteristic to ING proteins (pfam12998, yellow; cd15584, green) have been evolutionary conserved.

ING1 protein is ubiquitously expressed in tissues and has a nuclear localisation within the cell. The gene spans over four exons and as a result of the use of different promoters or alternative splicing, it can be translated into five isoforms. The most abundant isoforms, and therefore the best studied, are p33ING1b and p47ING1a (Guérillon et al., 2013).

ING1's role in tumour progression has been established since 1996, when it was first linked to tumorigenesis (Garkavtsev et al., 1996). Loss of chromosomal locus, translocation to the mitochondria, mutation (rarely), but mainly decreased expression of ING1 have been documented in various mammalian cancers (Bose et al., 2014; Ythier et al., 2008).

For a very long time, ING proteins have been shown to suppress tumours by regulating cell proliferation and apoptosis (Helbing et al., 1997; Russell et al., 2006). In healthy tissue, ING1 is believed to induce apoptosis in response to DNA damage. Roles for ING1 in activating p53 through direct physical interaction and in promoting p53 stability have been reported (Russell et al., 2006; Thalappilly et al., 2011). In addition, ING1 appears to also be able to induce apoptosis in p53 independent ways (Russell et al., 2006).

Therefore, one acknowledged theory is that loss/misregulation of ING1 provides cancer cells with protection from apoptosis (Garkavtsev et al., 1998).

It is believed that ING1's ability to promote apoptosis upon DNA damage is dependent on the role of ING1 as a transcription factor. ING1 physically interacts with protein complexes with histone acetyltransferase (HAT) and histone deacetylase (HDAC) activity (Russell et al., 2006). Indeed, ING1b is a stable component of the Sin3A/HDAC1 and 2 protein complexes (Figure 4.3) and can additionally associate with subunits of the Brg1-based Swi/Snf chromatin remodelling complex (Kuzmichev et al., 2002; Peña et al., 2008), whilst an ING1a antiapoptotic role has been shown to be dependent on its interaction with Proliferating Cell Nuclear Antigen (PCNA) and p300 (Russell et al., 2006).

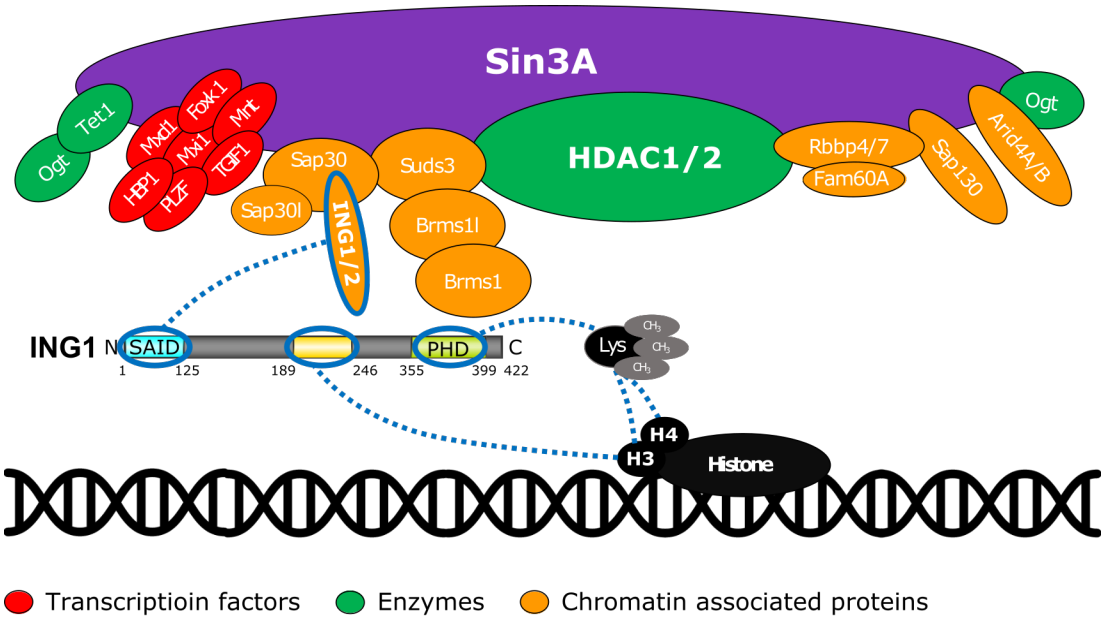


Figure 4.3 Schematic of Sin3A/HDAC complex

Sin3A/HDAC are multiproteic complexes comprising transcription factors (red), enzymes (green) and chromatin associated proteins (orange). ING1 is one of the many chromatin modulators that associates with the complex. ING1 brings the complex in proximity to the nucleosome by binding sap30 through its N-terminal domain and histone trimethylated lysine through its PHD domain. Figure adapted from (Adams et al., 2018).

More recently, studies have started linking ING protein family members with invasion. Overexpression of ING3, ING4 and ING5 proteins has been shown to inhibit migration and invasion (Li et al., 2008; Li et al., 2014; Li et al., 2013; Lu et al., 2012; Xie et al., 2008; Zhang et al., 2018), whilst downregulation can promote cell motility (Liu et al., 2017). A more recent publication suggests an oncogenic rather than tumour suppressive function for ING3, showing decreased cell invasion in DU145 prostate cancer cells upon ING3 knockdown (Almami et al., 2016). Moreover, overexpression of ING4 was linked with decreased matrix-metalloproteinase activity, proteins that play an established role in cell migration and apoptosis (Shen et al., 2007). Increased ING2 activity was also linked with tumour progression and metastasis (Almami et al., 2016; Kumamoto et al., 2009; Zhong et al., 2013).

A growing body of studies now link ING1 to many other aspects of cell physiology as well. Low levels of ING1 are associated with increased motility, migration or invasion in colorectal and gastric cancers (Ahmed et al., 2001; Guo et al., 2011), ovarian cancers (Yang, 2019) and breast cancers (Thakur et al., 2014), but not melanomas (Campos et al., 2004; Cheung and Li, 2002). ING1 overexpression was recently shown to also inhibit cell migration and invasion *in vitro* (Jiang et al., 2018).

ING1 and ING2, as part of the Sin3/HDAC and HAT complexes, are also involved in transcription regulation through alterations of chromatin structure, affecting the epigenome and cell viability (Bose et al., 2014; Garkavtsev et al., 1998; Thakur et al., 2014).

Despite thorough descriptive investigations of ING1 reported for squamous cancers, there is scarce functional and mechanistic evidence for the role of ING1 during cancer invasion and metastasis. Therefore, further investigation of both ING1 and CG7379 could provide a crucial insight into the mechanisms underlying cancer progression through invasion.

4.2 Results

4.2.1 Evaluation of apoptosis involvement in cell delamination in response to CG7379 knockdown

It was previously reported that dying cells are extruded from the epithelial tissue in a caspase dependent manner (Andrade and Rosenblatt, 2011; Levayer et al., 2016). To ensure that the observed increase in invasion was not simply a consequence of cell death evasion, apoptotic cells were stained in Moe:GFP labelled WT and CG7379 KD clones using anti cleaved *Drosophila* cDcp-1 antibody and dUTP nick end labelling (Figure 4.4). CG7379 KD significantly reduced the amount of apoptosis both in pre-invasive ($p=0.001$) and total clonal cells ($p=0.03$) by 25% and 47% respectively, suggesting a role for CG7379 KD in preventing apoptosis. On average only approximately 12% of the pre-invasive cells are apoptotic following CG7379 KD, leaving 2.5x more viable pre-invasive cells in comparison to WT clones (Table 4.1).

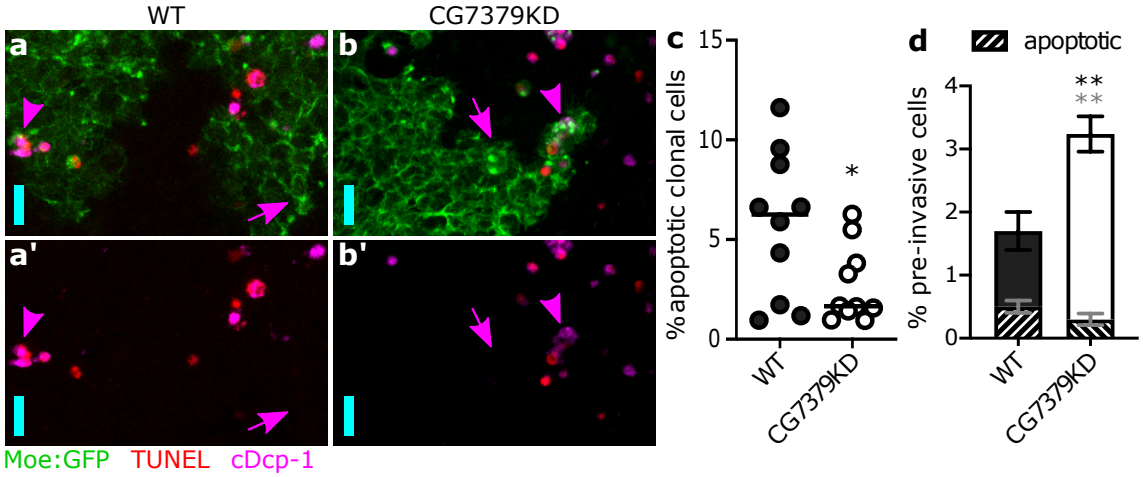


Figure 4.4 Only a subfraction of CG7379 knockdown-induced delamination is in response to caspase activation

(a,b) TUNEL (red) and cDcp-1 (magenta) Moe:GFP (green) labelled WT (a) and CG7379 KD (b) clones, highlighting both apoptotic (arrowhead) and non-apoptotic (arrow) pre-invasive cells. Pre-invasive cells are marked by the characteristic Moe:GFP accumulation towards one end of the cell. **(a',b')** TUNEL and cDcp-1 merged channels showing apoptotic cells in (a,b). **(c)** Quantification of the number of apoptotic Moe:GFP labelled cells, as determined by TUNEL and cDcp-1 staining. **(d)** Quantification of the proportion of apoptotic pre-invasive cells (stripped pattern). Significantly more pre-invasive cells (black asterisks) are observed, out of which significantly fewer were apoptotic (grey asterisks) following CG7379 KD in comparison to WT clones. Scale bar: 10µm. Error bars represent ± s.e.m. Unpaired Student's *t*-test was performed to determine statistical significance. *p<0.05; **p<0.01; n=10 animals for each genotype.

Table 4.1 Average levels of apoptosis within the clonal tissue

	WT	CG7379KD
Apoptotic clonal cells (%)	5.8±1.2	2.7±0.6
Pre-invasive cells (%)	1.7±0.4	3.3±0.3
Apoptotic pre-invasive cells (%)	33.1±4.5	11.7±3.2

It is possible that the invasive phenotype that we observe when knocking down CG7379 in the *Drosophila* notum could simply be due to the increased survival of invading cells, whereby invading cells are able to evade elimination via apoptosis. To further test this assumption, we overexpressed p35 specifically within Moe:GFP labelled *lgl-/-* mutant

clones (Figure 4.5a). Overexpression of p35 is known to prevent apoptotic death in a wide variety of tissues and is widely used in *Drosophila* cell death studies (Hay et al., 1994). If the increase in invasion observed in *lgl*-/-; CG7379 KD mutant clones (Figure 4.5c) was simply due to an inhibition of apoptosis, we would expect to see a similar increase in Moe:GFP positive cells beneath the epithelial sheet when expressing p35 in *lgl-/-* mutant clones. This however was not observed (Figure 4.5d). Although a significant increase in delaminated Moe:GFP positive cells was seen when comparing *lgl-/-* mutant clones with *lgl*-/-; *p35* clones, we did not see the dramatic increase in the number of invasive cells that we observe in *lgl*-/-; CG7379 KD clones (Table 4.2). This suggests that CG7379 must employ additional mechanisms in order to promote invasion.

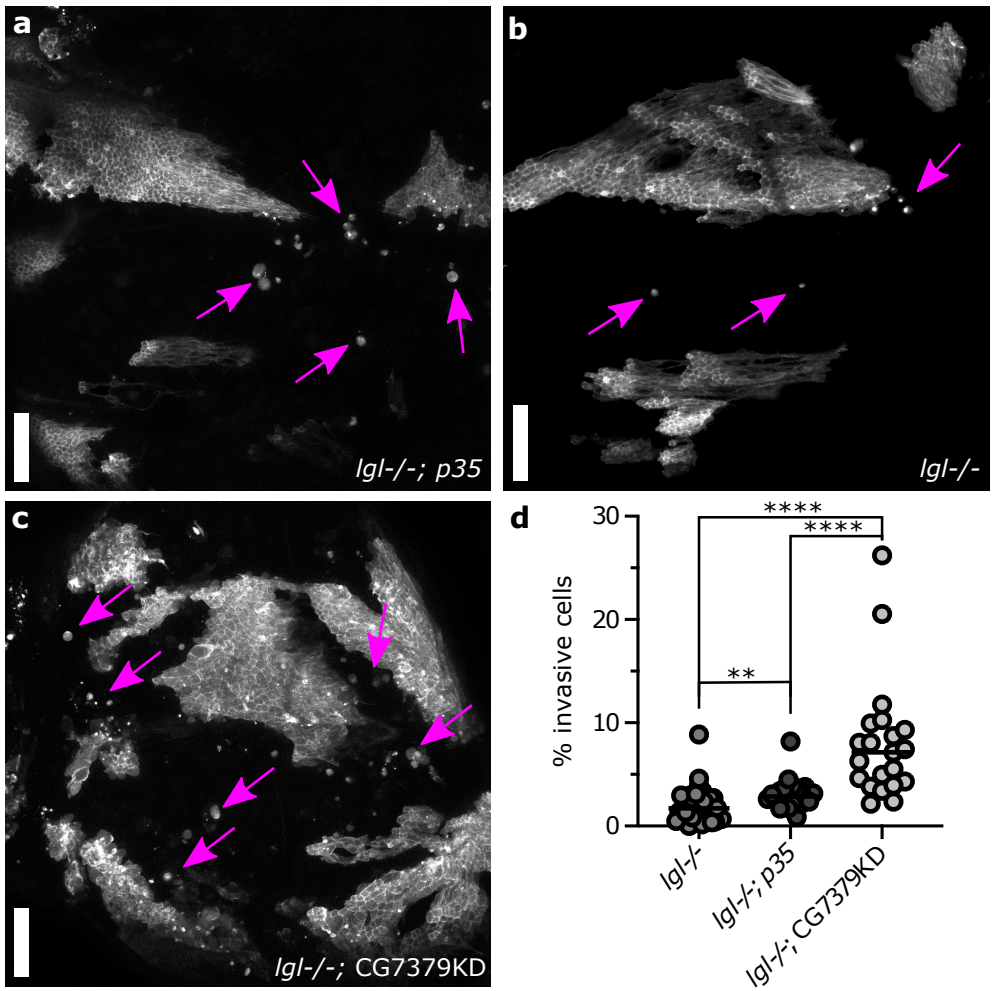


Figure 4.5 P35 overexpression in *lgl-/-* tumours does not phenocopy *lgl-/-;* CG7379 knockdown

(a-c) Representative confocal images of Moe:GFP labelled clones on the nota of the fruit fly. Images represent max projection of confocal z-stacks. Arrows point towards invasive cells. Genotype is specified on each image. **(d)** Quantification of invasion levels in (a-c). n=32, (*lgl-/-)*; n=21 *(p35)*, n=31 (*lgl-/-*; CG7379 KD). Kruskall-Wallis test was performed to determine statistical significance. **p<0.01; ****p<0.0001. Scale bar: 50µm

Table 4.2 Comparison between the average level of invasion induced by CG7379 knockdown and p35 overexpression

lgl-/-	*lgl-/-; p35*	*lgl-/-;* CG7379KD
1.9±0.3%	3.1±0.3%	7.4±1%

4.2.2 Ectopic localisation of adherens junction, septate junction and apicobasal polarity constituents in CG7379 knockdown clones

Since only a subfraction of the increase in cell delamination produced by *lgl*-/-; CG7379 KD could be attributed to cell death evasion, additional molecular mechanisms that could affect epithelial cell organisation in CG7379 KD tissue were investigated. Impaired cell-cell adhesion could account for the observed invasive phenotype following CG7379 KD. To directly test this hypothesis, positively marked mutant clones, surrounded by wild-type tissue were generated, thereby allowing us to directly compare junction composition inside and outside mutant clones in the same tissue. We visualised cell-cell adhesion in mutant clones for *lgl*-/-; CG7379 KD, CG7379 KD alone and *lgl-/-* alone using antibodies to proteins that localise to either the adherens junction (AJ) or septate junction (SJ), the functional equivalent of tight junctions (TJ) in insects.

To visualise AJ organisation we stained for E-cadherin, armadillo (β-catenin), and α-catenin. While AJ within the lgl-/- clones were mostly unaffected when compared to the surrounding WT tissue, CG7379 KD showed a severely altered distribution of all AJ proteins investigated. Protein localisation was reduced, and AJ integrity was severely disrupted as protein localisation appeared fragmented and poorly distributed along cell junctions, in both lgl-/-; CG7379 KD and CG7379 KD clones, with minor effects observed in lgl-/- clones (Figure 4.6). Similarly, some absent junctions were noticed in adjacent cells from lgl-/-; CG7379 KD and CG7379 KD clones. An exception is α-catenin whose protein levels and localisation were also affected by lgl-/-. These junctional abnormalities were very rarely observed in the neighbouring WT tissue, confirming that the phenotype was not a methodological artefact. Quantification of fluorescence intensity levels at epithelial junctions confirmed that CG7379 KD significantly reduced junction protein levels (Figure 4.6d,-i,-n, Table 4.3). Additionally, the proportion of disruptive events was also significantly increased by CG7379 KD (Figure 4.6e,-j,-o, Table 4.3).

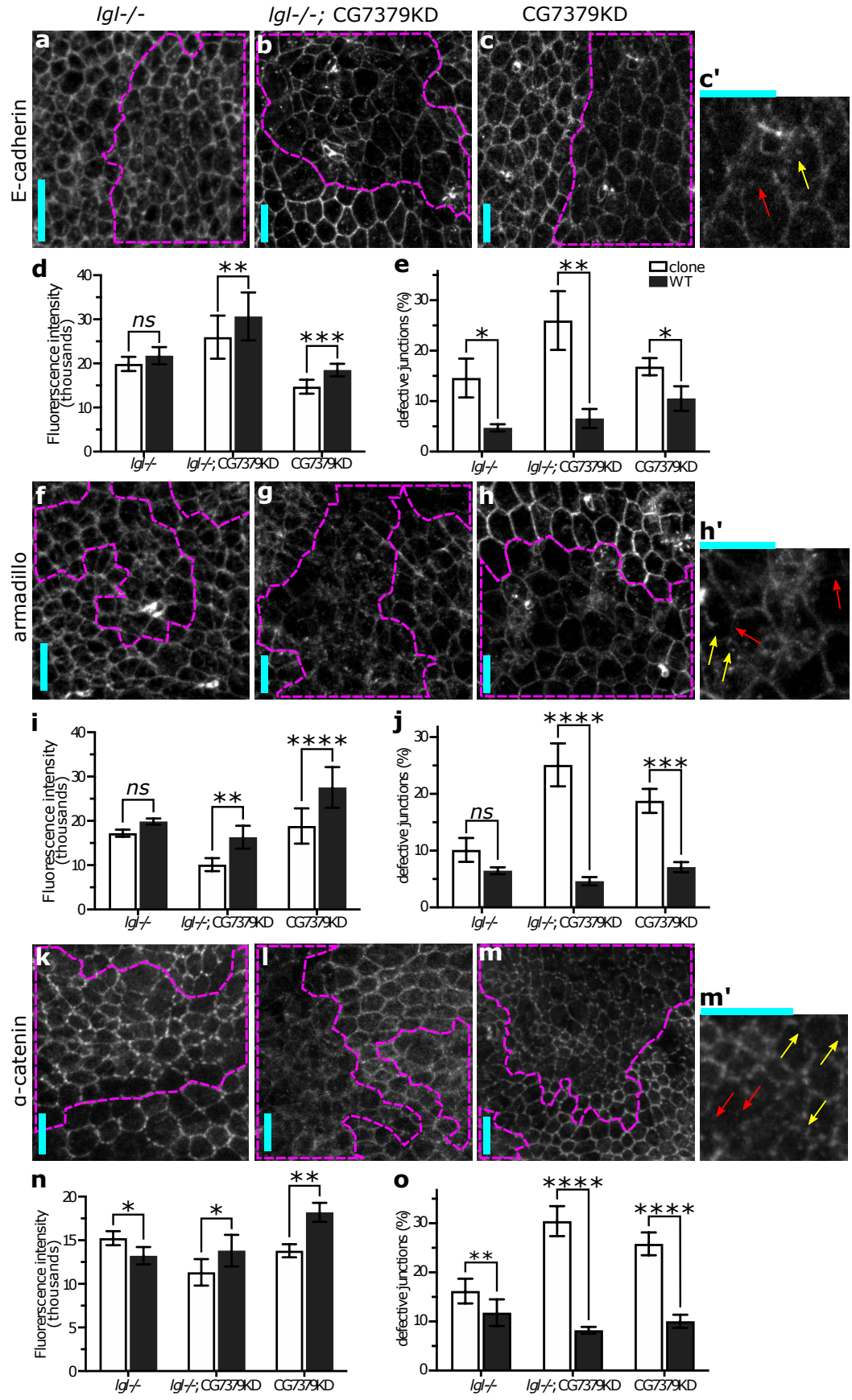

lgl-/-
lgl-/-; CG7379KD
CG7379KD
E-cadherin
a
b
c
c'
d
Fluorescence intensity (thousands)
ns
**
***
lgl-/-
lgl-/-; CG7379KD
CG7379KD
e
defective junctions (%)
clone
WT
*
**
*
armadillo
f
g
h
h'
i
Fluorescence intensity (thousands)
ns
**
****
j
defective junctions (%)
ns
****
***
α-catenin
k
l
m
m'
n
Fluorescence intensity (thousands)
*
*
**
o
defective junctions (%)
**
****
****

Figure 4.6 CG7379 knockdown disrupts adherens junction protein localisation

Drosophila nota 20-24 hr APF containing Moe:GFP labelled *lgl-/-*, *lgl-/-*; CG7379 KD and CG7379 KD clones (highlighted by dashed lines) were dissected and stained for several AJ proteins: E-cadherin **(a-c)**, armadillo (the fly ortholog of β-catenin) **(f-h)**, α-catenin **(k-m)**. A severe disruption in junction protein localisation and junction integrity was observed in *lgl-/-*; CG7379 KD and CG7379 KD clones; α-catenin localisation was also disrupted by *lgl-/-*. **(c', h', m')** Zoom in panels of CG7379 KD clones highlighting junction defects: absent junctions (red arrows) and fragmented junctions (yellow arrows). **(d, i, n)** Quantification of fluorescence intensity at AJ level reflecting protein expression levels of E-cadherin (j) armadillo (i) and α-catenin (n) in mutant vs. neighbouring WT tissue. **(e, j, o)** Quantification of abnormalities in E-cadherin (e), armadillo (j) and α-catenin (o) distribution that affects AJ architecture in mutant vs. neighbouring WT tissue. n ≥ 65 junctions per tissue from a minimum of 9 animals for each genotype. Error bars represent ± s.e.m. Paired Student's *t*-test was performed to determine statistical significance. *p<0.05; **p<0.01; ***p<0.001; ****p<0.0001. Images represent max intensity Z projection of relevant confocal z-slices. Scale bars: 10 μm.

Table 4.3 Mean fluorescence intensity representative of protein expression at adherens junctions and mean proportion of disrupted junctions

	lgl-/-		*lgl-/-;* CG7379 KD		WT; CG7379 KD	
	clone	WT	clone	WT	clone	WT
Fluorescence intensity (arbitrary fluorescence units)						
E-cadherin	19892.1± 1608.7	21748.3± 1946.1	25958.5± 4875.8	30654± 5426.9	14731± 1582.9	18508.5± 1405.4
armadillo	17219.1± 793.3	19849.4± 693.3	10116± 1459.7	16307.3± 2578.2	18842.7± 3987.3	27542.4± 4591.4
α-catenin	15232.8± 807.9	13221.5± 997.5	11325± 1515.6	13810.4± 1812.9	13793± 749.3	18202.8± 1090.2
Defective junctions (%)						
E-cadherin	14.6±3.8	4.7±0.7	26.0±5.8	6.6±1.9	16.8±1.7	10.5±2.4
armadillo	10.1±2.1	6.4±0.6	25.1±3.8	4.6+±0.7	18.8±2.1	7.0±0.9
α-catenin	16.2±2.5	11.8±2.7	30.4±3.1	8.2±0.6	25.8±2.3	10.0±1.3

To visualise SJ organisation, we stained for Fasciclin III, coracle and discs large (SJ proteins). In the majority of cases, SJ protein localisation was significantly reduced and the integrity of the junctions was severely disrupted in both *lgl-/-*; CG7379 KD and CG7379 KD clones, with minor effects observed in *lgl-/-* clones (Figure 4.7). The only exception was dlg, where the most severe effects were noticed in *lgl-/-* clones (Figure 4.7a). Quantification of fluorescence intensity levels and disruptive events confirmed statistical significance of the observed phenotypes (Figure 4.7d-e, i-j, n-o, Table 4.4).

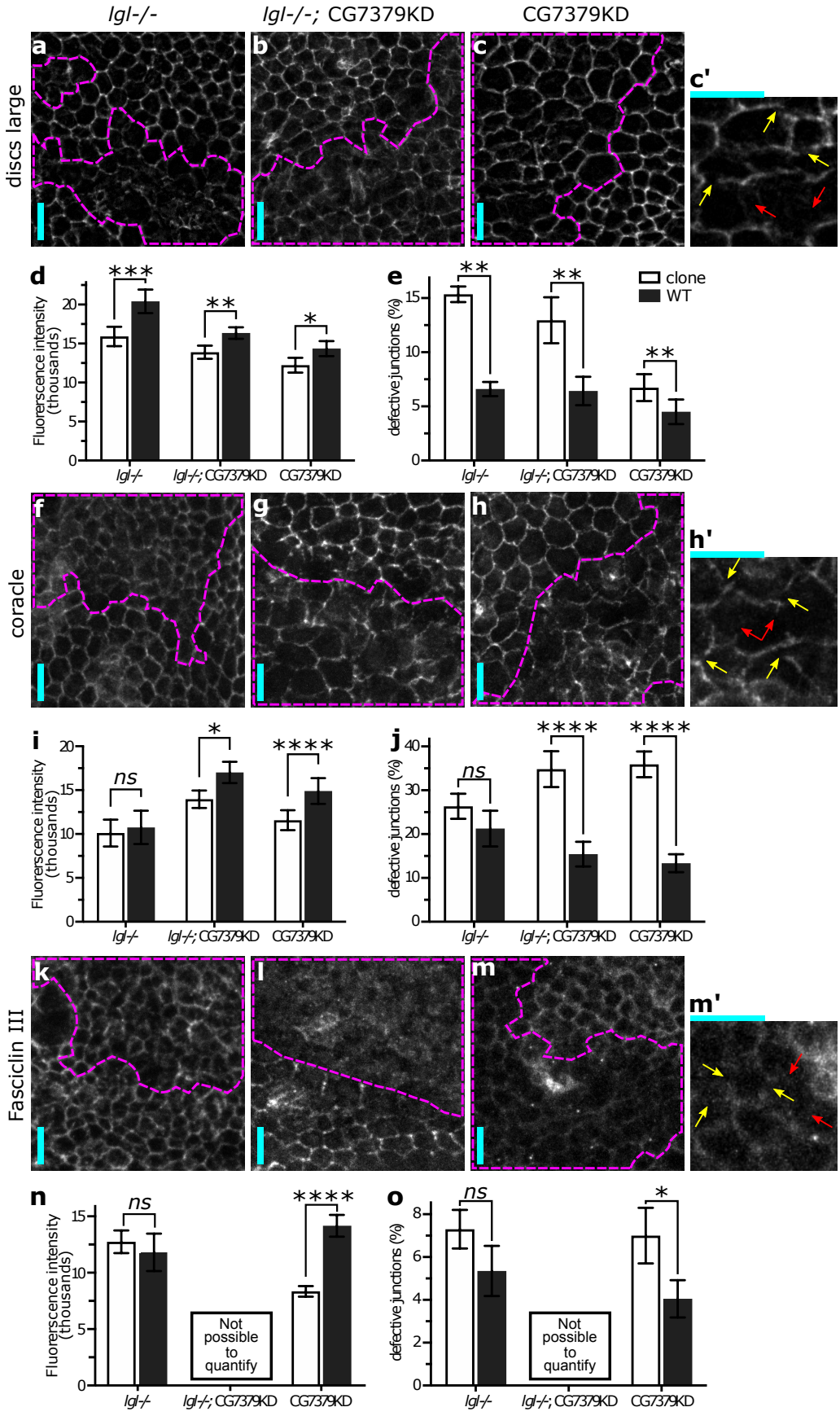

lgl-/-
lgl-/-; CG7379KD
CG7379KD
discs large
a
b
c
c'
d
Fluorerscence intensity (thousands)
***
**
*
lgl-/-
lgl-/-; CG7379KD
CG7379KD
e
defective junctions (%)
clone
WT
**
**
**
lgl-/-
lgl-/-; CG7379KD
CG7379KD
coracle
f
g
h
h'
i
Fluorerscence intensity (thousands)
ns
*
****
lgl-/-
lgl-/-; CG7379KD
CG7379KD
j
defective junctions (%)
ns
****
****
lgl-/-
lgl-/-; CG7379KD
CG7379KD
Fasciclin III
k
l
m
m'
n
Fluorerscence intensity (thousands)
ns
****
Not possible to quantify
lgl-/-
lgl-/-; CG7379KD
CG7379KD
o
defective junctions (%)
ns
*
Not possible to quantify
lgl-/-
lgl-/-; CG7379KD
CG7379KD

Figure 4.7 CG7379 knockdown disrupts septate junction protein localisation

Drosophila nota 20-24 hr APF containing Moe:GFP labelled *lgl-/-*, *lgl-/-*; CG7379 KD and CG7379 KD clones (highlighted by dashed lines) were dissected and stained for several SJ proteins: discs large **(a-c)**, coracle **(f-h)**, Fasciclin III **(k-m)**. A severe disruption in junction protein localisation and junction integrity was observed in *lgl-/-*; CG7379 KD and CG7379 KD clones; discs large disruption was most severe in *lgl-/-* mutant clones. **(c', h', m')** Zoom in panels of CG7379 KD clones highlighting junction defects: absent junctions (red arrows) and fragmented junctions (yellow arrows). **(d, i, n)** Quantification of fluorescence intensity at SJ level reflecting protein expression levels of discs large (j) coracle (i) and Fasciclin III (n) in mutant vs. neighbouring WT tissue. **(e, j, o)** Quantification of abnormalities in discs large (e), coracle (j) and Fasciclin III (o) distribution that affects SJ architecture in mutant vs. neighbouring WT tissue. n≥ 65 junctions per tissue from a minimum of 9 (discs large); 7 (coracle); 9 (Fasciclin III) animals for each genotype. Error bars represent ± s.e.m. Student's *t*-test was performed to determine statistical significance. *p<0.05; **p<0.01; ***p<0.001; ****p<0.0001. Images represent max intensity Z projection of relevant confocal z-slices. Scale bars: 10 µm.

Table 4.4 Mean fluorescence intensity representative of protein expression at septate junctions and mean proportion of junctions with a disrupted architecture

	lgl-/-		*lgl-/-;* CG7379 KD		WT; CG7379 KD	
	clone	wt	clone	wt	clone	wt
Fluorescence intensity (arbitrary fluorescence units)						
discs large	15911.6± 1238.4	20407.1± 1505.6	13891.9± 843.8	16349.2± 741	12224.4± 943.9	14353.5± 964.4
coracle	10105.9± 1527.9	10753.9± 1898.2	13961.6± 997.8	17016.2± 1213.7	11570.8± 1140.0	14895.8± 1466.7
Fasciclin III	1273± 1003.4	11806.1± 1659.2			8345.9± 465.5	14162.7± 963.6
Defective junctions (%)						
discs large	15.3±0.7	6.6± 0.6	12.9±2.1	6.4±1.3	6.7±1.2	4.5±1.1
coracle	16.3±2.8	21.3± 4.0	34.8±4.1	15.4±2.8	35.9±2.9	13.5±2.0
Fasciclin III	19.8±2.7	12.0± 2.3	-	-	17.0±2.7	11.8±1.7

Since disruption of apicobasal polarity frequently promotes invasion (Khursheed and Bashyam, 2014), we posited that apicobasal polarity could be affected as a result of CG7379 KD. We looked at whether the apicobasal polarity determinants, aPKC, bazooka (Par3) or crumbs, were affected in these mutant clones (Figure 4.8). We however only found a significant effect on aPKC localisation, which is likely due to a loss of *lgl-/-* function, as no significant changes in protein expression level and protein distribution alongside the cell-cell interface was noticed in CG7379 KD clones (Figure 4.8a-d, Table 4.5). The additional effects on cell polarity in *lgl-/-* mutant clones (e.g. the mislocalisation of both dlg and aPKC) likely explain the increased multilayering and invasion observed in *lgl-/-*; CG7379 KD clones, when compared with CG7379 KD alone.

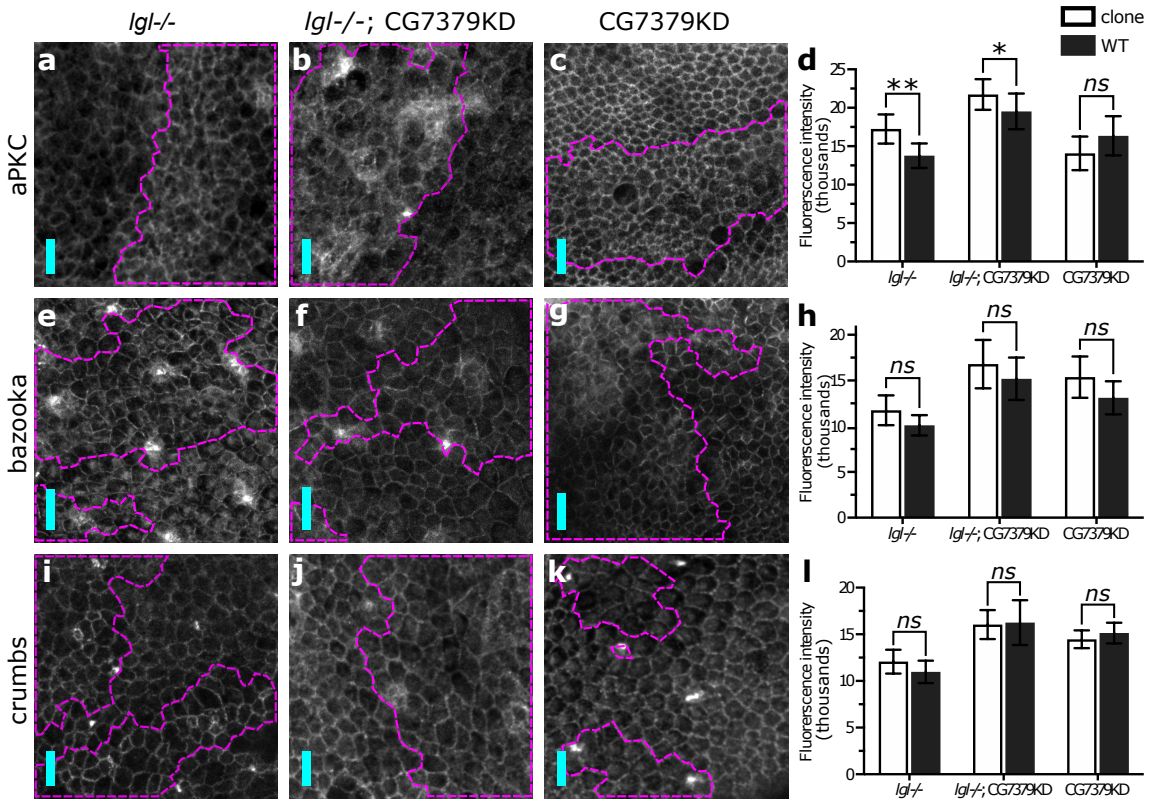


Figure 4.8 Apicobasal polarity determinants localisation is not affected by CG7379 knockdown

Drosophila nota dissected 20-24 hr APF containing *lgl-/-*, *lgl-/-*; CG7379 KD and CG7379 KD Moe:GFP labelled clones (highlighted by dashed lines) were dissected and stained for several apicobasal polarity determinants: aPKC **(a-c)** bazooka (the fly ortholog of Par3) **(e-g)** crumbs **(i-k)**. Tissue surrounding the clones is wild-type and was used as a positive control. A severe disruption in aPKC localisation was observed in *lgl-/-* and *lgl-/-*; CG7379 KD but not CG7379 KD clones, as quantified in panel **(d)**. No effect was observed when staining for the apical polarity proteins bazooka and crumbs. Quantification in **(h,l)** n≥ 65 junctions per tissue from a minimum of 6 (bazooka); 9 (aPKC); 9 (Crumbs) animals for each genotype. Error bars represent ±s.e.m. Paired Student's *t*-test was performed to determine statistical significance. *p<0.05; **p<0.01. Images represent max intensity Z projection of relevant confocal z-slices. Scale bar: 10 µm.

Table 4.5 Mean fluorescence intensity representative of aPKC levels at cell cortex

	lgl-/-		*lgl-/-;* CG7379 KD		WT; CG7379 KD	
	clone	wt	clone	wt	clone	wt
aPKC	17243.2± 1899.2	13769.3± 1595.8	21726± 1986.4	19526.7± 2322.6	14074.4± 2185.8	16349.3± 2548.7

As E-cadherin is at the core of cell-cell junction adhesion and its levels were downregulated by CG7379 KD, we hypothesised that if E-cadherin levels would be restored, the cell-cell junction defects might be rescued and consequently cells would not delaminate at the same rate. Therefore, we further tried to rescue the invasive phenotype relative to CG7379 KD alone by overexpressing E-cadherin under the Ubi-p63E promoter in mosaic flies for CG7379 KD (*shg*$_{ubq}$; CG7379 KD). The construct we used has been shown to substitute for a null *shg* allele and to function and behave normally in the absence of intact E-cadherin (Oda and Tsukita, 2001). E-cadherin overexpression did not have any significant impact on the level of cell delamination from CG7379 KD tissue (Figure 4.9).

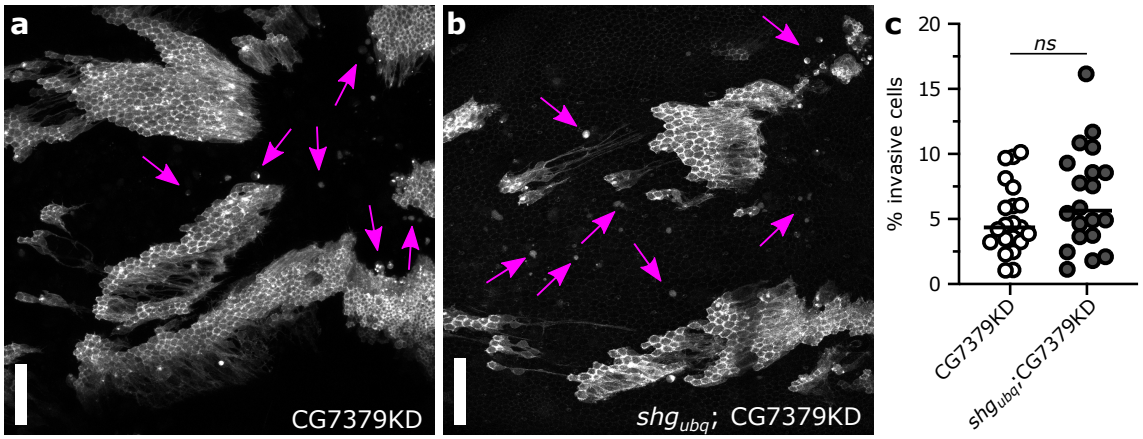


Figure 4.9 E-cadherin overexpression alone cannot rescue CG7379 knockdown induced cell delamination

(a-b) Representative confocal images of Moe:GFP labelled clones on the nota of the fruit fly. Images represent max projection of confocal z-stack. Arrows point towards invasive cells. Genotype is specified on each image. **(c)** Quantification of invasion levels in (a-b). Mann-Whitney U test was performed to determine statistical significance, n≥ 20. Scale bar: 50µm

4.2.3 ING1 knockdown promotes invasion in a human adenocarcinoma *in vitro* model employing similar mechanisms of action as CG7379

We then wanted to test whether the human orthologue, ING1, would also act in a similar way. Previous experiments performed in the lab highlighted the ability of ING1 KD to increase invasion *in vitro* in different types of cancer: breast adenocarcinoma (MDA-MB-231 cells) and glioblastoma (U87 cells) (Cornhill, 2017). We wanted to further test whether ING1 KD would phenocopy CG7379 KD phenotype in terms of cell-cell adhesion impairment. For this purpose the MCF-7 breast adenocarcinoma cell line was chosen as an experimental model because it retains expression of epithelial markers such as E-cadherin (Kohn et al., 2014). According to Expression Atlas (Petryszak et al., 2015), MCF-7 cells already express low levels of ING1. Therefore, we first tested weather ING1 KD would be sufficient to promote invasion in this model. A mixed pool of siRNA was used to transiently KD ING1 expression as assessed by qPCR (Figure 4.10c,f). ING1 KD significantly increased migration and invasion in MCF-7 cells in a transwell migration assay (Table 4.6, Figure 4.10a, b). Assessment of E-cadherin localisation within transiently transfected cells revealed a 2.6-fold increase in junction breaks compared to cells transfected with non-targeting siRNA (Table 4.6, Figure 4.10d, e). The protein expression level was not assessed.

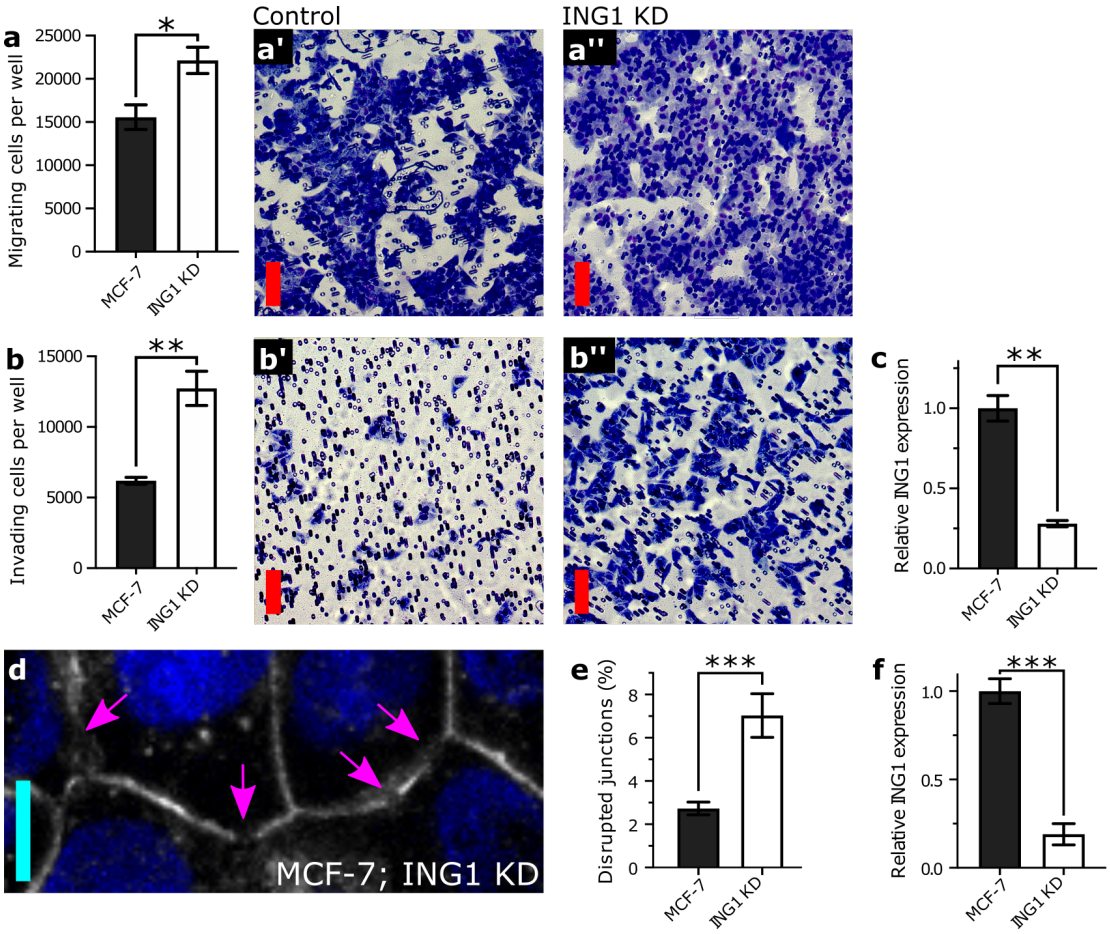


Figure 4.10 ING1 knockdown promotes invasion in a breast adenocarcinoma cell line by disrupting E-cadherin localisation at cell-cell junctions

(a) Transwell migration assay for MCF-7 cells showing a significant increase in the number of cells that migrated through an 8 µm pore membrane following ING1 KD in comparison to MCF-7 cells treated with non-targeting siRNA pool. **(b)** Transwell invasion assay. For the invasion assay the membrane was coated with 100 µg Matrigel. n=4. Representative images of the bottom of the hanging insert membrane are shown for migration **(a'-a'')** and invasion **(b'-b'')**. **(c)** Relative ING1 mRNA levels, determined by qRT-PCR 48h post transient siRNA transfection prior to invasion assays. **(d)** E-cadherin stain in MCF-7 cells transfected with siRNA against ING1. Image represents max Z projection of relevant confocal z-slices. **(e)** Quantification of (d). n=6060 ING1 KD; 8231 control junctions from a total of 3 biological repeats. **(f)** Relative ING1 mRNA levels, determined by qPCR 48h post transient siRNA transfection prior to E-cadherin stain. Error bars represent ±s.e.m. *p<0.05; **p<0.01, ***p<0.001.

Table 4.6 Average number of migratory/ invasive MCF-7 cells and average proportion of disrupted junctions

	MCF-7	ING1 KD
Migratory cells	15562±1423 cells	22144±1523 cells
Invasive cells	6189±241 cells	12728±1213 cells
Disrupted junctions	2.7±0.2%	7±0.6%

4.2.4 ING1 knockdown severely affects the transcriptome of MCF-7 cells

The ability of ING1 to affect gene expression regulation has been documented (Russell et al., 2006). Therefore, we hypothesised that ING1 might regulate the expression of cell-cell junction components or the expression of genes that regulate cell junction or cytoskeletal behaviour. To test this hypothesis, the downstream effect that ING1 KD has on gene expression was assessed through genome wide microarray transcriptomic analysis. Total RNA was extracted from untreated MCF-7 cells, cells treated with either non-targeting siRNA or ING1 siRNA and sent to the Nottingham Arabidopsis Stock Centre (NASC) for processing (n=3 samples/experimental condition).

The validity and variability of the results were first assessed. Principal component analysis (PCA) is a statistical procedure that assesses the correlation between variables by converting a set of numerical observations into an uncorrelated orthogonal set of linear values. Following PCA analysis, samples from the same experimental condition clustered together in all three cases (Figure 4.11a). Furthermore, ING1 KD samples (green) are clearly separated from both control groups (untreated, blue; non-targeting siRNA, red) – which cluster close to each other, despite an apparent increase in internal variability within the ING1 KD group in comparison to controls. Further on, the variability within the same group was assessed and compared between the experimental conditions by calculating the mean signal to noise ratio of all computed variables (Figure 4.11b). The variability between different experimental groups (knockdown status) is

larger than the variability between samples from the same group (error). Taken together, this suggests that we can confidently assume that changes in gene expression observed between the groups are due to ING1 KD.

In order to determine which genes were differentially expressed following ING1 silencing, one-way ANOVA analysis of expression fold-change (cut off: <-1,5; >1,5) against p-value ($p<0.01$, FDR< 0.05) was performed. When comparing ING1 KD to cells treated with non-targeting siRNA, we found 919 genes to be differentially expressed (Appendix 2), 71% of which were downregulated as a consequence of the knockdown. As a control, comparisons of un-transfected cells relative to cells treated with non-targeting siRNA and of ING1 KD relative to un-transfected cells were also performed. As expected, gene expression was not significantly changed after treatment with non-targeting siRNA (Figure 4.11c), and the pattern of DEG was highly similar when comparing ING1 KD to any of the control groups (Figure 4.11d vs. e), further highlighting the robustness of the experiment. A panel consisting of three DEG (RHOC, DIAPH1, ECT2) and the knockdown gene (ING1), was chosen to further validate their expression levels by quantitative reverse-transcriptase PCR. This panel of genes was chosen so that it would i) confirm the KD, ii) confirm both upregulation and downregulation of DEG and iii) confirm the more subtle changes in gene expression (genes that showed a fold-change lower than 2 or higher than -2 were included alongside genes showing a greater fold-change). Results confirmed a significant increase in RHOC levels and significant decrease in DIAPH1 and ECT2 levels, in addition to significant decrease in ING1 levels that further confirmed successful knockdown (Figure 4.11f, g). Moreover, results obtained through the two analysis show high correlation (Pearson's correlation test: $r=0.89$, $p=0.05$).

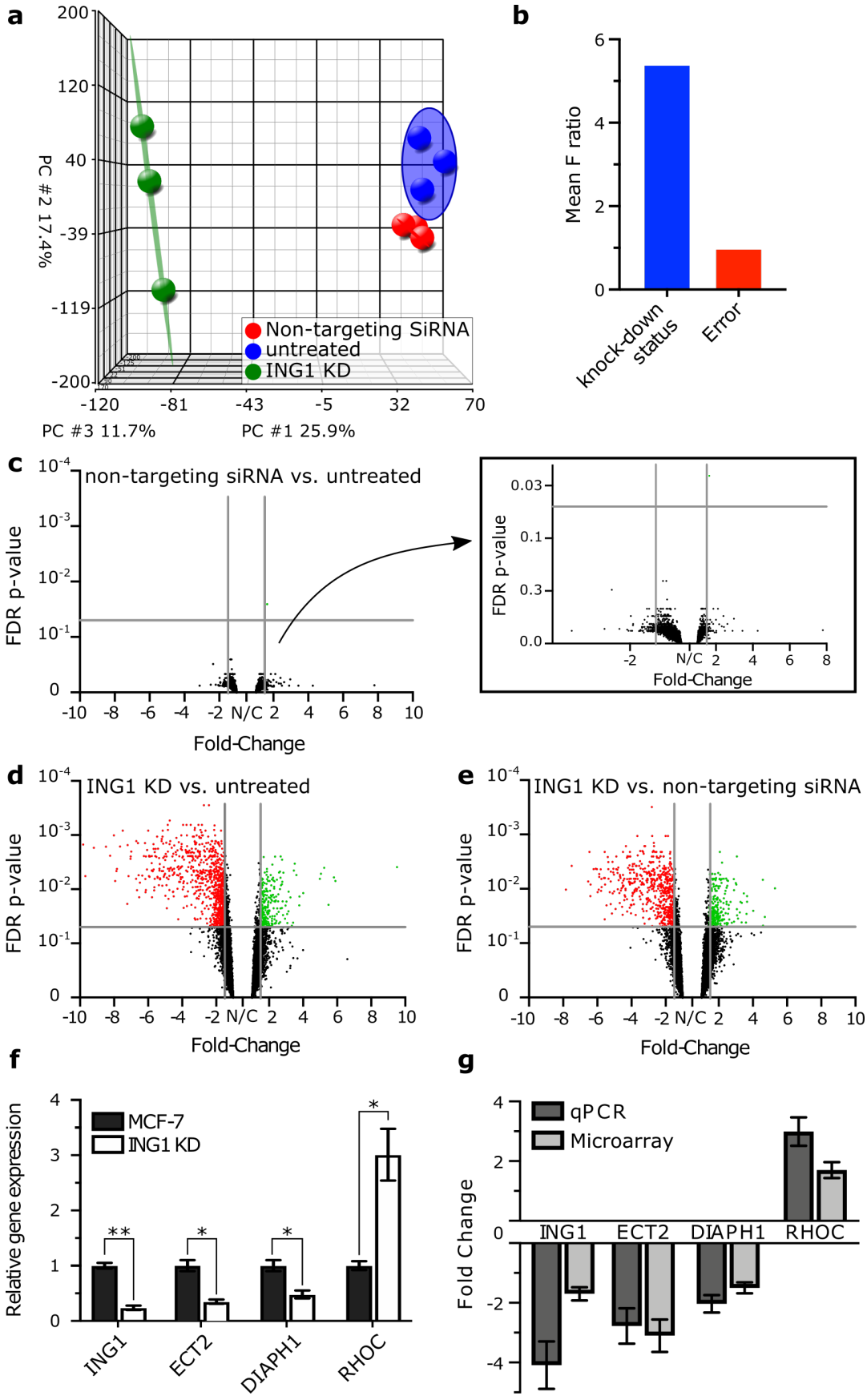

a
200
120
40
-39
-119
-200
PC # 2 17.4%
Non-targeting SiRNA
untreated
ING1 KD
-120
-81
-43
-5
32
70
PC #3 11.7%
PC #1 25.9%
b
Mean F ratio
6
4
2
0
knock-down status
Error
c
non-targeting siRNA vs. untreated
FDR p-value
Fold-Change
0.03
0.1
0.3
0.0
d
ING1 KD vs. untreated
e
ING1 KD vs. non-targeting siRNA
f
Relative gene expression
MCF-7
ING1 KD
ING1
ECT2
DIAPH1
RHOC
g
qPCR
Microarray
Fold Change
ING1
ECT2
DIAPH1
RHOC

Figure 4.11 Identification of differences in gene expression induced by ING1 knockdown in microarray analysis of MCF-7 transcriptome

(a) PCA analysis of genome-wide mRNA expression shows that samples clearly cluster together based on the experimental conditions used: transfection with ING1 siRNA (green), non-targeting siRNA (red) or no treatment (blue). Each dot represents one sample. **(b)** Assessment of the source of variation in the microarray analysis. **(c-e)** DEG between controls: cells treated with non-targeting siRNA vs. untreated cells (c) and treatment vs. controls: ING1 KD vs. untreated cells (d) and ING1 KD vs. cells treated with non-targeting siRNA (e). One-way ANOVA analysis was performed to determine statistical significance. Grey lines represent cut-off points: FC $\in$ [-1.5; 1.5], FDR corrected p value<0.05; black dots: genes that did not show a statistically significant change in their expression level; green dots: upregulated genes; red dots: downregulated genes. **(f)** Relative gene expression of ING1, RHOC, DIAPH1 and ECT2 in MCF-7 cells treated with ING1 siRNA as shown by qPCR. **(g)** Comparison between qPCR and microarray results for a panel of four genes. All genes show the same trend of expression. No significant differences were registered between qPCR and microarray results for either of the genes. Error bars represent ±s.e.m. Student's *t*-test was performed to determine statistical significance. *p<0.05, **p<0.01.

The biological meaning of ING1 KD differentially expressed genes was then explored. GO enrichment analysis using the online tool DAVID Bioinformatics Resources 6.8 (Huang et al., 2007) revealed 59 significantly enriched biological processes significantly affecting 13 pathways (Appendix 3). The most affected biological processes and pathways were cell cycle, cell division and DNA replication. DAVID tool was also used to identify associated diseases (database used: GAD). Out of the 12 diseases identified, 11 were cancer related, with breast cancer showing the strongest association (Appendix 3).

The mRNA levels of neither the AJ or SJ components, apart from p120, were affected following ING1 KD in MCF-7 cells. Due to the high number of DEG, a more targeted approach was employed to identify misregulated genes that might impact cell-cell junction stability. Given that cell junctions were affected in a similar way in both flies and human cells, we concluded that the mechanism responsible should have been evolutionarily conserved. The 'interactions' tool from flybase (Attrill et al., 2015) was used to generate a list of genetic and protein interactors of the cell-cell junction components that were affected by CG7379 KD. DIOPT (Hu et al., 2016) was then used to generate a list of human orthologues showing moderate or high homology to any of the

interactors identified in the previous step (Appendix 4). This list was then compared against the list of DEG identified through genome-wide mRNA expression analysis following ING1 KD. This led to the identification of 9 upregulated and 18 downregulated genes that are likely to regulate cell-cell junction stability.

Unsupervised hierarchical clustering based on the gene expression level of the 27 genes identified as potential cell junction modulators was performed (Figure 4.12). Expression data from untreated and non-targeting siRNA treated cells clustered together and no outliers were identified, further increasing the confidence in our results.

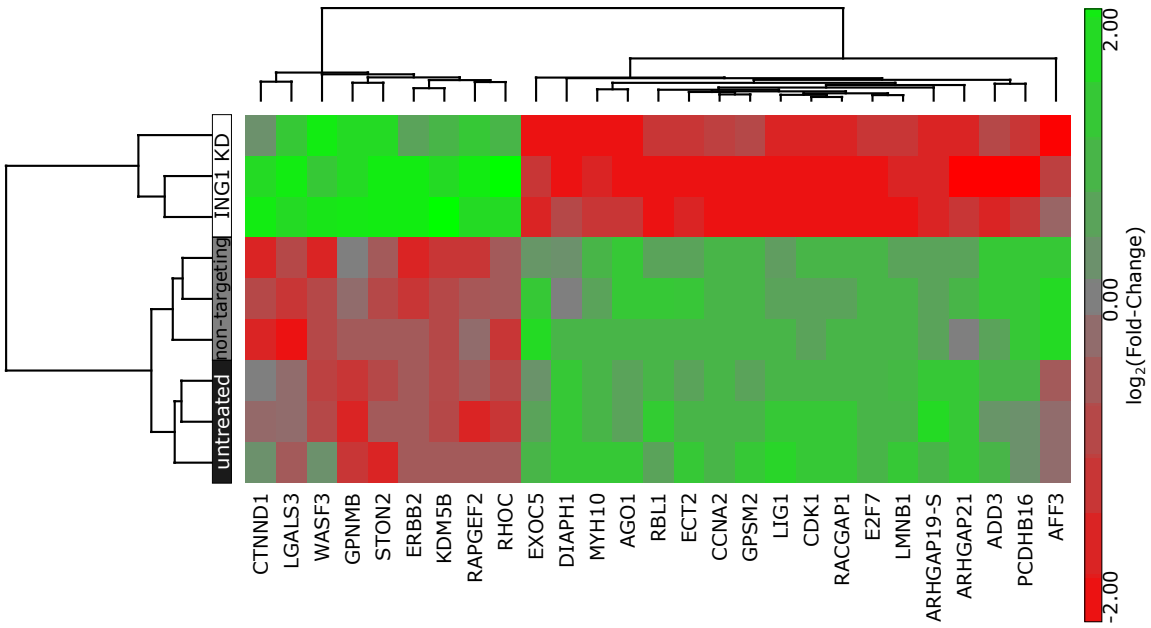


Figure 4.12 Hierarchical clustering of a selection of differentially expressed genes putatively associated with cell-cell junction stability

Heat map showing how gene expression of 27 candidate genes that might regulate cell-cell junction stability changes in response to ING1 KD in MCF-7 cells. Columns represent genes and rows represent samples. Treatment groups are specified on the figure.

GO enrichment of this subset of DEG, performed using the online DAVID analysis tool (Huang et al., 2007), revealed four significantly altered biological processes, including regulation of cell shape and cytoskeleton organisation, and three affected pathways, including AJ (Figure 4.13, Table 4.7).

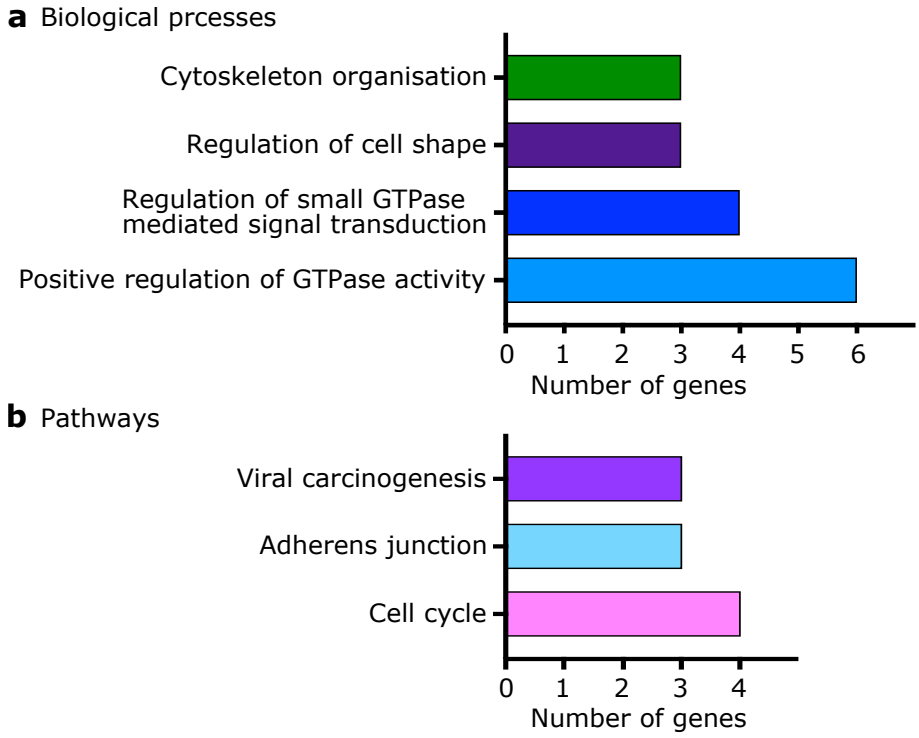


Figure 4.13 Gene ontology enrichment analysis of a selection of differentially expressed genes putatively associated with cell-cell junction stability

GO enrichment of biological processes (a) and pathways (b) of a subset of 27 DEG in response to ING1 KD in MCF-7 cells was investigated using DAVID functional annotation tool. The following databases were used: GOTERM BP DIRECT (for biological processes) and KEGG (for pathways). A list of genes clustered in each GO term can be found in Table 4.7.

Table 4.7 Significantly enriched biological processes and pathways by a panel of selected 27 differentially expressed genes following ING1 knockdown

ID	Term	p-value*	Genes
Biological Processes			
GO:0051056	Regulation of small GTPase mediated signal transduction	0.0010	ARHGAP19, RHOC, ECT2, RACGAP1.
GO:0043547	Positive regulation of GTPase activity	0.0013	ARHGAP21, ARHGAP19, ECT2, RACGAP1, RAPGEF2, ERBB2.
GO:0008360	Regulation of cell shape	0.0183	WASF3, DIAPH1, MYH10.
GO:0007010	Cytoskeleton organization	0.0237	WASF3, DIAPH1, ADD3.
Pathways			
hsa04110	Cell cycle	6.25E-04	CDK1, E2F2, RBL1, CCNA2.
hsa04520	Adherens junction	0.0045	WASF3, ERBB2, CTNND1.
hsa05203	Viral carcinogenesis	0.0339	CDK1, RBL1, CCNA2.

*DAVID functional annotation performed on the 06th of June 2020

Additionally, the Cytoscape plugin GeneManya (Warde-Farley et al., 2010) was used to assess interactions between the selected subset of DEG and AJ components. A list of the 27 DEG and genes encoding AJ components was used as input. GO molecular function-based network weighting was used. A maximum of 20 linker genes were added to the network in order to generate experimentally validated genetic and physical interactions between the input genes. Gene expression of the newly introduced genes following ING1 KD was assessed. An extra seven (out of 20) genes were found to be missregulated by ING1 KD in the transcriptomics experiment. Further on, the list of remaining linker genes was manually curated so that only linker genes that connect AJ components to DEG would be included in the final network. The generated network (Figure 4.14) reveals a total of 141 genetic interactions and 116 physical interactions. A detailed list of the genes and interactions can be found in Appendix 5.

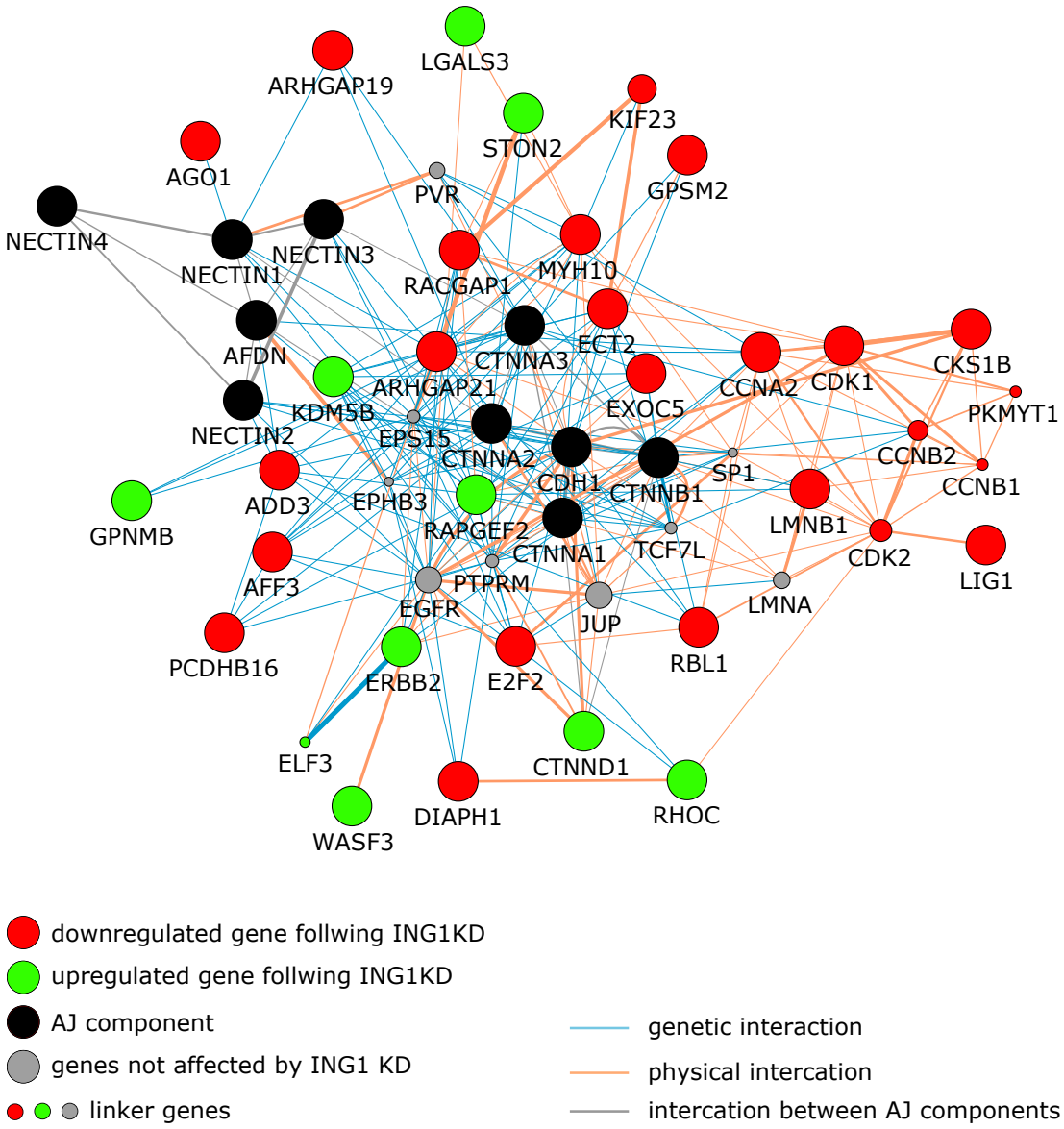


Figure 4.14 Interaction network of a subset of differentially expressed genes following ING1 knockdown and adherens junction components

Genetic (blue) and physical (orange) interactions between a panel of upregulated (green) and downregulated (red) genes in response to ING1 KD and genes encoding proteins localised at AJ (black). Some of the interactions are indirect and require linker genes (smaller nodes), node size and edge thickness are indicative of the score, node colour is indicative of expression levels following ING1 KD: green, upregulated; red, downregulated; grey, not affected).

4.2.5 Assessment of Rho1 impact on CG7379 knockdown induced cell delamination

Data from the microarray analysis of the MCF-7 transcriptome revealed a role for ING1 in the regulation of RhoC mRNA levels, as RhoC was significantly upregulated in response to ING1 depletion (Figure 4.12). Additionally, RhoC has been previously shown to play a role in cell junction regulation (Sahai and Marshall, 2002). The closest fly orthologue for RhoC is Rho1 and therefore we tried to rescue the increased cell delamination from CG7379 KD clones by reducing the level of Rho1. Moe:GFP labelled clones expressing RNAi against CG7379 and a dominant negative form of Rho1 were generate on the back of the fruit fly (*Rho1*^{N19}; CG7379 KD). Dominant negative mutations act antagonistically to WT alleles rendering the protein inactive. No significant changes in the proportion of Moe:GFP cells extruding from the clonal tissue was recorded (Figure 4.15).

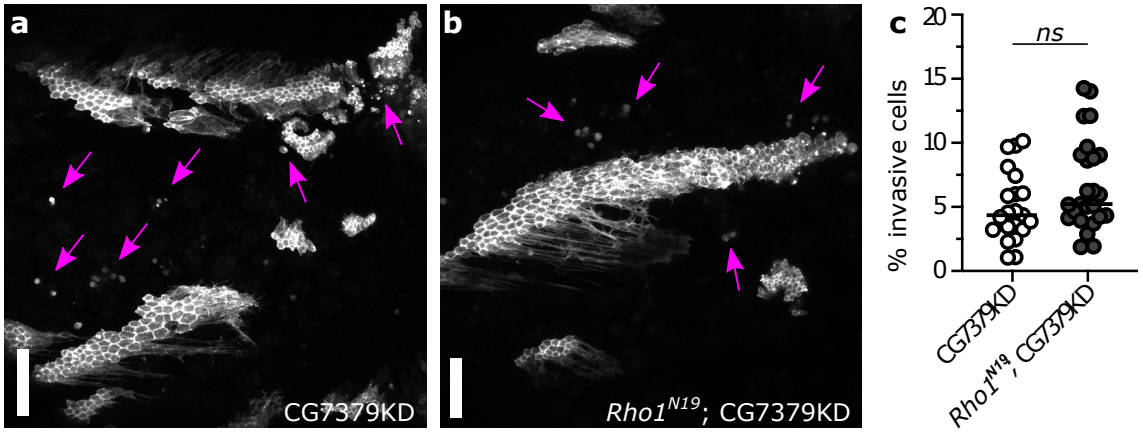


Figure 4.15 Expression of dominant negative Rho1 cannot rescue CG7379 knockdown induced cell delamination

(a-b) Representative confocal images of Moe:GFP labelled clones on the nota of the fruit fly. Images represent max Z projection of confocal z-stack. Arrows point towards invasive cells. Genotype is specified on each image. **(c)** Quantification of invasion levels in (a-b). Mann-Whitney U test was performed to determine statistical significance, n≥21 animals/genotype. Scale bar: 50µm.

4.3 Discussion

4.3.1 CG7379 regulates cell invasion by modulating apoptosis and cell-cell adhesion

It is widely accepted that apoptotic cells extrude from the epithelia in order to preserve its barrier function (Andrade and Rosenblatt, 2011). Levayer, Dupont and Moreno showed that caspase activation is required in *Drosophila* nota for this process (both inside and outside the midline) and that it always precedes cell delamination (Levayer et al., 2016). Thus, before proceeding to identify the mechanism through which CG7379 KD promotes invasion, we tested whether the observed delaminating cells were invasive or whether they were apoptotic cells extruded from the tissue. *Drosophila* nota 20-24 hr APF were dissected, fixed and stained for cleaved dcp-1. Additionally, TUNEL was also performed on the same tissues to ensure labelling of a broader range of apoptotic stages. In Chapter 3, we showed that in our system, areas prone to invasion exhibit actin accumulations in form of a bright GFP spot. We used this characteristic behaviour that almost always preceded cell delamination in order to identify pre-invasive cells from WT and CG7379 KD Moe:GFP labelled clones. As expected, pre-invasive cells were in part apoptotic. However, CG7379 KD increased the amount of pre-invasive cells and concomitantly reduced the amount of apoptosis, inducing a more than two-fold increase in viable pre-invasive cells. This finding is in line with the established role for the CG7379 human orthologue as a type II tumour suppressor gene: ING1 induces apoptosis in damaged cells (Bose et al., 2014; Russell et al., 2006) and its loss promotes apoptosis resistance (Helbing et al., 1997).

Furthermore, cell delamination occurs as a natural process as part of the topological reorganisation events that take place earlier in pupae development (Marinari et al., 2012). This raises the question whether the invasive phenotype that we observe when knocking down CG7379 in the *Drosophila* notum is simply the result of cell death evasion.

We hypothesised that cell delamination might occur at an increased rate earlier in development, and that lack of CG7379 would provide delaminated cells with the ability to evade apoptosis, consequently causing an increase in invading cells. To test this assumption, we took an indirect approach and blocked apoptosis through p35 overexpression specifically within Moe:GFP labelled *lgl* null mutant clones. P35 has been shown to inactivate executioner caspases in *Drosophila* through conformation changes (Hay et al., 1994). Overexpression of p35 significantly increased cell delamination in *lgl-/-* mutant tissue, however it did not phenocopy the dramatic increase in invasion induced by *lgl-/-;* CG7379 KD, suggesting that CG7379 KD must employ additional mechanisms to facilitate invasion.

Cell invasion requires spatially regulated changes to cell adhesion (Ridley, 2001). Decreases in junctional protein expression is very often correlated with the ability of tumours to invade and metastasize (Bruner and Derksen, 2018; Martin and Jiang, 2009; van de Ven et al., 2016). The adhesive state is modulated through cell junction reorganisation (Ridley, 2001). Lu et al. recently placed E-cadherin endocytosis at the core of cell transformation, linking it to polarity loss and EMT (Lu et al., 2018). Even though apical polarity proteins are not labelled as tumour suppressors, they play an important accessory role in epithelial malignancy and have been shown to be a target of neoplastic transformation. Loss of some of the proteins involved in polarity maintenance has been shown to promote metastatic phenotypes (Baum and Georgiou, 2011). Therefore, CG7379 KD impact on cell-cell adhesion and polarity was next assessed.

We found that CG7379 KD severely decreased E-cadherin, armadilo, α-catenin, Fasciclin III and coracle protein levels at the adherens and septate junctions respectively, both alone and in combination with the *lgl* null mutation. In addition, cell-cell junction architecture was compromised. These findings likely explain the increase in delamination induced by CG7379 KD. E-cadherin and armadillo are often differentially expressed in human cancers, which often correlates with increases in invasion (Conacci-Sorrell et al.,

2002). Fasciclin III promotes homophilic interactions between cells enhancing cell-cell adhesion and changes in Fasciclin III expression alone can be sufficient to alter intercellular adhesion (Wells et al., 2013). Moreover, fasciclin-like proteins were associated with metastasis in human cancers (Sasaki et al., 2001; Yoshioka et al., 2002). Coracle, as a member of the Yrt/Cora-group proteins, may act towards stabilizing the lateral actin cytoskeleton (Lamb et al., 1998; Laprise et al., 2009), which in turn acts on cell-cell junction stability. In addition, CG7379 KD significantly decreased discs large levels, but it did not affect its distribution.

Our data indicates that CG7379 KD might not have a drastic effect on apicobasal polarity as in our experiments neither localization nor protein expression of aPKC, bazooka and crumbs were affected following the knockdown. Even though mutations that compromise cell-cell adhesion are known to affect epithelial polarity, decreased expression of only certain AJ components might not be sufficient to induce loss of apicobasal polarity (Bilder et al., 2003). Moreover, *lgl* null clones showing undisturbed apicobasal polarity have been previously reported in similar systems (Bilder et al., 2003; Grzeschik et al., 2007). However, we cannot exclude a possible shift in protein localisation in the xz/yz planes following CG7379 KD as one limitation of the imaging method used is poor resolution on the z axis.

E-cadherin is at the very core of cell-cell junction adhesion. P120, β-catenin and α-Catenin are directly or indirectly linked to E-cadherin. In addition, α-catenin and p120 can simultaneously link TJ/SJ components. Furthermore, the adherens and tight/septate junctions are initially jointly assembled, and E-cadherin interactions across two cells is the first step of this assembly (Rusu and Georgiou, 2020). Therefore, if E-cadherin levels are hypothetically insufficient, then intercellular E-cadherin interactions would be predicted to be weak and consequently the other junctional proteins would also be recruited at a lower level. This could, in theory explain the systemic effect CG7379 KD has on cell-cell junction architecture. Ubiquitous over-expression of E-cadherin in the fly

did not significantly affect the level of delamination caused by CG7379 KD. Junctional discontinuities and defects in the organisation of the actin cytoskeleton were previously observed in *Drosophila* tissue defective for E-cadherin turnover (Georgiou et al., 2008). Taken together, these hypotheses suggest a possible role for CG7379 in regulation of E-cadherin localisation and/or turnover. Our inability to rescue the increase in invasion by reintroducing E-cadherin into the system is consistent with other *in vitro* studies. These studies found that the localisation of E-cadherin to cell junctions is under the control of Ras, and artificial increase of E-cadherin levels without manipulation of Ras expression leads to cytoplasmic accumulation of the overexpressed protein (Li and Mattingly, 2008; Schmidt et al., 2004). Therefore, further experiments should aim to asses E-cadherin distribution in CG7379 KD tissue that simultaneously overexpresses E-cadherin.

4.3.2 ING1 regulates cell invasion at a transcriptional level

4.3.2.1 ING1 knockdown increases invasion and disrupts adherens junction integrity in MCF-7 cells

Previous studies reported an increase in cell migration and invasion following ING1 KD as well as decreased migratory, invasive and metastatic capabilities following ING1 overexpression (Cornhill, 2017; Jiang et al., 2018; Thakur et al., 2014). We here report ING1's ability to modulate expression of key players in the EMT process by regulating their transcription.

Based on the results obtained in the CG7379 KD experiments we wanted to assess ING1's effect on cell junction integrity. For this purpose, the MCF-7 breast adenocarcinoma cell line was selected for further *in vitro* studies, as it retains E-cadherin expression (Kohn et al., 2014). ING1 KD increased migration by 72% and invasion by 105% relative to the control transfected with non-targeting siRNA. Disruption of the E-cadherin localisation

alongside the cell-cell junction was also noted as a consequence of insufficient ING1 expression levels, suggesting that ING1 KD might disrupt cell-cell adhesion in a similar way to its fly orthologue. This indicates that the mechanism of action employed by CG7379 KD to increase invasion was, at least in part, evolutionarily conserved. Therefore, in this instance, findings from the *Drosophila in vivo* cancer model are likely to be of relevance to human disease.

4.3.2.2 Microarray analysis of genome-wide gene expression reveals a possible role for ING1 in cell-cell adhesion regulation

It has been proposed that the functional role of ING1 in apoptosis and cell cycle regulation is a consequence of its ability to modulate gene expression (Vieyra et al., 2002a). ING1 can repress gene expression by interacting with the Sin3A/HDAC complex (Cheng et al., 2014; Guérillon et al., 2013) or activate gene expression by interacting with histone acetylase complexes (Guérillon et al., 2013). Additionally, ING1 has been shown to regulate p53 activity (Guérillon et al., 2013), and p53 can modulate E-cadherin expression and invasion levels by controlling the expression level of its transcriptional modulator, Slug (Wang et al., 2009). We hypothesised that the ING1 KD effect on cell-cell junction integrity might also be a consequence of ING1's transcription regulatory properties.

Microarray analysis of genome-wide gene expression was performed following ING1 KD in MCF-7 cells in order to test whether the ability of ING1 to regulate cell junction integrity could also be attributed to its transcription factor function. ING1 KD led to significant changes in the expression pattern of 919 genes, most of which were downregulated. GO-enrichment analysis and pathway analysis showed that most of the significantly misregulated genes are involved in cell cycle regulation, DNA replication, cell senescence and p53 pathway which corroborates previous work on ING1 function (Russell et al., 2006; Ythier et al., 2008). However, neither Slug nor Twist, well

characterised transcriptional modulators of E-cadherin expression (Baranwal and Alahari, 2009), were differentially expressed in our study. The only component of the junctional complexes that was transcriptionally altered by ING1 KD was p120, suggesting a role for ING1 in E-cadherin turnover. This is in line with our E-cadherin overexpression experiment in flies, where increased levels of E-cadherin failed to rescue the CG7379 KD-induced invasion, suggesting that modulators of E-cadherin behaviour are likely to be affected by the knockdown. A targeted search for interactors of junctional proteins did indeed reveal a number of misregulated genes that are likely to affect both cell-cell junction integrity and promote invasive phenotypes, including EXOC5, WASF3, CTNND1, and RHOC. There is extensive evidence linking the misregulation of these genes with a disruption to cell-cell junction integrity and/or the promotion of invasion.

Exocyst Complex Component 5 (EXOC5), was significantly downregulated and shows high homology to *Drosophila* sec10. Sec10 has been shown to interact with armadillo (β-catenin) and α-catenin (Langevin et al., 2005) via sec5 and 15 and can reduce E-cadherin, armadillo and/or α-catenin levels at AJ in *Drosophila* due to an increase in protein turnover (Langevin et al., 2005). Furthermore, increased EXOC5 mRNA levels were previously correlated with E-cadherin overexpression within the lymphovascular embolus of inflammatory breast cancer (Ye et al., 2010).

WASP Family Member 3 (WASF3), the homologue of *Drosophila* SCAR, was significantly upregulated in our study. SCAR, a well-known regulator of the actin cytoskeleton, has been linked to α-catenin function in *Drosophila* embryos (Sarpal et al., 2012). WASF3 has been shown to be overexpressed in high-grade breast and gastric cancer and to collaborate with Erb-B2 Receptor Tyrosine Kinase 2 (ERBB2) overexpression to promote invasion in MCF-7 cells through Janus Kinase 2/Signal Transducer And Activator Of Transcription (JAK/STAT) signalling (Hu et al., 2018; Teng et al., 2016). Moreover, WASF3 KD significantly decreased cell migration and invasion of gastrointestinal cells *in vitro* (Hu et al., 2018). ERBB2 was also overexpressed following ING1 KD in our study,

together with Catenin Delta 1 (CTNND1, p120). Previous work has shown that ERBB2 overexpression increases motility and invasion in breast cancer by upregulating CTNND1 (Johnson et al., 2010). P120 can exert both pro- and anti-tumorigenic functions. E-cadherin loss during EMT can lead to an increase in cytoplasmic p120, which would further drive invasion by modulating Rho and Rac activation (Yanagisawa and Anastasiadis, 2006). Additionally, recent work on p120 suggests that both loss and overexpression of p120 can inhibit E-cadherin turn-over at cell-cell junctions (Greig and Bulgakova, 2019).

Rap Guanine Nucleotide Exchange Factor 2 (RAPGEF2/PDZ-GEF-I) was upregulated in response to ING1 depletion. RAPGEF2 mediates cell adhesion and cell-cell junction formation by regulating Rap1 and Rap2 activity. It has been proposed that RAPGEF2 might play a role in regulation of E-cadherin trafficking (Asuri et al., 2008) and actomyosin contractility, as tissues overexpressing dPDZ-GEF in *Drosophila* acquired a rounded geometry (Boettner and Van Aelst, 2007). Another *Drosophila* study showed that *Drosophila* RAPGEF2 modulates the formation of AJs and modulates E-cadherin, armadillo and α-catenin expression at cell-cell junctions (Wang et al., 2006).

Adducin 3 (ADD3) expression, two-fold decreased in our study, was found to be both increased or decreased in malignant tissues depending on the cancer type. Increased invasion upon ADD3 knockout was recently reported *in vitro* in a lung cancer cell line (Lechuga et al., 2017). Adducin proteins are critical for proper formation and stabilization of the membrane cytoskeleton and regulation of cell motility and cell-cell adhesion (Luo and Shen, 2017). ADD3 depletion was shown to negatively affect both AJ and TJ reassembly and to impair the assembly of actin filaments associated with newly formed junctions in colon epithelial cells (Naydenov and Ivanov, 2010). Similarly, in *Drosophila* embryos, *hu-li tai shao* (*hts*), the fly orthologue of human adducins, was shown to partially co-localise with discs large and to regulate discs large targeting to the membrane. Moreover, *hts* mutants displayed phenotypes indicative of disruptions to the

epithelial integrity (decreased cuticle secretion in embryos) (Wang et al., 2011). In *Drosophila* oocytes, improper localisation of *hts* RNA led to the overgrowth of actin filaments (Pokrywka et al., 2014).

In our experiment, Lysine Demethylase 5B (KDM5B) expression was upregulated following ING1 KD. Increased KDM5B expression is associated with poor clinical outcome in breast cancer patients (Bamodu et al., 2016; Hayami et al., 2010). In breast cancer, KDM5B and E-cadherin present reverse patterns of expression (Bamodu et al., 2016). Moreover, ectopic expression of KDM5B has been shown to promote EMT by downregulating E-cadherin through Snail dependent mechanisms (Bamodu et al., 2016). Overexpression of KDM5B can also increase invasion *in vitro* and metastatic potential of gastric tumours *in vivo*, by activating the Akt pathway. It is therefore very likely to modulate cytoskeleton dynamics (Wang et al., 2014). In *Drosophila* haemocytes, *little imaginal discs* (*lid*), the fly orthologue of KDM5B, modulates *Rac* and *Ras* expression and consequently the actin cytoskeleton organisation. *Lid* depletion triggered lamellipodia formation and hyperpolymerization of F-actin (Morán et al., 2015).

These results fit both our transcriptomics results, and the disruption we see in junction integrity in *Drosophila* nota when knocking down CG7379 expression. Moreover, a functionally validated network of genes which were selected as potential regulators of cell-cell junction integrity in our system, and members of the AJ pathway revealed a plethora of genetic and physical interactions between the two groups. Some of the linker genes that mediated these interactions also proved to be differentially expressed in response to ING1 KD, further validating our hypothesis that the ability of ING1 KD to disrupt cell-cell junction integrity is dependent on its role in transcription regulation.

GO enrichment analysis of this subset of ING1 KD differentially expressed genes has identified AJ as a significantly enriched pathway and regulation of GTPase activity as an enriched biological process validating our speculations. Additionally, other enriched

biological processes were cytoskeleton organisation and regulation of cell shape, which are consistent with Rho hyperactivation, impaired cell-cell junctions and increased cell motility. Taken together, data from the genome-wide transcriptomics experiment performed on MCF-7 cells with depleted ING1 expression, strongly suggests a role for ING1 in cytoskeleton dynamics and cell-cell junction protein trafficking.

4.3.2.3 Microarray analysis of genome-wide gene expression identifies ING1 as a potential modulator of Rho activity

The increase in invasion and disrupted junctional architecture could potentially be explained by many other genes that were differentially expressed following ING1 KD, although interpretation of their exact involvement might be complex. Many of these genes were found to be both upregulated and downregulated in cancer depending on cancer type, cancer grade or experimental procedure, whilst many others were studied primarily for their involvement in cell proliferation or apoptosis.

For instance, data from the microarray experiment revealed a significant increase in RHOC mRNA expression. RHOC is a marker of metastatic potential in some breast cancers (Wu et al., 2010) and its overexpression has been associated with increased cell motility and invasion through stress fibre formation and focal adhesion. In contrast, RHOC knockdown has been shown to decrease invasion and nuclear β-catenin levels (Pillé et al., 2005; Ridley, 2013; Simpson et al., 2004; Spangler et al., 2012; Wu et al., 2010). Both decreases and increases in RHOC expression levels have been associated with decreased cell adhesion through different mechanisms (Kawata et al., 2014; Wu et al., 2010). An increase in RHOC expression in MCF-7 cells was reported to induce a decrease in E-cadherin levels at the AJ (but not overall E-cadherin levels). Additionally, the Snail and Twist expression levels were not affected in that study and no nuclear β-catenin accumulation was observed (Kawata et al., 2014). Surprisingly, DIAPH1 (mDia1) and Myosin Heavy Chain 10 (MYH10, Myo-IIB) expression were significantly reduced

following ING1 knockdown. Increased DIAPH1 expression is associated with invasion and increased metastatic potential (Li et al., 2019; Lin et al., 2015; Lin et al., 2014). Similarly, Myo-IIB silencing has been shown to impair cell migration and invasion and to upregulate E-cadherin expression (Wang et al., 2018). In another study, the integrity of the cadherin junction architecture has been shown to be compromised following Myo-IIB depletion (Smutny et al., 2010). However, although mDia1 can be activated by RhoC, formin-like2 and 3 (FMNL2/3) appear to be RhoC-specific interactors (Kitzing et al., 2010; Vega et al., 2011) , and FMNL2 and FMNL3 levels were not affected by ING1 KD in our study. Rho proteins were also shown to preferentially regulate Myo-IIA activity (Conti and Adelstein, 2008; Wang et al., 2018). Additionally, Myo-IIA can account for Myo-IIB loss in some tissues (Conti and Adelstein, 2008).

Additionally, ING1 KD induced changes to the expression levels of several Rho activity modulators (Anillin Actin Binding Protein (ANLN), cyclin 2 (CCNA2), Rac GTPase Activating Protein 1 (RACGAP1), Kinesin Family Member 23 (KIF23)). Moreover, hyperactivation of Rho proteins would be consistent with the behaviour of the pre-invasive and invasive cells observed in *Drosophila* (rounding of the cells). Therefore, in the light of these new results, we made another attempt at rescuing the invasive phenotype induced by CG7379 KD in flies. Rho1 is the fly orthologue of RhoA, RhoB and RhoC and we postulated that if hyperactivation of Rho is responsible for the increase in cell invasion, then a decrease in Rho levels should balance out this phenotype. Co-expression of dominant negative Rho with RNAi against CG7379 KD in Moe:GFP labelled clones did not however change the level of cell delamination in pupae 20-24 hrAPF. There are several possible explanations for this: i) in flies, Rho1 is the closest homologue of both RhoA and RhoC. Only RhoC and not RhoA mRNA levels were affected by ING1 KD in MCF-7 cells (although we cannot exclude the possibility that RhoA activation was affected by the expression of other genes altered by ING1 KD). RhoA and RhoC have been shown to play distinct roles in cell invasion (Vega et al., 2011) and as such, ING1 KD induced invasive behaviour might be specific to RhoC. RhoC has a greater

affinity for ROCK than RhoA and therefore RhoC activation is more likely to disrupt cell-cell junction architecture (Sahai and Marshall, 2002). However, this is unlikely given that depletion of both CG7379 and ING1 seem to employ the same mechanism to induce invasion; ii) the expression and phenotypic behaviour of cell-cell junction components and consequently the invasive phenotype, might be extremely sensitive to the levels of Rho activation, and both overexpression and insufficient levels of Rho might promote invasion; iii) it has been previously shown that modulation of only E-cadherin expression levels or only Ras-ERK-MAPK (MAPK, mitogen-activated protein kinase) activity are insufficient to rescue EMT phenotypes. However, when E-cadherin expression was enforced and MAPK activity was simultaneously inhibited, cells restore epithelial morphology (Li and Mattingly, 2008). Similarly, it is possible that cells bearing CG7379 KD need both E-cadherin and Rho expression to be restored to the original levels in order to reduce invasive potential. To verify this, further experiments would involve assessment of E-cadherin distribution by immunofluorescence at AJ in tissues deficient in CG7379 and Rho1 expression and assessment of invasion from tissues simultaneously expressing an RNAi against CG7379, a double negative Rho1 construct and overexpression of E-cadherin. A recombination between tomato–E-cadherin and UAS-Rho1.N19 on the 2nd chromosome would first need to be performed for the latter experiment.

Chapter 5 – CG7379 and ING1 involvement in cell proliferation

5.1 Introduction

5.1.1 ING1's involvement in cell growth and cell cycle progression

ING1 was first isolated in 1996 in a study looking to select growth inhibitory genes. It was named 'inhibitor of growth' because of its ability to i) inhibit growth when overexpressed; ii) promote growth in soft agar and induce foci in focus-forming assays when expressed in anti-sense orientation in non-tumorigenic mouse epithelial cells (Garkavtsev et al., 1996). Later on, the same group showed that ING1 expression changes during the cell cycle: ING1 expression decreases upon entering the cell cycle (G0 to G1 transition) but increases towards the end of G1 and peaks during the S phase to then gradually decrease again during G2 (Garkavtsev and Riabowol, 1997). Further on, the Gudkov lab also showed that ING1 KD can rescue p53-induced growth and postulated that ING1's proliferative effects are p53-dependent (Garkavtsev et al., 1998). In contrast, ING1 negatively regulates cell growth in p53-deficient fibroblasts suggesting that ING1 might play a p53-independent role in the regulation of cell proliferation (Coles et al., 2007). Since then, several other studies investigating the effect of ING1 on cell proliferation, reported cells accumulating in G0/G1 upon ING1b overexpression in a range of cell lines from normal fibroblasts to cancer cells derived from metastatic sites (Abad et al., 2011; He et al., 2014; Jia et al., 2015; Jiang et al., 2018). However, the effect that ING1 silencing has on cell proliferation was investigated by only a few groups. As discussed above, Garkavtsev et al. reported extended proliferative life span and growth promotion upon ING1 KD and showed that downregulation of ING1 can rescue p53 induced growth inhibition (Garkavtsev et al., 1998; Garkavtsev and Riabowol, 1997). ING1 knockout mouse embryonic fibroblasts also exhibited increased growth rates in one study (Coles et al., 2007). However, all these studies targeted only one ING1 transcript, namely p33ING1b. When all ING1 isoforms were knocked out *in vivo* in mice, the resulting animals exhibited reduced size in comparison to the controls, but no

significant difference in term of cell cycle progression was noticed *in vitro* between knockout and WT embryonic fibroblasts (Kichina et al., 2006).

As for its role in the regulation of apoptosis, ING1's antiproliferative effects were also linked to its ability to modulate transcription. Deletion of the N-terminal SAID domain of p33ING1b reduces the growth suppression effect of p33ING1b overexpression in embryonic adherent mouse fibroblasts. The N-terminal domain is required for ING1-Sin3/HDAC interaction (Figure 4.3) and therefore directly links the ability of ING1 to modulate cell growth to an ability to control transcription (Kuzmichev et al., 2002). Additionally, ING1 has been shown to modulate expression of several micro RNAs, which in turn further regulate gene expression (Chen et al., 2013; He et al., 2014).

The ability of ING1 to modulate the cell cycle progression has been closely linked to senescence and response to DNA damage. ING1 is a key player in multiple DNA repair pathways and the ING1b isoform is upregulated in response to a variety of DNA damaging agents (UVB, UVC and ionizing irradiation, cisplatin, hydrogen peroxide, neocarzinostatin, etoposide, doxorubicin) and appears to function in both p53-dependent and -independent manners (Ceruti et al., 2013; Cheung and Li, 2002; Garate et al., 2007). Overexpression of ING1b stimulates DNA repair whilst ING1 KD impairs DNA repair activity. This impairment appears to be the result of an exacerbated early response to DNA damage. Similarly, mutant forms of ING1b, which carry missense mutations in the PhD domain that affect the 3D structure of the domain, are not only unable to stimulate DNA repair, but can actually impair the process (Ceruti et al., 2013). However, the ability of ING1 to stimulate the DNA repair machinery is stimuli and cell-type specific. For instance, ING1 dependent DNA damage response has been observed in MMRU cells, but not in mouse fibroblasts or HCT116 cells upon doxorubicin treatment (Garate et al., 2007). UVB irradiation does not trigger ING1 dependent DNA repair in mouse epidermal fibroblast, but does so in mouse keratinocytes (Cheung and

Li, 2002). ING1 DNA damage-induced apoptosis has also been reported in p37ING1b null mouse embryonic fibroblasts (Coles et al., 2007).

Overexpression of ING1b has been associated with senescence and increased p21 levels from early reports (Garkavtsev et al., 1998; Garkavtsev and Riabowol, 1997). Increased p21 expression can lead to CDK1/2/4 or 6 inhibition and consequently pRb hyperactivation. As a result, E2F transcription factors are kept inactive and therefore cell cycle is arrested at G1/S or G2/M transition (Georgakilas et al., 2017). ING1a has been shown to act on this pathway (Rajarajacholan et al., 2013). Often, the G1 cell cycle arrest induced by ING1 overexpression exhibits features of oncogene-induced senescence (Abad et al., 2011). Moreover, oncogenic stress induces ING1 expression. However, whilst some studies report p33ING1b but not p47ING1a overexpression (Abad et al., 2011), others report decreased p33ING1b levels and increased p47ING1a levels (Li et al., 2011; Soliman et al., 2008; Vieyra et al., 2002b). However, increased p33ING1b binding to chromatin was observed in one study, and ING1b overexpression was shown to induce senescence despite a decrease in ING1b expression in senescent cells in another context (Li et al., 2011; Soliman et al., 2008). All these studies used human fibroblasts.

Studies investigating p33ING1b therefore portray ING1 as a master regulator of cell proliferation. Several lines of evidence show that by modulating cell cycle progression, senescence, the response to several DNA damaging agents and apoptosis, increased levels of ING1 promote G0/G1 cell cycle arrest. Conversely, decreases in ING1 expression are expected to promote hyperproliferation. However, the results from the few studies investigating the effect of ING1 knockdown or knockout are rather contradictory. Moreover, under normal conditions ING1 expression is at a maximum during the S phase (Garkavtsev and Riabowol, 1997), suggesting that some level of ING1 expression might be needed for successful cell proliferation. We decided therefore to examine the effect that CG7379 and ING1 knockdown had on cell proliferation and cell cycle progression in MCF-7 cells.

5.2 Results

5.2.1 Clonal analysis of CG7379 knockdown indicates a cell proliferation role for CG7379 during early development of the notum

One other phenotype that became apparent when analysing the CG7379 related data from the cancer genetic screen performed in the lab, was a decrease in the area covered by the tumour-like tissues formed following CG7379 KD (Figure 5.1a, b). Although in the screen CG7379 was not picked up as a hit for the 'clonal tissue' category, which estimates the clonal coverage, quantitative measurements revealed a significant decrease in clonal coverage (p=0.0006) when CG7379 was knocked down in *lgl-/-* clones, in comparison to *lgl-/-* alone (Figure 5.1a-c). Three different RNAi lines were used to ensure that the decreased clonal surface was indeed induced by CG7379 silencing and was not an off-target effect. Significant decrease in the average clonal surface was observed when using either of the three RNAi lines when compared to *lgl-/-* clones (Table 5.1, Figure 5.1c). As before, for practical reasons, only two RNAi lines were used for the rest of the experiments. For consistency, we chose to use the same RNAi lines that were used throughout the rest of the thesis (27988, 27989).

As for the invasive phenotype, the specificity of the phenotype for the knockdown was tested. Moe:GFP labelled CG7379 KD clones were generated in an otherwise WT background on the back of the fruit fly and the clonal surface was measured using the Fiji software. Moe:GFP clones were approximately 30% smaller than their WT counterparts when using RNAi lines against CG7379 KD (Figure 5.1, Table 5.1), confirming that CG7379 KD has the ability to reduce clonal coverage in the epithelium from the *Drosophila* notum. The use of the *lgl* null mutation induces loss of cell polarity and subsequent loss of tissue architecture, generating multilayered regions within the clonal tissue (Figure 5.1b'). As a consequence, the ability to confidently estimate the

number of cells might be impaired. Therefore, we focused on investigating CG7379 KD clones as they present relatively normal epithelial organisation.

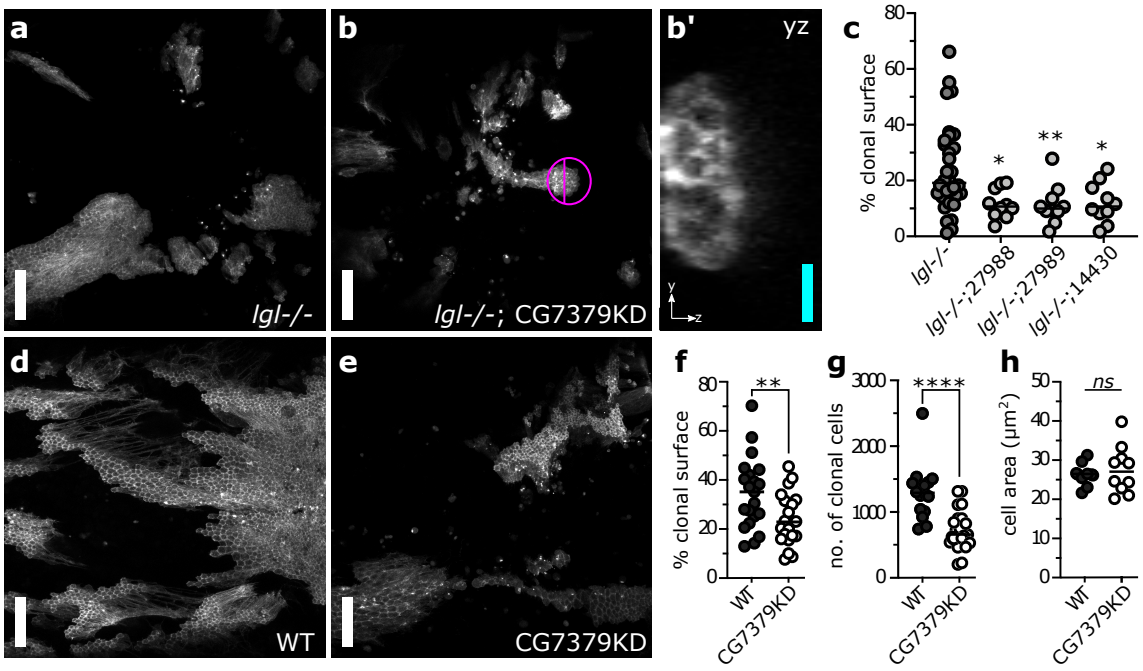


Figure 5.1 CG7379 knockdown decreases clonal coverage

Lgl-/- **(a)**; *lgl-/-;* CG7379 KD **(b)**; WT **(d)**; CG7379 KD **(e)** Moe:GFP labelled clones in *Drosophila* nota, 20-24 hr APF. Images represent Z projections of confocal z-stacks of the dorsal thorax epithelium. **(b')** YZ orthogonal view of the area marked in (b). Note the multilayering of the clonal tissue. White scale bar: 50 μm, cyan scale bar: 10 μm. **(c)** Quantification of the amount of tumour-like tissue induced by independently expressing three different RNAi lines (27988, 27989 and 14430) against CG7379 in *lgl-/-* mutated background. The total amount of clonal tissue was calculated as a percentage of GFP labelled tissue surface out of the entire notum. n=10 animals/RNAi line; n=32 for *lgl-/-*. **(f)** Quantification of percentage clonal coverage induced by CG7379 KD alone. **(g)** Quantification of the number of clonal cells in the nota. Cells were counted on a 1225 μm^2 area and the total number of cells was estimated based on the measured clonal area. n=21 animals/genotype. **(h)** Quantification of the clonal cell area. n=50 cells/animal for 10 animals for each genotype. For statistical analysis, unpaired Student's *t*-test or Mann-Whitney U test were performed as dictated by the data distribution. * p≤0.05; **p≤0.01; ***p≤0.001; ***p≤0.0001.

Table 5.1 Average size of Moe:GFP labelled cells and clonal tissue

	WT	CG7379KD	*lgl-/-*	*lgl-/-*; 27988	*lgl-/-*; 27989	*lgl-/-*; 14430
Clonal surface (%)	34.5±3.2	23.8±2.3	24.2±2.8	11.7±1.7	11.4±2.2	12±1.3
No. of clonal cells	1300±102	733±67				
Cell area (μm^2)	26.3±0.9	27.5±1.9				

The number of clonal cells was estimated to determine whether the decrease in clonal coverage was a consequence of cell shrinkage or whether it reflected a decrease in the number of clonal cells. CG7379 silencing significantly reduced the number of clonal cells, estimated as half the number of a WT Moe:GFP labelled clone (Figure 5.1g, Table 5.1). To ensure the reliability of the analysis, cell area was also measured in Moe:GFP labelled clones of the two genotypes. Cell area was determined at the apex level based on the junctional actomyosin ring labelled by Moe:GFP. As expected, the average cell surface did not change in response to CG7379 knockdown (Figure 5.1h, Table 5.1).

5.2.2 ING1 expression is putatively required for G1/S transition in MCF-7 cells

The role of ING1 in cell proliferation was also assessed in MCF-7 cells. For this, cells were collected 48 hr after siRNA treatment, fixed, treated with RNase and stained with propidium iodide (PI). PI is commonly used in “snapshot” flow cytometry cell cycle progression studies. All cells in G0/G1 phases of the cell cycle have uniform DNA content. Similarly, cells in G2/M have uniform DNA content, but double that of G1/G0 cells. PI is a fluorescent intercalating agent that labels nucleic acids without any sequence specificity and as such PI fluorescence intensity directly reflects DNA content. Therefore, the single time point measurements of DNA content allow for the identification of cells in the following stages of the cell cycle: G0/G1; S; G2/M. Kaluza software was used for data analysis. To ensure the accuracy of the analysis, the single cell population was first

determined. The side scatter was plotted against the forward scatter (Figure 5.2a) in order to exclude cell debris and apoptotic cells. Apoptotic cells are characterised by fragmented DNA and therefore represented with plot values ~zero. The acquired signal was then filtered to exclude multi-cell clumps. Cells are approximately rounded in shape and therefore the height and area of the pulse generated when the cell passes through the detector should be directly proportional. Clumped cells in contrast, would be predicted to exhibit an unexpectedly large area in relation to the intensity of the signal. The pulse height was therefore plotted against the pulse area and the single cell population was selected for analysis (Figure 5.2b). Further on, cell count was plotted against pulse area (Figure 5.2c) to determine the accuracy of DNA content measurement. The mean fluorescence coefficient of variation of cells in G1 (width of the first peak in Figure 5.2c) should not exceed 6%. Cell cycle analysis was performed using the Michael H. Fox algorithm.

ING1 KD significantly increased ($p<0.0001$, Figure 5.2e) the population of G1 cells from an average of 60.3±2% in MCF-7 cells treated with non-targeting siRNA to 87.8±1.2% in cells treated with siRNA against ING1. Consequently, the S and G2/M populations were significantly decreased following ING1 KD (Table 5.2). Representative examples of the cell cycle plots are shown in Figure 5.2d, f. A cell count of MCF-7 cells 48 hr post transfection was also performed. ING1 KD slightly, but significantly (Table 5.2, $p=0.016$) decreased the number of cells when compared to the group treated with mock siRNA (Figure 5.2h), mimicking what we see in the fly when knocking down CG7379 expression. We next aimed to assess the effect of ING1 KD on apoptosis. The sub G0 population from flow cytometry cell cycle analysis experiments is typically considered to represent apoptosis in the analysed samples. The sub G0 population was however underrepresented in all samples showing values around 0% in both control and knockdown samples.

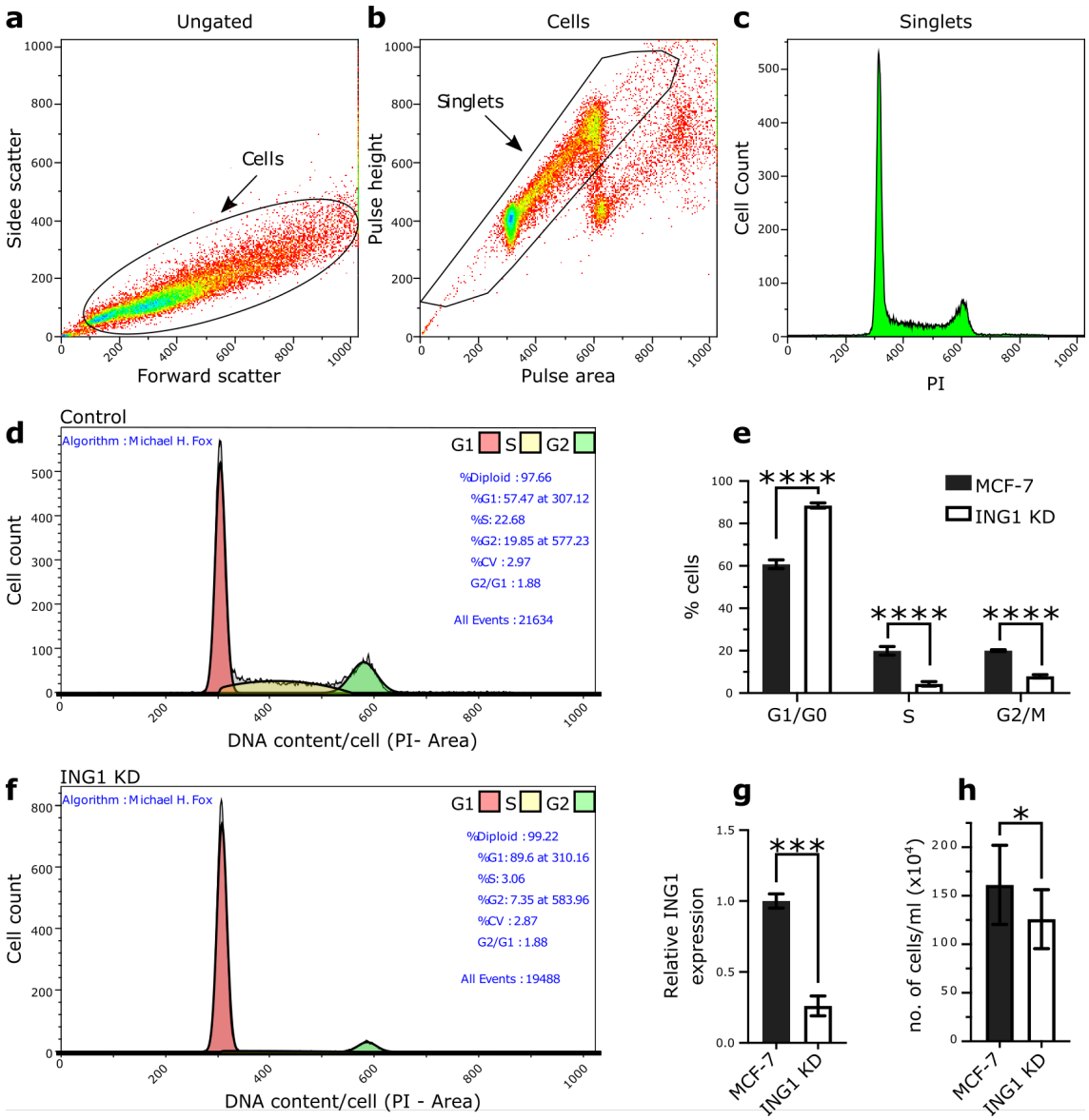


Figure 5.2 Analysis of cell cycle distribution following ING1 knockdown

(a) Forward vs. side scatter density plot to identify the cells population and exclude debris. Cell debris and apoptotic cells have lower forward scatter levels reflecting DNA fragmentation. **(b)** Pulse shape analysis to identify single cells. **(c)** DNA histogram showing the distribution of the DNA content within the single cell population. **(d, f)** Representative examples of cell cycle plots generated after cell cycle analysis of DNA histogram using the Michael H. Fox algorithm: control cells (d) and ING1 KD cells (f). **(e)** Statistical analysis of cell cycle profiles shows a significant increase in G1/G0 population following ING1 KD. **(g)** Relative ING1 expression following siRNA treatment determined by qPCR. **(h)** Cell count of MCF-7 cells treated with mock or ING1 siRNA 48 hr post-transfection. Student's *t*-tests were performed to determine statistical significance. Error bars represent ±s.e.m; n=5; *p<0.05; ***p<0.001; ****p<0.0001.

Table 5.2 Mean number of MCF-7 cells treated with mock siRNA or siRNA against ING1 that grew in 48 hr and their cell cycle distribution expressed as proportion of cells in each stage of the cell cycle

	MCF-7	ING1 KD
Cell count		
No. of cells/ml	161±18	126±14
Cell cycle distribution		
G0/G1 (%)	60.3±2	87.8±1.2
S (%)	19.8±2	4.3±1
G2/M (%)	19.9±0.4	7.8±0.8

To assess the impact of ING1 KD on apoptosis under the described treatment conditions, a combined fluorescence microscopy and flow cytometry approach was adopted. MCF-7 cells were collected 48hr post transfection, fixed and stained for DNA content using PI dye. The apoptosis wizard provided by the ImageStream Data Analysis and Exploration Software (IDEAS) was used for data analysis. In short, single cells that are in focus are first selected. The apoptotic cells are then gated based on their morphology: apoptotic cells should exhibit a low nuclear area and high brightfield contrast (Figure 5.3a-c). No significant difference in the population of apoptotic cells was observed between the treatment (ING1 KD) and the control (mock siRNA) groups using this approach (Figure 5.3f).

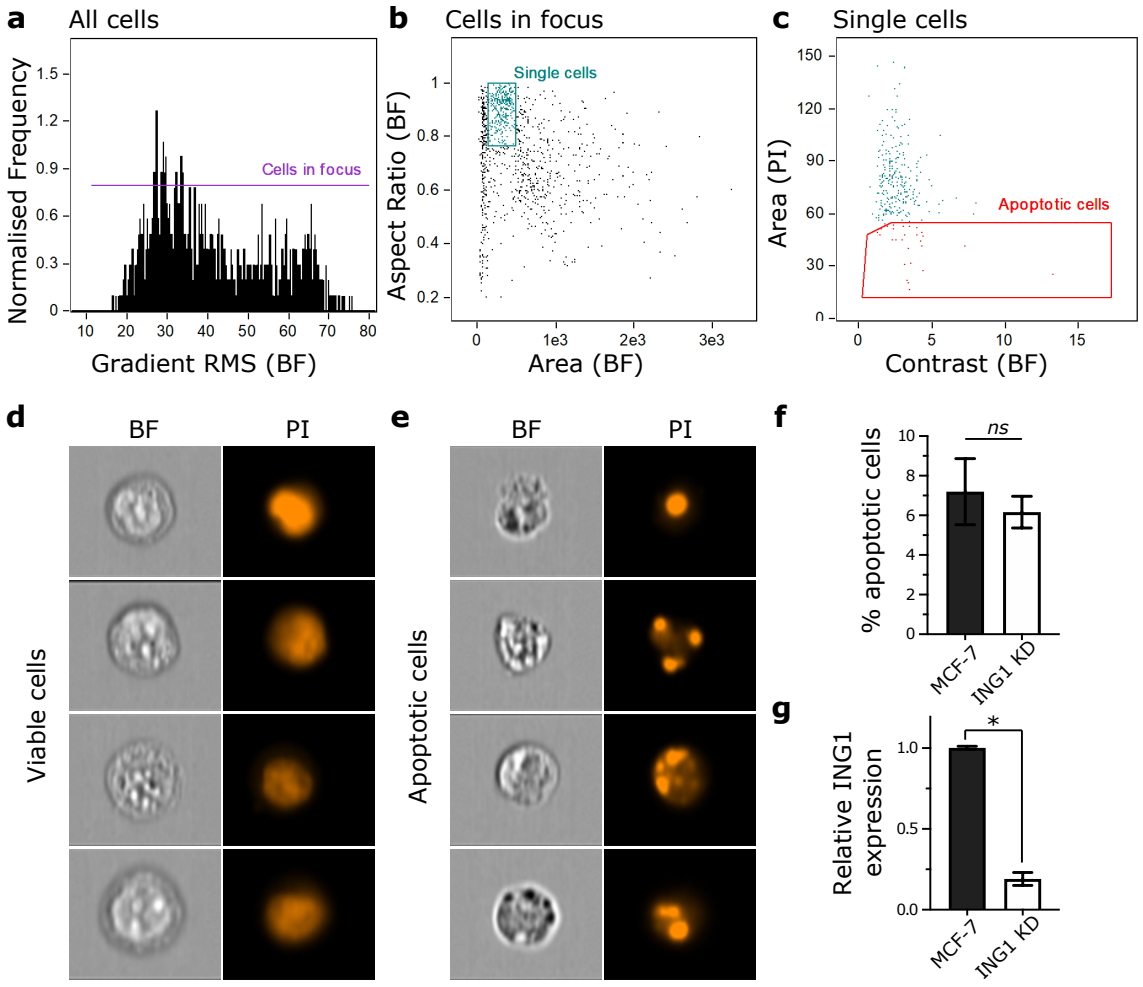


Figure 5.3 ING1 knockdown does not affect apoptosis in MCF-7 cells

(a) Gradient RMS histogram of all analysed cells. Cells in focus, characterised by higher gradient RMS values were selected. **(b)** Scatter plot of area versus aspect ratio of the pulse for the cells in focus. Single cells, characterised by an intermediate area value and a high aspect ratio, were selected. **(c)** Scatter plot of the brightfield contrast versus the area of the nucleus for single cells. Apoptotic cells, characterised by low nuclear area and high brightfield contrast, were selected and the percentage of apoptotic cells out of single cells was calculated. **(d)** Representative examples of non-apoptotic cells under brightfield (BF) and stained with propidium iodide (PI). **(e)** Representative example of apoptotic cell. **(f)** Quantification of apoptotic events. n=3 (control); 2 (ING1 KD). **(g)** Relative ING1 expression as shown by qPCR. Unpaired Student's *t*-test was performed to determine statistical significance. Error bars represent ±s.e.m. *p<0.05

5.3 Discussion

Clonal analysis of the Sin3A complex components in the developing wing tissue of *Drosophila* 3rd instar larvae revealed reduced clonal size following RNAi mediated CG7379 KD (Barnes et al., 2018). In line with this, our experiments revealed significantly reduced clonal coverage following mosaic knockdown of CG7379 in the dorsal thorax of *Drosophila* pupae. In addition to the striking increase in invasion, three other hypotheses could also explain the decrease in tissue size: i) increased cell death as a result of cell competition; ii) reduced cell surface; iii) decreased cell proliferation. We have shown that CG7379 KD confers cells the ability to evade anoikis (Chapters 3.2.1) and apoptosis (Chapters 4.2.1). To our knowledge, no reports have linked CG7379 nor ING1 to necrosis so far. On the contrary, Vieyra et al. show that p33ING1b induced cell death exhibits characteristics of apoptosis rather than necrosis (Vieyra et al., 2002b). A decrease in cell death within the mutant tissue would be expected to increase the number of clonal cells, yet CG7379 KD significantly decreases the number of clonal cells when compared to WT clones. Furthermore, cell area was not affected by CG7379 KD in our experimental settings. We therefore speculate that CG7379 might play an active role in cell proliferation in early stages of *Drosophila* development.

The gene expression analysis described in Chapter 4.2.4 implicates ING1 in the regulation of cell proliferation. Consistent with the roles previously described in the literature for ING1 (Soliman and Riabowol, 2007), GO enrichment analysis of the entire set of DEG suggests a role for ING1 in cell division, cell cycle progression DNA replication and various DNA repair mechanisms (Appendix 3). MCF-7 cells harbour a wild-type p53 gene (Berglind et al., 2008). Consistent with the ability of ING1 to act in a p53 dependent manner (Guérillon et al., 2013), the p53 signalling pathway was significantly enriched following GO enrichment analysis of DEG following ING1 KD in MCF-7 cells. Interestingly, 77% of the genes involved in cell cycle progression have been downregulated in response to ING1 KD (Figure 5.4) including master regulators of cell cycle progression such as

cyclin A, B, D, E, CDC25A, C and CDK1, 2. Moreover, the only protein from the pathway to have elevated mRNA levels was the universal CDK inhibitor p21, which can induce growth arrest in the G1 and S phase of the cell cycle (Georgakilas et al., 2017). Consistent with the mRNA expression analysis, ING1 KD significantly increased the proportion of cells in the G0/G1 phase of the cell cycle, and significantly decreased the number of cells that grew during the first 48hr after transfection when compared to cells treated with mock siRNA. In addition, ING1 KD did not appear to manifest a significant effect on the level of apoptosis. This data strongly suggests that, in our system, ING1 KD negatively regulates cell proliferation, which disagrees with the role previously proposed for ING1 as a growth inhibitor (Abad et al., 2011; Coles et al., 2007; Garkavtsev et al., 1998; He et al., 2014; Jia et al., 2015; Jiang et al., 2018).

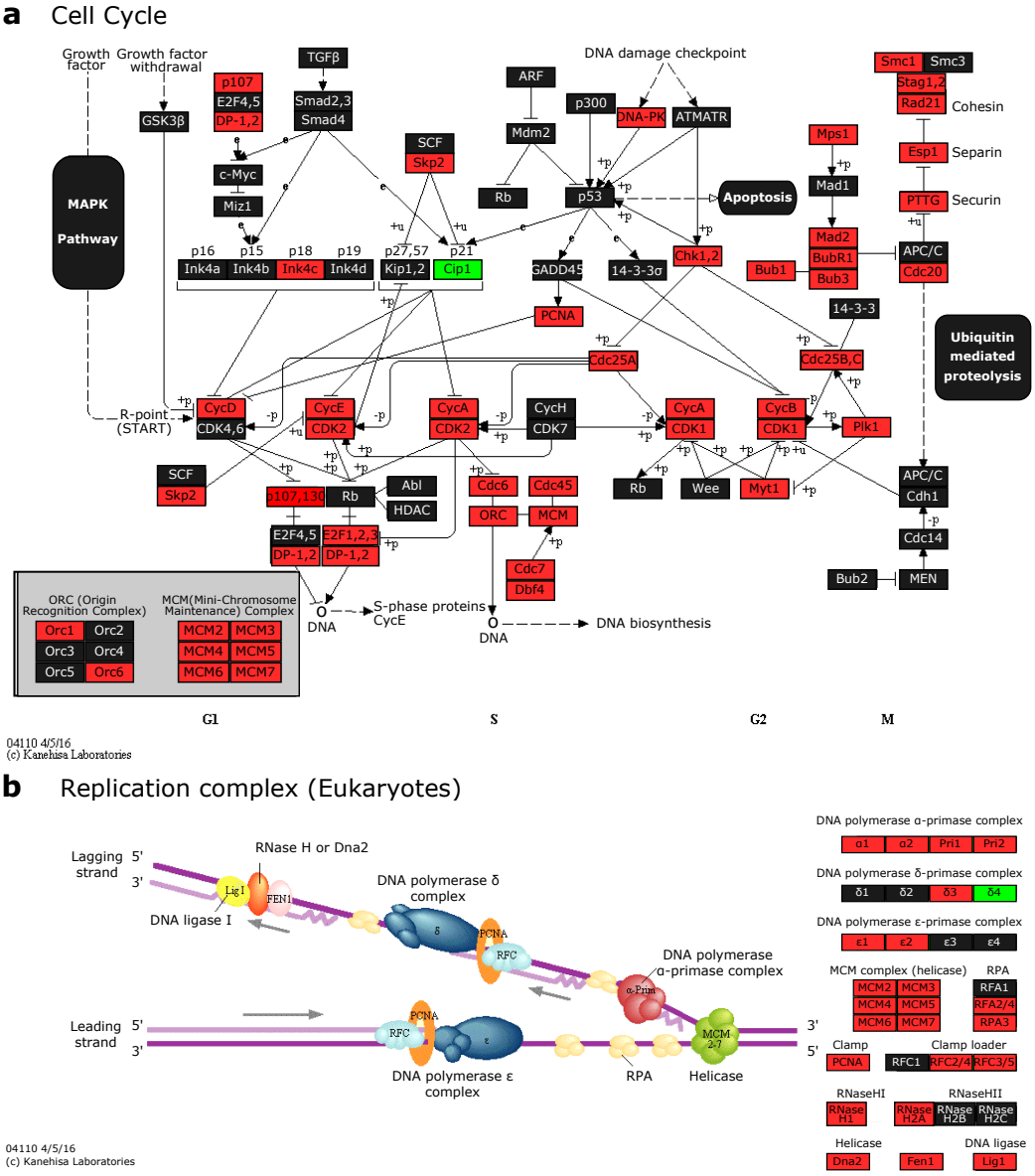


Figure 5.4 Schematic representation of ING1 knockdown effects on cell cycle and DNA replication pathways

(a) KEGG pathway for cell cycle progression. The origin recognition (ORC) and mini-chromosome maintenance (MCM) complexes are represented on the left-hand side corner. Cell cycle stages are indicated at the bottom. **(b)** KEGG pathway for DNA replication. Left hand-side: schematic representation of DNA replication. Right hand-side: molecular complexes involved in DNA replication. Figures were generated using Partek pathways software. Rounded rectangles depict intersections with other pathways. Rectangles represent gene products acting in this pathway. Group of merged rectangles represent protein complexes. Colour code as follows: black – mRNA levels were unaffected; red – downregulated; green – upregulated by ING1 KD. Arrows represent interactions between nodes: blunt arrows – inhibition; regular arrows – activation; dashed line – indirect link; +p – phosphorylation; -p – dephosphorylation; +u – ubiquitination.

To our knowledge only two other groups investigated the effect of total ING1 downregulation on cell proliferation. When all ING1 transcripts were knocked out in mice, the resulting animals displayed a significant reduction in body weight, although no significant differences in cell cycle progression were observed *in vitro* between knockout and wild-type cultured embryonic fibroblasts (Kichina et al., 2006). The other study, performed in a mouse mammary epithelial cell line, reported an increase in anchorage dependent growth upon ING1 KD, concomitant with a p53 dependent increase in cyclin B1 mRNA levels (Takahashi et al., 2002). We however noticed a 3.4-fold decrease in cyclin B1 expression upon ING1 KD. Similarly, we noticed significant downregulation of DTL, LMNB1, CCNE2 and KIFC1 expression and significant upregulation of GPNMB and SIAE expression, genes that were reported to show the same trend upon cell senescence induced by p33ING1b overexpression (Abad et al., 2011). Interestingly, all these genes showed opposite expression patterns upon WT p33ING1b and chromatin binding deficient p33ING1b overexpression (Abad et al., 2011), strongly suggesting that the ability to modulate chromatin binding is crucial for ING1's ability to modulate cell proliferation.

A synergistic role for ING1 isoforms in cell proliferation regulation has been previously proposed (Skowyra et al., 2001; Soliman et al., 2008). All three ING1 isoforms have the ability to modulate gene transcription (Vieyra et al., 2002a; Xin et al., 2004), however they were shown to have different impact on chromatin remodelling (Vieyra et al., 2002a). Therefore, the gene expression profiles would be expected to differ between simultaneous knockdown of all ING1 isoforms, and knockdown of only one isoform. Moreover, ING1 isoforms have differential abilities to modulate biological processes: whilst p33ING1b overexpression induces apoptosis in human skin fibroblasts, p47ING1a has no effect (Vieyra et al., 2002a); whilst both p33ING1b and p47ING1a overexpression can induce senescence, senescent fibroblasts display a decrease in p33ING1b and an increase in p47ING1a levels (Soliman et al., 2008). This could explain the apparent discrepancy between our results, suggestive of a G1/G0 cell cycle arrest upon ING1 KD,

and the studies showing increased cell proliferation upon ING1b KD (Coles et al., 2007; Garkavtsev et al., 1998), as we simultaneously knocked down all three isoforms of ING1 in MCF-7 cells.

A major methodological difference between our study and previous studies investigating the role of ING1 KD in cell proliferation, senescence or cell cycle progression (regardless of the isoform), is the method of choice for gene knockdown. Most studies used a retroviral approach for downregulating ING1 expression whilst we used siRNA and a lipid-based transfection reagent (Chapter 2.3.3). ING1 knockout mouse fibroblast were previously shown to exhibit slightly increased sensitivity to cytotoxic agents; application of some cytotoxic treatments (UVB, doxorubicin, taxol) slightly decreased the proportion of ING1 knockout cells in G2 when compared to WT cells treated under the same conditions. This effect was related to the cytotoxicity of the treatment, as untreated ING1 cells did not show any cell cycle progression abnormalities (Kichina et al., 2006). Moreover, the increased sensitivity to DNA damage induced by ING1 was associated with increased p21 mRNA levels (Ceruti et al., 2013), which is consistent with our results. Therefore, we cannot exclude the possibility that the effects seen on cell cycle progression following ING1 KD in our system might be due in part, to the response of ING1 KD cells to the cytotoxicity of the lipid-based transfection reagent used.

More experiments should be performed before any conclusion with regards to ING1 KD-mediated effects in cell proliferation and apoptosis in MCF-7 cells can be made. Firstly, the sample size for the apoptosis experiment was low and more repeats should be added and/or different experimental approaches should be additionally employed to investigate cell death. A similar flow cytometry method to the one used, but that can more confidently distinguish between apoptosis and necrosis, has been described (Pietkiewicz et al., 2015) and could be of use here. Cell cycle profiling should be assessed at different time points to provide a better indication of when the cell cycle is arrested and if the observed arrest can be reversed. Of help here could be the use of the

fluorescent ubiquitination-based cell cycle indicator (FUCCI) which allows for live assessment of cell cycle progression. The FUCCI system uses geminin and cdt1 reporters linked to fluorescent proteins labelling cell nuclei red (G1), green (S/G2/M) or yellow (S) depending of the stage of the cell cycle. Combined use of the FUCCI reporter and immunohistochemical techniques would allow for exact identification of the cell cycle stage, as the FUCCI reporter does not label G0 and late M (Sakaue-Sawano et al., 2008; Xouri et al., 2004). Additionally, metabolic assays should also be performed at several time points. Furthermore, as mentioned above, the methodology used to perform the knockdown might have an impact on the results and therefore experiments should be repeated using a different approach, for instance using retroviral particles as transduction vehicles.

Chapter 6 – Discussion

In the 1970's, cancer research was revolutionised by the finding that cancer is a genetic disease (Knudson, 1973). A decade later, the field was revolutionised again by the discovery that epigenetics might play an equally important role in tumour progression (Feinberg and Vogelstein, 1983). Although shadowed by cancer genetics for a long time, cancer epigenetic events were increasingly studied in the past couple of decades. It is now believed that driver mutations often happen in genes coding for epigenetic regulators (Dawson and Kouzarides, 2012). Moreover, many oncogenes and TSGs encode for transcription factors. Under normal physiological conditions, transcription factors control gene expression patterns. Therefore, aberrant expression or activity can lead to the simultaneous deregulation of multiple signalling pathways. It is as such believed that only a number of oncogenes and TSGs are actually indispensable in cancer, despite the increased heterogenicity and genomic instability of tumours (Libermann and Zerbini, 2006). The most feared ability that cancer cells develop, is the acquisition of invasive and metastatic properties and several transcription factors have been shown to be able to control EMT (Tania et al., 2014). Therefore, transcription factors in general and transcription factors that affect EMT in particular, are desirable points of therapeutic interference in cancer, with reactivation of TSGs being of particular interest (Libermann and Zerbini, 2006; Tania et al., 2014). However, before being able to design specific therapies we must understand how these transcription factors act and we must be aware of all implications associated with deregulating such transcription factor expression.

6.1 CG7379/ING1 as tumour suppressors

ING1 has long been established as a type II TSG due to its ability to modulate gene transcription, cell proliferation and apoptosis (Soliman and Riabowol, 2007). More recent studies have highlighted a potential role for ING1 in cell invasion and metastasis (Guo et al., 2011; Jiang et al., 2018; Thakur et al., 2014).

CG7379 is largely uncharacterised in *Drosophila*; its role was only briefly investigated as a component of the Sin3A complex. That study reported that CG7379 is required for viability in flies and that CG7379 is likely to positively regulate cell proliferation in flies, disputing its putative function as a tumour suppressor (Barnes et al., 2018). A genetic screen for tumour progression modulators performed in our laboratory has identified CG7379 as a modulator of individual cell invasion and cytoskeleton dynamics (Canales Coutiño et al., 2020). By taking a loss-of-function approach to further characterise CG7379 involvement in tumorigenesis, we proved that CG7379 acts as a tumour suppressor in flies despite the fact that it reduces the amount of cancer-like tissue. We have shown that CG7379 KD confers apoptosis resistance to cells, modulates cytoskeleton dynamics and leads to massive disruptions in cell-cell junction architecture, culminating in increased invasion and metastatic spreading. These phenotypes have not been previously linked to CG7379, but are similar with phenotypes induced by Sin3a KD (Das et al., 2013), protein that CG7379 forms complexes with (Barnes et al., 2018). Sin3a KD in *Drosophila* wing disc led to a significant increase in cell delamination and reduced levels of E-cadherin, Armadillo and Discs large at cell-cell interface, phenotypes that were attributed in part to the ability of Sin3a to regulate actin remodelling factors at a transcriptional level (Das et al., 2013). We also show that CG7379 KD further cooperates with a loss-of-function mutation for the *lgl* polarity gene, further increasing the invasive potential of tumour-like cells. Furthermore, clones lose their relatively normal epithelial organisation displaying multi-layered structures.

ING1, the CG7379 human orthologue, was repeatedly reported to impair cell transformation (Garkavtsev et al., 1996). ING1 modulates cell proliferation by regulating cellular response to DNA damage, senescence and apoptosis. ING1 has been shown to act in cell cycle progression at both the G0/G1 and G2/M transition boundaries (Guérillon et al., 2013; Soliman and Riabowol, 2007). More recently, loss of ING1 expression has been proposed to impact on the cellular ability to invade and metastasize. However, most of these studies are correlational and implicate ING1 in invasion by being targeted

by micro RNAs that have the ability to regulate cell invasion (Guo et al., 2011; Han et al., 2015; Jiang et al., 2018). To our knowledge, only three studies directly investigated the role of ING1 in invasion (Cheung and Li, 2002; Jiang et al., 2018; Thakur et al., 2014), and they focused on the anti-invasive effect of ING1b overexpression. One of these studies however, knocked down ING1 expression in MDA-MB-231 cells and noticed an increase in migration and invasion (Thakur et al., 2014). The mechanisms through which ING1 modulates invasive cell behaviour are however unclear. These studies propose that ING1 modulates metalloproteinase expression whereby MMP-2 and MMP-9 were downregulated by ING1b overexpression (Jiang et al., 2018), possibly by acting on the PDGF/PDGFR pathway (PDGFA and PDGFRB were upregulated upon ING1 KD) (Seo et al., 2013; Thakur et al., 2014).

We propose a different mechanism of action whereby ING1 regulates invasion by modulating cytoskeleton dynamics. ING1 KD in MCF-7 cells disrupted E-cadherin distribution and dysregulated the expression of several genes involved in cytoskeleton remodelling, yet we did not detect significant changes in MMP or PDGF/PDGFR mRNA expression. Furthermore, ERBB2 (a growth factor receptor) and RhoC expression levels were increased following ING1 KD, supporting a role for ING1 in cytoskeleton remodelling. Prolonged ERBB2 signalling from a homodimer of the receptor has been shown to induce EMT *in vitro* (Jenndahl et al., 2005). E-cadherin overexpression could not impair this ERBB2 induced EMT (Nilsson et al., 2014), much like how *shg* (the gene coding for E-cadherin in *Drosophila*) overexpression could not rescue the CG7379 KD-induced invasion in our fly model. When overexpressed in cells isolated after EMT, E-cadherin adhesiveness to the cytoskeleton was compromised as suggested by lipid membrane extraction experiments (Nilsson et al., 2014). Another study shows that ERBB2 signalling can induce destabilisation of the cortical cytoskeleton (Hedjazifar et al., 2005). Such cytoskeletal rearrangements could explain decreased cell-cell adhesion despite E-cadherin overexpression. The initial actin depolymerisation events of the cortical cytoskeleton destabilisation appeared to be Rho-independent (Hedjazifar et al.,

2005). In contrast, RhoC has been shown to have higher affinity for ROCK than RhoA and is thus more potent in inducing cytoskeleton contractions (Sahai and Marshall, 2002), which in turn can alter AJ architecture (Sahai and Marshall, 2002). Rho involvement in ING1 KD driven invasion would be consistent with the rounded morphology observed in pre-invasive and invasive cells in *Drosophila* following CG7379 KD.

In epithelial cells, the distribution of TJ proteins at the cell-cell interface appears to be dependent of the level of actin depolymerisation (Stevenson and Begg, 1994). Moreover, actin depolymerisation was shown to induce E-cadherin expression in several metastatic cancer cell lines, including MDA-MB-231 and U87. Conversely, actin stabilisation in MCF-7 cells reduced E-cadherin levels (Shankar and Nabi, 2015). The same study proposes that migration and expression of EMT/MET markers might be modulated differently by cytoskeleton dynamics, as actin depolymerisation inhibited migration of normal fibroblasts without changing the expression of mesenchymal/epithelial markers (Shankar and Nabi, 2015). This might explain the increased invasion following ING1 KD noted in previous experiments performed in our laboratory in MDA-MB-231 and U87 cells, malignant breast and brain cancer cells respectively, that do not express E-cadherin (Cornhill, 2017). Conversely, although AJ architecture was clearly disrupted in both *Drosophila* and MCF-7 cells, ING1 KD might employ additional strategies to increase cell invasion. It is likely that ING1 has the ability to modulate cell-matrix adhesion, as expression of several integrins and integrin modulators was affected following ING1KD in MCF-7 cells. Moreover, ERBB2 was shown to supress matrix adhesion by inactivating integrin β1 and further cooperate with Rho to delay stress fibre formation (Hedjazifar et al., 2005).

Using the fly model, we show that most CG7379 KD invasive cells do not delaminate in response to apoptosis, nor do they undergo anoikis following detachment. Apoptosis assessment following ING1 KD in MCF-7 cells showed a decreasing trend, although not significant. It is very likely that the lack of statistical significance is due to a reduced sample size, as data from the transcriptomics experiment supports a role for ING1 KD in

apoptosis resistance. MCF-7 cells do not express caspase 3, but they undergo a form of apoptosis that is morphologically indistinguishable from the classic caspase 3-dependent apoptosis. The main difference is that the caspase cascade governing the intrinsic apoptotic machinery in MCF-7 cells relies on caspases 9, 7 and 6 (caspase 9 activation, in response to cytochrome c release, activates caspase 7 which subsequently activate caspase 6) (D'Mello et al., 2000). The apoptotic signal transduction through the caspase cascade is likely to be disrupted following ING1 KD, as caspase 7 mRNA levels are significantly downregulated. Additionally, mRNA expression of CASP8A2 (flash) was also decreased following ING1 KD. Flash is required for pro-caspase 8 activation in response to external apoptotic signals (Imai et al., 1999; Morgan et al., 2004). Furthermore, CXCL12 (stromal cell-derived factor 1) levels were also downregulated in consequence to ING1 KD, suggesting that ING1 expression might positively regulate anoikis, similar to CG7379 in our *Drosophila* experiments. CXCL12 overexpression has been found to promote anoikis in a colorectal cancer model by utilising the intrinsic apoptotic machinery (Drury et al., 2010). It is however crucial that further analysis of apoptosis is performed in this system in order to test our speculations with regards to the effect that ING1 KD has on MCF-7 cell survival.

Several cell cycle regulators, such as CDK1, Cyclin A2 and cyclin B1, which were downregulated following ING1 KD, are overexpressed in cancer. However, reduced expression levels were found to correlate with poor survival, increased invasion and/or increased metastasis (Arsic et al., 2012; Bendris et al., 2012; Korenaga et al., 2002; Zhang et al., 2011). CDK1 KD has been shown to promote EZH2 phosphorylation, which in turn promotes cancer cell migration and invasion in MCF-7 cells (Wei et al., 2011). Cyclin B1 silencing was found to increase invasion by downregulating E-cadherin. Similarly, depletion of cyclin A2 in fibroblasts was sufficient to increase cell motility in 2D and 3D assays. It has been postulated that cyclin A2 modulates cytoskeleton dynamics through downregulation of the RhoA-ROCK pathway and upregulation of RhoC activity (Arsic et al., 2012; Bendris et al., 2012).

It was proposed that proliferation and invasion are mutually exclusive (Bhandari et al., 2015; Waldman et al., 2013), as the cytoskeleton rearrangements required for either phenotype are incompatible (Qian et al., 2013). Using a live fluorescent reporter of cell cycle kinetics, Yano et. all showed that most invasive cancer cells are in the G1 stage of cell cycle progression. Very few invasive cells could replicate within this reported model and invasion was abrogated when such cells were actively dividing, with invasion trajectory only resumed once cell division had been completed (Yano et al., 2014). An *in vivo* study of cell invasion in *C. elegans* also highlighted a requirement for cells to arrest in G1 prior to the acquisition of invasive properties. This study suggests that the G1 arrest might be needed in order to induce a change in the transcriptional programme which will promote acquisition of invasive properties (Matus et al., 2015). The G1 arrest in the context of cell invasion was attributed to high levels of p21 or p15 and low levels of cyclin E, cyclin D1 or cyclin D2 (Hu et al., 2008; Mejlvang et al., 2007; Qian et al., 2013; Vega et al., 2004). Indeed, ING1 KD induced upregulation of p21 mRNA and downregulation of cyclin D1, D3 and E2 mRNA levels. Furthermore, several DEG selected by us as potential drivers of EMT following ING1 KD are established modulators of cell cycle progression (Figure 4.13b, Table 4.1). However, several other studies support a positive correlation between cell proliferation and invasion (Dissanayake et al., 2003; Haass et al., 2014; Kagawa et al., 2013; Tumuluri et al., 2004). Mejlvang et al. propose that proliferative and invasive behaviours can be uncoupled and that the association between G0/G1 cell cycle arrest and increased invasion is not a prerequisite for EMT in general, but is rather a characteristic of the mechanism by which EMT was induced (Mejlvang et al., 2007).

6.2 ING1 modulation of gene expression is associated with hallmarks of cancer

In our study, ING1 proved to be responsible for modulating the expression of 919 genes. We noticed that some of those genes were encoding transcription factors (e.g. FOXM1, E2F1, E2F2, E2F7, E2F8, KDM5B, RBL1), modulators of transcription factor activity (e.g. HIPK3) and proteins that modulate mRNA levels (AGO1), suggesting that ING1 modulates a cascade of genome-wide transcriptional events. For instance, KDM5B can modulate E2F2 and E2F1 expression (Hayami et al., 2010), which in turn can modulate the expression of several other genes, including CCNA2, CCNB1, CDC25A, RBL1, FEN1, CASP7, PCNA, MCM3, MCM5, MCM6, CDC6, RAD51, UNG, FANCA, FANCC (Ren et al., 2002; Tategu et al., 2007). All these genes were found to be differentially expressed in response to ING1 KD. One methodological limitation of our study is that it does not identify the genes directly affected by the ING1 KD from the 919 DEG. Moreover, RBL1 can negatively regulate the expression of E2F1, creating a loop of transcriptional activity regulation (O'Connor et al., 2001).

Cheng *et al.* found that the ability of ING1 to repress gene expression might be limited, as the ability of the Sin3A complex to bind chromatin upon ING1 loss of function, can be partially accounted for by E2F4, another chromatin associated protein (Cheng et al., 2014). This is reflected in our study, as two thirds of the DEG following ING1 KD were downregulated, suggesting a major function for ING1 in activating gene expression.

GO enrichment analysis of ING1 KD differentially expressed genes (Appendix 3) reinforced the common belief that cell cycle progression, DNA replication and DNA repair mechanisms are controlled by ING1 at transcription level. Additionally, the p53 pathway was significantly affected by ING1 KD. This is in line with the previously described ability of ING1 to modulate proliferation, apoptosis and cell cycle progression, in part by interacting with p53 (Guérillon et al., 2013; Thalappilly et al., 2011). We here propose

that the ability of ING1 to modulate cell invasion is also dependent on an ability to modulate transcription. Our analysis of DEG following ING1 KD revealed that ING1 might also be able to modulate cytoskeleton dynamics and cell shape, which is likely to be responsible for the invasive behaviour displayed by the cells bearing ING1 KD.

We believe that all processes controlled by ING1 expression are highly interconnected and dependent on each other (Figure 6.1). We propose a model by which, under normal conditions, ING1 primarily regulates cell proliferation ensuring smooth transition through the cell cycle by modulating DNA damage repair and apoptosis at a transcription level. If insufficiently expressed however, ING1 triggers a transcriptional switch causing cytoskeleton rearrangements that promote cell invasion over proliferation.

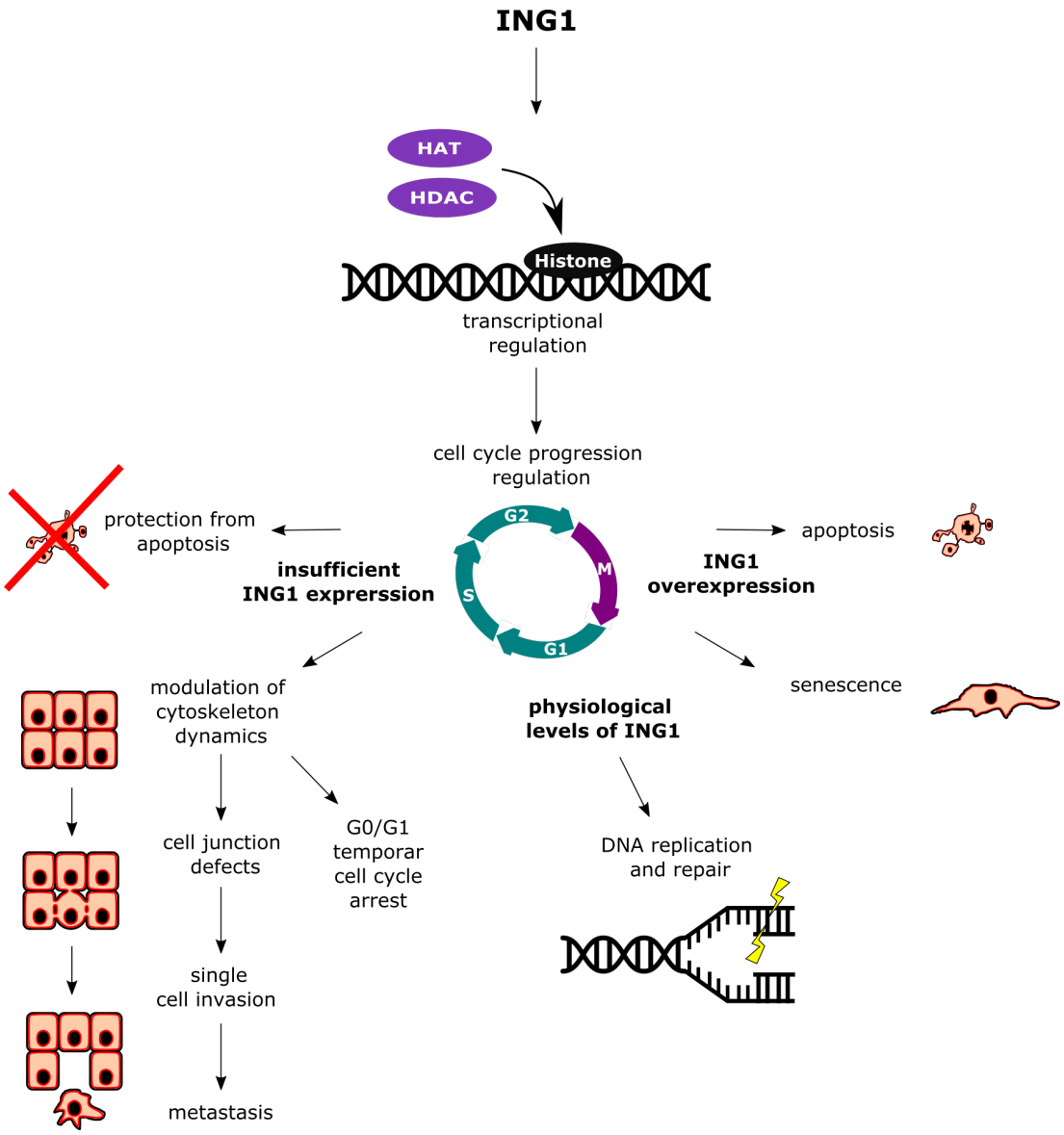


Figure 6.1 Proposed model for the role of ING1 as tumour suppressor

ING1 is considered a type II tumour suppressor gene. We propose that under physiological conditions, ING1 and its fly orthologue (CG7379) regulate gene transcription and are functionally associated with DNA damage monitoring and ensuring correct DNA replication. When overexpressed, ING1 was previously shown to induce apoptosis and G0/G1 cell cycle arrest, often associated with cell senescence. Here we show that ING1 knockdown can also induce accumulation of cells in G0/G1, concomitant with decreased cell-cell adhesion and increased cell invasion. Additionally, when knocked down, CG7379 also reduced apoptosis.

According to GAD, the diseases associated with the genes that were differentially expressed following ING1 KD in our study (Appendix 3), are predominantly cancers, including both solid tumours (breast, bladder, ovarian, cervical, lung, pancreatic, colorectal, neck and head) and hematologic neoplasms, reinforcing the common theme in the literature that ING1 acts as a tumour suppressor (Ahmed et al., 2001; Garkavtsev et al., 1996; Guérillon et al., 2013; Thakur et al., 2014; Ythier et al., 2008). Additionally, our data suggests that ING1 might play a role in systemic lupus erythematosus and Fanconi anaemia, as the pathways characteristic to these two diseases were significantly enriched following ING1 KD. Indeed, ING1 has been found to be differentially methylated both in Fanconi anaemia and systemic lupus erythematosus patients in comparison to healthy individuals (Belo et al., 2015, Jeffries et al., 2011).

CG7379 has been identified as a component of the SIN3A protein complex (Spain et al., 2010) and as a p53 interactor (Lunardi et al., 2010). CG7379 was predicted to be a target of Brahma and Earmuff, transcription factors involved in chromatin remodelling and mRNA transcription respectively (Koe et al., 2014). This together with the fact that CG7379 displays a highly conserved plant homeodomain (PHD) motif (He et al., 2004) and CG7379 KD has very similar phenotypic effects as ING1 KD, indicates that CG7379 might also regulate proliferation, apoptosis and invasion by modulating gene expression. In support to his hypothesis, when comparing the data from the ING1 KD microarray experiment with data from the screen we noticed that 16% of the genes that had a significant effect on invasion, multilayering and/or cell body rounding in the screen have a corresponded homologue gene in the list of DEG following ING1 KD (asp, RBf1, CG9572, RhoGAP19D, CG5245, CG11180, Sdr, su(Hw), Sema-2a, CG6867, Rbf2, Ac78C, p120ctn, CG5245, Exn, CG6867, dhc62B, klu, ih). In the screen, these genes have been associated with apex and protrusion defects, decreased clonal tissue and increased cell body rounding, multilayering and/or invasion (Canales Coutiño et al., 2020).

6.3 Future perspectives

Studies designed to investigate ING1 involvement in the complete disease spectrum from tumour initiation to metastatic spreading are lacking. To completely characterise the role of ING1 in tumour development, both acute gain and loss-of-function should be studied in the same experimental system/model with respect to apoptosis, cell proliferation, invasion and metastasis, and these phenotypes should be assessed under the umbrella of transcription regulation. Therefore, we consider that overexpression of CG7379 in *Drosophila* nota (in a similar manner to how the knockdown was performed) would be extremely beneficial for a better understanding of how CG7379 acts to protect epithelial tissue against malignancy. Furthermore, phenotypes induced by CG7379 KD and overexpression should also be investigated during embryogenesis, as CG7379 appears to be required for normal *Drosophila* development (Barnes et al., 2018).

In our *Drosophila* experiments we show not only that AJ and TJ architecture was compromised by CG7379 KD, but that protein levels of several junctional components were decreased precisely at cell-cell interfaces. We did not test for overall protein levels, and therefore we cannot exclude the possibility that these proteins are expressed at normal levels, but do not localise at cell-cell junctions as expected, which would suggest an impairment to the endocytic/trafficking machinery. Results from the transcriptomics experiment support this hypothesis, as ING1 KD induced a 2.4-fold upregulation of STON2 expression, a component of the endocytic machinery. STON2 overexpression was shown to perturb AP-2 localisation to the cell membrane and to inhibit internalisation of several endocytic receptors (Martina et al., 2001). We hypothesise that the disruption in AJ architecture triggered by ING1 KD might be a consequence of defective E-cadherin turnover, as reduced E-cadherin levels at AJ could account for impaired localisation of all the other investigated proteins. In order to test this hypothesis, E-cadherin turnover could be investigated by ubiquitously expressing E-cadherin fluorescent constructs and measuring E-cadherin recovery time at AJ after photobleaching (FRAP assays) within and

outside the clonal tissue. Three E-cadherin fluorescent constructs are available: tomato–E-cadherin, mCherry–E-cadherin and E-cadherin–GFP. Preliminary experiments performed indicate that the fluorescence exhibited by the mCherry and tomato constructs is not strong enough for the FRAP assays to be carried out. The tumour induction system we use is based on Moe:GFP labelling whose cellular localisation and fluorescence emission overlaps with that of Ubi-shg:GFP, and therefore the two constructs cannot be utilised together. The first step to assess E-cadherin turnover with minimal changes to the design of our system would have to be the establishment of a UAS-Moe:mCherry (Millard and Martin, 2008) – FRT40A recombination on the 2nd chromosome that could be used to induce Moe:RFP labelled clones.

Whilst it is clear from our study that, similarly to CG7379, ING1 has the ability to control cell-cell adhesion, we did not manage to elucidate the exact mechanism employed. From the transcriptomics data, we anticipate that ING1 acts on several pathways simultaneously. This could be further investigated by assessing the impact on cell invasion of double ING1-ERBB2 KD. Furthermore, pull-down activation assays followed by western blot using specific antibodies for RhoA and RhoC could be conducted following ING1 KD, to asses activation of the small GTPases and determine if the balance is indeed shifted towards RhoC as anticipated.

It would also be interesting to explore alternative mechanisms employed by ING1 KD to induce cell motility. Given that our data suggests a potential role for ING1 in integrin function modulation, a good starting point would be visualization of F-actin by phalloidin staining to assess stress fibre morphology.

CG7379 KD in *Drosophila* culminated with induction of brain metastasis. Fruit flies are not the best model for the study of metastasis as they possess an open circulatory system, so processes such as angiogenesis, intravasation and extravasation are not required for secondary tumour growth. However, evidence from *Drosophila* justifies the

use of larger organisms to study this process, especially since ING1 has been implicated in angiogenesis regulation in glioblastoma (Tallen et al., 2009). The design of an appropriate model, to determine if ING1 KD alone is sufficient to induce metastasis, will be a challenge. For this, non-tumorigenic epithelial mammary gland cells (e.g. MCF10A) stably transduced to either simultaneously overexpress all ING1 isoforms, or express ING1 anti-sense constructs targeting all ING1 isoforms, should be generated. Injection of these cells into the mammary fat pads of mice would allow for assessment of tumour development. If tumours develop, this system would also allow for characterisation of tumour growth. For metastasis studies, MCF710A cells bearing ING1 KD and tagged with luciferase using the MSCV Luciferase PGK-hygromycin (Addgene) retroviral vector could be inoculated in mice by intra-cardiac injection. Metastases could then be monitored by bioluminescence imaging. Highly metastatic MDA-MB231-luc2 cells could be used as a positive control (Wang et al., 2012).

6.4 Conclusions

Cancer research has greatly progressed over the past few decades, but it still faces several challenges due to the overwhelming complexity of the disease. The research presented here contributes towards providing a better understanding of tumour progression, by investigating a novel role for the ING1 tumour suppressor gene as a modulator of single cell invasion and by aiming to integrate this novel role with the canonical tumour suppressor functions previously described for this gene. The present work provides evidence that decreased levels of ING1, increase the invasive potential of cells by affecting cell junction and cell adhesion integrity, potentially by modulating cytoskeleton dynamics. We also propose that ING1 acts as a master regulator of several cancer-related biological processes by modulating genome-wide gene transcription. Moreover, the mechanism of action of ING1 seems to have been, at least in part, evolutionarily conserved, given that cell proliferation was negatively affected and cell invasion was significantly increased in both *Drosophila* and human breast cancer MCF-7

cells as a consequence of CG7379 and ING1 KD respectively. Overall, the research presented in this study might be of relevance for clinical applications as it highlights the possibility of addressing several aspects of tumour progression by modulating the expression of only one gene. It is hoped that future research will further elucidate the molecular mechanism behind coupling/decoupling cell proliferation and invasion and potential additional molecular mechanisms governed by ING1, with the distant aim of clinical translation and improvement of public health.

Bibliography

ABAD, M., MORENO, A., PALACIOS, A., NARITA, M., BLANCO, F., MORENO-BUENO, G., NARITA, M. & PALMERO, I. 2011. The tumor suppressor ING1 contributes to epigenetic control of cellular senescence. *Aging Cell,* 10**,** 158-171.

ABE, K. & TAKEICHI, M. 2008. EPLIN mediates linkage of the cadherin–catenin complex to F-actin and stabilizes the circumferential actin belt. *Proceedings of the National Academy of Sciences,* 105**,** 13-19.

ADAMS, G. E., CHANDRU, A. & COWLEY, S. M. 2018. Co-repressor, co-activator and general transcription factor: the many faces of the Sin3 histone deacetylase (HDAC) complex. *Biochemical Journal,* 475**,** 3921-3932.

ADAMS, M. D., CELNIKER, S. E., HOLT, R. A., EVANS, C. A., GOCAYNE, J. D., AMANATIDES, P. G., SCHERER, S. E., LI, P. W., HOSKINS, R. A., GALLE, R. F., GEORGE, R. A., LEWIS, S. E., RICHARDS, S., ASHBURNER, M., HENDERSON, S. N., SUTTON, G. G., WORTMAN, J. R., YANDELL, M. D., ZHANG, Q., CHEN, L. X., BRANDON, R. C., ROGERS, Y.-H. C., BLAZEJ, R. G., CHAMPE, M., PFEIFFER, B. D., WAN, K. H., DOYLE, C., BAXTER, E. G., HELT, G., NELSON, C. R., GABOR, G. L., MIKLOS, ABRIL, J. F., AGBAYANI, A., AN, H.-J., ANDREWS-PFANNKOCH, C., BALDWIN, D., BALLEW, R. M., BASU, A., BAXENDALE, J., BAYRAKTAROGLU, L., BEASLEY, E. M., BEESON, K. Y., BENOS, P. V., BERMAN, B. P., BHANDARI, D., BOLSHAKOV, S., BORKOVA, D., BOTCHAN, M. R., BOUCK, J., BROKSTEIN, P., BROTTIER, P., BURTIS, K. C., BUSAM, D. A., BUTLER, H., CADIEU, E., CENTER, A., CHANDRA, I., CHERRY, J. M., CAWLEY, S., DAHLKE, C., DAVENPORT, L. B., DAVIES, P., PABLOS, B. D., DELCHER, A., DENG, Z., MAYS, A. D., DEW, I., DIETZ, S. M., DODSON, K., DOUP, L. E., DOWNES, M., DUGAN-ROCHA, S., DUNKOV, B. C., DUNN, P., DURBIN, K. J., EVANGELISTA, C. C., FERRAZ, C., FERRIERA, S., FLEISCHMANN, W., FOSLER, C., GABRIELIAN, A. E., GARG, N. S., GELBART, W. M., GLASSER, K., GLODEK, A., GONG, F., GORRELL, J. H., GU, Z., GUAN, P., HARRIS, M., HARRIS, N. L., HARVEY, D., HEIMAN, T. J., HERNANDEZ, J. R., HOUCK, J., HOSTIN, D., HOUSTON, K. A., HOWLAND, T. J., WEI, M.-H., et al. 2000. The Genome Sequence of *Drosophila melanogaster*. *Science,* 287**,** 2185.

AGUILAR-ARAGON, M., ELBEDIWY, A., FOGLIZZO, V., FLETCHER, G. C., LI, V. S. W. & THOMPSON, B. J. 2018. Pak1 Kinase Maintains Apical Membrane Identity in Epithelia. *Cell Reports,* 22**,** 1639-1646.

AHMED, I. A. M., NOUMAN, G. S., LUNEC, J., KELLY, S. B., ANDERSON, J. J. & ANGUS, B. 2001. Expression of p33/ING1 gene products in colorectal cancer and its correlation with survival. *Gastroenterology,* 120**,** A300.

ALMAMI, A., HEGAZY, S. A., NABBI, A., ALSHALALFA, M., SALMAN, A., ABOU-OUF, H., RIABOWOL, K. & BISMAR, T. A. 2016. ING3 is associated with increased cell invasion and lethal outcome in ERG-negative prostate cancer patients. *Tumor Biology,* 37**,** 9731-9738.

ANASTASIADIS, P. Z. 2007. p120-ctn: A nexus for contextual signaling via Rho GTPases. *Biochimica et Biophysica Acta (BBA) - Molecular Cell Research,* 1773**,** 34-46.

ANDRADE, D. & ROSENBLATT, J. 2011. Apoptotic regulation of epithelial cellular extrusion. *Apoptosis,* 16**,** 491-501.

ARSIC, N., BENDRIS, N., PETER, M., BEGON-PESCIA, C., REBOUISSOU, C., GADÉA, G., BOUQUIER, N., BIBEAU, F., LEMMERS, B. & BLANCHARD, J. M. 2012. A novel function for Cyclin A2: Control of cell invasion via RhoA signaling. *Journal of Cell Biology,* 196**,** 147-162.

ARTERO, R. D., AKAM, M. & PÉREZ-ALONSO, M. 1992. Oligonucleotide probes detect splicing variants in situ in Drosophila embryos. *Nucleic Acids Research,* 20**,** 5687-5690.

ARVELO, F., SOJO, F. & COTTE, C. 2016. Cancer and the metastatic substrate. *Ecancermedicalscience,* 10**,** 701-701.

ASSÉMAT, E., BAZELLIÈRES, E., PALLESI-POCACHARD, E., LE BIVIC, A. & MASSEY-HARROCHE, D. 2008. Polarity complex proteins. *Biochimica et Biophysica Acta (BBA) - Biomembranes,* 1778**,** 614-630.

ASURI, S., YAN, J., PARANAVITANA, N. C. & QUILLIAM, L. A. 2008. E-cadherin dis-engagement activates the Rap1 GTPase. *Journal of Cellular Biochemistry,* 105**,** 1027-1037.

ATTRILL, H., FALLS, K., GOODMAN, J. L., MILLBURN, G. H., ANTONAZZO, G., REY, A. J., MARYGOLD, S. J. & CONSORTIUM, T. F. 2015. FlyBase: establishing a Gene Group resource for Drosophila melanogaster. *Nucleic Acids Research,* 44**,** 786-792.

BALDA, M. S. & MATTER, K. 2008. Tight junctions at a glance. *Journal of cell science,* 121**,** 3677-3682.

BALDA, M. S. & MATTER, K. 2009. Tight junctions and the regulation of gene expression. *Biochimica Et Biophysica Acta (BBA)-Biomembranes,* 1788**,** 761-767.

BALDA, M. S. & MATTER, K. 2016. Tight junctions as regulators of tissue remodelling. *Current Opinion in Cell Biology,* 42**,** 94-101.

BAMODU, O. A., HUANG, W.-C., LEE, W.-H., WU, A., WANG, L. S., HSIAO, M., YEH, C.-T. & CHAO, T.-Y. 2016. Aberrant KDM5B expression promotes aggressive breast cancer through MALAT1 overexpression and downregulation of hsa-miR-448. *BMC cancer,* 16**,** 160.

BARANWAL, S. & ALAHARI, S. K. 2009. Molecular mechanisms controlling E-cadherin expression in breast cancer. *Biochemical and Biophysical Research Communications,* 384**,** 6-11.

BARNES, V. L., LAITY, K. A., PILECKI, M. & PILE, L. A. 2018. Systematic Analysis of SIN3 Histone Modifying Complex Components During Development. *Scientific Reports,* 8**,** 17048.

BAUER, H., ZWEIMUELLER-MAYER, J., STEINBACHER, P., LAMETSCHWANDTNER, A. & BAUER, H. 2010. The dual role of zonula occludens (ZO) proteins. *BioMed Research International,* 2010**,** 1-11.

BAUM, B. & GEORGIOU, M. 2011. Dynamics of adherens junctions in epithelial establishment, maintenance, and remodeling. *The Journal of cell biology,* 192**,** 907-917.

BAUMBACH, J., HUMMEL, P., BICKMEYER, I., KOWALCZYK, KATARZYNA M., FRANK, M., KNORR, K., HILDEBRANDT, A., RIEDEL, D., JÄCKLE, H. & KÜHNLEIN, RONALD P. 2014. A Drosophila In Vivo Screen Identifies Store-Operated Calcium Entry as a Key Regulator of Adiposity. *Cell Metabolism,* 19**,** 331-343.

BEAUCHER, M., GOODLIFFE, J., HERSPERGER, E., TRUNOVA, S., FRYDMAN, H. & SHEARN, A. 2007. Drosophila brain tumor metastases express both neuronal and glial cell type markers. *Developmental Biology,* 301**,** 287-297.

BENDRIS, N., ARSIC, N., LEMMERS, B. & BLANCHARD, J. M. 2012. Cyclin A2, Rho GTPases and EMT. *Small GTPases,* 3**,** 225-228.

BERGLIND, H., PAWITAN, Y., KATO, S., ISHIOKA, C. & SOUSSI, T. 2008. Analysis of p53 mutation status in human cancer cell lines: a paradigm for cell line cross-contamination. *Cancer Biology & Therapy,* 7**,** 699-708.

BHANDARI, D., LOPEZ-SANCHEZ, I., TO, A., LO, I. C., AZNAR, N., LEYME, A., GUPTA, V., NIESMAN, I., MADDOX, A. L., GARCIA-MARCOS, M., FARQUHAR, M. G. & GHOSH, P. 2015. Cyclin-dependent kinase 5 activates guanine nucleotide exchange factor GIV/Girdin to orchestrate migration–proliferation dichotomy. *Proceedings of the National Academy of Sciences,* 112**,** E4874.

BIENZ, M. & TREMML, G. 1988. Domain of Ultrabithorax expression in Drosophila visceral mesoderm from autoregulation and exclusion. *Nature,* 333**,** 576-578.

BILDER, D. & PERRIMON, N. 2000. Localization of apical epithelial determinants by the basolateral PDZ protein Scribble. *Nature,* 403**,** 676-680.

BILDER, D., SCHOBER, M. & PERRIMON, N. 2003. Integrated activity of PDZ protein complexes regulates epithelial polarity. *Nature Cell Biology,* 5**,** 53-58.

BOETTNER, B. & VAN AELST, L. 2007. The Rap GTPase Activator Drosophila PDZ-GEF Regulates Cell Shape in Epithelial Migration and Morphogenesis. *Molecular and Cellular Biology,* 27**,** 7966.

BOSE, P., THAKUR, S. S., BROCKTON, N. T., KLIMOWICZ, A. C., KORNAGA, E., NAKONESHNY, S. C., RIABOWOL, K. T. & DORT, J. C. 2014. Tumor cell apoptosis mediated by cytoplasmic ING1 is associated with improved survival in oral squamous cell carcinoma patients. *Oncotarget,* 5**,** 3210-3219.

BRAND, A. H. & PERRIMON, N. 1993. Targeted gene expression as a means of altering cell fates and generating dominant phenotypes. *Development,* 118**,** 401.

BRUNER, H. C. & DERKSEN, P. W. C. S. H. P. I. B. 2018. Loss of E-cadherin-dependent cell–cell adhesion and the development and progression of cancer. *Cold Spring Harbor perspectives in biology,* 10**,** a029330.

BUSS, F., SPUDICH, G. & KENDRICK-JONES, J. 2004. MYOSIN VI: Cellular Functions and Motor Properties. *Annual Review of Cell and Developmental Biology,* 20**,** 649-676.

CALLEJA, M., HERRANZ, H., ESTELLA, C., CASAL, J., LAWRENCE, P., SIMPSON, P. & MORATA, G. 2000. Generation of medial and lateral dorsal body domains by the pannier gene of Drosophila. *Development,* 127**,** 3971.

CAMPANALE, J. P., SUN, T. Y. & MONTELL, D. J. 2017. Development and dynamics of cell polarity at a glance. *Journal of Cell Science,* 130**,** 1201.

CAMPBELL, K., ROSSI, F., ADAMS, J., PITSIDIANAKI, I., BARRIGA, F. M., GARCIA-GERIQUE, L., BATLLE, E., CASANOVA, J. & CASALI, A. 2019.

Collective cell migration and metastases induced by an epithelial-to-mesenchymal transition in Drosophila intestinal tumors. *Nature Communications,* 10**,** 2311.

CAMPOS, E. I., MARTINKA, M., MITCHELL, D. L., DAI, D. L. & LI, G. 2004. Mutations of the ING1 tumor suppressor gene detected in human melanoma abrogate nucleotide excision repair. *International journal of oncology,* 25**,** 73-80.

CANALES COUTIÑO, B., CORNHILL, Z. E., COUTO, A., MACK, N. A., RUSU, A. D., NAGARAJAN, U., NGAN FAN, Y., HADJICHARALAMBOUS, M. R., CASTELLANOS URIBE, M., BURROWS, A., LOURDUSAMY, A., MAY, S. T., RAHMAN, R. & GEORGIOU, M. 2020. A genetic analysis of tumour progression in Drosophila identifies the cohesin complex as a suppressor of individual and collective cell invasion. *iScience*, 23(6), 101237.

CANALES COUTIÑO, B. I. 2019. *An in vivo loss of function genetic screen in Drosophila identifies novel roles for the Cohesin complex in single and collective cell invasion.* PhD, University of Nottingham.

CAO, F., MIAO, Y., XU, K. & LIU, P. 2015. Lethal (2) giant larvae: an indispensable regulator of cell polarity and cancer development. *International journal of biological sciences,* 11**,** 380-389.

CERUTI, J. M., OGARA, M. F., MENÉNDEZ, C., PALMERO, I. & CÁNEPA, E. T. 2013. Inhibitor of growth 1 (ING1) acts at early steps of multiple DNA repair pathways. *Molecular and Cellular Biochemistry,* 378**,** 117-126.

CHEN, C.-L., SCHROEDER, M. C., KANGO-SINGH, M., TAO, C. & HALDER, G. 2012. Tumor suppression by cell competition through regulation of the Hippo pathway. *Proceedings of the National Academy of Sciences,* 109**,** 484.

CHEN, J., ARONOW, B. J. & JEGGA, A. G. 2009. Disease candidate gene identification and prioritization using protein interaction networks. *BMC bioinformatics,* 10**,** 73.

CHEN, J., TRAN, U. M., RAJARAJACHOLAN, U., THALAPPILLY, S. & RIABOWOL, K. 2013. ING1b-inducible microRNA203 inhibits cell proliferation. *British Journal of Cancer,* 108**,** 1143-1148.

CHENG, J., BLUM, R., BOWMAN, C., HU, D., SHILATIFARD, A., SHEN, S. & DYNLACHT, BRIAN D. 2014. A Role for H3K4 Monomethylation in Gene Repression and Partitioning of Chromatin Readers. *Molecular Cell,* 53**,** 979-992.

CHEUNG, K. & LI, G. 2002. The tumour suppressor p33ING1 does not regulate migration and angiogenesis in melanoma cells. *International journal of oncology,* 21**,** 1361-1365.

CHRUSCICKI, A., MACDONALD, V. E., YOUNG, B. P., LOEWEN, C. J. R. & HOWE, L. J. 2010. Critical determinants for chromatin binding by Saccharomyces cerevisiae Yng1 exist outside of the plant homeodomain finger. *Genetics,* 185**,** 469-477.

CLARK, A. G. & VIGNJEVIC, D. M. 2015. Modes of cancer cell invasion and the role of the microenvironment. *Current Opinion in Cell Biology,* 36**,** 13-22.

CLAVIER, A., RINCHEVAL-ARNOLD, A., COLIN, J., MIGNOTTE, B. & GUÉNAL, I. 2016. Apoptosis in Drosophila: which role for mitochondria? *Apoptosis,* 21**,** 239-251.

COLES, A. H., LIANG, H., ZHU, Z., MARFELLA, C. G. A., KANG, J., IMBALZANO, A. N. & JONES, S. N. 2007. Deletion of p37Ing1 in Mice Reveals a p53-Independent Role for Ing1 in the Suppression of Cell Proliferation, Apoptosis, and Tumorigenesis. *Cancer Research,* 67**,** 2054.

CONACCI-SORRELL, M., ZHURINSKY, J. & BEN-ZE'EV, A. 2002. The cadherin-catenin adhesion system in signaling and cancer. *The Journal of clinical investigation,* 109**,** 987-991.

CONTI, M. A. & ADELSTEIN, R. S. 2008. Nonmuscle myosin II moves in new directions. *Journal of Cell Science,* 121**,** 11.

COOPER, G. M. 2000. The Eukaryotic Cell Cycle. *The Cell: A Molecular Approach 2nd edition.* Sunderland (MA).

CORDELIÉRES, F. P. Manual Tracking: a semi-automated tool to keep a track of movements in 2 and 3D. 2006.

CORDENONSI, M., D'ATRI, F., HAMMAR, E., PARRY, D. A., KENDRICK-JONES, J., SHORE, D. & CITI, S. 1999. Cingulin contains globular and coiled-coil domains and interacts with ZO-1, ZO-2, ZO-3, and myosin. *The Journal of cell biology,* 147**,** 1569-1582.

CORNHILL, Z. 2017. *An RNAi-mediated genetic screen identifies genes that promote tumour progression in a living epithelium.* PhD, University of Nottingham.

COUTO, A., MACK, N. A., FAVIA, L. & GEORGIOU, M. 2017. An apicobasal gradient of Rac activity determines protrusion form and position. *Nature Communications,* 8**,** 15385.

D'ATRI, F. & CITI, S. 2001. Cingulin interacts with F-actin in vitro. *FEBS letters,* 507**,** 21-24.

D'MELLO, S. R., KUAN, C.-Y., FLAVELL, R. A. & RAKIC, P. 2000. Caspase-3 is required for apoptosis-associated DNA fragmentation but not for cell death in neurons deprived of potassium. *Journal of Neuroscience Research,* 59**,** 24-31.

DAS, T. K., SANGODKAR, J., NEGRE, N., NARLA, G. & CAGAN, R. L. 2013. Sin3a acts through a multi-gene module to regulate invasion in Drosophila and human tumors. *Oncogene,* 32**,** 3184-3197.

DAWSON, MARK A. & KOUZARIDES, T. 2012. Cancer Epigenetics: From Mechanism to Therapy. *Cell,* 150**,** 12-27.

DE MADRID, B. H., GREENBERG, L. & HATINI, V. 2015. RhoGAP68F controls transport of adhesion proteins in Rab4 endosomes to modulate epithelial morphogenesis of Drosophila leg discs. *Developmental Biology,* 399**,** 283-295.

DEAKIN, N. O. & TURNER, C. E. 2010. Distinct roles for paxillin and Hic-5 in regulating breast cancer cell morphology, invasion, and metastasis. *Molecular Biology of the Cell,* 22**,** 327-341.

DIEPENBRUCK, M. & CHRISTOFORI, G. 2016. Epithelial–mesenchymal transition (EMT) and metastasis: yes, no, maybe? *Current Opinion in Cell Biology,* 43**,** 7-13.

DIETZL, G., CHEN, D., SCHNORRER, F., SU, K.-C., BARINOVA, Y., FELLNER, M., GASSER, B., KINSEY, K., OPPEL, S., SCHEIBLAUER, S., COUTO, A., MARRA, V., KELEMAN, K. & DICKSON, B. J. 2007. A genome-wide transgenic RNAi library for conditional gene inactivation in Drosophila. *Nature,* 448**,** 151-156.

DILLON, M. E., CAHN, L. R. Y. & HUEY, R. B. 2007. Life history consequences of temperature transients in <em>Drosophila melanogaster</em&gt. *Journal of Experimental Biology,* 210**,** 2897.

DISSANAYAKE, U., JOHNSON, N. W. & WARNAKULASURIYA, K. A. A. S. 2003. Comparison of cell proliferation in the centre and advancing fronts of oral squamous cell carcinomas using Ki-67 index. *Cell Proliferation,* 36**,** 255-264.

DRURY, L. J., WENDT, M. K. & DWINELL, M. B. 2010. CXCL12 chemokine expression and secretion regulates colorectal carcinoma cell anoikis through Bim-mediated intrinsic apoptosis. *PloS one,* 5**,** e12895-e12895.

DUPRE-CROCHET, S., FIGUEROA, A., HOGAN, C., FERBER, E. C., BIALUCHA, C. U., ADAMS, J., RICHARDSON, E. C. N. & FUJITA, Y. 2007. Casein Kinase 1 Is a Novel Negative Regulator of E-Cadherin-Based Cell-Cell Contacts. *Molecular and Cellular Biology,* 27**,** 3804.

EDWARDS, K. A., DEMSKY, M., MONTAGUE, R. A., WEYMOUTH, N. & KIEHART, D. P. 1997. GFP-Moesin Illuminates Actin Cytoskeleton Dynamics in Living Tissue and Demonstrates Cell Shape Changes during Morphogenesis inDrosophila. *Developmental Biology,* 191**,** 103-117.

ENOMOTO, M., SIOW, C. & IGAKI, T. 2018. Drosophila as a cancer model. *Drosophila Models for Human Diseases.* Springer.

ETOURNAY, R., ZWAENEPOEL, I., PERFETTINI, I., LEGRAIN, P., PETIT, C. & EL-AMRAOUI, A. 2007. Shroom2, a myosin-VIIa-and actin-binding protein, directly interacts with ZO-1 at tight junctions. *Journal of cell science,* 120**,** 2838-2850.

FANNING, A. S. 2001. Organization and Regulation of the Tight Junction by the Actin–Myosin Cytoskeleton. *Tight Junctions (Second Edition).* 265-284: CRC Press LLC.

FANNING, A. S., JAMESON, B. J., JESAITIS, L. A. & ANDERSON, J. M. 1998. The tight junction protein ZO-1 establishes a link between the transmembrane protein occludin and the actin cytoskeleton. *Journal of Biological Chemistry,* 273**,** 29745-29753.

FANNING, A. S., LITTLE, B. P., RAHNER, C., UTEPBERGENOV, D., WALTHER, Z. & ANDERSON, J. M. 2007. The unique-5 and-6 motifs of ZO-1 regulate tight junction strand localization and scaffolding properties. *Molecular biology of the cell,* 18**,** 721-731.

FARBER, E. 1984. The multistep nature of cancer development. *Cancer Res,* 44**,** 4217-4223.

FARGE, E. 2003. Mechanical induction of Twist in the Drosophila foregut/stomodeal primordium. *Current biology,* 13**,** 1365-1377.

FARQUHAR, M. G. & PALADE, G. E. 1963. Junctional complexes in various epithelia. *The Journal of cell biology,* 17**,** 375-412.

FEINBERG, A. P. & VOGELSTEIN, B. 1983. Hypomethylation distinguishes genes of some human cancers from their normal counterparts. *Nature,* 301**,** 89-92.

FILBY, A., PERUCHA, E., SUMMERS, H., REES, P., CHANA, P., HECK, S., LORD, G. M. & DAVIES, D. 2011. An imaging flow cytometric method for measuring cell division history and molecular symmetry during mitosis. *Cytometry Part A,* 79**,** 496-506.

FISTON-LAVIER, A.-S., SINGH, N. D., LIPATOV, M. & PETROV, D. A. 2010. Drosophila melanogaster recombination rate calculator. *Gene,* 463**,** 18-20.

FOK, S. Y. Y., RUBIN, J. S., PIXLEY, F., CONDEELIS, J., BRAET, F. & SOON, L. L. 2006. Rapid chemokinetic movement and the invasive potential of lung cancer cells; a functional molecular study. *BMC Cancer,* 6**,** 151.

FOUAD, Y. A. & AANEI, C. 2017. Revisiting the hallmarks of cancer. *American journal of cancer research,* 7**,** 1016-1036.
FUJITA, Y., KRAUSE, G., SCHEFFNER, M., ZECHNER, D., LEDDY, H. E. M., BEHRENS, J., SOMMER, T. & BIRCHMEIER, W. 2002. Hakai, a c-Cbl-like protein, ubiquitinates and induces endocytosis of the E-cadherin complex. *Nature Cell Biology,* 4**,** 222-231.
FURUSE, M., HIRASE, T., ITOH, M., NAGAFUCHI, A., YONEMURA, S., TSUKITA, S. & TSUKITA, S. 1993. Occludin: a novel integral membrane protein localizing at tight junctions. *The Journal of Cell Biology,* 123**,** 1777-1788.
FURUSE, M., SASAKI, H., FUJIMOTO, K. & TSUKITA, S. 1998. A Single Gene Product, Claudin-1 or -2, Reconstitutes Tight Junction Strands and Recruits Occludin in Fibroblasts. *The Journal of Cell Biology,* 143**,** 391-401.
GARATE, M., CAMPOS, E. I., BUSH, J. A., XIAO, H. & LI, G. 2007. Phosphorylation of the tumor suppressor p33ING1b at Ser-126 influences its protein stability and proliferation of melanoma cells. *The FASEB Journal,* 21**,** 3705-3716.
GARATE, M., WONG, R. P. C., CAMPOS, E. I., WANG, Y. & LI, G. 2008. NAD(P)H quinone oxidoreductase 1 inhibits the proteasomal degradation of the tumour suppressor p33ING1b. *EMBO reports,* 9**,** 576-581.
GARKAVTSEV, I., GRIGORIAN, I. A., OSSOVSKAYA, V. S., CHERNOV, M. V., CHUMAKOV, P. M. & GUDKOV, A. V. 1998. The candidate tumour suppressor p33ING1cooperates with p53 in cell growth control. *Nature,* 391**,** 295-298.
GARKAVTSEV, I., KAZAROV, A., GUDKOV, A. & RIABOWOL, K. 1996. Suppression of the novel growth inhibitor p33ING1 promotes neoplastic transformation. *Nature Genetics,* 14**,** 415-420.
GARKAVTSEV, I. & RIABOWOL, K. 1997. Extension of the replicative life span of human diploid fibroblasts by inhibition of the p33ING1 candidate tumor suppressor. *Molecular and Cellular Biology,* 17**,** 2014.
GAUDET, P., LIVSTONE, M. S., LEWIS, S. E. & THOMAS, P. D. 2011. Phylogenetic-based propagation of functional annotations within the Gene Ontology consortium. *Briefings in Bioinformatics,* 12**,** 449-462.
GEHNE, N., LAMIK, A., LEHMANN, M., HASELOFF, R. F., ANDJELKOVIC, A. V. & BLASIG, I. E. 2017. Cross-over endocytosis of claudins is mediated by interactions via their extracellular loops. *PloS one,* 12**,** e0182106.
GELBART, W. M. & EMMERT, D. B. 2013. Flybase high throughput expression pattern data. *Accessible online at http://flybase. org*.
GEORGAKILAS, A. G., MARTIN, O. A. & BONNER, W. M. 2017. p21: a two-faced genome guardian. *Trends in molecular medicine,* 23**,** 310-319.
GEORGIOU, M. & BAUM, B. 2010. Polarity proteins and Rho GTPases cooperate to spatially organise epithelial actin-based protrusions. *Journal of Cell Science,* 123**,** 1089.
GEORGIOU, M., MARINARI, E., BURDEN, J. & BAUM, B. 2008. Cdc42, Par6, and aPKC Regulate Arp2/3-Mediated Endocytosis to Control Local Adherens Junction Stability. *Current Biology,* 18**,** 1631-1638.
GIACINTI, C. & GIORDANO, A. 2006. RB and cell cycle progression. *Oncogene,* 25**,** 5220-5227.
GLADDEN, A. B., HEBERT, A. M., SCHNEEBERGER, E. E. & MCCLATCHEY, A. I. 2010. The NF2 Tumor Suppressor, Merlin, Regulates Epidermal Development

through the Establishment of a Junctional Polarity Complex. *Developmental Cell,* 19**,** 727-739.
GLIGORIJEVIC, B., BERGMAN, A. & CONDEELIS, J. 2014. Multiparametric classification links tumor microenvironments with tumor cell phenotype. *PLoS biology,* 12**,** e1001995-e1001995.
GÓMEZ-CUADRADO, L., TRACEY, N., MA, R., QIAN, B. & BRUNTON, V. G. 2017. Mouse models of metastasis: progress and prospects. *Disease Models & Mechanisms,* 10**,** 1061.
GOTTARDI, C. J., WONG, E. & GUMBINER, B. M. 2001. E-cadherin suppresses cellular transformation by inhibiting β-catenin signaling in an adhesion-independent manner. *The Journal of cell biology,* 153**,** 1049-1060.
GRATZ, S. J., CUMMINGS, A. M., NGUYEN, J. N., HAMM, D. C., DONOHUE, L. K., HARRISON, M. M., WILDONGER, J. & O'CONNOR-GILES, K. M. 2013. Genome Engineering of *Drosophila* with the CRISPR RNA-Guided Cas9 Nuclease. *Genetics,* 194**,** 1029.
GREENSPAN, R. J. 1997. *Fly pushing: the theory and practice of Drosophila genetics*.
GREIG, J. & BULGAKOVA, N. A. 2019. E-cadherin endocytosis is modulated by p120-catenin through the opposing actions of RhoA and Arf1. *bioRxiv*.
GREVENGOED, E. E. & PEIFER, M. 2003. Cytoskeletal connections: building strong cells in new ways. *Current Biology,* 13**,** R568-R570.
GRIFONI, D., SOLLAZZO, M., FONTANA, E., FROLDI, F. & PESSION, A. 2015. Multiple strategies of oxygen supply in Drosophila malignancies identify tracheogenesis as a novel cancer hallmark. *Scientific Reports,* 5**,** 9061.
GRZESCHIK, N. A., AMIN, N., SECOMBE, J., BRUMBY, A. M. & RICHARDSON, H. E. 2007. Abnormalities in cell proliferation and apico-basal cell polarity are separable in Drosophila lgl mutant clones in the developing eye. *Developmental Biology,* 311**,** 106-123.
GUÉRILLON, C., LARRIEU, D. & PEDEUX, R. 2013. ING1 and ING2: multifaceted tumor suppressor genes. *Cellular and molecular life sciences,* 70**,** 3753-3772.
GUMBINER, B., STEVENSON, B. & GRIMALDI, A. 1988. The role of the cell adhesion molecule uvomorulin in the formation and maintenance of the epithelial junctional complex. *The Journal of Cell Biology,* 107**,** 1575-1587.
GÜNZEL, D. & YU, A. S. L. 2013. Claudins and the Modulation of Tight Junction Permeability. *Physiological Reviews,* 93**,** 525-569.
GUO, X.-B., JING, C.-Q., LI, L.-P., ZHANG, L., SHI, Y.-L., WANG, J.-S., LIU, J.-L. & LI, C.-S. 2011. Down-regulation of miR-622 in gastric cancer promotes cellular invasion and tumor metastasis by targeting ING1 gene. *World journal of gastroenterology,* 17**,** 1895-1902.
HAASS, N. K., BEAUMONT, K. A., HILL, D. S., ANFOSSO, A., MRASS, P., MUNOZ, M. A., KINJYO, I. & WENINGER, W. 2014. Real-time cell cycle imaging during melanoma growth, invasion, and drug response. *Pigment Cell & Melanoma Research,* 27**,** 764-776.
HAKKINEN, K. M., HARUNAGA, J. S., DOYLE, A. D. & YAMADA, K. M. 2010. Direct Comparisons of the Morphology, Migration, Cell Adhesions, and Actin Cytoskeleton of Fibroblasts in Four Different Three-Dimensional Extracellular Matrices. *Tissue Engineering Part A,* 17**,** 713-724.

HAN, X., CHEN, Y., YAO, N., LIU, H. & WANG, Z. 2015. MicroRNA let-7b suppresses human gastric cancer malignancy by targeting ING1. *Cancer Gene Therapy,* 22**,** 122-129.
HANAHAN, D. & WEINBERG, R. A. 2000. The hallmarks of cancer. *Cell,* 100**,** 57-70.
HANAHAN, D. & WEINBERG, ROBERT A. 2011. Hallmarks of Cancer: The Next Generation. *Cell,* 144**,** 646-674.
HARRIS, K. P. & TEPASS, U. 2008. Cdc42 and Par proteins stabilize dynamic adherens junctions in the *Drosophila* neuroectoderm through regulation of apical endocytosis. *The Journal of Cell Biology,* 183**,** 1129-1143.
HARTMAN, C. D., ISENBERG, B. C., CHUA, S. G. & WONG, J. Y. 2017. Extracellular matrix type modulates cell migration on mechanical gradients. *Experimental Cell Research,* 359**,** 361-366.
HATTE, G., PRIGENT, C. & TASSAN, J.-P. 2018. Tight junctions negatively regulate mechanical forces applied to adherens junctions in vertebrate epithelial tissue. *J Cell Sci,* 131**,** jcs208736.
HAULING, T., KRAUTZ, R., MARKUS, R., VOLKENHOFF, A., KUCEROVA, L. & THEOPOLD, U. 2014. A Drosophila immune response against Ras-induced overgrowth. *Biology Open,* 3**,** 250.
HAY, B. A., WOLFF, T. & RUBIN, G. M. 1994. Expression of baculovirus P35 prevents cell death in Drosophila. *Development,* 120**,** 2121.
HAYAMI, S., YOSHIMATSU, M., VEERAKUMARASIVAM, A., UNOKI, M., IWAI, Y., TSUNODA, T., FIELD, H. I., KELLY, J. D., NEAL, D. E. & YAMAUE, H. 2010. Overexpression of the JmjC histone demethylase KDM5B in human carcinogenesis: involvement in the proliferation of cancer cells through the E2F/RB pathway. *Molecular cancer,* 9**,** 59.
HE, D., MIAO, H., XU, Y., XIONG, L., WANG, Y., XIANG, H., ZHANG, H. & ZHANG, Z. 2014. MiR-371-5p facilitates pancreatic cancer cell proliferation and decreases patient survival. *PloS one,* 9**,** e112930-e112930.
HE, G. H. Y., HELBING, C. C., WAGNER, M. J., SENSEN, C. W. & RIABOWOL, K. 2004. Phylogenetic Analysis of the ING Family of PHD Finger Proteins. *Molecular Biology and Evolution,* 22**,** 104-116.
HEDJAZIFAR, S., JENNDAHL, L. E., SHIMOKAWA, H. & BAECKSTRÖM, D. 2005. PKB mediates c-erbB2-induced epithelial β1 integrin conformational inactivation through Rho-independent F-actin rearrangements. *Experimental Cell Research,* 307**,** 259-275.
HEITZLER, P., HAENLIN, M., RAMAIN, P., CALLEJA, M. & SIMPSON, P. 1996. A Genetic Analysis of pannier, a Gene Necessary for Viability of Dorsal Tissues and Bristle Positioning in Drosophila. *Genetics,* 143**,** 1271.
HELBING, C. C., VEILLETTE, C., RIABOWOL, K., JOHNSTON, R. N. & GARKAVTSEV, I. 1997. A Novel Candidate Tumor Suppressor, ING1, Is Involved in the Regulation of Apoptosis. *Cancer Research,* 57**,** 1255.
HENDERSON, D. S. 2004. *Drosophila cytogenetics protocols*, Springer Science & Business Media.
HENNE, W. M., BOUCROT, E., MEINECKE, M., EVERGREN, E., VALLIS, Y., MITTAL, R. & MCMAHON, H. T. 2010. FCHo proteins are nucleators of clathrin-mediated endocytosis. *Science,* 328**,** 1281-1284.

HEUSINKVELD, M. & VAN DER BURG, S. H. 2011. Identification and manipulation of tumor associated macrophages in human cancers. *Journal of translational medicine,* 9**,** 216.

HORN, C. & HANDLER, A. M. 2005. Site-specific genomic targeting in *Drosophila*. *Proceedings of the National Academy of Sciences of the United States of America,* 102**,** 12483.

HOSONO, C., MATSUDA, R., ADRYAN, B. & SAMAKOVLIS, C. 2015. Transient junction anisotropies orient annular cell polarization in the Drosophila airway tubes. *Nature Cell Biology,* 17**,** 1569-1576.

HU, C.-T., WU, J.-R., CHANG, T. Y., CHENG, C.-C. & WU, W.-S. 2008. The transcriptional factor Snail simultaneously triggers cell cycle arrest and migration of human hepatoma HepG2. *Journal of Biomedical Science,* 15**,** 343-355.

HU, Y., AN, G., LIU, Y.-Q., WANG, Y.-X., SONG, L.-J., CHEN, M. & ZHANG, J. 2018. WASF3 is associated with tumour invasiveness and confers a poor prognosis in human gastric cancer. *Translational Cancer Research,* 7**,** 353-362.

HU, Y., COMJEAN, A., ROESEL, C., VINAYAGAM, A., FLOCKHART, I., ZIRIN, J., PERKINS, L., PERRIMON, N. & MOHR, S. E. 2016. FlyRNAi.org—the database of the Drosophila RNAi screening center and transgenic RNAi project: 2017 update. *Nucleic Acids Research,* 45**,** D672-D678.

HUANG, D. W., SHERMAN, B. T., TAN, Q., KIR, J., LIU, D., BRYANT, D., GUO, Y., STEPHENS, R., BASELER, M. W., LANE, H. C. & LEMPICKI, R. A. 2007. DAVID Bioinformatics Resources: expanded annotation database and novel algorithms to better extract biology from large gene lists. *Nucleic Acids Research,* 35**,** W169-W175.

HUMBERT, P., RUSSELL, S. & RICHARDSON, H. 2003. Dlg, Scribble and Lgl in cell polarity, cell proliferation and cancer. *BioEssays,* 25**,** 542-553.

HUMBERT, P. O., GRZESCHIK, N. A., BRUMBY, A. M., GALEA, R., ELSUM, I. & RICHARDSON, H. E. 2008. Control of tumourigenesis by the Scribble/Dlg/Lgl polarity module. *Oncogene,* 27**,** 6888-6907.

HUO, L., WEN, W., WANG, R., KAM, C., XIA, J., FENG, W. & ZHANG, M. J. T. E. J. 2011. Cdc42-dependent formation of the ZO-1/MRCKβ complex at the leading edge controls cell migration. *the EMBO journal,* 30**,** 665-678.

IKENOUCHI, J., FURUSE, M., FURUSE, K., SASAKI, H., TSUKITA, S. & TSUKITA, S. 2005. Tricellulin constitutes a novel barrier at tricellular contacts of epithelial cells. *The Journal of cell biology,* 171**,** 939-945.

IMAI, Y., KIMURA, T., MURAKAMI, A., YAJIMA, N., SAKAMAKI, K. & YONEHARA, S. 1999. The CED-4-homologous protein FLASH is involved in Fas-mediated activation of caspase-8 during apoptosis. *Nature,* 398**,** 777-785.

INDRA, I., HONG, S., TROYANOVSKY, R., KORMOS, B. & TROYANOVSKY, S. 2013. The adherens junction: a mosaic of cadherin and nectin clusters bundled by actin filaments. *Journal of Investigative Dermatology,* 133**,** 2546-2554.

ISHIYAMA, N., LEE, S.-H., LIU, S., LI, G.-Y., SMITH, M. J., REICHARDT, L. F. & IKURA, M. 2010. Dynamic and static interactions between p120 catenin and E-cadherin regulate the stability of cell-cell adhesion. *Cell,* 141**,** 117-128.

ISHIYAMA, N., TANAKA, N., ABE, K., YANG, Y. J., ABBAS, Y. M., UMITSU, M., NAGAR, B., BUELER, S. A., RUBINSTEIN, J. L. & TAKEICHI, M. 2013. An

autoinhibited structure of α-catenin and its implications for vinculin recruitment to adherens junctions. *Journal of Biological Chemistry,* 288**,** 15913-15925.

IVANOV, A. I., HUNT, D., UTECH, M., NUSRAT, A. & PARKOS, C. A. 2005. Differential Roles for Actin Polymerization and a Myosin II Motor in Assembly of the Epithelial Apical Junctional Complex. *Molecular Biology of the Cell,* 16**,** 2636-2650.

JAUFFRED, B. & BELLAICHE, Y. 2012. Analyzing frizzled signaling using fixed and live imaging of the asymmetric cell division of the Drosophila sensory organ precursor cell. *Planar Cell Polarity.* Springer.

JEANES, A., GOTTARDI, C. J. & YAP, A. S. 2008. Cadherins and cancer: how does cadherin dysfunction promote tumor progression? *Oncogene,* 27**,** 6920-6929.

JENNDAHL, L. E., ISAKSON, P. & BAECKSTRÖM, D. 2005. c-erbB2-induced epithelial-mesenchymal transition in mammary epithelial cells is suppressed by cell-cell contact and initiated prior to E-cadherin downregulation. *International journal of oncology,* 27**,** 439-448.

JIA, A. I., LV, Y., GUO, X., REN, L. I. & QIN, J. 2015. Ectopic expression of p33ING1b suppresses proliferation and induces apoptosis in colonic adenocarcinoma cells. *Oncology letters,* 10**,** 1517-1522.

JIANG, M., ZHOU, L.-Y., XU, N. & AN, Q. 2018. Down-regulation of miR-500 and miR-628 suppress non-small cell lung cancer proliferation, migration and invasion by targeting ING1. *Biomedicine & Pharmacotherapy,* 108**,** 1628-1639.

JOHNSON, E., SEACHRIST, D. D., DELEON-RODRIGUEZ, C. M., LOZADA, K. L., MIEDLER, J., ABDUL-KARIM, F. W. & KERI, R. A. 2010. HER2/ErbB2-induced breast cancer cell migration and invasion require p120 catenin activation of Rac1 and Cdc42. *Journal of Biological Chemistry,* 285**,** 29491-29501.

KAGAWA, Y., MATSUMOTO, S., KAMIOKA, Y., MIMORI, K., NAITO, Y., ISHII, T., OKUZAKI, D., NISHIDA, N., MAEDA, S., NAITO, A., KIKUTA, J., NISHIKAWA, K., NISHIMURA, J., HARAGUCHI, N., TAKEMASA, I., MIZUSHIMA, T., IKEDA, M., YAMAMOTO, H., SEKIMOTO, M., ISHII, H., DOKI, Y., MATSUDA, M., KIKUCHI, A., MORI, M. & ISHII, M. 2013. Cell cycle-dependent Rho GTPase activity dynamically regulates cancer cell motility and invasion in vivo. *PloS one,* 8**,** e83629-e83629.

KALTSCHMIDT, J. A., LAWRENCE, N., MOREL, V., BALAYO, T., FERNÁNDEZ, B. G., PELISSIER, A., JACINTO, A. & MARTINEZ ARIAS, A. 2002. Planar polarity and actin dynamics in the epidermis of Drosophila. *Nature Cell Biology,* 4**,** 937-944.

KATSUNO, T., UMEDA, K., MATSUI, T., HATA, M., TAMURA, A., ITOH, M., TAKEUCHI, K., FUJIMORI, T., NABESHIMA, Y.-I. & NODA, T. 2008. Deficiency of zonula occludens-1 causes embryonic lethal phenotype associated with defected yolk sac angiogenesis and apoptosis of embryonic cells. *Molecular biology of the cell,* 19**,** 2465-2475.

KAVERINA, I., KRYLYSHKINA, O., BENINGO, K., ANDERSON, K., WANG, Y.-L. & SMALL, J. V. 2002. Tensile stress stimulates microtubule outgrowth in living cells. *Journal of Cell Science,* 115**,** 2283-2291.

KAWATA, H., KAMIAKITO, T., OMOTO, Y., MIYAZAKI, C., HOZUMI, Y. & TANAKA, A. 2014. RhoC upregulation is correlated with reduced E-cadherin in

human breast cancer specimens after chemotherapy and in human breast cancer MCF-7 cells. *Hormones and Cancer,* 5**,** 414-423.

KHANAL, I., ELBEDIWY, A., DIAZ DE LA LOZA, M. D. C., FLETCHER, G. C. & THOMPSON, B. J. 2016. Shot and Patronin polarise microtubules to direct membrane traffic and biogenesis of microvilli in epithelia. *Journal of Cell Science,* 129**,** 2651.

KHURSHEED, M. & BASHYAM, M. D. 2014. Apico-basal polarity complex and cancer. *Journal of biosciences,* 39**,** 145-155.

KICHINA, J. V., ZEREMSKI, M., ARIS, L., GUROVA, K. V., WALKER, E., FRANKS, R., NIKITIN, A. Y., KIYOKAWA, H. & GUDKOV, A. V. 2006. Targeted disruption of the mouse ing1 locus results in reduced body size, hypersensitivity to radiation and elevated incidence of lymphomas. *Oncogene,* 25**,** 857-866.

KIM, V. N. 2003. RNA interference in functional genomics and medicine. *Journal of Korean medical science,* 18**,** 309-318.

KIM, Y. H., CHOI, Y. W., LEE, J., SOH, E. Y., KIM, J.-H. & PARK, T. J. 2017. Senescent tumor cells lead the collective invasion in thyroid cancer. *Nature Communications,* 8**,** 15208.

KITZING, T. M., WANG, Y., PERTZ, O., COPELAND, J. W. & GROSSE, R. 2010. Formin-like 2 drives amoeboid invasive cell motility downstream of RhoC. *Oncogene,* 29**,** 2441-2448.

KNUDSON, A. G. 1973. Mutation and Human Cancer. *In:* KLELN, G., WEINHOUSE, S. & HADDOW, A. (eds.) *Advances in Cancer Research.* Academic Press.

KOE, C. T., LI, S., ROSSI, F., WONG, J. J. L., WANG, Y., ZHANG, Z., CHEN, K., AW, S. S., RICHARDSON, H. E. & ROBSON, P. 2014. The Brm-HDAC3-Erm repressor complex suppresses dedifferentiation in Drosophila type II neuroblast lineages. *Elife,* 3**,** e01906.

KOHN, K. W., ZEEBERG, B. M., REINHOLD, W. C. & POMMIER, Y. 2014. Gene expression correlations in human cancer cell lines define molecular interaction networks for epithelial phenotype. *PloS one,* 9.

KORENAGA, D., TAKESUE, F., YASUDA, M., HONDA, M., NOZOE, T. & INUTSUKA, S. 2002. The relationship between cyclin B1 overexpression and lymph node metastasis in human colorectal cancer. *Surgery,* 131**,** S114-S120.

KOVACS, E. M., VERMA, S., ALI, R. G., RATHEESH, A., HAMILTON, N. A., AKHMANOVA, A. & YAP, A. S. 2011. N-WASP regulates the epithelial junctional actin cytoskeleton through a non-canonical post-nucleation pathway. *Nature cell biology,* 13**,** 934.

KUMAMOTO, K., FUJITA, K., KUROTANI, R., SAITO, M., UNOKI, M., HAGIWARA, N., SHIGA, H., BOWMAN, E. D., YANAIHARA, N., OKAMURA, S., NAGASHIMA, M., MIYAMOTO, K., TAKENOSHITA, S., YOKOTA, J. & HARRIS, C. C. 2009. ING2 is upregulated in colon cancer and increases invasion by enhanced MMP13 expression. *International Journal of Cancer,* 125**,** 1306-1315.

KUNDA, P., PELLING, A. E., LIU, T. & BAUM, B. 2008. Moesin Controls Cortical Rigidity, Cell Rounding, and Spindle Morphogenesis during Mitosis. *Current Biology,* 18**,** 91-101.

KUZMICHEV, A., ZHANG, Y., ERDJUMENT-BROMAGE, H., TEMPST, P. & REINBERG, D. 2002. Role of the Sin3-histone deacetylase complex in growth

regulation by the candidate tumor suppressor p33ING1. *Molecular and cellular biology,* 22**,** 835-848.
LAMB, R. S., WARD, R. E., SCHWEIZER, L. & FEHON, R. G. 1998. Drosophila coracle, a Member of the Protein 4.1 Superfamily, Has Essential Structural Functions in the Septate Junctions and Developmental Functions in Embryonic and Adult Epithelial Cells. *Molecular Biology of the Cell,* 9**,** 3505-3519.
LANGEVIN, J., MORGAN, M. J., ROSSÉ, C., RACINE, V., SIBARITA, J.-B., ARESTA, S., MURTHY, M., SCHWARZ, T., CAMONIS, J. & BELLAÏCHE, Y. 2005. Drosophila Exocyst Components Sec5, Sec6, and Sec15 Regulate DE-Cadherin Trafficking from Recycling Endosomes to the Plasma Membrane. *Developmental Cell,* 9**,** 365-376.
LAPRISE, P., LAU, K. M., HARRIS, K. P., SILVA-GAGLIARDI, N. F., PAUL, S. M., BERONJA, S., BEITEL, G. J., MCGLADE, C. J. & TEPASS, U. 2009. Yurt, Coracle, Neurexin IV and the Na+,K+-ATPase form a novel group of epithelial polarity proteins. *Nature,* 459**,** 1141-1145.
LAWSON, C. D. & RIDLEY, A. J. 2017. Rho GTPase signaling complexes in cell migration and invasion. *Journal of Cell Biology,* 217**,** 447-457.
LECHUGA, S., AMIN, P. H. & IVANOV, A. I. 2017. Adducin regulates migration and invasion of normal lung epithelial cells and lung cancer cells. *The FASEB Journal,* 31**,** 465.3-465.3.
LECUIT, T. & YAP, A. S. 2015. E-cadherin junctions as active mechanical integrators in tissue dynamics. *Nature cell biology,* 17**,** 533-539.
LEE, T. & LUO, L. 1999. Mosaic Analysis with a Repressible Cell Marker for Studies of Gene Function in Neuronal Morphogenesis. *Neuron,* 22**,** 451-461.
LEE, T. & LUO, L. 2001. Mosaic analysis with a repressible cell marker (MARCM) for Drosophila neural development. *Trends in Neurosciences,* 24**,** 251-254.
LEIBFRIED, A., FRICKE, R., MORGAN, M. J., BOGDAN, S. & BELLAICHE, Y. 2008. Drosophila Cip4 and WASp Define a Branch of the Cdc42-Par6-aPKC Pathway Regulating E-Cadherin Endocytosis. *Current Biology,* 18**,** 1639-1648.
LEVAYER, R., DUPONT, C. & MORENO, E. 2016. Tissue Crowding Induces Caspase-Dependent Competition for Space. *Current Biology,* 26**,** 670-677.
LEVAYER, R., PELISSIER-MONIER, A. & LECUIT, T. 2011. Spatial regulation of Dia and Myosin-II by RhoGEF2 controls initiation of E-cadherin endocytosis during epithelial morphogenesis. *Nature Cell Biology,* 13**,** 529-540.
LI, J., MARTINKA, M. & LI, G. 2008. Role of ING4 in human melanoma cell migration, invasion and patient survival. *Carcinogenesis,* 29**,** 1373-1379.
LI, M., ZHU, Y., ZHANG, H., LI, L., HE, P., XIA, H., ZHANG, Y. & MAO, C. 2014. Delivery of inhibitor of growth 4 (ING4) gene significantly inhibits proliferation and invasion and promotes apoptosis of human osteosarcoma cells. *Scientific Reports,* 4**,** 7380.
LI, N., LI, Q., CAO, X., ZHAO, G., XUE, L. & TONG, T. 2011. The tumor suppressor p33ING1b upregulates p16INK4a expression and induces cellular senescence. *FEBS Letters,* 585**,** 3106-3112.
LI, Q. & MATTINGLY, R. R. 2008. Restoration of E-cadherin cell-cell junctions requires both expression of E-cadherin and suppression of ERK MAP kinase activation in Ras-transformed breast epithelial cells. *Neoplasia (New York, N.Y.),* 10**,** 1444-1458.

LI, S., FAN, T., LIU, H., CHEN, J., QIN, C. & REN, X. 2013. Tumor suppressor ING4 overexpression contributes to proliferation and invasion inhibition in gastric carcinoma by suppressing the NF-κB signaling pathway. *Molecular biology reports,* 40**,** 5723-5732.

LI, Y.-Y., JIANG, G.-T., CHEN, L.-J., JIANG, Y.-H. & JIAO, J.-D. 2019. Formin mDia1 contributes to migration and epithelial-mesenchymal transition of tubular epithelial cells exposed to TGF-β1. *Journal of Cellular Biochemistry,* n/a.

LIANG, X., GOMEZ, G. & S YAP, A. 2015. Current perspectives on cadherin-cytoskeleton interactions and dynamics. *Cell Health and Cytoskeleton,* 7**,** 11-24.

LIBERMANN, T. A. & ZERBINI, L. F. 2006. Targeting transcription factors for cancer gene therapy. *Current gene therapy,* 6**,** 17-33.

LIGON, L. A. & HOLZBAUR, E. L. 2007. Microtubules tethered at epithelial cell junctions by dynein facilitate efficient junction assembly. *Traffic,* 8**,** 808-819.

LIGON, L. A., KARKI, S., TOKITO, M. & HOLZBAUR, E. L. 2001. Dynein binds to β-catenin and may tether microtubules at adherens junctions. *Nature cell biology,* 3**,** 913-917.

LIN, Y.-N., BHUWANIA, R., GROMOVA, K., FAILLA, A. V., LANGE, T., RIECKEN, K., LINDER, S., KNEUSSEL, M., IZBICKI, J. R. & WINDHORST, S. 2015. Drosophila homologue of Diaphanous 1 (DIAPH1) controls the metastatic potential of colon cancer cells by regulating microtubule-dependent adhesion. *Oncotarget,* 6**,** 18577-18589.

LIN, Y.-N., IZBICKI, J. R., KÖNIG, A., HABERMANN, J. K., BLECHNER, C., LANGE, T., SCHUMACHER, U. & WINDHORST, S. 2014. Expression of DIAPH1 is up-regulated in colorectal cancer and its down-regulation strongly reduces the metastatic capacity of colon carcinoma cells. *International Journal of Cancer,* 134**,** 1571-1582.

LIU, X.-L., ZHANG, X.-T., MENG, J., ZHANG, H.-F., ZHAO, Y., LI, C., SUN, Y., MEI, Q.-B., ZHANG, F. & ZHANG, T. 2017. ING5 knockdown enhances migration and invasion of lung cancer cells by inducing EMT via EGFR/PI3K/Akt and IL-6/STAT3 signaling pathways. *Oncotarget,* 8**,** 54265-54276.

LOEB, L. A. 2011. Human cancers express mutator phenotypes: origin, consequences and targeting. *Nature Reviews Cancer,* 11**,** 450-457.

LU, M., CHEN, F., WANG, Q., WANG, K., PAN, Q. & ZHANG, X. 2012. Downregulation of inhibitor of growth 3 is correlated with tumorigenesis and progression of hepatocellular carcinoma. *Oncology letters,* 4**,** 47-52.

LU, M., WU, J., HAO, Z.-W., SHANG, Y.-K., XU, J., NAN, G., LI, X., CHEN, Z.-N. & BIAN, H. 2018. Basolateral CD147 induces hepatocyte polarity loss by E-cadherin ubiquitination and degradation in hepatocellular carcinoma progress. *Hepatology,* 68**,** 317-332.

LUCAS, E. P., KHANAL, I., GASPAR, P., FLETCHER, G. C., POLESELLO, C., TAPON, N. & THOMPSON, B. J. 2013. The Hippo pathway polarizes the actin cytoskeleton during collective migration of Drosophila border cells. *The Journal of Cell Biology,* 201**,** 875-885.

LUNARDI, A., DI MININ, G., PROVERO, P., DAL FERRO, M., CAROTTI, M., DEL SAL, G. & COLLAVIN, L. 2010. A genome-scale protein interaction profile of Drosophila; p53 uncovers additional nodes of the human p53 network. *Proceedings of the National Academy of Sciences,* 107**,** 6322.

LUO, C. & SHEN, J. 2017. Adducin in tumorigenesis and metastasis. *Oncotarget,* 8**,** 48453-48459.
MACK, N. A. & GEORGIOU, M. 2014. The interdependence of the Rho GTPases and apicobasal cell polarity. *Small GTPases,* 5**,** e973768.
MANGOLD, S., NORWOOD, S. J., YAP, A. S. & COLLINS, B. M. 2012. The juxtamembrane domain of the E-cadherin cytoplasmic tail contributes to its interaction with Myosin VI. *Bioarchitecture,* 2**,** 185-188.
MARCHAL, C., VINATIER, G., SANIAL, M., PLESSIS, A., PRET, A.-M., LIMBOURG-BOUCHON, B., THÉODORE, L. & NETTER, S. 2012. The HIV-1 Vpu protein induces apoptosis in Drosophila via activation of JNK signaling. *PLoS One,* 7.
MARINARI, E., MEHONIC, A., CURRAN, S., GALE, J., DUKE, T. & BAUM, B. 2012. Live-cell delamination counterbalances epithelial growth to limit tissue overcrowding. *Nature,* 484**,** 542-545.
MARTIN, T. A. & JIANG, W. G. 2009. Loss of tight junction barrier function and its role in cancer metastasis. *Biochimica et Biophysica Acta (BBA) - Biomembranes,* 1788**,** 872-891.
MARTINA, J. A., BONANGELINO, C. J., AGUILAR, R. C. & BONIFACINO, J. S. 2001. Stonin 2: An Adaptor-like Protein That Interacts with Components of the Endocytic Machinery. *Journal of Cell Biology,* 153**,** 1111-1120.
MARY, S., CHARRASSE, S., MERIANE, M., COMUNALE, F., TRAVO, P., BLANGY, A. & GAUTHIER-ROUVIERE, C. J. M. B. O. T. C. 2002. Biogenesis of N-cadherin-dependent cell-cell contacts in living fibroblasts is a microtubule-dependent kinesin-driven mechanism. *Molecular biology of the cell,* 13**,** 285-301.
MATTER, K. & BALDA, M. S. 2003. Signalling to and from tight junctions. *Nature reviews Molecular cell biology,* 4**,** 225–237.
MATTER, K. & BALDA, M. S. 2007. Epithelial tight junctions, gene expression and nucleo-junctional interplay. *Journal of cell science,* 120**,** 1505-1511.
MATUS, DAVID Q., LOHMER, LAUREN L., KELLEY, LAURA C., SCHINDLER, ADAM J., KOHRMAN, ABRAHAM Q., BARKOULAS, M., ZHANG, W., CHI, Q. & SHERWOOD, DAVID R. 2015. Invasive Cell Fate Requires G1 Cell-Cycle Arrest and Histone Deacetylase-Mediated Changes in Gene Expression. *Developmental Cell,* 35**,** 162-174.
MCINTOSH, J. R. & KOONCE, M. P. 1989. Mitosis. *Science,* 246**,** 622.
MCMAHON, H. T. & BOUCROT, E. 2011. Molecular mechanism and physiological functions of clathrin-mediated endocytosis. *Nat Rev Mol Cell Biol,* 12**,** 517-33.
MEJLVANG, J., KRIAJEVSKA, M., VANDEWALLE, C., CHERNOVA, T., SAYAN, A. E., BERX, G., MELLON, J. K. & TULCHINSKY, E. 2007. Direct Repression of Cyclin D1 by SIP1 Attenuates Cell Cycle Progression in Cells Undergoing an Epithelial Mesenchymal Transition. *Molecular Biology of the Cell,* 18**,** 4615-4624.
MELTZER, S., YADAV, S., LEE, J., SOBA, P., YOUNGER, S. H., JIN, P., ZHANG, W., PARRISH, J., JAN, L. Y. & JAN, Y.-N. 2016. Epidermis-derived semaphorin promotes dendrite self-avoidance by regulating dendrite-substrate adhesion in Drosophila sensory neurons. *Neuron,* 89**,** 741-755.
MENG, W., MUSHIKA, Y., ICHII, T. & TAKEICHI, M. 2008. Anchorage of microtubule minus ends to adherens junctions regulates epithelial cell-cell contacts. *Cell,* 135**,** 948-959.

MENG, W. & TAKEICHI, M. 2009. Adherens junction: molecular architecture and regulation. *Cold Spring Harbor perspectives in biology,* 1**,** a002899.
MERCK. 2020. *Boyden Chamber Technique* [Online]. Merck KGaA. Available: https://www.merckmillipore.com/GB/en/life-science-research/antibodies-assays/assays-overview/cell-invasion-migration-assays/boyden-chamber-technique/I0qb.qB.KSMAAAFANtY.1ZcQ,nav [Accessed 26 May 2020].
MICCHELLI, C. A. 2014. Whole-mount immunostaining of the adult Drosophila gastrointestinal tract. *Methods (San Diego, Calif.),* 68**,** 273-279.
MILES, W. O., DYSON, N. J. & WALKER, J. A. 2011. Modeling tumor invasion and metastasis in *Drosophila*. *Disease Models & Mechanisms,* 4**,** 753.
MILLARD, T. H. & MARTIN, P. 2008. Dynamic analysis of filopodial interactions during the zippering phase of Drosophila dorsal closure. *Development,* 135**,** 621-626.
MIYAKE, Y., INOUE, N., NISHIMURA, K., KINOSHITA, N., HOSOYA, H. & YONEMURA, S. 2006. Actomyosin tension is required for correct recruitment of adherens junction components and zonula occludens formation. *Experimental Cell Research,* 312**,** 1637-1650.
MORÁN, T., BERNUÉS, J. & AZORÍN, F. 2015. The Drosophila histone demethylase dKDM5/LID regulates hematopoietic development. *Developmental Biology,* 405**,** 260-268.
MORGAN, R., NALLIAH, A. & MORSI EL-KADI, A. S. 2004. FLASH, a component of the FAS–CAPSASE8 apoptotic pathway, is directly regulated by Hoxb4 in the notochord. *Developmental Biology,* 265**,** 105-112.
MUKAKA, M. M. 2012. Statistics corner: A guide to appropriate use of correlation coefficient in medical research. *Malawi medical journal : the journal of Medical Association of Malawi,* 24**,** 69-71.
MUMMERY-WIDMER, J. L., YAMAZAKI, M., STOEGER, T., NOVATCHKOVA, M., BHALERAO, S., CHEN, D., DIETZL, G., DICKSON, B. J. & KNOBLICH, J. A. 2009. Genome-wide analysis of Notch signalling in Drosophila by transgenic RNAi. *Nature,* 458**,** 987-992.
NAGATA, S. 2018. Apoptosis and Clearance of Apoptotic Cells. *Annual Review of Immunology,* 36**,** 489-517.
NANES, B. A., CHIASSON-MACKENZIE, C., LOWERY, A. M., ISHIYAMA, N., FAUNDEZ, V., IKURA, M., VINCENT, P. A. & KOWALCZYK, A. P. 2012. p120-catenin binding masks an endocytic signal conserved in classical cadherins. *The Journal of Cell Biology,* 199**,** 365-380.
NATZLE, J. E. & MCCARTHY, B. J. 1984. Regulation of Drosophila α- and β-tubulin genes during development. *Developmental Biology,* 104**,** 187-198.
NAYDENOV, N. G. & IVANOV, A. I. 2010. Adducins Regulate Remodeling of Apical Junctions in Human Epithelial Cells. *Molecular Biology of the Cell,* 21**,** 3506-3517.
NILSSON, G., AKHTAR, N., KANNIUS-JANSON, M. & BAECKSTRÖM, D. 2014. Loss of E-cadherin expression is not a prerequisite for c-erbB2-induced epithelial-mesenchymal transition. *International journal of oncology,* 45**,** 82-94.
NISHIMURA, T. & TAKEICHI, M. 2009. Remodeling of the adherens junctions during morphogenesis. *Current topics in developmental biology,* 89**,** 33-54.

NOORDSTRA, I., LIU, Q., NIJENHUIS, W., HUA, S., JIANG, K., BAARS, M., REMMELZWAAL, S., MARTIN, M., KAPITEIN, L. C. & AKHMANOVA, A. 2016. Control of apico–basal epithelial polarity by the microtubule minus-end-binding protein CAMSAP3 and spectraplakin ACF7. *Journal of Cell Science,* 129**,** 4278.

O'CONNOR, R. J., SCHALEY JE FAU - FEENEY, G., FEENEY G FAU - HEARING, P. & HEARING, P. 2001. The p107 tumor suppressor induces stable E2F DNA binding to repress target promoters.

ODA, H. & TSUKITA, S. 2001. Real-time imaging of cell-cell adherens junctions reveals that Drosophila mesoderm invagination begins with two phases of apical constriction of cells. *Journal of Cell Science,* 114**,** 493.

OKADA, T., YOU, L. & GIANCOTTI, F. G. 2007. Shedding light on Merlin's wizardry. *Trends in cell biology,* 17**,** 222-229.

OKAMURA, K., CHUNG, W.-J., RUBY, J. G., GUO, H., BARTEL, D. P. & LAI, E. C. 2008. The Drosophila hairpin RNA pathway generates endogenous short interfering RNAs. *Nature,* 453**,** 803-806.

ORSULIC, S., HUBER, O., ABERLE, H., ARNOLD, S. & KEMLER, R. 1999. E-cadherin binding prevents beta-catenin nuclear localization and beta-catenin/LEF-1-mediated transactivation. *Journal of cell science,* 112**,** 1237-1245.

OTTO, T. & SICINSKI, P. 2017. Cell cycle proteins as promising targets in cancer therapy. *Nature Reviews Cancer,* 17**,** 93-115.

PAGLIARINI, R. A. & XU, T. 2003. A Genetic Screen in Drosophila for Metastatic Behavior. *Science,* 302**,** 1227.

PALACIOS, F., TUSHIR, J. S., FUJITA, Y. & SOUZA-SCHOREY, C. 2005. Lysosomal Targeting of E-Cadherin: a Unique Mechanism for the Down-Regulation of Cell-Cell Adhesion during Epithelial to Mesenchymal Transitions. *Molecular and Cellular Biology,* 25**,** 389-402.

PEGLION, F. & ETIENNE-MANNEVILLE, S. 2013. p120catenin alteration in cancer and its role in tumour invasion. *Philosophical Transactions of the Royal Society B: Biological Sciences,* 368**,** 20130015.

PEINADO, H., ZHANG, H., MATEI, I. R., COSTA-SILVA, B., HOSHINO, A., RODRIGUES, G., PSAILA, B., KAPLAN, R. N., BROMBERG, J. F., KANG, Y., BISSELL, M. J., COX, T. R., GIACCIA, A. J., ERLER, J. T., HIRATSUKA, S., GHAJAR, C. M. & LYDEN, D. 2017. Pre-metastatic niches: organ-specific homes for metastases. *Nature Reviews Cancer,* 17**,** 302-317.

PEÑA, P. V., HOM, R. A., HUNG, T., LIN, H., KUO, A. J., WONG, R. P. C., SUBACH, O. M., CHAMPAGNE, K. S., ZHAO, R., VERKHUSHA, V. V., LI, G., GOZANI, O. & KUTATELADZE, T. G. 2008. Histone H3K4me3 Binding Is Required for the DNA Repair and Apoptotic Activities of ING1 Tumor Suppressor. *Journal of Molecular Biology,* 380**,** 303-312.

PETRYSZAK, R., KEAYS, M., TANG, Y. A., FONSECA, N. A., BARRERA, E., BURDETT, T., FÜLLGRABE, A., FUENTES, A. M.-P., JUPP, S., KOSKINEN, S., MANNION, O., HUERTA, L., MEGY, K., SNOW, C., WILLIAMS, E., BARZINE, M., HASTINGS, E., WEISSER, H., WRIGHT, J., JAISWAL, P., HUBER, W., CHOUDHARY, J., PARKINSON, H. E. & BRAZMA, A. 2015. Expression Atlas update—an integrated database of gene and protein expression in humans, animals and plants. *Nucleic Acids Research,* 44**,** D746-D752.

PFAFFL, M. W. 2001. A new mathematical model for relative quantification in real-time RT–PCR. *Nucleic acids research,* 29**,** e45-e45.

PIETKIEWICZ, S., SCHMIDT, J. H. & LAVRIK, I. N. 2015. Quantification of apoptosis and necroptosis at the single cell level by a combination of Imaging Flow Cytometry with classical Annexin V/propidium iodide staining. *Journal of Immunological Methods,* 423**,** 99-103.

PILLÉ, J. Y., DENOYELLE, C., VARET, J., BERTRAND, J. R., SORIA, J., OPOLON, P., LU, H., PRITCHARD, L. L., VANNIER, J. P., MALVY, C., SORIA, C. & LI, H. 2005. Anti-RhoA and Anti-RhoC siRNAs Inhibit the Proliferation and Invasiveness of MDA-MB-231 Breast Cancer Cells in Vitro and in Vivo. *Molecular Therapy,* 11**,** 267-274.

POINCLOUX, R., COLLIN, O., LIZÁRRAGA, F., ROMAO, M., DEBRAY, M., PIEL, M. & CHAVRIER, P. 2011. Contractility of the cell rear drives invasion of breast tumor cells in 3D Matrigel. *Proceedings of the National Academy of Sciences,* 108**,** 1943.

POKRYWKA, N. J., ZHANG, H. & RALEY-SUSMAN, K. 2014. Distinct roles for hu li tai shao and swallow in cytoskeletal organization during Drosophila oogenesis. *Developmental Dynamics,* 243**,** 906-916.

POTTER, C. J., HUANG, H. & XU, T. 2001. Drosophila Tsc1 Functions with Tsc2 to Antagonize Insulin Signaling in Regulating Cell Growth, Cell Proliferation, and Organ Size. *Cell,* 105**,** 357-368.

POTTER, C. J., TURENCHALK, G. S. & XU, T. 2000. Drosophila in cancer research: an expanding role. *Trends in Genetics,* 16**,** 33-39.

POZAROWSKI, P. & DARZYNKIEWICZ, Z. 2004. Analysis of cell cycle by flow cytometry. *Checkpoint controls and cancer.* Springer.

QIAN, X., HULIT, J., SUYAMA, K., EUGENIN, E. A., BELBIN, T. J., LOUDIG, O., SMIRNOVA, T., ZHOU, Z. N., SEGALL, J., LOCKER, J., PHILLIPS, G. R., NORTON, L. & HAZAN, R. B. 2013. p21CIP1 mediates reciprocal switching between proliferation and invasion during metastasis. *Oncogene,* 32**,** 2292-2303.

RAJARAJACHOLAN, U. K., THALAPPILLY, S. & RIABOWOL, K. 2013. The ING1a tumor suppressor regulates endocytosis to induce cellular senescence via the Rb-E2F pathway. *PLoS biology,* 11**,** e1001502-e1001502.

RALEIGH, D. R., MARCHIANDO, A. M., ZHANG, Y., SHEN, L., SASAKI, H., WANG, Y., LONG, M. & TURNER, J. R. 2010. Tight junction–associated MARVEL proteins marvelD3, tricellulin, and occludin have distinct but overlapping functions. *Molecular biology of the cell,* 21**,** 1200-1213.

REN, B., CAM, H., TAKAHASHI, Y., VOLKERT, T., TERRAGNI, J., YOUNG, R. A. & DYNLACHT, B. D. 2002. E2F integrates cell cycle progression with DNA repair, replication, and G2/M checkpoints. *Genes & development,* 16**,** 245-256.

RIDLEY, A. J. 2001. Rho GTPases and cell migration. *Journal of Cell Science,* 114**,** 2713.

RIDLEY, A. J. 2013. RhoA, RhoB and RhoC have different roles in cancer cell migration. *Journal of Microscopy,* 251**,** 242-249.

RIKITAKE, Y. & TAKAI, Y. 2011. Chapter three - Directional Cell Migration: Regulation by Small G Proteins, Nectin-like Molecule-5, and Afadin. *In:* JEON, K. W. (ed.) *International Review of Cell and Molecular Biology.* Academic Press.

ROBERTSON, H. M., PRESTON, C. R., PHILLIS, R. W., JOHNSON-SCHLITZ, D. M., BENZ, W. K. & ENGELS, W. R. 1988. A stable genomic source of P element transposase in Drosophila melanogaster. *Genetics,* 118**,** 461.

RODRIGUEZ-BOULAN, E. & MACARA, I. G. 2014. Organization and execution of the epithelial polarity programme. *Nature Reviews Molecular Cell Biology,* 15**,** 225-242.

ROOTE, J. & PROKOP, A. 2013. How to Design a Genetic Mating Scheme: A Basic Training Package for *Drosophila* Genetics. *G3: Genes|Genomes|Genetics,* 3**,** 353.

ROTSTEIN, B. & PAULULAT, A. 2016. On the morphology of the Drosophila heart. *Journal of cardiovascular development and disease,* 3**,** 15.

ROYER, C. & LU, X. 2011. Epithelial cell polarity: a major gatekeeper against cancer? *Cell Death & Differentiation,* 18**,** 1470-1477.

RUBIN, G. M. & SPRADLING, A. C. 1983. Vectors for P element-mediated gene transfer in Drosophila. *Nucleic Acids Research,* 11**,** 6341-6351.

RUSSELL, M., BERARDI, P., GONG, W. & RIABOWOL, K. 2006. Grow-ING, Age-ING and Die-ING: ING proteins link cancer, senescence and apoptosis. *Experimental Cell Research,* 312**,** 951-961.

RUSU, A. D. & GEORGIOU, M. 2020. The multifarious regulation of the apical junctional complex. *Open Biology,* 10.

SAHAI, E. & MARSHALL, C. J. 2002. ROCK and Dia have opposing effects on adherens junctions downstream of Rho. *Nature cell biology,* 4**,** 408-415.

SAJ, A., ARZIMAN, Z., STEMPFLE, D., VAN BELLE, W., SAUDER, U., HORN, T., DÜRRENBERGER, M., PARO, R., BOUTROS, M. & MERDES, G. 2010. A Combined Ex Vivo and In Vivo RNAi Screen for Notch Regulators in Drosophila Reveals an Extensive Notch Interaction Network. *Developmental Cell,* 18**,** 862-876.

SAKAUE-SAWANO, A., KUROKAWA, H., MORIMURA, T., HANYU, A., HAMA, H., OSAWA, H., KASHIWAGI, S., FUKAMI, K., MIYATA, T., MIYOSHI, H., IMAMURA, T., OGAWA, M., MASAI, H. & MIYAWAKI, A. 2008. Visualizing Spatiotemporal Dynamics of Multicellular Cell-Cycle Progression. *Cell,* 132**,** 487-498.

SALDIVAR, J. C., HAMPERL, S., BOCEK, M. J., CHUNG, M., BASS, T. E., CISNEROS-SOBERANIS, F., SAMEJIMA, K., XIE, L., PAULSON, J. R., EARNSHAW, W. C., CORTEZ, D., MEYER, T. & CIMPRICH, K. A. 2018. An intrinsic S/G2 checkpoint enforced by ATR. *Science,* 361**,** 806.

SARPAL, R., PELLIKKA, M., PATEL, R. R., HUI, F. Y. W., GODT, D. & TEPASS, U. 2012. Mutational analysis supports a core role for Drosophila α-catenin in adherens junction function. *Journal of cell science,* 125**,** 233-245.

SASAKI, H., AUCLAIR, D., FUKAI, I., KIRIYAMA, M., YAMAKAWA, Y., FUJII, Y. & CHEN, L. B. 2001. Serum level of the periostin, a homologue of an insect cell adhesion molecule, as a prognostic marker in nonsmall cell lung carcinomas. *Cancer,* 92**,** 843-848.

SATO, K., WATANABE, T., WANG, S., KAKENO, M., MATSUZAWA, K., MATSUI, T., YOKOI, K., MURASE, K., SUGIYAMA, I., OZAWA, M. & KAIBUCHI, K. 2011. Numb controls E-cadherin endocytosis through p120 catenin with aPKC. *Molecular Biology of the Cell,* 22**,** 3103-3119.

SAWYER, J. K., HARRIS, N. J., SLEP, K. C., GAUL, U. & PEIFER, M. 2009. The *Drosophila* afadin homologue Canoe regulates linkage of the actin cytoskeleton to adherens junctions during apical constriction. *The Journal of Cell Biology,* 186**,** 57-73.

SCHINDELIN, J., ARGANDA-CARRERAS, I., FRISE, E., KAYNIG, V., LONGAIR, M., PIETZSCH, T., PREIBISCH, S., RUEDEN, C., SAALFELD, S., SCHMID, B., TINEVEZ, J.-Y., WHITE, D. J., HARTENSTEIN, V., ELICEIRI, K., TOMANCAK, P. & CARDONA, A. 2012. Fiji: an open-source platform for biological-image analysis. *Nature Methods,* 9**,** 676-682.

SCHMIDT, C. R., GI, Y. J., COFFEY, R. J., BEAUCHAMP, R. D. & PEARSON, A. S. 2004. Oncogenic Ras dominates overexpression of E-cadherin in malignant transformation of intestinal epithelial cells. *Surgery,* 136**,** 303-309.

SCHMITTGEN, T. D. & LIVAK, K. J. 2008. Analyzing real-time PCR data by the comparative CT method. *Nature Protocols,* 3**,** 1101-1108.

SCHNORRER, F., SCHÖNBAUER, C., LANGER, C. C. H., DIETZL, G., NOVATCHKOVA, M., SCHERNHUBER, K., FELLNER, M., AZARYAN, A., RADOLF, M., STARK, A., KELEMAN, K. & DICKSON, B. J. 2010. Systematic genetic analysis of muscle morphogenesis and function in Drosophila. *Nature,* 464**,** 287-291.

SEO, K. W., LEE, S. J., KIM, Y. H., BAE, J. U., PARK, S. Y., BAE, S. S. & KIM, C. D. 2013. Mechanical stretch increases MMP-2 production in vascular smooth muscle cells via activation of PDGFR-β/Akt signaling pathway. *PLoS One,* 8.

SHANKAR, J. & NABI, I. R. 2015. Actin cytoskeleton regulation of epithelial mesenchymal transition in metastatic cancer cells. *PloS one,* 10**,** e0119954-e0119954.

SHANNON, P., MARKIEL A FAU - OZIER, O., OZIER O FAU - BALIGA, N. S., BALIGA NS FAU - WANG, J. T., WANG JT FAU - RAMAGE, D., RAMAGE D FAU - AMIN, N., AMIN N FAU - SCHWIKOWSKI, B., SCHWIKOWSKI B FAU - IDEKER, T. & IDEKER, T. 2003. Cytoscape: a software environment for integrated models of biomolecular interaction networks. *Genome Research,* 13(11)**,** 2498-504.

SHEN, J.-C., UNOKI, M., YTHIER, D., DUPERRAY, A., VARTICOVSKI, L., KUMAMOTO, K., PEDEUX, R. & HARRIS, C. C. 2007. Inhibitor of growth 4 suppresses cell spreading and cell migration by interacting with a novel binding partner, liprin α1. *Cancer research,* 67**,** 2552-2558.

SHEN, Y., HIRSCH, D. S., SASIELA, C. A. & WU, W. J. 2008. Cdc42 regulates E-cadherin ubiquitination and degradation through an epidermal growth factor receptor to Src-mediated pathway. *Journal of Biological Chemistry,* 283**,** 5127-5137.

SHEWAN, A. M., MADDUGODA, M., KRAEMER, A., STEHBENS, S. J., VERMA, S., KOVACS, E. M. & YAP, A. S. 2005. Myosin 2 Is a Key Rho Kinase Target Necessary for the Local Concentration of E-Cadherin at Cell–Cell Contacts. *Molecular Biology of the Cell,* 16**,** 4531-4542.

SILICHEVA, M., GOLOVNIN, A., POMERANTSEVA, E., PARSHIKOV, A., GEORGIEV, P. & MAKSIMENKO, O. 2009. Drosophila mini-white model system: new insights into positive position effects and the role of transcriptional

terminators and gypsy insulator in transgene shielding. *Nucleic Acids Research,* 38**,** 39-47.

SIMPSON, K. J., DUGAN, A. S. & MERCURIO, A. M. 2004. Functional analysis of the contribution of RhoA and RhoC GTPases to invasive breast carcinoma. *Cancer research,* 64**,** 8694-8701.

SKOWYRA, D., ZEREMSKI, M., NEZNANOV, N., LI, M., CHOI, Y., UESUGI, M., HAUSER, C. A., GU, W., GUDKOV, A. V. & QIN, J. 2001. Differential Association of Products of Alternative Transcripts of the Candidate Tumor Suppressor ING1 with the mSin3/HDAC1 Transcriptional Corepressor Complex. *Journal of Biological Chemistry,* 276**,** 8734-8739.

SMUTNY, M., COX, H. L., LEERBERG, J. M., KOVACS, E. M., CONTI, M. A., FERGUSON, C., HAMILTON, N. A., PARTON, R. G., ADELSTEIN, R. S. & YAP, A. S. 2010. Myosin II isoforms identify distinct functional modules that support integrity of the epithelial zonula adherens. *Nature Cell Biology,* 12**,** 696.

SOLIMAN, M. A., BERARDI, P., PASTYRYEVA, S., BONNEFIN, P., FENG, X., COLINA, A., YOUNG, D. & RIABOWOL, K. 2008. ING1a expression increases during replicative senescence and induces a senescent phenotype. *Aging Cell,* 7**,** 783-794.

SOLIMAN, M. A. & RIABOWOL, K. 2007. After a decade of study-ING, a PHD for a versatile family of proteins. *Trends in Biochemical Sciences,* 32**,** 509-519.

SPAIN, M. M., CARUSO, J. A., SWAMINATHAN, A. & PILE, L. A. 2010. Drosophila SIN3 isoforms interact with distinct proteins and have unique biological functions. *Journal of Biological Chemistry,* 285**,** 27457-27467.

SPANGLER, B., KAPPELMANN, M., SCHITTEK, B., MEIERJOHANN, S., VARDIMON, L., BOSSERHOFF, A. K. & KUPHAL, S. 2012. ETS-1/RhoC signaling regulates the transcription factor c-Jun in melanoma. *International Journal of Cancer,* 130**,** 2801-2811.

STAEHELIN, L. A. 1973. Further observations on the fine structure of freeze-cleaved tight junctions. *J Cell Sci,* 13**,** 763-86.

STEHBENS, S. J., PATERSON, A. D., CRAMPTON, M. S., SHEWAN, A. M., FERGUSON, C., AKHMANOVA, A. & PARTON, R. G. 2006. Dynamic microtubules regulate the local concentration of E-cadherin at cell-cell contacts. *Journal of cell science,* 119**,** 1801-1811.

STELLER, H. 2009. Staying alive: Apoptosome feedback inhibition. *Nature cell biology,* 10**,** 1387-8.

STEVENSON, B. R. & BEGG, D. A. 1994. Concentration-dependent effects of cytochalasin D on tight junctions and actin filaments in MDCK epithelial cells. *Journal of Cell Science,* 107**,** 367.

SU, W. & KOWALCZYK, A. P. 2016. The VE-cadherin cytoplasmic domain undergoes proteolytic processing during endocytosis. *Molecular Biology of the Cell,* 28**,** 76-84.

SULLIVAN, W., ASHBURNER, M. & HAWLEY, R. S. 2000. *Drosophila protocols*, Cold Spring Harbor Laboratory Press.

TAKAHASHI, M., SEKI, N., OZAKI, T., KATO, M., KUNO, T., NAKAGAWA, T., WATANABE, K.-I., MIYAZAKI, K., OHIRA, M., HAYASHI, S., HOSODA, M., TOKITA, H., MIZUGUCHI, H., HAYAKAWA, T., TODO, S. & NAKAGAWARA, A. 2002. Identification of the p33ING1regulated Genes that

Include Cyclin B1 and Proto-oncogene DEK by Using cDNA Microarray in a Mouse Mammary Epithelial Cell Line NMuMG. *Cancer Research,* 62**,** 2203.

TAKAI, Y., IKEDA, W., OGITA, H. & RIKITAKE, Y. 2008. The immunoglobulin-like cell adhesion molecule nectin and its associated protein afadin. *Annual review of cell and developmental biology,* 24**,** 309-342.

TALKENBERGER, K., CAVALCANTI-ADAM, E. A., VOSS-BÖHME, A. & DEUTSCH, A. 2017. Amoeboid-mesenchymal migration plasticity promotes invasion only in complex heterogeneous microenvironments. *Scientific Reports,* 7**,** 9237.

TALLEN, G., FARHANGI, S., TAMANNAI, M., HOLTKAMP, N., MANGOLDT, D., SHAH, S., SUZUKI, K., TRUSS, M., HENZE, G. & RIABOWOL, K. 2009. The inhibitor of growth 1 (ING1) proteins suppress angiogenesis and differentially regulate angiopoietin expression in glioblastoma cells. *Oncology Research Featuring Preclinical and Clinical Cancer Therapeutics,* 18**,** 95-105.

TAMURA, M., GU, J., TAKINO, T. & YAMADA, K. M. 1999. Tumor Suppressor PTEN Inhibition of Cell Invasion, Migration, and Growth: Differential Involvement of Focal Adhesion Kinase and p130Cas. *Cancer Research,* 59**,** 442.

TANIA, M., KHAN, M. A. & FU, J. 2014. Epithelial to mesenchymal transition inducing transcription factors and metastatic cancer. *Tumor Biology,* 35**,** 7335-7342.

TATEGU, M., ARAUCHI, T., TANAKA, R., NAKAGAWA, H. & YOSHIDA, K. 2007. Systems Biology-Based Identification of Crosstalk between E2F Transcription Factors and the Fanconi Anemia Pathway. *Gene Regulation and Systems Biology,* 1**,** 117762500700100001.

TENG, Y., PI, W., WANG, Y. & COWELL, J. K. 2016. WASF3 provides the conduit to facilitate invasion and metastasis in breast cancer cells through HER2/HER3 signaling. *Oncogene,* 35**,** 4633-4640.

TEPASS, U., GRUSZYNSKI-DEFEO, E., HAAG, T. A., OMATYAR, L., TÖRÖK, T. & HARTENSTEIN, V. 1996. shotgun encodes Drosophila E-cadherin and is preferentially required during cell rearrangement in the neurectoderm and other morphogenetically active epithelia. *Genes & development,* 10**,** 672-685.

THAKUR, S., SINGLA, A. K., CHEN, J., TRAN, U., YANG, Y., SALAZAR, C., MAGLIOCCO, A., KLIMOWICZ, A., JIRIK, F. & RIABOWOL, K. 2014. Reduced ING1 levels in breast cancer promotes metastasis. *Oncotarget,* 5**,** 4244-4256.

THALAPPILLY, S., FENG, X., PASTYRYEVA, S., SUZUKI, K., MURUVE, D., LAROCQUE, D., RICHARD, S., TRUSS, M., VON DEIMLING, A., RIABOWOL, K. & TALLEN, G. 2011. The p53 tumor suppressor is stabilized by inhibitor of growth 1 (ING1) by blocking polyubiquitination. *PloS one,* 6**,** e21065-e21065.

THEODOSIOU, N. A. & XU, T. 1998. Use of FLP/FRT System to Study Drosophila Development. *Methods,* 14**,** 355-365.

THEVENEAU, E. & LINKER, C. 2017. Leaders in collective migration: are front cells really endowed with a particular set of skills? *F1000Research,* 6**,** 1899-1899.

TO, T.-L., PIGGOTT, B. J., MAKHIJANI, K., YU, D., JAN, Y. N. & SHU, X. 2015. Rationally designed fluorogenic protease reporter visualizes spatiotemporal dynamics of apoptosis in vivo. *Proceedings of the National Academy of Sciences,* 112**,** 3338.

TSAI, JEFF H., DONAHER, JOANA L., MURPHY, DANIELLE A., CHAU, S. & YANG, J. 2012. Spatiotemporal Regulation of Epithelial-Mesenchymal Transition Is Essential for Squamous Cell Carcinoma Metastasis. *Cancer Cell,* 22**,** 725-736.

TUMULURI, V., THOMAS, G. A. & FRASER, I. S. 2004. The relationship of proliferating cell density at the invasive tumour front with prognostic and risk factors in human oral squamous cell carcinoma. *Journal of Oral Pathology & Medicine,* 33**,** 204-208.

UMEDA, K., IKENOUCHI, J., KATAHIRA-TAYAMA, S., FURUSE, K., SASAKI, H., NAKAYAMA, M., MATSUI, T., TSUKITA, S., FURUSE, M. & TSUKITA, S. 2006. ZO-1 and ZO-2 Independently Determine Where Claudins Are Polymerized in Tight-Junction Strand Formation. *Cell,* 126**,** 741-754.

VAEZI, A., BAUER, C., VASIOUKHIN, V. & FUCHS, E. 2002. Actin Cable Dynamics and Rho/Rock Orchestrate a Polarized Cytoskeletal Architecture in the Early Steps of Assembling a Stratified Epithelium. *Developmental Cell,* 3**,** 367-381.

VAN DE VEN, R. A. H., DE GROOT, J. S., PARK, D., VAN DOMSELAAR, R., DE JONG, D., SZUHAI, K., VAN DER WALL, E., RUEDA, O. M., ALI, H. R., CALDAS, C., VAN DIEST, P. J., HETZER, M. W., SAHAI, E. & DERKSEN, P. W. B. 2016. p120-catenin prevents multinucleation through control of MKLP1-dependent RhoA activity during cytokinesis. *Nature Communications,* 7**,** 13874.

VAN ITALLIE, C. M. & ANDERSON, J. M. 2014. Architecture of tight junctions and principles of molecular composition. *Seminars in cell & developmental biology,* 36**,** 157-165.

VAN ITALLIE, C. M., TIETGENS, A. J. & ANDERSON, J. M. 2016. Visualizing the dynamic coupling of claudin strands to the actin cytoskeleton through ZO-1. *Molecular Biology of the Cell,* 28**,** 524-534.

VEGA, F. M., FRUHWIRTH, G., NG, T. & RIDLEY, A. J. 2011. RhoA and RhoC have distinct roles in migration and invasion by acting through different targets. *Journal of Cell Biology,* 193**,** 655-665.

VEGA, S., MORALES, A. V., OCAÑA, O. H., VALDÉS, F., FABREGAT, I. & NIETO, M. A. 2004. Snail blocks the cell cycle and confers resistance to cell death. *Genes & development,* 18**,** 1131-1143.

VERMA, S., HAN, S. P., MICHAEL, M., GOMEZ, G. A., YANG, Z., TEASDALE, R. D., RATHEESH, A., KOVACS, E. M., ALI, R. G. & YAP, A. S. 2012. A WAVE2–Arp2/3 actin nucleator apparatus supports junctional tension at the epithelial zonula adherens. *Molecular Biology of the Cell,* 23**,** 4601-4610.

VIEYRA, D., LOEWITH, R., SCOTT, M., BONNEFIN, P., BOISVERT, F.-M., CHEEMA, P., PASTYRYEVA, S., MEIJER, M., JOHNSTON, R. N. & BAZETT-JONES, D. P. 2002a. Human ING1 proteins differentially regulate histone acetylation. *Journal of Biological Chemistry,* 277**,** 29832-29839.

VIEYRA, D., TOYAMA, T., HARA, Y., BOLAND, D., JOHNSTON, R. & RIABOWOL, K. 2002b. ING1 Isoforms Differentially Affect Apoptosis in a Cell Age-dependent Manner. *Cancer Research,* 62**,** 4445.

VIGNJEVIC, D. & MONTAGNAC, G. 2008. Reorganisation of the dendritic actin network during cancer cell migration and invasion. *Seminars in Cancer Biology,* 18**,** 12-22.

VINCENT, T. L. & GATENBY, R. A. 2008. An evolutionary model for initiation, promotion, and progression in carcinogenesis. *International journal of oncology,* 32**,** 729-737.

VOGELSTEIN, B., PAPADOPOULOS, N., VELCULESCU, V. E., ZHOU, S., DIAZ, L. A. & KINZLER, K. W. 2013. Cancer Genome Landscapes. *Science,* 339**,** 1546.

WALDMAN, Y. Y., GEIGER, T. & RUPPIN, E. 2013. A genome-wide systematic analysis reveals different and predictive proliferation expression signatures of cancerous vs. non-cancerous cells. *PLoS genetics,* 9**,** e1003806-e1003806.

WANG, H., SINGH, S. R., ZHENG, Z., OH, S.-W., CHEN, X., EDWARDS, K. & HOU, S. X. 2006. Rap-GEF Signaling Controls Stem Cell Anchoring to Their Niche through Regulating DE-Cadherin-Mediated Cell Adhesion in the Drosophila Testis. *Developmental Cell,* 10**,** 117-126.

WANG, K., XIE, S., REN, Y., XIA, H., ZHANG, X. & HE, J. 2012. Establishment of a bioluminescent MDA-MB-231 cell line for human triple-negative breast cancer research. *Oncology reports,* 27**,** 1981-1989.

WANG, S., YANG, J., TSAI, A., KUCA, T., SANNY, J., LEE, J., DONG, K., HARDEN, N. & KRIEGER, C. 2011. Drosophila adducin regulates Dlg phosphorylation and targeting of Dlg to the synapse and epithelial membrane. *Developmental Biology,* 357**,** 392-403.

WANG, S.-P., WANG, W.-L., CHANG, Y.-L., WU, C.-T., CHAO, Y.-C., KAO, S.-H., YUAN, A., LIN, C.-W., YANG, S.-C., CHAN, W.-K., LI, K.-C., HONG, T.-M. & YANG, P.-C. 2009. p53 controls cancer cell invasion by inducing the MDM2-mediated degradation of Slug. *Nature Cell Biology,* 11**,** 694-704.

WANG, Y., YANG, Q., CHENG, Y., GAO, M., KUANG, L. & WANG, C. 2018. Myosin Heavy Chain 10 (MYH10) Gene Silencing Reduces Cell Migration and Invasion in the Glioma Cell Lines U251, T98G, and SHG44 by Inhibiting the Wnt/β-Catenin Pathway. *Medical science monitor : international medical journal of experimental and clinical research,* 24**,** 9110-9119.

WANG, Z., TANG, F., QI, G., YUAN, S., ZHANG, G., TANG, B. & HE, S. 2014. KDM5B is overexpressed in gastric cancer and is required for gastric cancer cell proliferation and metastasis. *American journal of cancer research,* 5**,** 87-100.

WARDE-FARLEY, D., DONALDSON, S. L., COMES, O., ZUBERI, K., BADRAWI, R., CHAO, P., FRANZ, M., GROUIOS, C., KAZI, F., LOPES, C. T., MAITLAND, A., MOSTAFAVI, S., MONTOJO, J., SHAO, Q., WRIGHT, G., BADER, G. D. & MORRIS, Q. 2010. The GeneMANIA prediction server: biological network integration for gene prioritization and predicting gene function. *Nucleic Acids Research,* 38**,** W214-W220.

WATABE-UCHIDA, M., UCHIDA, N., IMAMURA, Y., NAGAFUCHI, A., FUJIMOTO, K., UEMURA, T., VERMEULEN, S., VAN ROY, F., ADAMSON, E. D. & TAKEICHI, M. 1998. α-Catenin-vinculin interaction functions to organize the apical junctional complex in epithelial cells. *The Journal of cell biology,* 142**,** 847-857.

WEE, P. & WANG, Z. 2017. Epidermal growth factor receptor cell proliferation signaling pathways. *Cancers,* 9**,** 52.

WEI, Y., CHEN, Y.-H., LI, L.-Y., LANG, J., YEH, S.-P., SHI, B., YANG, C.-C., YANG, J.-Y., LIN, C.-Y., LAI, C.-C. & HUNG, M.-C. 2011. CDK1-dependent phosphorylation of EZH2 suppresses methylation of H3K27 and promotes

osteogenic differentiation of human mesenchymal stem cells. *Nature Cell Biology,* 13**,** 87-94.
WEIGELIN, B., BAKKER, G.-J. & FRIEDL, P. 2012. Intravital third harmonic generation microscopy of collective melanoma cell invasion. *IntraVital,* 1**,** 32-43.
WEINBERG, R. A. 1994. Oncogenes and tumor suppressor genes. *CA: A Cancer Journal for Clinicians,* 44**,** 160-170.
WELLS, B. S. & JOHNSTON, L. A. 2012. Maintenance of imaginal disc plasticity and regenerative potential in Drosophila by p53. *Developmental biology,* 361**,** 263-276.
WELLS, C. D., FAWCETT, J. P., TRAWEGER, A., YAMANAKA, Y., GOUDREAULT, M., ELDER, K., KULKARNI, S., GISH, G., VIRAG, C. & LIM, C. 2006. A Rich1/Amot complex regulates the Cdc42 GTPase and apical-polarity proteins in epithelial cells. *Cell,* 125**,** 419-421.
WELLS, R. E., BARRY, J. D., WARRINGTON, S. J., CUHLMANN, S., EVANS, P., HUBER, W., STRUTT, D. & ZEIDLER, M. P. 2013. Control of tissue morphology by Fasciclin III-mediated intercellular adhesion. *Development,* 140**,** 3858.
WENG, L., ENOMOTO, A., MIYOSHI, H., TAKAHASHI, K., ASAI, N., MORONE, N., JIANG, P., AN, J., KATO, T., KURODA, K., WATANABE, T., ASAI, M., ISHIDA-TAKAGISHI, M., MURAKUMO, Y., NAKASHIMA, H., KAIBUCHI, K. & TAKAHASHI, M. 2014. Regulation of cargo-selective endocytosis by dynamin 2 GTPase-activating protein girdin. *The EMBO Journal,* 33**,** 2098-2112.
WEST, J. J. & HARRIS, T. J. C. 2016. Cadherin Trafficking for Tissue Morphogenesis: Control and Consequences. *Traffic,* 17**,** 1233-1243.
WHITEHEAD, J., VIGNJEVIC, D., FÜTTERER, C., BEAUREPAIRE, E., ROBINE, S. & FARGE, E. 2008. Mechanical factors activate ß-catenin-dependent oncogene expression in APC1638N/+ mouse colon. *HFSP journal,* 2**,** 286-294.
WILKINSON, S., PATERSON, H. F. & MARSHALL, C. J. 2005. Cdc42–MRCK and Rho–ROCK signalling cooperate in myosin phosphorylation and cell invasion. *Nature Cell Biology,* 7**,** 255-261.
WITTCHEN, E. S., HASKINS, J. & STEVENSON, B. R. 1999. Protein interactions at the tight junction actin has multiple binding partners, and zo-1 forms independent complexes with ZO-2 and ZO-3. *Journal of Biological Chemistry,* 274**,** 35179-35185.
WOICHANSKY, I., BERETTA, C. A., BERNS, N. & RIECHMANN, V. 2016. Three mechanisms control E-cadherin localization to the zonula adherens. *Nature Communications,* 7**,** 10834.
WONG, E. W. P., MRUK, D. D., LEE, W. M. & CHENG, C. Y. 2010. Regulation of blood–testis barrier dynamics by TGF-β3 is a Cdc42-dependent protein trafficking event. *Proceedings of the National Academy of Sciences,* 107**,** 11399-11404.
WU, J. S. & LUO, L. 2006. A protocol for dissecting Drosophila melanogaster brains for live imaging or immunostaining. *Nature Protocols,* 1**,** 2110-2115.
WU, M., WU, Z. F., ROSENTHAL, D. T., RHEE, E. M. & MERAJVER, S. D. 2010. Characterization of the roles of RHOC and RHOA GTPases in invasion, motility, and matrix adhesion in inflammatory and aggressive breast cancers. *Cancer,* 116**,** 2768-2782.

WU, S. K., GOMEZ, G. A., MICHAEL, M., VERMA, S., COX, H. L., LEFEVRE, J. G., PARTON, R. G., HAMILTON, N. A., NEUFELD, Z. & YAP, A. S. 2014. Cortical F-actin stabilization generates apical–lateral patterns of junctional contractility that integrate cells into epithelia. *Nature cell biology,* 16**,** 167-178.

XIE, Y., ZHANG, H., SHENG, W., XIANG, J., YE, Z. & YANG, J. 2008. Adenovirus-mediated ING4 expression suppresses lung carcinoma cell growth via induction of cell cycle alteration and apoptosis and inhibition of tumor invasion and angiogenesis. *Cancer Letters,* 271**,** 105-116.

XIN, H., YOON, H.-G., SINGH, P. B., WONG, J. & QIN, J. 2004. Components of a Pathway Maintaining Histone Modification and Heterochromatin Protein 1 Binding at the Pericentric Heterochromatin in Mammalian Cells. *Journal of Biological Chemistry,* 279**,** 9539-9546.

XOURI, G., LYGEROU, Z., NISHITANI, H., PACHNIS, V., NURSE, P. & TARAVIRAS, S. 2004. Cdt1 and geminin are down-regulated upon cell cycle exit and are over-expressed in cancer-derived cell lines. *European Journal of Biochemistry,* 271**,** 3368-3378.

YAMADA, S., POKUTTA, S., DREES, F., WEIS, W. I. & NELSON, W. J. 2005. Deconstructing the cadherin-catenin-actin complex. *Cell,* 123**,** 889-901.

YAMAZAKI, D., KURISU, S. & TAKENAWA, T. 2005. Regulation of cancer cell motility through actin reorganization. *Cancer Science,* 96**,** 379-386.

YANAGISAWA, M. & ANASTASIADIS, P. Z. 2006. p120 catenin is essential for mesenchymal cadherin–mediated regulation of cell motility and invasiveness. *Journal of Cell Biology,* 174**,** 1087-1096.

YANAGISAWA, M., HUVELDT, D., KREINEST, P., LOHSE, C. M., CHEVILLE, J. C., PARKER, A. S., COPLAND, J. A. & ANASTASIADIS, P. Z. 2008. A p120 catenin isoform switch affects Rho activity, induces tumor cell invasion, and predicts metastatic disease. *Journal of Biological Chemistry,* 283**,** 18344-18354.

YANG, Y. 2019. ING1 Impacts Ovarian Cancer by Altering EMT (Unpublished doctoral thesis). *University of Calgary, Calgary, AB.*

YANO, S., MIWA, S., MII, S., HIROSHIMA, Y., UEHARA, F., YAMAMOTO, M., KISHIMOTO, H., TAZAWA, H., BOUVET, M., FUJIWARA, T. & HOFFMAN, R. M. 2014. Invading cancer cells are predominantly in G0/G1 resulting in chemoresistance demonstrated by real-time FUCCI imaging. *Cell Cycle,* 13**,** 953-960.

YE, Y., TELLEZ, J. D., DURAZO, M., BELCHER, M., YEARSLEY, K. & BARSKY, S. H. 2010. E-cadherin accumulation within the lymphovascular embolus of inflammatory breast cancer is due to altered trafficking. *Anticancer research,* 30**,** 3903-3910.

YILMAZ, M. & CHRISTOFORI, G. 2010. Mechanisms of motility in metastasizing cells. *Mol Cancer Res,* 8**,** 629-42.

YIU, T. T. & LI, W. 2015. Pediatric cancer epigenome and the influence of folate. *Epigenomics,* 7**,** 961-973.

YONEMURA, S. 2011. Cadherin–actin interactions at adherens junctions. *Current opinion in cell biology,* 23**,** 515-522.

YONEMURA, S., WADA, Y., WATANABE, T., NAGAFUCHI, A. & SHIBATA, M. 2010. α-Catenin as a tension transducer that induces adherens junction development. *Nature cell biology,* 12**,** 533-542.

YOSHIOKA, N., FUJI, S., SHIMAKAGE, M., KODAMA, K., HAKURA, A., YUTSUDO, M., INOUE, H. & NOJIMA, H. 2002. Suppression of Anchorage-Independent Growth of Human Cancer Cell Lines by the TRIF52/Periostin/OSF-2 Gene. *Experimental Cell Research,* 279**,** 91-99.

YTHIER, D., LARRIEU, D., BRAMBILLA, C., BRAMBILLA, E. & PEDEUX, R. 2008. The new tumor suppressor genes ING: Genomic structure and status in cancer. *International Journal of Cancer,* 123**,** 1483-1490.

ZHANG, C., ELKAHLOUN, A. G., ROBERTSON, M., GILLS, J. J., TSURUTANI, J., SHIH, J. H., FUKUOKA, J., HOLLANDER, M. C., HARRIS, C. C. & TRAVIS, W. D. 2011. Loss of cytoplasmic CDK1 predicts poor survival in human lung cancer and confers chemotherapeutic resistance. *PloS one,* 6.

ZHANG, G.-J., ZHAO, J., JIANG, M.-L. & ZHANG, L.-C. 2018. ING5 inhibits cell proliferation and invasion in esophageal squamous cell carcinoma through regulation of the Akt/NF-κB/MMP-9 signaling pathway. *Biochemical and Biophysical Research Communications,* 496**,** 387-393.

ZHONG, J., YANG, L., LIU, N., ZHENG, J. & LIN, C.-Y. 2013. Knockdown of inhibitor of growth protein 2 inhibits cell invasion and enhances chemosensitivity to 5-FU in human gastric cancer cells. *Digestive diseases and sciences,* 58**,** 3189-3197.

ZIHNI, C., BALDA, M. S. & MATTER, K. 2014. Signalling at tight junctions during epithelial differentiation and microbial pathogenesis. *J Cell Sci,* 127**,** 3401-3413.

ZIHNI, C., MILLS, C., MATTER, K. & BALDA, M. S. 2016. Tight junctions: from simple barriers to multifunctional molecular gates. *Nature reviews Molecular cell biology,* 17**,** 564-580.

Appendixes

Appendix 1. CG7379 knockdown phenotypic scores in the large-scale genetic screen

Two different RNAi lines (27988, 27989) were independently used to knockdown CG7379 expression during the large-scale genetic screen. If the RNAi line was assigned a score above or below the IQR, it was considered a 'hit' for that category (highlighted in yellow).

			Cut-off		Average Scores	
Phenotype	Description	Scoring System	below	above	27988	27989
Not developed	Animal did not reach the pupal stage (lethal).	0 – No 1 – Yes			0.000	0.000
Malformed	Animal did not develop properly and was too misshapen to be mounted.	0 – No 1 – Yes			0.000	0.000
Cuticle	Folding in the supracellular cuticle.	0 – Normal 1 – Deep folding	0.133	0.867	0.545	0.400
Closure defects	Failure in the dorsal closure process.	0 – No 1 – Yes	-0.050	0.550	0.091	0.300
No clones	No labelled cells are observed.	0 – No 1 – Yes			0.000	0.000
Single cell clones	Presence of single cell clones.	0 – No 1 – Yes	-0.100	0.500	0.182	0.400

Phenotype	Description	Scoring System	Cut-off below	Cut-off above	Average Scores 27988	Average Scores 27989
continued						
Cyst-like clones	Presence of rounded cyst-like clones.	0 – No 1 – Yes	-0.100	0.100	0.000	0.000
Clonal Tissue	Percentage of tissue (notum) covered by the GFP labelled cells.	- 2 – 0-5% - 1 – 5-15% 0 – 15-35% +1 – 35-50% +2 – >50%	-0.900	0.300	-0.182	-0.100
Individual clone size	Approximate area of the individual clones.	- 1 – mostly small 0 – mixture/ mostly medium +1 – mostly large +2 – very large	-0.300	0.300	-0.182	0.000
Clonal shape	Clones were round or oval in shape.	- 1 – mostly round 0 – mixture +1 – mostly long	-0.200	0.600	0.091	0.300

Phenotype	Description	Scoring System	Cut-off		Average Scores	
			below	above	27988	27989
continued						
Junction defects	Presence of breaks in the architecture of the cortical actin ring labelled by Moe:GFP.	0 – No 1 – Yes	0.000	0.800	0.727	0.400
Dividing cells	Amount of cells in mitosis, identified by the characteristic rounding of the cortical actin ring labelled by Moe:GFP.	- 2 – none - 1 – very few 0 – medium +1 – lots +2 – extensive	-0.633	0.367	-0.091	0.100
Invading cells	Amount of cells that detached basally from the epithelium.	- 2 – none - 1 – very few 0 – medium +1 – lots +2 – extensive	-0.600	0.600	1.364	-0.100
Invading cells with protrusions	Presence of protrusions in invading cells.	0 – No 1 – Yes	-0.033	0.433	0.455	0.300

Phenotype	Description	Scoring System	Cut-off below	Cut-off above	Average Scores 27988	Average Scores 27989
continued						
Type of invasion	Describes the actin localization within the invading cell. Polarized denotes an accumulation of actin on one side of the cell.	- 1 – mostly non-polarised 0 – mixture +1 – mostly polarised	-0.300	0.500	0.455	0.200
Apex size	Estimated size of the apical area of the cells.	- 2 – very small - 1 – small 0 – normal +1 – large	-0.836	0.036	-0.091	-0.400
Defective apex	Percentage of clonal tissue comprising of cells whose apexes lost their characteristic geometrical shape.	0 – none +1 – up to 50% +2 – >50%	0.100	0.900	0.182	0.800
No apex	Percentage of clonal tissue comprising of cells that lost their polarized shape and therefore do not present an apex.	- 1 – none 0 – 0-15% +1 – 15-50% +2 – >50%	-0.400	0.400	-0.091	0.000

Phenotype	Description	Scoring System	Cut-off below	Cut-off above	Average Scores 27988	Average Scores 27989
continued						
Cell body rounding	Percentage of clonal tissue comprising of rounded cells that lost their columnar shape.	- 1 – none 0 – 0-15% +1 – 15-50% +2 – >50%	0.267	1.733	1.091	0.400
Polarised cytoskeleton	Non-symmetrical actin accumulation.	- 1 – none 0 – very few +1 – medium +2 – lots	0.000	0.800	0.545	0.400
Basal bundles	Formation of protrusions bundles.	0 – No 1 – Yes	0.000	0.600	0.273	0.700
Long apical/intermediate protrusions	Length of apical/intermediate protrusions.	0 – No 1 – Yes	-0.100	0.300	0.545	0.400
Very long protrusions	Presence of very long protrusions.	0 – No 1 – Yes	0.200	0.800	0.727	0.800

Phenotype	Description	Scoring System	Cut-off below	Cut-off above	Average Scores 27988	Average Scores 27989
continued						
Blebbing mitotic cells	Presence of membrane blebbing in mitotic cells.	0 – No 1 – Yes	-0.027	0.573	0.182	0.100
Basal actin-rich spots	Actin rich spots visible at the base of the cell.	0 – No 1 – Yes	-0.150	0.350	0.182	0.100
Thick protrusion	Protrusions wider than the characteristic protrusion width in *lgl* null clones.	0 – No 1 – Yes	-0.173	0.373	0.364	0.400
Bright protrusions	Protrusions displaying an increase in fluorescence intensity.	0 – No 1 – Yes	-0.100	0.300	0.545	0.400
Branched protrusions	Presence of branches in protrusions.	0 – No 1 – Yes	-0.189	0.411	0.636	0.400
Basal protrusions	Estimated length of basal protrusions.	-3 – absent -2 – small -1 – normal 0 – long +1 – very long	-0.500	0.500	-1.545	-0.600

Phenotype	Description	Scoring System	Cut-off below	Cut-off above	Average Scores 27988	Average Scores 27989
continued						
Apoptosis	Estimation of apoptotic events by identification of ruptured, fragmented or highly abnormal cells.	0 – none +1 – little +2 – medium +3 – lots	0.000	0.600	0.364	0.200
Multilayering	Percentage of clonal surface displaying a loss of cell contact inhibition and consequently cells growing on top of each other.	- 1 – none 0 – 0-15% +1 – 15-50% +2 – >50%	0.000	1.400	0.727	0.700
Cell length	Cell length in microns (from apex to base).	-2 – short (<7 μm) -1 – normal (8-12 μm) 0 – long (13-19 μm) +1 – very long (>20 μm)	-0.250	0.750	-0.091	-0.200

Appendix 2. List of differentially expressed genes in response to ING1 knockdown in MCF-7 cells

Gene Symbol	Transcript ID	RefSeq ID	FDR adjusted p-values	Fold-Change
ARHGAP19	TC1000012580.hg.1	NM_001204300	0.0011	-1.9
FEN1	TC1100013021.hg.1	NM_004111	0.0011	-3.7
NETO2	TC1600010181.hg.1	NM_001201477	0.0011	-2.8
SUV39H1	TC0X00007200.hg.1	NM_001282166	0.0011	-2.0
SMC1A	TC0X00009760.hg.1	NM_001281463	0.0014	-2.7
ATAD2	TC0800011679.hg.1	NM_014109	0.0016	-3.2
HIST1H2BF	TC0600007282.hg.1	NM_003522	0.0016	-2.7
KNTC1	TC1200009209.hg.1	NM_014708	0.0016	-3.2
PSMC3IP	TC1700010731.hg.1	NM_001256014	0.0016	-4.3
CENPJ	TC1300008371.hg.1	NM_018451	0.0020	-2.7
HIST1H2AG	TC0600014083.hg.1	NM_021064	0.0020	-3.4
MMS22L	TC0600012631.hg.1	NM_198468	0.0020	-3.5
CDK1	TC1000007748.hg.1	NM_001170406	0.0021	-5.6
CHEK1	TC1100013111.hg.1	NM_001114121	0.0021	-3.3
DHFR	TC0500011280.hg.1	NM_000791	0.0021	-2.3
DNAJC9	TC1000012564.hg.1	NM_015190	0.0021	-2.2
DPY30	TC0200016647.hg.1	NM_032574	0.0021	-2.6
E2F8	TC1100010290.hg.1	NM_001256371	0.0021	-4.5
FANCC	TC0900010878.hg.1	NM_000136	0.0021	-1.7
HELLS	TC1000012477.hg.1	NM_001289067	0.0021	-4.1
KIF15	TSUnmapped00000627.hg.1	ENST00000631233	0.0021	-6.5
KIFAP3	TC0100016366.hg.1	NM_001204514	0.0021	2.1

Gene Symbol	Transcript ID	RefSeq ID	FDR adjusted p-values	Fold-Change
continued				
RFC3	TC1300006847.hg.1	NM_002915	0.0021	-2.5
XRCC3	TC1400010331.hg.1	NM_001100118	0.0021	-2.8
GEMIN4	TC1700009327.hg.1	NM_015721	0.0023	-1.8
NEMP1	TC1200010946.hg.1	NM_001130963	0.0023	-3.3
NUSAP1	TC1500006999.hg.1	NM_001243142	0.0024	-3.6
MCM4	TC0800007552.hg.1	NM_005914	0.0025	-2.3
PRIM1	TC1200012804.hg.1	NM_000946	0.0025	-4.2
DDX11	TC1200007208.hg.1	NM_001257144	0.0025	-2.3
ELOVL2	TC0600010802.hg.1	NM_017770	0.0025	-2.7
FAM3B	TC2100007204.hg.1	NM_058186	0.0025	3.1
FAM83D	TC2000007341.hg.1	NM_030919	0.0025	-4.1
HIST1H3I	TC0600011233.hg.1	NM_003533	0.0025	-4.1
KIFC1	TC0600007700.hg.1	NM_002263	0.0025	-4.2
MCM10	TC1000006819.hg.1	NM_018518	0.0025	-4.9
MFSD14B	TC0900008028.hg.1	NM_032558	0.0025	-2.1
MIS18A	TC2100007949.hg.1	NM_018944	0.0025	-2.1
PHGDH	TC0100009621.hg.1	NM_006623	0.0025	-2.8
SMC4	TC0300009337.hg.1	NM_001002800	0.0025	-2.5
GINS2	TC1600011574.hg.1	NM_016095	0.0026	-5.4
ZWINT	TC1000010686.hg.1	NM_001005413	0.0027	-2.5
CDCA3	TC1200009759.hg.1	NM_001297602	0.0027	-4.3
MCM3	TC0600012038.hg.1	NM_001270472	0.0027	-2.4
ARHGAP19-SLIT1	TC1000012581.hg.1	NR_037909	0.0027	-1.7
MCM5	TC2200007206.hg.1	NM_006739	0.0031	-3.5

Gene Symbol	Transcript ID	RefSeq ID	FDR adjusted p-values	Fold-Change
continued				
DHFR	TC1800008333.hg.1	BC070280	0.0032	-2.4
ESCO2	TC0800007119.hg.1	NM_001017420	0.0032	-5.1
RFC2	TC0700011510.hg.1	NM_001278791	0.0032	-2.9
RFC5	TC1200009065.hg.1	NM_001130112	0.0032	-2.7
RNASEH2A	TC1900007098.hg.1	NM_006397	0.0032	-2.8
SPC25	TC0200014845.hg.1	NM_020675	0.0032	-5.4
POLD3	TC1100013071.hg.1	NM_006591	0.0032	-1.7
ANKRD42	TC1100008627.hg.1	NM_001300972	0.0033	2.2
UBE2T	TC0100016952.hg.1	NM_001310326	0.0033	-2.9
ARPP19	TC1500009458.hg.1	NM_001306191	0.0035	-1.7
HIST1H2AB	TC0600011125.hg.1	NM_003513	0.0035	-3.8
RACGAP1	TC1200010650.hg.1	NM_001126103	0.0035	-3.4
SPATA5	TC0400008620.hg.1	NM_145207	0.0035	-1.8
CDCA7	TC0200009994.hg.1	NM_031942	0.0035	-3.9
WDHD1	TC1400009242.hg.1	NM_001008396	0.0037	-4.1
CDC6	TC1700007790.hg.1	NM_001254	0.0038	-3.5
HIST1H3G	TC0600011142.hg.1	NM_003534	0.0038	-3.7
KIF22	TC1600007425.hg.1	NM_001256269	0.0038	-2.1
ANP32E	TC0100015725.hg.1	NM_001136478	0.0038	-3.7
EXO1	TC0100012172.hg.1	NM_003686	0.0038	-7.5
PHTF2	TC0700008149.hg.1	NM_001127357	0.0038	-3.0
RAD21	TC0800011565.hg.1	NM_006265	0.0038	-1.7
RNF26	TC1100009248.hg.1	NM_032015	0.0038	-2.4
CDT1	TC1600008845.hg.1	NM_030928	0.0038	-3.9
BLM	TC1500008328.hg.1	NM_000057	0.0041	-4.8

Gene Symbol	Transcript ID	RefSeq ID	FDR adjusted p-values	Fold-Change
continued				
EZH2	TC0700012959.hg.1	NM_001203247	0.0041	-2.1
FKBP9	TC0700007132.hg.1	NM_001284341	0.0041	-1.8
HIST1H1D	TC0600011138.hg.1	NM_005320	0.0041	-4.2
HIST1H2BG	TC0600011136.hg.1	NM_003518	0.0041	-2.5
NET1	TC1000006617.hg.1	NM_001047160	0.0041	-1.7
SLC7A1	TC1300008487.hg.1	NM_003045	0.0041	-2.0
NCAPD2	TC1200006627.hg.1	NM_014865	0.0042	-3.2
SCLT1	TC0400012964.hg.1	NM_001300897	0.0042	-2.2
CCT6A	TC0700007630.hg.1	NM_001009186	0.0042	-1.5
PKMYT1	TC1600011468.hg.1	NM_001258450	0.0042	-3.5
DTL	TC0100011512.hg.1	NM_001286229	0.0043	-6.1
RAD54L	TC0100008150.hg.1	NM_001142548	0.0043	-5.1
ASPM	TC0100016831.hg.1	NM_001206846	0.0043	-4.9
DCK	TC0400012811.hg.1	NM_000788	0.0043	-2.7
E2F7	TC1200011330.hg.1	NM_203394	0.0043	-6.0
FAM72C	TC0100015550.hg.1	NM_001287385	0.0043	-3.3
H1F0	TC2200007318.hg.1	NM_005318	0.0043	-2.1
HIST1H2BM	TC0600007377.hg.1	NM_003521	0.0043	-6.2
MND1	TC0400009037.hg.1	NM_001253861	0.0043	-5.4
NUDT3	TC0600014283.hg.1	NM_006703	0.0043	-1.6
SEPHS1	TC1000009844.hg.1	NM_001195602	0.0043	-1.5
SSRP1	TC1100010887.hg.1	NM_003146	0.0043	-2.0
HIST2H3A	TC0100009877.hg.1	ENST00000403683	0.0044	-5.8
C17orf53	TC1700007982.hg.1	NM_001171251	0.0045	-2.7
CDCA2	TC0800007065.hg.1	NM_152562	0.0045	-4.0

Gene Symbol	Transcript ID	RefSeq ID	FDR adjusted p-values	Fold-Change
continued				
HIST1H1B	TC0600011232.hg.1	NM_005322	0.0045	-4.8
LMNB1	TC0500008544.hg.1	NM_001198557	0.0045	-4.1
POLQ	TC0300012164.hg.1	NM_199420	0.0045	-3.9
OXCT1	TC0500010599.hg.1	NM_000436	0.0045	-1.8
CAMSAP2	TC0100011148.hg.1	NM_001297707	0.0047	-1.5
CENPK	TC0500010928.hg.1	NM_001267038	0.0047	-2.8
LIG1	TC1900011060.hg.1	NM_000234	0.0047	-2.7
UBE2E2	TC0300006827.hg.1	NM_152653	0.0047	-2.3
AURKA	TC2000009550.hg.1	NM_003600	0.0048	-3.3
CDCA5	TC1100013184.hg.1	NM_080668	0.0048	-5.2
CDK2	TC1200007819.hg.1	NM_001290230	0.0048	-1.8
DPYSL5	TC0200007047.hg.1	NM_001253723	0.0048	-2.1
KIF23	TC1500007699.hg.1	NM_001281301	0.0048	-3.0
SNRPB	TC2000009972.hg.1	NM_003091	0.0048	-1.5
CCNF	TC1600006610.hg.1	NM_001761	0.0049	-3.2
DEK	TC0600010962.hg.1	NM_001134709	0.0049	-1.9
CENPP	TC0900007953.hg.1	NM_001012267	0.0050	-2.1
CKS1B	TC0100010100.hg.1	NM_001826	0.0050	-2.6
SGOL1	TC0300010476.hg.1	NM_001012409	0.0050	-5.1
FANCA	TC1600011292.hg.1	NM_000135	0.0050	-3.8
KIF20B	TC1000008406.hg.1	NM_001284259	0.0051	-3.0
POLA2	TC1100008008.hg.1	NM_002689	0.0051	-3.0
TACC3	TC0400006538.hg.1	NM_006342	0.0051	-4.8
VOPP1	TC0700011139.hg.1	NM_001284282	0.0051	-2.0
HIST2H4B	TC0100009870.hg.1	NM_001034077	0.0051	-3.0

Gene Symbol	Transcript ID	RefSeq ID	FDR adjusted p-values	Fold-Change
continued				
EFNA1	TC0100010111.hg.1	NM_004428	0.0051	2.0
FANCI	TC1500008252.hg.1	NM_001113378	0.0051	-4.1
ABHD15	TC1700010247.hg.1	NM_198147	0.0053	1.6
RFC4	TC0300013447.hg.1	NM_002916	0.0053	-3.1
MELK	TC0900007129.hg.1	NM_001256685	0.0053	-3.7
TMED5	TC0100014947.hg.1	NM_001167830	0.0053	-2.0
CENPI	TC0X00007936.hg.1	NM_006733	0.0054	-5.9
E2F1	TC2000008894.hg.1	NM_005225	0.0054	-2.9
GALNT10	TC0500013261.hg.1	NM_198321	0.0054	1.6
HIST2H4A	TC0100015707.hg.1	NM_003548	0.0054	-2.9
IKBKE	TC0100011374.hg.1	NM_001193321	0.0054	1.8
UBE2S	TC1900011470.hg.1	NM_014501	0.0054	-2.7
NEK7	TC0100011096.hg.1	NM_133494	0.0054	-2.2
NUP107	TC1200008113.hg.1	NM_020401	0.0054	-1.8
RANBP1	TC2200006641.hg.1	NM_001278639	0.0054	-1.9
ATG2B	TC1400010100.hg.1	NM_018036	0.0054	1.5
GALNT7	TC0400009322.hg.1	NM_017423	0.0055	-2.8
MYBL2	TC2000007438.hg.1	NM_001278610	0.0055	-5.0
C12orf76	TC1200011894.hg.1	NM_207435	0.0055	2.1
MCM6	TC0200014404.hg.1	NM_005915	0.0055	-2.4
ACBD7	TC1000012525.hg.1	NM_001039844	0.0055	-2.1
CHN1	TC0200015002.hg.1	NM_001025201	0.0055	-1.7
CLSPN	TC0100013700.hg.1	NM_001190481	0.0055	-4.7
DIAPH3	TC1300009088.hg.1	NM_001042517	0.0055	-4.5
DNMT3B	TC2000007132.hg.1	NM_001207055	0.0055	-1.5

Gene Symbol	Transcript ID	RefSeq ID	FDR adjusted p-values	Fold-Change
continued				
EXOSC8	TC1300006890.hg.1	NM_181503	0.0055	-2.7
FN3KRP	TC1700009274.hg.1	NM_024619	0.0055	-1.6
HIST1H1C	TC0600011127.hg.1	NM_005319	0.0055	-2.9
INCENP	TC1100007833.hg.1	NM_001040694	0.0055	-2.4
LOXL3	TC0200013113.hg.1	NM_001289164	0.0055	-2.3
MNS1	TC1500009522.hg.1	NM_018365	0.0055	-3.7
NRM	TC0600011377.hg.1	NM_001270707	0.0055	-2.7
ORC1	TC0100014202.hg.1	NM_001190818	0.0055	-3.5
RMI1	TC0900007740.hg.1	NM_024945	0.0055	-2.8
SASS6	TC0100015058.hg.1	NM_001304829	0.0055	-3.5
CTDSPL	TC0300007055.hg.1	NM_001008392	0.0057	-2.0
KIF18B	TC1700010851.hg.1	NM_001264573	0.0057	-2.9
GTSE1	TC2200007662.hg.1	NM_016426	0.0058	-3.7
KNSTRN	TC1500006951.hg.1	NM_001142761	0.0058	-2.9
PCNA	TC2000008279.hg.1	NM_002592	0.0058	-3.4
TK1	TC1700011892.hg.1	NM_003258	0.0059	-4.7
SHCBP1	TC1600010168.hg.1	NM_024745	0.0060	-5.9
AGO1	TC0100007786.hg.1	NM_012199	0.0061	-2.0
CBX5	TC1200010833.hg.1	NM_001127321	0.0061	-2.3
GINS3	TC1600011405.hg.1	NM_001126129	0.0061	-1.6
POLA1	TC0X00006823.hg.1	NM_016937	0.0061	-2.3
PRIM2	TC0600014139.hg.1	NM_000947	0.0061	-2.3
SLC25A10	TC1700012315.hg.1	NM_001270888	0.0061	-1.9
VRK1	TC1400010649.hg.1	NM_003384	0.0061	-2.4
DNA2	TC1000010847.hg.1	NM_001080449	0.0063	-2.0

Gene Symbol	Transcript ID	RefSeq ID	FDR adjusted p-values	Fold-Change
continued				
HIST2H3A	TC0100015701.hg.1	NM_001005464	0.0063	-5.6
PLOD2	TC0300012718.hg.1	NM_000935	0.0063	-1.9
POLE2	TC1400009108.hg.1	NM_001197330	0.0063	-4.6
TEKT4P2	TC2100007534.hg.1	NR_038327	0.0063	1.8
TRIP13	TC0500006472.hg.1	NM_001166260	0.0063	-5.6
C4orf46	TC0400012251.hg.1	NM_001008393	0.0064	-2.3
CENPO	TC0200006977.hg.1	NM_001199803	0.0065	-2.5
NDC1	TC0100014243.hg.1	NM_001168551	0.0065	-2.3
STON2	TC1400009839.hg.1	NM_001256430	0.0065	2.4
ADAM20	TC1400009579.hg.1	NM_003814	0.0065	2.3
ADGRE5	TC1900007173.hg.1	NM_001025160	0.0065	1.6
BRCA1	TC1700010763.hg.1	NM_007294	0.0065	-3.8
CXCL12	TC1000010468.hg.1	NM_000609	0.0065	-3.4
FOXM1	TC1200009621.hg.1	NM_001243088	0.0065	-3.9
HIST1H2BJ	TC0600011184.hg.1	NM_021058	0.0065	-2.8
KHK	TC0200007053.hg.1	NM_000221	0.0065	-1.7
KIF15	TSUnmapped00000242.hg.1	ENST00000627705	0.0065	-2.0
KIF15	TSUnmapped00000127.hg.1	ENST00000625939	0.0065	-5.3
MTMR4	TC1700011260.hg.1	NM_004687	0.0065	-1.8
NCEH1	TC0300013151.hg.1	NM_001146276	0.0065	2.1
RBPJ	TC0400007120.hg.1	NM_005349	0.0065	-2.5
RHOBTB2	TC0800007004.hg.1	NM_001160036	0.0065	1.7
TMEM106C	TC1200007499.hg.1	NM_001143841	0.0065	-1.6
TOPBP1	TC0300012475.hg.1	NM_007027	0.0065	-2.0

Gene Symbol	Transcript ID	RefSeq ID	FDR adjusted p-values	Fold-Change
continued				
UHRF1	TC1900006727.hg.1	NM_001048201	0.0065	-4.0
ARHGAP11B	TC1500010709.hg.1	OTTHUMT00000430732	0.0066	-3.1
CENPE	TC0400011477.hg.1	NM_001286734	0.0066	-4.4
HADH	TC0400008348.hg.1	NM_001184705	0.0066	-1.5
WDR76	TC1500007077.hg.1	NM_001167941	0.0066	-4.1
ASF1B	TC1900009807.hg.1	NM_018154	0.0066	-3.6
BLNK	TC1000011515.hg.1	NM_001114094	0.0066	2.2
CHPT1	TC1200012698.hg.1	NM_020244	0.0066	-2.0
DDIAS	TC1100013075.hg.1	NM_145018	0.0066	-5.8
DYNLRB2	TC1600008559.hg.1	NM_001305017	0.0066	1.7
GINS1	TC2000007016.hg.1	NM_021067	0.0066	-2.8
HIST1H3B	TC0600011124.hg.1	NM_003537	0.0066	-3.8
MYH10	TC1700009694.hg.1	NM_001256012	0.0066	-1.6
SBF2	TC1100010077.hg.1	NM_030962	0.0066	1.8
SPDL1	TC0500009377.hg.1	NM_017785	0.0066	-3.1
HIST1H2BL	TC0600011224.hg.1	NM_003519	0.0066	-2.0
HJURP	TC0200016099.hg.1	NM_001282962	0.0066	-4.3
KRT81	TC1200012792.hg.1	NM_002281	0.0066	2.0
MTBP	TC0800012349.hg.1	NM_022045	0.0066	-1.7
SKA3	TC1300008280.hg.1	NM_001166017	0.0066	-2.7
ATP6V0A4	TC0700012754.hg.1	NM_020632	0.0066	2.9
HIST1H2AI	TC0600007374.hg.1	NM_003509	0.0068	-1.9
ORC6	TC1600007718.hg.1	NM_014321	0.0068	-2.8
TTLL12	TC2200008906.hg.1	NM_015140	0.0068	-2.0

Gene Symbol	Transcript ID	RefSeq ID	FDR adjusted p-values	Fold-Change
continued				
CCT2	TC1200008147.hg.1	NM_001198842	0.0069	-1.9
ELF3	TC0100011205.hg.1	NM_001114309	0.0069	1.7
GPNMB	TC0700006913.hg.1	NM_001005340	0.0069	4.6
WDR34	TC0900011650.hg.1	NM_052844	0.0069	-1.9
ERMP1	TC0900009470.hg.1	NM_024896	0.0069	-1.9
LHPP	TC1000012505.hg.1	NM_001167880	0.0069	2.1
MCMBP	TC1000012025.hg.1	NM_001256378	0.0069	-1.7
TEX15	TC0800010045.hg.1	NM_031271	0.0069	-1.8
TMPO	TC1200008568.hg.1	NM_001032283	0.0069	-2.5
APLF	TC0200016466.hg.1	OTTHUMT00000327029	0.0069	-1.5
C11orf54	TC1100008790.hg.1	NM_001286067	0.0069	1.8
KIF11	TC1000008471.hg.1	NM_004523	0.0069	-4.8
KIF15	TSUnmapped00000190.hg.1	ENST00000627473	0.0069	-2.6
NAP1L1	TC1200011313.hg.1	hsa_circ_0000422	0.0069	-1.9
HIST1H2BI	TC0600007293.hg.1	NM_003525	0.0070	-3.1
LIN9	TC0100017523.hg.1	NM_001270409	0.0070	-2.3
NOP56	TC2000006518.hg.1	NM_006392	0.0070	-1.6
RBL1	TC2000009026.hg.1	NM_002895	0.0070	-2.8
YBEY	TC2100007462.hg.1	NM_001006114	0.0070	2.5
CASP8AP2	TC0600008780.hg.1	NM_001137667	0.0070	-1.7
ECT2	TC0300009524.hg.1	NM_001258315	0.0071	-3.1
PSMC3	TC1100010738.hg.1	NM_002804	0.0071	-1.7
AURKB	TC1700009679.hg.1	NM_001256834	0.0071	-4.5
MTHFD1	TC1400007440.hg.1	NM_005956	0.0071	-1.6

Gene Symbol	Transcript ID	RefSeq ID	FDR adjusted p-values	Fold-Change
continued				
CCDC34	TC1100010397.hg.1	NM_030771	0.0071	-1.8
DDX12P	TC1200009868.hg.1	NR_033399	0.0072	-2.6
MYRFL	TC1200012664.hg.1	NM_182530	0.0072	2.5
REEP4	TC0800009830.hg.1	NM_025232	0.0072	-1.9
TMEM216	TC1100007805.hg.1	NM_001173990	0.0072	-1.5
ZNF732	TC0400012882.hg.1	NM_001137608	0.0072	-1.9
FAM72B	TC0100015509.hg.1	NM_001100910	0.0072	-3.5
NCAPH	TC0200008502.hg.1	NM_001281710	0.0073	-6.5
CDC25A	TC0300011009.hg.1	NM_001789	0.0073	-3.8
HIST1H2AM	TC0600011235.hg.1	NM_003514	0.0073	-2.8
NUP155	TC0500010515.hg.1	NM_001278312	0.0073	-1.9
CENPU	TC0400012620.hg.1	NM_024629	0.0073	-5.2
ATAD5	TC1700007469.hg.1	NM_024857	0.0074	-4.1
RTKN2	TC1000010758.hg.1	NM_001282941	0.0075	-2.1
CENPN	TC1600008567.hg.1	NM_001100624	0.0076	-2.0
CEP128	TC1400009829.hg.1	NM_152446	0.0076	-3.8
FAM72D	TC0100009723.hg.1	NM_207418	0.0076	-3.4
FREM2	TC1300006919.hg.1	NM_207361	0.0076	-1.5
TCF19	TC0600007565.hg.1	NM_001077511	0.0076	-3.1
UBE2C	TC2000007503.hg.1	NM_001281741	0.0076	-4.1
BRCA2	TC1300006802.hg.1	NM_000059	0.0077	-4.1
HIST1H3A	TC0600007262.hg.1	NM_003529	0.0077	-2.8
CDC20	TC0100008057.hg.1	NM_001255	0.0078	-4.5
STAG1	TC0300012534.hg.1	NM_005862	0.0078	-1.9
LGALS3	TC1400007227.hg.1	NM_001177388	0.0078	2.2

Gene Symbol	Transcript ID	RefSeq ID	FDR adjusted p-values	Fold-Change
continued				
SFT2D2	TC0100010525.hg.1	NM_199344	0.0079	-1.5
BARD1	TC0200015643.hg.1	NM_000465	0.0079	-2.3
MCM7	TC0700011969.hg.1	NM_001278595	0.0079	-2.7
PDE9A	TC2100007263.hg.1	NM_001001567	0.0079	3.0
PRC1	TC1500010463.hg.1	NM_001267580	0.0079	-4.0
MAD2L1	TC0400011721.hg.1	NM_002358	0.0079	-3.9
MASTL	TC1000007092.hg.1	NM_001172303	0.0081	-3.3
ANO9	TC1100009667.hg.1	NM_001012302	0.0081	1.7
RNF5	TC0600007636.hg.1	NM_006913	0.0081	-1.8
HIST1H1E	TC0600007273.hg.1	NM_005321	0.0081	-1.9
MCM2	TC0300008702.hg.1	NM_004526	0.0083	-3.4
BRIP1	TC1700011364.hg.1	NM_032043	0.0083	-3.4
CDC45	TC2200006607.hg.1	NM_001178010	0.0083	-6.4
CDCA4	TC1400010394.hg.1	NM_017955	0.0083	-2.4
CDKN1A	TC0600007847.hg.1	NM_000389	0.0083	3.0
DEPDC1	TC0100014543.hg.1	NM_001114120	0.0083	-5.5
GMNN	TC0600007207.hg.1	NM_001251989	0.0083	-2.8
MAGED1	TC0X00007267.hg.1	NM_001005332	0.0083	1.7
NCAPG2	TC0700013290.hg.1	NM_001281932	0.0083	-4.1
NEK2	TC0100017216.hg.1	NM_001204182	0.0083	-3.3
PIM1	TC0600007862.hg.1	NM_001243186	0.0083	-2.7
RRM1	TC1100006644.hg.1	NM_001033	0.0083	-2.3
STX4	TC1600011387.hg.1	NM_001272095	0.0083	1.5
TNFRSF21	TC0600011960.hg.1	NM_014452	0.0083	-1.6
ZDHHC13	TC1100007026.hg.1	NM_001001483	0.0083	-1.5

Gene Symbol	Transcript ID	RefSeq ID	FDR adjusted p-values	Fold-Change
continued				
HMGB3	TC0X00008724.hg.1	NM_001301228	0.0086	-2.2
MKI67	TC1000012235.hg.1	NM_001145966	0.0087	-4.5
RILP	TC1700009393.hg.1	NM_031430	0.0087	1.9
ARHGAP11B	TC1500006785.hg.1	NM_001039841	0.0088	-4.5
MR1	TC0100010815.hg.1	NM_001194999	0.0088	2.5
CCP110	TC1600007112.hg.1	NM_001199022	0.0090	-2.3
CEP78	TC0900007663.hg.1	NM_001098802	0.0090	-2.7
CLN6	TC1500010887.hg.1	NM_017882	0.0090	-1.6
CNPY4	TC0700008524.hg.1	NM_152755	0.0090	1.8
H2AFX	TC1100012513.hg.1	NM_002105	0.0090	-2.5
HAUS6	TC0900009645.hg.1	NM_001270890	0.0090	-1.7
MYBL1	TC0800010685.hg.1	NM_001080416	0.0090	-2.8
PLSCR3	TC1700009637.hg.1	NM_001201576	0.0090	2.1
ZWILCH	TC1500007616.hg.1	NM_001287821	0.0090	-2.8
CSE1L	TC2000007627.hg.1	NM_001256135	0.0090	-1.8
CD82	TC1100007394.hg.1	NM_001024844	0.0090	2.0
DNMT1	TC1900011860.hg.1	NM_001130823	0.0090	-1.8
HIST1H2AJ	TC0600011225.hg.1	NM_021066	0.0090	-2.3
PHF19	TC0900011388.hg.1	NM_001009936	0.0090	-2.2
ARL3	TC1000011690.hg.1	NM_004311	0.0091	-1.5
CDK12	TC1700012245.hg.1	ENST00000558240	0.0092	1.7
CYP2S1	TC1900008141.hg.1	NM_030622	0.0092	-1.5
KIF20A	TC0500008777.hg.1	NM_005733	0.0092	-4.5
SYNE2	TC1400007430.hg.1	NM_015180	0.0092	-2.7
TTK	TC0600008630.hg.1	NM_001166691	0.0093	-5.7

Gene Symbol	Transcript ID	RefSeq ID	FDR adjusted p-values	Fold-Change
continued				
A4GALT	TC2200008888.hg.1	NM_017436	0.0094	-2.0
ZNF98	TC1900011920.hg.1	NM_001098626	0.0094	-1.8
CENPM	TC2200008847.hg.1	NM_001002876	0.0095	-3.6
NPY1R	TC0400012305.hg.1	NM_000909	0.0095	-2.9
NEMP2	TC0200015231.hg.1	NM_001142645	0.0095	-1.9
ORAI3	TC1600011386.hg.1	NM_152288	0.0096	2.5
FBXO5	TC0600013602.hg.1	NM_001142522	0.0096	-3.0
POLE	TC1200012533.hg.1	NM_006231	0.0096	-2.3
ITGA2	TC0500007368.hg.1	NM_002203	0.0096	-2.1
SLC31A2	TC0900008482.hg.1	NM_001860	0.0097	1.6
SSU72	TC0100012487.hg.1	NM_014188	0.0097	-1.9
BCAS1	TC2000009516.hg.1	NM_003657	0.0098	5.3
CASC5	TC1500006963.hg.1	NM_144508	0.0098	-4.6
RASSF3	TC1200008005.hg.1	NM_178169	0.0098	-1.7
SNX25	TC0400009519.hg.1	NM_031953	0.0098	2.0
MSH6	TC0200016445.hg.1	NM_000179	0.0098	-1.8
ZNF85	TC1900007502.hg.1	NM_001256171	0.0098	-1.5
TBC1D31	TC0800008726.hg.1	NM_001145088	0.0099	-1.9
DCBLD2	TC0300011815.hg.1	NM_080927	0.0100	-1.8
DCLRE1A	TC1000011885.hg.1	NM_001271816	0.0100	-2.0
DPY19L4	TC0800008266.hg.1	NM_181787	0.0100	-1.5
DSN1	TC2000009016.hg.1	NM_001145315	0.0100	-2.7
FANCB	TC0X00009117.hg.1	NM_001018113	0.0100	-2.4
ITGB3BP	TC0100014428.hg.1	NM_001206739	0.0100	-4.3
LMCD1	TC0300006520.hg.1	NM_001278233	0.0100	-1.5

Gene Symbol	Transcript ID	RefSeq ID	FDR adjusted p-values	Fold-Change
continued				
PRR3	TC0600007534.hg.1	NM_025263	0.0100	-1.7
RET	TC1000007403.hg.1	NM_020630	0.0100	-1.5
TYMS	TC1800006448.hg.1	NM_001071	0.0100	-3.8
ERCC6L	TC0X00010025.hg.1	NM_017669	0.0101	-2.8
ESPL1	TC1200007707.hg.1	NM_012291	0.0101	-1.8
FAM72A	TC0100017094.hg.1	NM_001123168	0.0101	-3.7
ZBTB7B	TC0100010104.hg.1	NM_001252406	0.0101	1.8
CCNA2	TC0400011748.hg.1	NM_001237	0.0102	-4.8
S100A13	TC0100015873.hg.1	NM_001024210	0.0102	1.6
FAM111B	TC1100007727.hg.1	NM_001142703	0.0103	-7.8
MED1	TC1700010571.hg.1	NM_004774	0.0103	-1.8
SUSD3	TC0900007976.hg.1	NM_001287005	0.0103	-1.7
PNP	TC1400006521.hg.1	NM_000270	0.0104	-1.5
NDC80	TC1800006484.hg.1	NM_006101	0.0104	-5.9
DUT	TC1500007163.hg.1	NM_001025248	0.0104	-2.1
ODC1	TC0200011720.hg.1	NM_001287188	0.0104	-1.7
GABPB1	TC1500009386.hg.1	NM_002041	0.0104	-1.8
FIGNL1	TC0700011050.hg.1	NM_001042762	0.0106	-3.0
PRR11	TC1700012285.hg.1	NM_018304	0.0106	-4.3
FANCD2	TC0300006575.hg.1	NM_001018115	0.0106	-3.8
PSMG3	TC0700010020.hg.1	NM_001134340	0.0106	-1.6
B3GALNT1	TC0300012975.hg.1	NM_001038628	0.0106	-1.6
CNOT6	TC0500009725.hg.1	NM_001303241	0.0106	-1.8
RUNDC3B	TC0700008261.hg.1	NM_001134405	0.0106	2.9
DUS2	TC1600011416.hg.1	NM_001271762	0.0107	-2.2

Gene Symbol	Transcript ID	RefSeq ID	FDR adjusted p-values	Fold-Change
continued				
CIT	TC1200012143.hg.1	NM_001206999	0.0108	-4.6
EXOSC9	TC0400008604.hg.1	NM_001034194	0.0108	-1.9
KRCC1	TC0200013357.hg.1	NM_001304526	0.0109	1.6
PARPBP	TC1200008642.hg.1	NM_017915	0.0109	-2.3
BRI3BP	TC1200009300.hg.1	NM_080626	0.0109	-2.5
ARHGAP11B	TC1500010707.hg.1	BC105788	0.0110	-3.7
CHMP4C	TC0800008088.hg.1	NM_152284	0.0110	1.6
DLGAP5	TC1400009248.hg.1	NM_001146015	0.0110	-5.8
HMGB2	TC0400012432.hg.1	NM_001130688	0.0110	-3.5
MFAP3L	TC0400012992.hg.1	NM_001009554	0.0110	2.4
PUS10	TC0200012727.hg.1	NM_144709	0.0110	1.8
SLC17A5	TC0600012299.hg.1	NM_012434	0.0110	1.9
TCOF1	TC0500009088.hg.1	NM_000356	0.0110	-2.2
VAMP3	TC0100006723.hg.1	NM_004781	0.0110	-2.1
ANKH	TC0500010169.hg.1	NM_054027	0.0110	-1.9
CDCA7L	TC0700010435.hg.1	NM_001127370	0.0110	-2.7
CCL3	TC1700010459.hg.1	NM_002983	0.0110	-1.6
CDCA8	TC0100007841.hg.1	NM_001256875	0.0110	-3.8
RAD51AP1	TC1200006561.hg.1	NM_001130862	0.0112	-5.0
TRAPPC1	TC1700012352.hg.1	NM_001166621	0.0113	-2.0
DHTKD1	TC1000006794.hg.1	NM_018706	0.0115	-1.9
EBP	TC0X00007191.hg.1	NM_006579	0.0115	-1.5
C14orf80	TC1400010705.hg.1	NM_001134875	0.0115	-1.8
TMX1	TC1400007139.hg.1	NM_030755	0.0115	-1.6
TPX2	TC2000007089.hg.1	NM_012112	0.0115	-3.1

Gene Symbol	Transcript ID	RefSeq ID	FDR adjusted p-values	Fold-Change
continued				
KIF14	TC0100016891.hg.1	NM_001305792	0.0115	-5.3
CEP55	TC1000008482.hg.1	NM_001127182	0.0116	-6.0
RAD51	TC1500006965.hg.1	NM_001164269	0.0116	-3.8
POC1A	TC0300011154.hg.1	NM_001161580	0.0116	-2.2
C19orf48	TC1900011221.hg.1	NM_001290149	0.0118	-1.8
H2AFZ	TC0400011424.hg.1	NM_002106	0.0119	-2.1
PARP2	TC1400006513.hg.1	NM_001042618	0.0119	-1.8
CCNB1	TC0500007665.hg.1	NM_031966	0.0119	-3.4
GAS2L3	TC1200008597.hg.1	NM_001303130	0.0119	-3.9
KIF15	TSUnmapped00000496.hg.1	ENST00000629073	0.0119	-2.1
SPAST	TC0200007174.hg.1	NM_014946	0.0119	-2.0
BUB1	TC0200013878.hg.1	NM_001278616	0.0119	-4.7
ZNF519	TC1800009258.hg.1	NM_145287	0.0119	-1.5
MSH2	TC0200016442.hg.1	NM_000251	0.0121	-1.5
SLITRK4	TC0X00011012.hg.1	NM_001184749	0.0121	-1.5
AOX1	TC0200010421.hg.1	NM_001159	0.0122	3.5
JADE1	TC0400008680.hg.1	NM_001287437	0.0122	-2.0
XRCC2	TC0700013119.hg.1	NM_005431	0.0122	-5.1
ZNF670	TC0100018081.hg.1	NM_001204220	0.0122	-2.3
ZAK	TC0200009986.hg.1	NM_016653	0.0122	-1.9
KIF15	TSUnmapped00000255.hg.1	ENST00000627272	0.0124	-3.9
MAPRE3	TC0200007048.hg.1	NM_001303050	0.0124	2.4
BIRC5	TC1700009043.hg.1	NM_001012270	0.0128	-3.4
SNX24	TC0500008483.hg.1	NM_014035	0.0131	-1.8

Gene Symbol	Transcript ID	RefSeq ID	FDR adjusted p-values	Fold-Change
continued				
TOP2A	TC1700010618.hg.1	NM_001067	0.0131	-4.4
ARMC1	TC0800010663.hg.1	NM_001286702	0.0134	-1.9
CKAP2	TC1300007248.hg.1	NM_001098525	0.0134	-2.2
EPHX2	TC0800007110.hg.1	NM_001256482	0.0134	1.8
GEN1	TC0200006833.hg.1	NM_001130009	0.0134	-2.1
PINX1	TC0800012386.hg.1	NM_001284356	0.0134	-1.5
GPN2	TC0100013408.hg.1	NM_018066	0.0134	-1.7
PIGK	TC0100014638.hg.1	NM_005482	0.0134	-1.6
RRM2	TC0200006677.hg.1	NM_001034	0.0136	-4.0
MCM8	TC2000006628.hg.1	NM_001281520	0.0136	-2.6
CDRT1	TC1700012361.hg.1	NM_001282540	0.0136	3.7
PIK3C2B	TC0100017029.hg.1	NM_002646	0.0136	1.5
NUF2	TC0100010397.hg.1	NM_031423	0.0137	-6.4
HIST1H4A	TC0600007263.hg.1	NM_003538	0.0139	-3.5
SNRPG	TC0200012994.hg.1	NM_003096	0.0139	-1.8
BBS4	TC1500007804.hg.1	NM_001252678	0.0140	1.7
CDC25C	TC0500012166.hg.1	NM_001287582	0.0140	-4.4
HAUS8	TC1900009943.hg.1	NM_001011699	0.0140	-1.5
ZNF107	TC0700013370.hg.1	NM_001013746	0.0140	-1.7
QSER1	TC1100007217.hg.1	NM_001076786	0.0140	-1.5
TMEM97	TC1700007360.hg.1	NM_014573	0.0140	-2.3
SIAH2	TC0300012807.hg.1	NM_005067	0.0140	-1.7
RBL2	TC1600007887.hg.1	NM_005611	0.0140	1.5
RIBC2	TC2200007615.hg.1	NM_015653	0.0140	-1.7
LINC00493	TC2000009895.hg.1	NR_015432	0.0143	1.5

Gene Symbol	Transcript ID	RefSeq ID	FDR adjusted p-values	Fold-Change
continued				
LRRC28	TC1500008511.hg.1	NM_001284400	0.0143	1.5
HIST1H4D	TC0600011134.hg.1	NM_003539	0.0145	-2.6
DERL1	TC0800011669.hg.1	NM_001134671	0.0145	-1.6
ZNF211	TC1900011819.hg.1	NM_001265597	0.0145	1.9
ARL6IP1	TC1600011494.hg.1	NM_015161	0.0147	-1.8
FLYWCH1	TC1600006644.hg.1	NM_001308068	0.0147	1.5
LOC728554	TC0500013271.hg.1	NR_003615	0.0147	-1.7
RAD54B	TC0800011137.hg.1	NM_001205262	0.0148	-3.0
NCS1	TC0900008949.hg.1	NM_001128826	0.0149	-1.9
RAI14	TC0500007114.hg.1	NM_001145520	0.0150	-1.8
RAB26	TC1600006593.hg.1	NM_001308053	0.0150	2.3
CYP2J2	TC0100014365.hg.1	NM_000775	0.0151	1.7
STIL	TC0100018440.hg.1	NM_001048166	0.0151	-3.1
RNASEL	TC0100016629.hg.1	NM_021133	0.0151	1.9
HIST1H2AL	TC0600007380.hg.1	NM_003511	0.0153	-2.1
IGBP1	TC0X00007529.hg.1	NM_001551	0.0153	1.8
CCNB2	TC1500007392.hg.1	NM_004701	0.0155	-4.3
HIBCH	TC0200015225.hg.1	NM_014362	0.0156	1.5
PLK1	TC1600007235.hg.1	NM_005030	0.0157	-3.5
TIMELESS	TC1200010917.hg.1	NM_003920	0.0157	-2.4
DBF4B	TC1700008011.hg.1	NM_025104	0.0157	-1.9
THOC3	TC0500013414.hg.1	NM_032361	0.0157	-1.5
HIST1H3F	TC0600011140.hg.1	NM_021018	0.0158	-3.1
LBR	TC0100017488.hg.1	NM_002296	0.0158	-2.1
GATSL3	TC2200009337.hg.1	NM_001037666	0.0158	1.7

Gene Symbol	Transcript ID	RefSeq ID	FDR adjusted p-values	Fold-Change
continued				
NEIL3	TC0400009396.hg.1	NM_018248	0.0159	-3.0
VPS13D	TC0100006884.hg.1	NM_015378	0.0159	1.9
ANLN	TC0700007198.hg.1	NM_001284301	0.0161	-3.9
CDV3	TC0300008863.hg.1	NM_001134422	0.0161	-1.7
KPNA2	TC1700008719.hg.1	NM_002266	0.0161	-2.1
NEU1	TC0600011463.hg.1	ENST00000375631	0.0161	2.1
KIAA0101	TC1500009738.hg.1	NM_001029989	0.0162	-4.4
TUBB2B	TC0600010572.hg.1	NM_178012	0.0166	-1.5
CHTF18	TC1600006501.hg.1	NM_022092	0.0166	-1.5
MBOAT1	TC0600010991.hg.1	NM_001080480	0.0166	-3.0
NPHP3	TC0300014050.hg.1	NM_153240	0.0166	1.5
RTN4	TC0200016672.hg.1	NM_007008	0.0167	-1.5
SPIN4	TC0X00009867.hg.1	NM_001012968	0.0168	-1.7
ZBTB2	TC0600013570.hg.1	NM_020861	0.0172	-1.6
KDM1A	TC0100007303.hg.1	NM_001009999	0.0172	-1.5
NASP	TC0100008127.hg.1	NM_001195193	0.0172	-2.3
HIST3H2BB	TC0100011871.hg.1	NM_175055	0.0172	-2.4
SP110	TC0200015976.hg.1	NM_001185015	0.0172	2.1
LRR1	TC1400007086.hg.1	NM_152329	0.0172	-2.9
CCND1	TC1100008236.hg.1	NM_053056	0.0172	-2.0
FAM214B	TC0900009933.hg.1	NM_025182	0.0172	1.8
EXOC5	TC1400009295.hg.1	NM_006544	0.0173	-1.6
GSKIP	TC1400008116.hg.1	NM_001271904	0.0173	1.6
SERHL2	TC2200007525.hg.1	NM_001284334	0.0173	3.7
SLC16A4	TC0100015234.hg.1	NM_001201546	0.0173	2.5

Gene Symbol	Transcript ID	RefSeq ID	FDR adjusted p-values	Fold-Change
continued				
TMEM163	TC0200014382.hg.1	NM_030923	0.0175	2.7
P2RX2	TC1200009497.hg.1	NM_001282164	0.0175	3.3
TROAP	TC1200007559.hg.1	NM_001100620	0.0177	-3.1
NCKAP5	TC0200014362.hg.1	NM_207363	0.0178	2.0
PKIB	TC0600009327.hg.1	NM_001270393	0.0181	-2.3
UNG	TC1200008792.hg.1	NM_003362	0.0182	-1.5
ID1	TC2000007083.hg.1	NM_002165	0.0182	3.4
ARL15	TC0500010731.hg.1	NM_019087	0.0182	2.3
PBK	TC0800009970.hg.1	NM_001278945	0.0182	-4.7
MDC1	TC0600011379.hg.1	ENST00000376406	0.0185	-2.7
ZNFX1	TC2000010022.hg.1	NM_021035	0.0186	1.7
RELL2	TC0500008902.hg.1	NM_001130029	0.0187	1.7
EME1	TC1700008251.hg.1	NM_001166131	0.0190	-1.6
GRK6	TC0500009622.hg.1	NM_001004105	0.0190	-1.5
CDK5R1	TC1700007520.hg.1	NM_003885	0.0190	-1.5
KIF2C	TC0100008101.hg.1	NM_001297655	0.0191	-5.2
FANCE	TC0600007799.hg.1	NM_021922	0.0192	-1.7
BUB1B	TC1500010715.hg.1	NM_001211	0.0192	-3.3
LSM4	TC1900010011.hg.1	NM_001252129	0.0192	-1.5
ERLIN1	TC1000012584.hg.1	NM_001100626	0.0192	-1.5
SAT1	TC0X00006799.hg.1	NM_002970	0.0192	2.5
GPSM2	TC0100009333.hg.1	NM_013296	0.0193	-3.1
KIF18A	TC1100010418.hg.1	NM_031217	0.0193	-3.9
SLC29A1	TC0600008127.hg.1	NM_001078175	0.0195	-2.1
NUP85	TC1700008895.hg.1	NM_001303276	0.0196	-1.6

Gene Symbol	Transcript ID	RefSeq ID	FDR adjusted p-values	Fold-Change
continued				
HIP1	TC0700011556.hg.1	NM_001243198	0.0197	-1.7
SCRN1	TC0700010619.hg.1	NM_001145513	0.0197	-1.7
SPAG5	TC1700012380.hg.1	NM_006461	0.0197	-4.0
PPIL1	TC0600011674.hg.1	NM_016059	0.0197	-1.5
CKAP5	TC1100010713.hg.1	NM_001008938	0.0197	-1.5
FMO5	TC0100015629.hg.1	NM_001144829	0.0197	1.9
KIAA1524	TC0300011943.hg.1	NM_020890	0.0197	-4.0
RPA3	TC0700010247.hg.1	NM_002947	0.0197	-2.6
USP2	TC1100012526.hg.1	NM_001243759	0.0199	2.6
DENND6B	TC2200009153.hg.1	NM_001001794	0.0201	1.8
NCAPG	TC0400006994.hg.1	NM_022346	0.0201	-5.5
HMMR	TC0500009320.hg.1	NM_001142556	0.0202	-4.0
HIST1H2AE	TC0600007285.hg.1	NM_021052	0.0203	-2.4
ZNF829	TC1900010543.hg.1	NM_001037232	0.0204	-2.2
SGK3	TC0800012313.hg.1	NM_001033578	0.0204	-2.5
SLC35D2	TC0900010910.hg.1	NM_001286990	0.0206	1.9
TRAIP	TC0300011083.hg.1	NM_005879	0.0206	-2.3
ARHGAP21	TC1000010065.hg.1	NM_020824	0.0211	-1.7
ETFDH	TC0400009132.hg.1	NM_001281737	0.0212	1.5
LCA5L	TC2100008171.hg.1	NM_152505	0.0212	1.9
CCNE2	TC0800011148.hg.1	NM_057749	0.0215	-4.6
CENPQ	TC0600008209.hg.1	NM_018132	0.0215	-2.3
IGF1R	TC1500008485.hg.1	NM_000875	0.0216	-1.5
CCDC109B	TC0400008380.hg.1	NM_017918	0.0217	-2.0
DNAJA1	TC0900006961.hg.1	NM_001539	0.0217	-1.9

Gene Symbol	Transcript ID	RefSeq ID	FDR adjusted p-values	Fold-Change
continued				
HEATR5B	TC0200012256.hg.1	NM_019024	0.0217	1.8
LMNB2	TC1900011841.hg.1	NM_032737	0.0217	-1.8
PISD	TC2200008487.hg.1	NM_014338	0.0217	1.7
MFSD13A	TC1000008733.hg.1	NM_024789	0.0217	-1.8
C5orf34	TC0500010641.hg.1	NM_198566	0.0217	-2.8
HMGN3	TC0600012363.hg.1	NM_001201362	0.0217	-1.9
GMCL1	TC0200007929.hg.1	NM_178439	0.0217	-1.7
GSAP	TC0700011586.hg.1	NM_017439	0.0221	1.9
VASP	TC1900008329.hg.1	NM_003370	0.0221	1.6
HIPK3	TC1100007227.hg.1	NM_001048200	0.0222	-1.6
CKLF	TC1600011408.hg.1	NM_001040138	0.0222	-1.8
CDKN3	TC1400007201.hg.1	NM_001130851	0.0222	-4.1
ENPP5	TC0600011943.hg.1	NM_001290072	0.0222	2.1
TRIM59	TC0300014075.hg.1	NM_173084	0.0223	-1.7
DTYMK	TC0200016369.hg.1	NM_001165031	0.0223	-2.1
ELMO2	TC2000009268.hg.1	NM_133171	0.0225	1.5
KPNA3	TC1300008926.hg.1	NM_002267	0.0225	-1.8
HIST1H2BH	TC0600007290.hg.1	NM_003524	0.0225	-1.8
CECR5	TC2200007892.hg.1	NM_017829	0.0227	-1.8
TICRR	TC1500008267.hg.1	NM_001308025	0.0227	-2.0
DNAJC16	TC0100006989.hg.1	NM_001287811	0.0227	1.7
ARHGAP12	TC1000010239.hg.1	NM_001270695	0.0229	1.6
CDC7	TC0100009020.hg.1	NM_001134419	0.0229	-2.2
PHLDB1	TC1100009212.hg.1	NM_001144758	0.0232	1.7
HECTD3	TC0100013998.hg.1	NM_024602	0.0232	1.5

Gene Symbol	Transcript ID	RefSeq ID	FDR adjusted p-values	Fold-Change
continued				
SKP2	TC0500007143.hg.1	NM_001243120	0.0232	-1.7
SLC27A2	TC1500007196.hg.1	NM_001159629	0.0232	-2.5
SLC16A1	TC0100015310.hg.1	NM_001166496	0.0232	-2.8
FAM64A	TC1700006696.hg.1	NM_001195228	0.0233	-2.9
TTF2	TC0100009561.hg.1	NM_003594	0.0233	-1.7
C1orf112	TC0100010553.hg.1	NM_018186	0.0233	-2.4
NYNRIN	TC1400006741.hg.1	NM_025081	0.0234	2.6
N4BP2	TC0400007306.hg.1	NM_018177	0.0234	-2.2
PALLD	TC0400009258.hg.1	NM_001166108	0.0234	-2.1
LACTB	TC1500007513.hg.1	NM_001288585	0.0235	2.3
PLK4	TC0400008664.hg.1	NM_001190799	0.0235	-4.9
RANGAP1	TC2200008819.hg.1	NM_001278651	0.0235	-1.5
TRMU	TC2200009288.hg.1	ENST00000476901	0.0235	-3.3
HERPUD1	TC1600007982.hg.1	NM_001010989	0.0237	3.1
NPNT	TC0400008331.hg.1	NM_001033047	0.0237	-1.6
GOLGB1	TC0300012170.hg.1	NM_001256486	0.0237	1.7
SGPL1	TC1000007936.hg.1	NM_003901	0.0237	1.5
TTLL3	TC0300013787.hg.1	NM_001025930	0.0241	2.0
ING1	TC1300008025.hg.1	NM_001267728	0.0243	-1.7
HIST2H2BF	TC0100015696.hg.1	NM_001024599	0.0245	-2.0
ACOT7	TC0100012675.hg.1	NM_007274	0.0245	-1.8
KLHL42	TC1200007163.hg.1	NM_020782	0.0245	-1.6
VPS9D1	TC1600011290.hg.1	NM_004913	0.0245	1.7
ZCCHC14	TC1600011168.hg.1	NM_015144	0.0247	-2.0
SHMT1	TC1700009974.hg.1	NM_001281786	0.0248	-1.5

Gene Symbol	Transcript ID	RefSeq ID	FDR adjusted p-values	Fold-Change
continued				
TM7SF2	TC1100013040.hg.1	NM_001277233	0.0248	1.8
RFWD3	TC1600010858.hg.1	NM_018124	0.0249	-1.9
CALML4	TC1500010886.hg.1	NM_001031733	0.0249	-1.8
LYAR	TC0400009856.hg.1	NM_001145725	0.0253	-1.6
TCP11L2	TC1200008726.hg.1	NM_001286262	0.0254	4.0
COMMD7	TC2000008860.hg.1	NM_001099339	0.0254	1.5
CCDC186	TC1000011892.hg.1	NM_018017	0.0255	1.6
CNIH2	TC1100008069.hg.1	NM_182553	0.0255	-2.7
KLC4	TC0600008069.hg.1	NM_001289034	0.0255	1.7
ARHGEF39	TC0900009948.hg.1	NM_032818	0.0256	-3.1
MRPL17	TC1100009983.hg.1	NM_022061	0.0257	-1.5
CERK	TC2200009028.hg.1	NM_022766	0.0258	-1.6
KIF15	TC0300007223.hg.1	NM_020242	0.0258	-3.3
NUP43	TC0600013531.hg.1	NM_198887	0.0258	-1.8
ANO6	TC1200007418.hg.1	NM_001025356	0.0261	-1.8
ZDHHC11	TC0500013282.hg.1	NM_024786	0.0261	1.9
MYO19	TC1700012391.hg.1	NM_001033580	0.0261	-1.6
ACOX3	TC0400009978.hg.1	NM_001101667	0.0261	2.2
C6orf52	TC0600010790.hg.1	NM_001145020	0.0261	1.8
DEPDC1B	TC0500010865.hg.1	NM_001145208	0.0261	-4.3
MRPS33	TC0700012824.hg.1	NM_016071	0.0264	-2.1
DHX33	TC1700012342.hg.1	NM_001199699	0.0267	-1.8
HIST1H2BE	TC0600007278.hg.1	NM_003523	0.0267	-1.7
NDE1	TC1600007014.hg.1	NM_017668	0.0267	-1.7
PARP11	TC1200012739.hg.1	NM_001286521	0.0267	1.6

Gene Symbol	Transcript ID	RefSeq ID	FDR adjusted p-values	Fold-Change
continued				
SIPA1L1	TC1400007595.hg.1	NM_001284245	0.0267	1.9
USP1	TC0100008554.hg.1	NM_001017415	0.0267	-1.7
C6orf203	TC0600009002.hg.1	NM_001142468	0.0268	1.8
SMC2	TC0900008286.hg.1	NM_001042550	0.0268	-2.5
CCDC92	TC1200012863.hg.1	ENST00000542348	0.0269	2.2
PLEKHO1	TC0100018288.hg.1	NM_001304722	0.0269	-1.8
TAF5	TC1000008769.hg.1	NM_006951	0.0269	-1.7
FKBP5	TC0600011635.hg.1	NM_001145775	0.0270	-1.5
MGST3	TC0100010454.hg.1	NM_004528	0.0270	1.6
TBC1D3B	TC1700012321.hg.1	NM_001001417	0.0270	1.5
WASF3	TC1300006658.hg.1	NM_001291965	0.0271	1.5
KCNQ5	TC0600008509.hg.1	NM_001160130	0.0272	-2.3
C1QL1	TC1700010856.hg.1	NM_006688	0.0272	-1.6
MVP	TC1600011378.hg.1	NM_001293204	0.0272	3.2
PNRC1	TC0600008757.hg.1	NM_006813	0.0272	1.8
CRLF3	TC1700010293.hg.1	NM_015986	0.0272	-1.7
ARHGAP26	TC0500008941.hg.1	NM_001135608	0.0272	1.5
BCAS3	TC1700008499.hg.1	NM_001099432	0.0272	1.6
NUP50	TC2200007607.hg.1	NM_007172	0.0272	-1.6
PCDHB16	TC0500013244.hg.1	NM_020957	0.0272	-1.9
SCMH1	TC0100013854.hg.1	NM_001031694	0.0272	-1.6
TOE1	TC0100008121.hg.1	NM_025077	0.0272	-1.5
SRSF7	TC0200012297.hg.1	NM_001031684	0.0273	-1.5
QPRT	TC1600011375.hg.1	NM_014298	0.0274	2.1
SUV39H2	TC1000006859.hg.1	NM_001193424	0.0275	-2.0

Gene Symbol	Transcript ID	RefSeq ID	FDR adjusted p-values	Fold-Change
continued				
PSIP1	TC0900009592.hg.1	NM_001128217	0.0276	-2.1
ST8SIA4	TC0500011579.hg.1	NM_005668	0.0277	1.5
PINK1	TC0100007207.hg.1	NM_032409	0.0279	1.7
KDELC2	TC1100012229.hg.1	NM_153705	0.0279	-1.8
TMEM209	TC0700012596.hg.1	NM_001301163	0.0279	-1.5
TMEM116	TC1200011961.hg.1	NM_001193453	0.0280	1.5
TMEM38B	TC0900008318.hg.1	NM_018112	0.0280	-2.1
MOB1B	TC0400012810.hg.1	NM_001244766	0.0281	-2.4
KDM5B	TC0100016963.hg.1	NM_006618	0.0281	2.4
CFAP53	TC1800008677.hg.1	NM_145020	0.0281	1.8
RAB27B	TC1800007360.hg.1	NM_004163	0.0283	1.9
HNRNPA1L2	TC1300007250.hg.1	NM_001011724	0.0284	-1.6
CENPA	TC0200016417.hg.1	NM_001042426	0.0284	-4.0
HIST2H2AB	TC0100015711.hg.1	NM_175065	0.0284	-2.1
KIF4A	TC0X00007537.hg.1	NM_012310	0.0285	-5.1
SPRY1	TC0400008628.hg.1	NM_001258038	0.0287	2.5
BCAR3	TC0100014958.hg.1	NM_001261408	0.0287	2.0
C7orf60	TC0700012296.hg.1	NM_152556	0.0288	1.9
PHLDB2	TC0300008324.hg.1	NM_001134437	0.0288	2.0
ABHD4	TC1400006652.hg.1	NM_022060	0.0288	1.5
ENTPD1	TC1000012482.hg.1	NM_001098175	0.0290	3.6
CTPS1	TC0100007980.hg.1	NM_001301237	0.0292	-1.9
KLHL23	TC0200016563.hg.1	NM_144711	0.0292	-2.4
PCP4	TC2100007176.hg.1	NM_006198	0.0292	-2.0
SIRT2	TC1900010632.hg.1	NM_001193286	0.0293	1.6

Gene Symbol	Transcript ID	RefSeq ID	FDR adjusted p-values	Fold-Change
continued				
COTL1	TC1600011060.hg.1	NM_021149	0.0294	-1.5
MYB	TC0600009534.hg.1	NM_001130172	0.0294	-1.7
RABGAP1L	TC0100010672.hg.1	NM_001035230	0.0294	1.7
MTERF2	TC1200011811.hg.1	NM_001033050	0.0296	1.7
AFF3	TC0200013616.hg.1	NM_001025108	0.0297	-1.9
GSN	TC0900012167.hg.1	NM_000177	0.0298	1.9
TEAD2	TC1900012000.hg.1	NM_001256658	0.0300	-1.5
PTTG1	TC0500009281.hg.1	NM_001282382	0.0301	-4.5
BORA	TC1300007483.hg.1	NM_001286746	0.0302	-1.8
REXO1L1P	TC0800011000.hg.1	ENST00000379010	0.0302	-1.6
GSG2	TC1700006592.hg.1	NM_031965	0.0303	-3.8
ARSB	TC0500011228.hg.1	NM_000046	0.0304	-1.8
PARP3	TC0300007454.hg.1	NM_001003931	0.0304	1.7
CDKN2C	TC0100008260.hg.1	NM_001262	0.0305	-1.9
STMN1	TC0100013369.hg.1	NM_001145454	0.0305	-2.6
UACA	TC1500009921.hg.1	NM_001008224	0.0305	-1.5
S100A14	TC0100015872.hg.1	NM_020672	0.0306	1.5
RTTN	TC1800008978.hg.1	NM_173630	0.0306	-1.8
HYOU1	TSUnmapped00000517.hg.1	ENST00000628429	0.0306	-1.5
KCTD11	TC1700006741.hg.1	NM_001002914	0.0306	1.7
MFAP3	TC0500013260.hg.1	ENST00000518497	0.0307	2.3
TCAF2	TC0700009508.hg.1	NM_001130025	0.0307	1.9
ATP7A	TC0X00007707.hg.1	NM_000052	0.0308	1.7
CELSR3	TC0300013973.hg.1	NM_001407	0.0308	1.6

Gene Symbol	Transcript ID	RefSeq ID	FDR adjusted p-values	Fold-Change
continued				
DLL1	TC0600014031.hg.1	NM_005618	0.0308	1.6
KIFC2	TC0800009262.hg.1	NM_145754	0.0308	1.6
MAPK8IP3	TC1600006561.hg.1	NM_001040439	0.0308	1.6
SLC25A19	TC1700011746.hg.1	NM_001126121	0.0308	-1.7
TOM1L2	TC1700009954.hg.1	NM_001033551	0.0308	2.3
RAB19	TC0700009369.hg.1	NM_001008749	0.0308	3.1
CACYBP	TC0100010686.hg.1	NM_001007214	0.0309	-1.5
CORO1A	TC1600007448.hg.1	NM_001193333	0.0309	-1.9
PRKDC	TC0800010360.hg.1	NM_001081640	0.0309	-1.5
TNFAIP8L1	TC1900006711.hg.1	NM_001167942	0.0311	-1.9
EI24	TC1100009419.hg.1	NM_001290135	0.0311	-1.6
ANXA3	TC0400007933.hg.1	NM_005139	0.0312	1.9
FAM234B	TC1200006905.hg.1	NM_020853	0.0312	1.9
STAT1	TC0200015242.hg.1	NM_007315	0.0312	1.5
APOBEC3B	TC2200009270.hg.1	NM_001270411	0.0312	-2.2
CPT1B	TC2200009364.hg.1	NM_001145134	0.0312	1.5
ERMAP	TC0100008033.hg.1	NM_001017922	0.0315	2.1
RCC2	TC0100013087.hg.1	NM_001136204	0.0315	-1.6
ENDOV	TC1700009128.hg.1	NM_001164637	0.0315	1.7
CCDC77	TC1200006444.hg.1	NM_001130146	0.0316	-1.9
TMEM167B	TC0100009339.hg.1	NM_020141	0.0318	1.6
FADS3	TC1100011052.hg.1	NM_021727	0.0318	1.6
PRELID3A	TC1800006733.hg.1	NM_001142405	0.0319	-1.7
C16orf59	TC1600006614.hg.1	NM_025108	0.0319	-1.5
WTAP	TC0600010056.hg.1	NM_001270531	0.0319	-1.5

Gene Symbol	Transcript ID	RefSeq ID	FDR adjusted p-values	Fold-Change
continued				
C6orf106	TC0600011594.hg.1	NM_022758	0.0320	-1.7
BUB3	TC1000009172.hg.1	NM_001007793	0.0323	-1.5
C5AR1	TC1900011770.hg.1	NM_001736	0.0323	2.0
GLB1L2	TC1100009618.hg.1	NM_138342	0.0323	-1.6
NMU	TC0400010750.hg.1	NM_001292045	0.0323	-2.5
NUP188	TC0900012181.hg.1	NM_015354	0.0323	-1.7
SACM1L	TC0300007242.hg.1	NM_014016	0.0323	-1.5
SCIN	TC0700006735.hg.1	NM_001112706	0.0323	-1.9
ZNF385B	TC0200015093.hg.1	NM_001113397	0.0323	-2.4
SYTL4	TC0X00010331.hg.1	NM_001129896	0.0324	-1.6
NIPSNAP3A	TC0900008297.hg.1	NM_015469	0.0324	1.7
AP1S2	TC0X00009139.hg.1	NM_001272071	0.0325	-1.8
CASP7	TC1000008954.hg.1	NM_001227	0.0329	-1.9
PAPD5	TC1600007811.hg.1	NM_001040284	0.0329	-2.3
QDPR	TC0400012905.hg.1	NM_000320	0.0329	1.5
TONSL	TC0800012214.hg.1	NM_013432	0.0329	-1.9
CALCR	TC0700011803.hg.1	NM_001164737	0.0330	4.7
PTP4A1	TC0600014142.hg.1	NM_003463	0.0330	-1.6
HLA-DQB1	TC0600011499.hg.1	NM_001243961	0.0331	1.9
PDE4A	TC1900006985.hg.1	NM_001111307	0.0331	-1.8
TRIM5	TC1100009940.hg.1	NM_033034	0.0332	1.9
CACNB2	TC1000006917.hg.1	NM_000724	0.0333	1.7
POLR3G	TC0500008054.hg.1	NM_006467	0.0333	-2.1
ZDHHC11	TC0500009824.hg.1	ZDHHC11.rAug10-unspliced	0.0333	1.9

Gene Symbol	Transcript ID	RefSeq ID	FDR adjusted p-values	Fold-Change
continued				
ADIPOR2	TC1200006472.hg.1	NM_024551	0.0333	2.0
FLOT2	TC1700010218.hg.1	NM_004475	0.0335	-1.7
RNFT2	TC1200009031.hg.1	NM_001109903	0.0335	-1.6
ALYREF	TC1700012078.hg.1	NM_005782	0.0338	-1.5
RSPH3	TC0600013740.hg.1	NM_031924	0.0339	1.8
SPECC1L-ADORA2A	TC2200009234.hg.1	NR_103546	0.0340	-1.8
DBF4	TC0700008263.hg.1	NM_006716	0.0340	-1.6
ZGRF1	TC0400011620.hg.1	NM_018392	0.0340	-3.3
CREBRF	TC0500009488.hg.1	NM_001168393	0.0340	2.1
E2F2	TC0100013287.hg.1	NM_004091	0.0340	-2.1
RBM14	TC1100013050.hg.1	NM_001198836	0.0341	-1.5
ADCY6	TC1200010592.hg.1	NM_015270	0.0342	1.5
DLEU2	TC1300008938.hg.1	NR_002612	0.0342	-2.5
HS6ST3	TC1300007761.hg.1	NM_153456	0.0342	1.6
SYF2	TC0100013348.hg.1	NM_015484	0.0342	1.6
PTRHD1	TC0200011990.hg.1	NM_001013663	0.0344	1.5
TRIM3	TC1100009971.hg.1	NM_001248006	0.0344	1.6
BCL2L12	TC1900008551.hg.1	NM_001040668	0.0347	-1.8
FHIT	TC0300011324.hg.1	NM_001166243	0.0347	1.8
DPEP3	TC1600010664.hg.1	NM_001129758	0.0349	-1.5
RPA2	TC0100013455.hg.1	NM_001286076	0.0351	-1.8
RBPMS2	TC1500009756.hg.1	NM_194272	0.0353	-2.1
CHRM1	TC1100011110.hg.1	NM_000738	0.0353	1.6
COLEC12	TC1800007850.hg.1	NM_130386	0.0353	-1.5

Gene Symbol	Transcript ID	RefSeq ID	FDR adjusted p-values	Fold-Change
continued				
MIR4728	TC1700012249.hg.1	NR_039881	0.0353	1.9
PSCA	TC0800009154.hg.1	NM_005672	0.0353	3.1
WNT10B	TC1200010606.hg.1	NM_003394	0.0353	-1.5
Sep-07	TC0700007178.hg.1	NM_001011553	0.0353	-1.5
DSCC1	TC0800011626.hg.1	NM_024094	0.0353	-2.6
CCND3	TC0600011809.hg.1	NM_001136017	0.0354	-1.6
GINS4	TC0800007416.hg.1	NM_032336	0.0355	-2.9
MCCC1	TC0300013334.hg.1	NM_001293273	0.0355	1.7
CSTA	TC0300008550.hg.1	NM_005213	0.0357	1.9
RAPGEF2	TC0400012857.hg.1	NM_014247	0.0358	1.7
B4GALNT1	TC1200012813.hg.1	NM_001276468	0.0359	-1.5
NKRF	TC0X00010642.hg.1	NM_001173487	0.0359	-1.5
GBP2	TC0100018451.hg.1	NM_004120	0.0360	2.0
HEBP1	TC1200009981.hg.1	NM_015987	0.0360	1.9
CENPW	TC0600009381.hg.1	NM_001012507	0.0362	-3.0
HIST2H2AA3	TC0100009876.hg.1	NM_003516	0.0363	-1.8
MIS18BP1	TC1400009066.hg.1	NM_018353	0.0363	-2.1
KIAA1683	TC1900010008.hg.1	NM_001145304	0.0364	1.6
ARHGAP32	TC1100012794.hg.1	NM_001142685	0.0364	1.7
DNAH3	TC1600009671.hg.1	NM_017539	0.0364	1.7
FAM214A	TC1500009460.hg.1	NM_001286495	0.0364	2.3
CALCOCO1	TC1200010812.hg.1	NM_001143682	0.0365	2.2
CENPF	TC0100011581.hg.1	NM_016343	0.0365	-5.6
WDR60	TC0700013493.hg.1	NM_018051	0.0365	1.6
PROM2	TC0200008462.hg.1	NM_001165977	0.0366	1.7

Gene Symbol	Transcript ID	RefSeq ID	FDR adjusted p-values	Fold-Change
continued				
EMCN	TC0400012948.hg.1	NM_001159694	0.0366	1.7
ID2	TC0200006627.hg.1	NM_002166	0.0366	2.6
NR1D2	TC0300006847.hg.1	NM_001145425	0.0367	-1.5
TDP2	TC0600011067.hg.1	NM_016614	0.0372	-1.5
HLA-DRB1	TC0600014273.hg.1	NM_001243965	0.0373	1.5
TBX4	TC1700008514.hg.1	NM_018488	0.0373	2.2
ADD3	TC1000008875.hg.1	NM_001121	0.0377	-2.1
DMC1	TC2200008704.hg.1	NM_001278208	0.0377	-2.2
C2orf27A	TC0200009350.hg.1	NM_013310	0.0378	2.2
PRMT5	TC1400008684.hg.1	NM_001039619	0.0378	-1.5
PTK2B	TC0800007102.hg.1	NM_004103	0.0379	1.8
ACY1	TC0300013839.hg.1	NM_000666	0.0380	1.5
ZNF18	TC1700009781.hg.1	NM_001303281	0.0380	1.8
RRAGD	TC0600012544.hg.1	NM_021244	0.0382	2.0
ERBB2	TC1700012250.hg.1	ENST00000584888	0.0385	2.2
CCDC14	TC0300012216.hg.1	NM_001308317	0.0387	-1.5
SHANK2	TC1100011485.hg.1	NM_012309	0.0389	2.1
ARHGEF28	TC0500007780.hg.1	NM_001080479	0.0391	-1.7
BLMH	TC1700010274.hg.1	NM_000386	0.0391	-1.9
MPG	TC1600006439.hg.1	NM_001015052	0.0391	1.7
HIST1H2BO	TC0600007384.hg.1	NM_003527	0.0396	-2.2
NCAPD3	TC1100012917.hg.1	NM_015261	0.0396	-1.7
PRTFDC1	TC1000010070.hg.1	NM_001282786	0.0397	-1.7
MAZ	TC1600011376.hg.1	NM_001042539	0.0398	-1.5
CCDC149	TC0400010256.hg.1	NM_001130726	0.0400	1.6

Gene Symbol	Transcript ID	RefSeq ID	FDR adjusted p-values	Fold-Change
continued				
KIAA0825	TC0500011478.hg.1	NM_001145678	0.0400	2.0
TERT	TC0500009852.hg.1	NM_001193376	0.0400	-1.6
RILPL1	TC1200012273.hg.1	NM_178314	0.0401	1.5
CCDC146	TC0700013394.hg.1	NM_020879	0.0402	2.9
GSTCD	TC0400008329.hg.1	NM_001031720	0.0404	-1.5
EFR3A	TC0800008916.hg.1	NM_015137	0.0405	-2.2
LSP1P3	TC0500007016.hg.1	NR_033961	0.0407	1.5
SEMA3C	TC0700011626.hg.1	NM_006379	0.0408	-1.5
MMAA	TC0400008912.hg.1	NM_172250	0.0409	1.7
SLC35A1	TC0600014154.hg.1	NM_001168398	0.0414	1.7
CTNND1	TC1100013004.hg.1	NM_001085458	0.0415	1.5
HCN3	TC0100010121.hg.1	NM_020897	0.0415	1.8
EOGT	TC0300011448.hg.1	NM_001278689	0.0417	1.8
PIGW	TC1700007636.hg.1	NM_178517	0.0417	-1.8
RIIAD1	TC0100009969.hg.1	NM_001144956	0.0417	3.3
SPINT1	TC1500006972.hg.1	NM_001032367	0.0417	1.6
IFNAR2	TC2100008494.hg.1	NM_000874	0.0417	-1.5
LRRC49	TC1500007735.hg.1	NM_001199017	0.0418	-2.2
DLG2	TC1100011812.hg.1	NM_001142699	0.0418	3.6
ZKSCAN7	TSUnmapped0000000 01.hg.1	ENST00000625422	0.0419	-1.6
SSBP2	TC0500013336.hg.1	NM_001256732	0.0420	1.6
KAT2B	TC0300006791.hg.1	NM_003884	0.0422	2.8
PSRC1	TC0100015192.hg.1	NM_001005290	0.0422	-2.2
MTHFD1L	TC0600009851.hg.1	NM_001242767	0.0424	-1.7

Gene Symbol	Transcript ID	RefSeq ID	FDR adjusted p-values	Fold-Change
continued				
HSD17B14	TC1900011099.hg.1	NM_016246	0.0425	2.5
DIAPH1	TC0500012280.hg.1	NM_001079812	0.0428	-1.5
MPPED2	TC1100010440.hg.1	NM_001145399	0.0431	-2.1
ANKMY2	TC0700010352.hg.1	NM_020319	0.0432	1.8
CDYL2	TC1600010966.hg.1	NM_152342	0.0432	1.8
GPR155	TC0200014991.hg.1	NM_001033045	0.0432	1.9
IRF6	TC0100017172.hg.1	NM_001206696	0.0432	2.5
PPFIBP2	TC1100006760.hg.1	NM_001256568	0.0432	2.5
TMTC2	TC1200008322.hg.1	NM_152588	0.0432	1.5
TUBB4B	TC0900009274.hg.1	NM_006088	0.0432	-1.6
XAF1	TC1700006709.hg.1	NM_017523	0.0432	-1.6
CLMN	TC1400010071.hg.1	NM_024734	0.0433	1.7
TBL1XR1	TC0300013215.hg.1	NM_024665	0.0433	-2.2
RAD18	TC0300010186.hg.1	NM_020165	0.0434	-1.8
CYP4B1	TC0100018230.hg.1	NM_000779	0.0436	2.3
ZNF737	TC1900011915.hg.1	NM_001159293	0.0436	1.6
C7orf49	TC0700012695.hg.1	NM_001243749	0.0437	-1.7
FAM107B	TC1000009863.hg.1	NM_001282695	0.0437	2.1
TFDP1	TC1300008144.hg.1	NM_007111	0.0437	-1.7
ZNF382	TC1900007947.hg.1	NM_001256838	0.0437	1.5
GGH	TC0800010630.hg.1	NM_003878	0.0437	-3.2
GREB1	TC0200006725.hg.1	NM_014668	0.0437	-1.9
OLFM1	TC0900009145.hg.1	NM_001282611	0.0437	-1.5
CKS2	TC0900007863.hg.1	NM_001827	0.0439	-2.3
NUCB2	TC1100012976.hg.1	NM_005013	0.0441	1.5

Gene Symbol	Transcript ID	RefSeq ID	FDR adjusted p-values	Fold-Change
continued				
ABCC5	TC0300013360.hg.1	NM_001023587	0.0441	2.0
RAB3GAP1	TC0200009431.hg.1	NM_001172435	0.0441	-2.0
REV3L	TC0600012863.hg.1	NM_001286431	0.0443	-1.7
AAAS	TC1200010798.hg.1	NM_001173466	0.0445	-1.5
ENPP4	TC0600008156.hg.1	NM_014936	0.0445	-1.5
GEMIN2	TC1400006965.hg.1	NM_001009182	0.0445	-1.9
IPO9	TC0100011192.hg.1	NM_018085	0.0445	-1.6
KIF16B	TC2000008473.hg.1	NM_001199865	0.0445	1.7
NGEF	TC0200016074.hg.1	NM_001114090	0.0446	1.6
FRS2	TC1200008142.hg.1	NM_001042555	0.0446	-1.8
SLC33A1	TC0300012881.hg.1	NM_001190992	0.0452	1.9
UCK2	TC0100018315.hg.1	NM_012474	0.0456	-1.6
SIAE	TC1100012681.hg.1	NM_001199922	0.0457	1.6
OLFM2	TC1900009603.hg.1	NM_001304347	0.0458	1.6
FBXL17	TC0500011655.hg.1	NM_001163315	0.0458	1.8
THOP1	TC1900006600.hg.1	NM_003249	0.0458	-1.5
RBM24	TC0600007084.hg.1	NM_001143941	0.0460	-2.1
GCOM1	TC1500010744.hg.1	NM_001018090	0.0460	2.5
SLC8B1	TC1200011993.hg.1	NM_024959	0.0466	1.5
SIK1	TC2100008297.hg.1	ENST00000270162	0.0472	1.8
YPEL5	TC0200007132.hg.1	NM_001127399	0.0472	2.1
FAM174A	TC0500008202.hg.1	NM_198507	0.0477	1.5
MBNL3	TC0X00010837.hg.1	NM_001170701	0.0477	-1.5
HIST1H3D	TC0600011135.hg.1	NM_003530	0.0477	-1.5
PVALB	TC2200008621.hg.1	NM_002854	0.0477	4.6

Gene Symbol	Transcript ID	RefSeq ID	FDR adjusted p-values	Fold-Change
continued				
PPP2R3A	TC0300008904.hg.1	NM_001190447	0.0478	1.6
FAM47E	TC0400007894.hg.1	NM_001136570	0.0479	1.5
CHEK2	TC2200008367.hg.1	NM_001005735	0.0480	-2.0
TMEM92	TC1700008247.hg.1	NM_001168215	0.0481	1.5
ASPH	TC0800010607.hg.1	NM_001164750	0.0481	-1.5
HMGB1	TC1300008517.hg.1	NM_002128	0.0484	-1.7
KPNB1	TC1700008133.hg.1	NM_001276453	0.0484	-1.5
PLBD1	TC1200010006.hg.1	NM_024829	0.0485	2.2
DYNC2LI1	TC0200007401.hg.1	NM_001193464	0.0486	1.7
ATP8B2	TC0100010075.hg.1	NM_001005855	0.0486	1.7
CHAF1B	TC2100008508.hg.1	NM_005441	0.0486	-2.8
DNAJC4	TC1100013032.hg.1	NM_001307980	0.0486	1.9
IFNGR2	TC2100006967.hg.1	NM_005534	0.0486	1.5
TUBD1	TC1700011298.hg.1	NM_001193609	0.0486	-2.0
ZNF367	TC0900010913.hg.1	NM_153695	0.0486	-2.2
CTSV	TC0900010933.hg.1	NM_001201575	0.0487	-2.0
NACC2	TC0900011962.hg.1	NM_144653	0.0488	1.8
RAD51C	TC1700008438.hg.1	NM_002876	0.0488	-1.6
RHOC	TC0100018463.hg.1	NM_001042678	0.0488	1.7
NUP205	TC0700009253.hg.1	NM_015135	0.0488	-1.5
POLD4	TC1100013191.hg.1	NM_001256870	0.0488	1.7
GSTM2	TC0100018262.hg.1	NM_000848	0.0489	1.6
HIST1H4C	TC0600007268.hg.1	NM_003542	0.0491	-2.3
LMAN2L	TC0200013535.hg.1	NM_001142292	0.0495	-1.6
RCC1	TC0100007559.hg.1	NM_001048194	0.0496	-1.5

Gene Symbol	Transcript ID	RefSeq ID	FDR adjusted p-values	Fold-Change
continued				
ERCC1	TC1900010941.hg.1	NM_001166049	0.0498	1.7
RNASET2	TC0600014371.hg.1	NM_003730	0.0498	2.0
TOM1	TC2200007196.hg.1	NM_001135729	0.0498	1.8
GSTM4	TC0100018261.hg.1	NM_000850	0.0498	1.6
PKMYT1	TC1600011467.hg.1	ENST00000382240	0.0498	-1.7

Appendix 3. Biological processes and pathways significantly enriched by ING1 knockdown differentially expressed genes and correlated diseases

ID	Term	Bonferroni adjusted p-value*	No. genes	Genes
Biological processes (GOTERM_BP_DIRECT)				
GO:0051301	Cell division	2.23E-43	97	ITGB3BP, KIFC1, KNTC1, AURKA, PTTG1, CDCA8, RAD21, CDCA7, MIS18A, CDCA2, CDCA5, CCNA2, CDCA4, CDCA3, STAG1, LIG1, TACC3, NCAPD3, NCAPD2, DCLRE1A, MAD2L1, TIMELESS, RCC2, SPAG5, ZWINT, MCMBP, CDCA7L, NUP43, NEK2, CHEK2, RCC1, SPC25, VRK1, NCAPG2, FBXO5, SKA3, HELLS, ERCC6L, CKAP5, NUF2, ARPP19, SPDL1, CDC20, NDC80, REEP4, FAM64A, SMC1A, BORA, FAM83D, CCNE2, KIF2C, NDE1, MASTL, CDC7, KIF14, CDC6, CDK1, KIF11, DSN1, CCNF, TPX2, PAPD5, UBE2C, CDK2, MCM5, CCND1, CCND3, BUB1B, HAUS8, UBE2S, MAPRE3, CKS1B, HAUS6, NCAPH, NCAPG, BUB1, KLHL42, ZWILCH, BUB3, PSRC1, KIF18B, CENPF, BIRC5, CENPE, CDC25C, KNSTRN, SMC2, CENPJ, SIRT2, CDC25A, SMC4, CCNB1, CCNB2, CKS2, KIF20B, CENPW, MIS18BP1.

ID	Term	Bonferroni adjusted p-value*	No. genes	Genes
Biological processes – continued				
GO:0006260	DNA replication	9.46E-37	62	CLSPN, DBF4, NAP1L1, MCM10, CDT1, MCM8, CDC45, MCM7, ORC6, ORC1, CDC7, CDK1, CDC6, DTL, LIG1, POLE, TOPBP1, MCM2, MCM3, RNASEH2A, MCM4, RMI1, MCM5, CDK2, MCM6, RFC5, RFC3, RFC4, TIMELESS, RFC2, RRM2, RRM1, DSCC1, BLM, TICRR, KIAA0101, POLA1, CHEK1, POLA2, RPA3, RPA2, POLE2, FEN1, EXO1, GINS2, SSRP1, GINS3, NASP, GINS4, BRIP1, CDC25C, BRCA1, CDC25A, POLD3, DNA2, POLD4, PCNA, CHTF18, RBM14, CHAF1B, BARD1, DUT.
GO:0007067	Mitotic nuclear division	1.13E-31	71	ITGB3BP, KIF22, BORA, KNTC1, PKMYT1, AURKA, PTTG1, AURKB, FAM83D, KIF2C, RAD21, INCENP, MIS18A, CDCA2, MASTL, CDCA5, CCNA2, ASPM, CDCA3, STAG1, CDK1, CDC6, KIF11, KIF15, CCNF, TPX2, PAPD5, PBK, CDK2, DCLRE1A, RCC2, TIMELESS, MCMBP, BUB1B, HAUS8, MAPRE3, NUP43, HAUS6, NEK2, ANLN, CEP55, RCC1, SPC25, VRK1, NCAPG2, BUB1, SKA3, FBXO5, KLHL42, ZWILCH, HELLS, ERCC6L, CENPN, CKAP5, ARPP19, NUF2, CENPF, NDC80, CDC20, BIRC5, CDC25C, REEP4, SIRT2, CDC25A, FAM64A, CCNB2, PLK1, KIF20B, CENPW, MIS18BP1, CIT.

ID	Term	Bonferroni adjusted p-value*	No. genes	Genes
Biological processes – continued				
GO:0007062	Sister chromatid cohesion	2.47E-31	48	ITGB3BP, KIF22, RAD51C, KNTC1, RANGAP1, AURKB, SPC25, KIF2C, CDCA8, NDE1, RAD21, DDX11, CENPA, INCENP, BUB1, ZWILCH, CDCA5, BUB3, STAG1, ERCC6L, CENPO, CENPN, CENPM, CKAP5, DSN1, CENPQ, CENPP, NUF2, KIF18A, CENPF, NUP85, NDC80, SPDL1, CENPE, BIRC5, CDC20, CENPK, CENPI, MAD2L1, RCC2, PLK1, ZWINT, MCMBP, BUB1B, CENPU, NUP107, SMC1A, NUP43.
GO:0000082	G1/S transition of mitotic cell cycle	2.34E-24	42	CRLF3, DBF4, POLA1, PKMYT1, POLA2, RCC1, MCM10, RPA3, CDT1, CCNE2, PRIM1, RPA2, TYMS, CDC45, MCM8, MCM7, POLE2, CDKN2C, PRIM2, FBXO5, RANBP1, ORC6, ORC1, CDCA5, CDC7, CDK1, CDC6, POLE, SKP2, MCM2, MCM3, CDKN3, MCM4, MCM5, CDK2, CDC25A, MCM6, CCND1, CDKN1A, DHFR, RRM2, PCNA.
GO:0000722	Telomere maintenance via recombination	2.97E-17	22	RAD51C, XRCC3, LIG1, POLE, POLA1, BRCA2, POLA2, RAD51, RPA3, RFC5, POLD3, PRIM1, POLD4, RPA2, DNA2, RFC3, RFC4, POLE2, RFC2, PRIM2, PCNA, FEN1.

ID	Term	Bonferroni adjusted p-value*	No. genes	Genes
Biological processes – continued				
GO:0006281	DNA repair	4.58E-16	51	KIF22, CLSPN, RAD51C, XRCC3, XRCC2, PTTG1, DDX11, FANCI, FANCA, FANCC, CDK1, GEN1, LIG1, POLE, TOPBP1, CDK2, RAD51, RFC5, UHRF1, RFWD3, FANCD2, RAD18, DMC1, UBE2T, BLM, ENDOV, TICRR, FOXM1, UNG, POLA1, CHEK1, RPA3, POLE2, POLQ, FEN1, ERCC1, EXO1, MSH6, SSRP1, RAD51AP1, MSH2, EME1, RAD54L, BRCA1, TEX15, PARPBP, PARP3, SMC1A, RBM14, PARP2, CHAF1B.
GO:0006270	DNA replication initiation	1.06E-15	21	CDC7, CDC6, GINS4, POLE, POLA1, TOPBP1, POLA2, MCM2, MCM10, MCM3, MCM4, MCM5, MCM6, CCNE2, PRIM1, CDC45, MCM7, POLE2, PRIM2, ORC6, ORC1.
GO:0006334	Nucleosome assembly	2.47E-15	36	HMGB2, NAP1L1, HIST2H4A, HIST2H4B, HIST1H2BO, HIST1H2BM, HIST1H4A, HIST1H2BL, CENPA, HIST1H2BI, HIST1H2BJ, H2AFX, HIST1H4C, HIST1H4D, ASF1B, HIST3H2BB, H1F0, HIST2H3A, HIST1H1E, HIST1H1D, HIST1H1C, HIST1H2BE, HIST1H2BF, HIST1H1B, NASP, HIST1H2BG, HIST1H2BH, ANP32E, MCM2, HIST2H2BF, HIST1H3A, HIST1H3B, HIST1H3D, HIST1H3F, HIST1H3G, HIST1H3I.

ID	Term	Bonferroni adjusted p-value*	No. genes	Genes
Biological processes – continued				
GO:0000070	Mitotic sister chromatid segregation	7.77E-11	16	KIFC1, NEK2, DSN1, NUSAP1, KIF18B, NDC80, ESPL1, KNSTRN, SMC4, MAD2L1, PLK1, CENPA, SPAG5, ZWINT, SMC1A, BUB3.
GO:0000086	G2/M transition of mitotic cell cycle	1.19E-10	33	HAUS6, NEK2, FOXM1, BORA, CEP78, PKMYT1, AURKA, CHEK1, CHEK2, HMMR, NDE1, MASTL, TUBB4B, CDK1, WNT10B, CCP110, CKAP5, ARPP19, SKP2, TPX2, BIRC5, CDC25C, CENPJ, CDK2, CDC25A, CCNB1, CDKN1A, PLK4, CCNB2, PLK1, HAUS8, CIT, MELK.
GO:0006271	DNA strand elongation involved in DNA replication	1.42E-10	13	GINS1, GINS2, GINS3, GINS4, POLA1, POLA2, PRIM1, POLD3, POLD4, RFC3, RFC4, PRIM2, PCNA.
GO:0000731	DNA synthesis involved in DNA repair	1.64E-10	18	EXO1, RAD51C, XRCC3, RAD51AP1, XRCC2, BLM, POLE, POLA1, BRCA2, BRIP1, RMI1, BRCA1, RAD51, POLD3, POLD4, DNA2, RFC3, BARD1.

ID	Term	Bonferroni adjusted p-value*	No. genes	Genes
Biological processes – continued				
GO:0034080	CENP-A containing nucleosome assembly	7.5E-10	19	ITGB3BP, CENPO, CENPN, CENPM, CENPQ, CENPP, HIST2H4A, CENPK, CENPI, HIST2H4B, HIST1H4A, HJURP, CENPA, MIS18A, CENPW, HIST1H4C, HIST1H4D, MIS18BP1, CENPU.
GO:0007059	Chromosome segregation	8.63E-09	22	CENPN, KIF11, NEK2, DSN1, NUF2, CENPF, NDC80, CENPE, RCC1, KNSTRN, ESCO2, BRCA1, SPC25, NDE1, SPAG5, HJURP, INCENP, MIS18A, CDCA2, CENPW, SKA3, TOP2A.
GO:0006302	Double-strand break repair	3.68E-07	20	APLF, MSH2, LIG1, EME1, MND1, BRIP1, PRKDC, BRCA2, CHEK2, ESCO2, BRCA1, RAD21, TDP2, PARP3, H2AFX, POLQ, CDCA5, ERCC1, FEN1, TRIP13.
GO:0000281	Mitotic cytokinesis	5.59E-07	14	CKAP2, KIF23, BBS4, KIF4A, CENPA, PLK1, NUSAP1, ANLN, STMN1, CEP55, RACGAP1, SPAST, KIF20A, MYH10.

ID	Term	Bonferroni adjusted p-value*	No. genes	Genes
Biological processes – continued				
GO:0008283	Cell proliferation	1.69E-06	48	STIL, CKS1B, CDK5R1, CDV3, ZAK, ERBB2, E2F8, DTYMK, POLA1, PRKDC, AURKB, MCM10, TRAIP, FAM83D, TYMS, KDM1A, KIF2C, MCM7, CSE1L, PRMT5, CKLF, BUB1, ERCC1, TFDP1, POLR3G, CDK1, MKI67, NASP, DLGAP5, KIF15, SKP2, PIM1, TPX2, CENPF, ITGA2, TACC3, CDC25C, CDC25A, IFNAR2, UHRF1, PLK1, CHRM1, PCNA, CKS2, BUB1B, TCF19, MELK, MYH10.
GO:0007080	Mitotic metaphase plate congression	1.73E-06	15	KIF14, KIF22, KIFC1, CHMP4C, PSRC1, KIF18A, CENPE, SPDL1, CEP55, CCNB1, KIF2C, CDCA8, CDCA5, KPNB1, PINX1.
GO:0000732	Strand displacement	1.85E-06	13	EXO1, RAD51C, DNA2, XRCC3, RAD51AP1, XRCC2, BLM, BRCA2, BRIP1, RMI1, BRCA1, RAD51, BARD1.
GO:0007049	Cell cycle	2.48E-06	35	E2F2, CKS1B, DBF4B, USP2, LIN9, FOXM1, DTYMK, AURKA, AURKB, WTAP, DDX12P, CASP8AP2, HJURP, SIK1, ING1, RBL2, NASP, GMNN, RBL1, PIM1, SUV39H1, CDC20, MCM2, CDKN3, ESCO2, BRCA1, SUV39H2, CCND1, UHRF1, CCND3, PTP4A1, CHTF18, SIAH2, CHAF1B, KCTD11.

ID	Term	Bonferroni adjusted p-value*	No. genes	Genes
Biological processes – continued				
GO:0006335	DNA replication-dependent nucleosome assembly	2.51E-06	14	NASP, HIST2H4A, HIST2H4B, HIST1H4A, HIST1H3A, HIST1H3B, HIST1H4C, HIST1H3D, HIST1H4D, HIST1H3F, ASF1B, HIST1H3G, CHAF1B, HIST1H3I.
GO:0036297	Interstrand cross-link repair	1.27E-05	16	XRCC3, RAD51AP1, USP1, EME1, RAD51, RPA3, RPA2, DCLRE1A, FANCI, FANCD2, FANCE, FANCA, UBE2T, ERCC1, FANCB, FANCC.
GO:0045814	Negative regulation of gene expression, epigenetic	1.74E-05	16	HIST2H3A, EZH2, HIST2H4A, HIST2H4B, PHF19, HIST1H4A, HIST1H3A, HIST1H3B, DNMT1, HIST1H4C, HIST1H3D, HIST1H4D, HIST1H3F, DNMT3B, HIST1H3G, HIST1H3I.
GO:0000183	Chromatin silencing at rDNA	2.06E-05	14	HIST2H3A, SUV39H1, HIST2H4A, SIRT2, HIST2H4B, HIST1H4A, HIST1H3A, HIST1H3B, HIST1H4C, HIST1H3D, HIST1H4D, HIST1H3F, HIST1H3G, HIST1H3I.
GO:0000724	Double-strand break repair via homologous recombination	2.21E-05	19	RAD51C, XRCC3, RAD51AP1, MMS22L, XRCC2, BLM, TONSL, GEN1, BRCA2, RAD54L, BRCA1, RAD51, RPA3, RPA2, MCM8, RAD54B, H2AFX, POLQ, FEN1.

ID	Term	Bonferroni adjusted p-value*	No. genes	Genes
Biological processes – continued				
GO:1901796	Regulation of signal transduction by p53 class mediator	5.28E-05	24	EXO1, SSRP1, CDK5R1, BLM, TAF5, TPX2, BRIP1, AURKA, CHEK1, TOPBP1, AURKB, CHEK2, RMI1, BRCA1, CDK2, RPA3, RFC5, RPA2, DNA2, RFC3, RFC4, RFC2, PRMT5, BARD1.
GO:0051726	Regulation of cell cycle	5.28E-05	24	E2F2, RBL2, DTL, FIGNL1, FOXM1, LIN9, CCNF, PRR11, RBL1, SKP2, KIAA0101, PKMYT1, CENPF, CDC25C, MYBL2, SIRT2, CDC25A, CCNE2, CCNB1, CCNB2, PLK1, CDK12, MASTL, MED1.
GO:0016925	Protein sumoylation	8.28E-05	23	BLM, NUP85, BIRC5, NUP188, RANGAP1, AURKB, NUP155, BRCA1, NDC1, CDCA8, RAD21, AAAS, MDC1, INCENP, NUP205, NUP50, PCNA, NUP107, SMC1A, SCMH1, TOP2A, NUP43, STAG1.
GO:0007018	Microtubule-based movement	1.01E-04	19	KIFC2, KIF14, KIF23, KIF22, KIFC1, KIF4A, KIF11, KIF15, KIF18A, DNAH3, KIF18B, CENPE, KIF16B, RACGAP1, KIF2C, KIFAP3, KIF20B, DYNLRB2, KIF20A.

ID	Term	Bonferroni adjusted p-value*	No. genes	Genes
Biological processes – continued				
GO:0000083	Regulation of transcription involved in G1/S transition of mitotic cell cycle	1.04E-04	11	CDK1, CDC6, TYMS, CDC45, DHFR, RRM2, PCNA, POLA1, FBXO5, ORC1, CDT1.
GO:0031047	Gene silencing by RNA	1.52E-04	22	HIST2H3A, NUP85, NUP188, HIST2H4A, NUP155, HIST2H4B, NDC1, AAAS, HIST1H4A, NUP205, NUP50, HIST1H3A, AGO1, HIST1H3B, HIST1H3D, HIST1H4C, HIST1H4D, NUP107, HIST1H3F, NUP43, HIST1H3G, HIST1H3I.
GO:0042769	DNA damage response, detection of DNA damage	1.54E-04	13	DTL, USP1, RPA3, POLD3, RFC5, POLD4, RPA2, RFC3, RFC4, RFC2, PCNA, DNAJA1, RAD18.
GO:0006297	Nucleotide-excision repair, DNA gap filling	1.71E-04	11	RFC5, POLD3, POLD4, RPA2, RFC3, RFC4, RFC2, LIG1, POLE, PCNA, RPA3.
GO:0007077	Mitotic nuclear envelope disassembly	2.20E-04	14	CDK1, NUP85, NUP188, NUP155, CCNB1, NDC1, VRK1, AAAS, CCNB2, PLK1, NUP205, NUP50, NUP107, NUP43.

ID	Term	Bonferroni adjusted p-value*	No. genes	Genes
Biological processes – continued				
GO:0032200	Telomere organization	6.44E-02	11	HIST1H4A, HIST1H3A, HIST1H3B, HIST1H3D, HIST1H4C, HIST1H4D, HIST1H3F, HIST2H4A, HIST1H3G, HIST1H3I, HIST2H4B.
GO:0007051	Spindle organization	6.56E-04	9	KIF11, CKAP5, SPAG5, TTK, AURKA, RANBP1, AURKB, KNSTRN, ASPM.
GO:0051290	Protein heterotetramerization	0.0010	13	HIST2H4A, HIST2H4B, HIST1H4A, RRM2, HIST1H3A, RRM1, HIST1H3B, HIST1H4C, HIST1H3D, HIST1H4D, HIST1H3F, HIST1H3G, HIST1H3I.
GO:0019985	Translesion synthesis	0.0012	12	RFC5, POLD3, POLD4, RPA2, RFC3, RFC4, DTL, RFC2, PCNA, KIAA0101, RPA3, REV3L.
GO:0007052	Mitotic spindle organization	0.0020	11	CCNB1, STIL, SPC25, KIF11, GPSM2, TTK, NDC80, AURKA, STMN1, RCC1, SMC1A.
GO:0007131	Reciprocal meiotic recombination	0.0020	11	RAD51C, MSH6, XRCC3, RAD21, XRCC2, MSH2, MND1, RAD54B, DMC1, RAD51, TRIP13.

ID	Term	Bonferroni adjusted p-value*	No. genes	Genes
Biological processes – continued				
GO:0006977	DNA damage response, signal transduction by p53 class mediator resulting in cell cycle arrest	0.0027	15	E2F1, CDK1, RBL2, E2F7, AURKA, CHEK2, CDC25C, CENPJ, CNOT6, CDK2, GTSE1, CCNB1, CDKN1A, PCNA, TFDP1.
GO:0042276	Error-prone translesion synthesis	0.0034	9	RFC5, RPA2, RFC3, RFC4, POLE2, RFC2, PCNA, RPA3, REV3L.
GO:0000910	Cytokinesis	0.0050	13	KIF23, PRC1, BRCA2, ESPL1, BIRC5, ECT2, ARL3, PLK1, INCENP, RHOC, CIT, NEK7, KIF20A.
GO:0071897	DNA biosynthetic process	0.0051	10	TYMS, LIN9, LIG1, PRIM2, CENPF, PAPD5, POLA2, POLQ, TERT, TK1.

ID	Term	Bonferroni adjusted p-value*	No. genes	Genes
Biological processes – continued				
GO:0006974	Cellular response to DNA damage stimulus	0.0062	28	XRCC3, BLM, APLF, KIAA0101, CHEK1, CHEK2, MCM10, MCM8, MCM7, DDX11, WDR76, H2AFX, MASTL, POLQ, TOP2A, DTL, SUV39H1, TOPBP1, ATAD5, BRCA1, RAD51, CDKN1A, CCND1, TIMELESS, RAD18, UBE2T, UBE2E2, BARD1.
GO:0007076	Mitotic chromosome condensation	0.0069	8	NCAPH, NCAPG, NUSAP1, CDCA5, SMC2, NCAPD3, SMC4, NCAPD2.
GO:0006284	Base-excision repair	0.0098	11	HMGB1, RPA2, MPG, DNA2, LIG1, UNG, NEIL3, POLQ, PARP2, FEN1, RPA3.
GO:0060968	Regulation of gene silencing	0.0119	7	HIST1H3A, HIST1H3B, HIST1H3D, HIST1H3F, HIST1H3G, CDK2, HIST1H3I.
GO:1900264	Positive regulation of DNA-directed DNA polymerase activity	0.0129	6	RFC5, RFC3, RFC4, RFC2, CHTF18, DSCC1.
GO:0032508	DNA duplex unwinding	0.0135	12	GINS1, GINS2, DNA2, CDC45, BLM, DDX11, GINS4, BRIP1, RAD54B, MCM3, MCM5, DDX12P.

ID	Term	Bonferroni adjusted p-value*	No. genes	Genes
Biological processes – continued				
GO:0045815	Positive regulation of gene expression, epigenetic	0.0157	14	HIST2H3A, KAT2B, DEK, HIST2H4A, HIST2H4B, HIST1H4A, HIST1H3A, HIST1H3B, HIST1H4C, HIST1H3D, HIST1H4D, HIST1H3F, HIST1H3G, HIST1H3I.
GO:0006342	Chromatin silencing	0.0171	12	HIST1H2AB, HIST2H2AA3, HIST2H2AB, HIST1H2AG, HIST1H2AE, H2AFZ, HIST1H2AI, H2AFX, HIST1H2AJ, HIST1H2AM, HIST1H2AL, SIRT2.
GO:0006310	DNA recombination	0.0213	16	EXO1, RAD51C, HMGB1, XRCC3, HMGB3, BLM, LIG1, RAD54L, BRCA1, RAD51, RPA3, RAD21, PSMC3IP, RBM14, RBPJ, ERCC1.
GO:0051310	Metaphase plate congression	0.0228	7	FAM83D, KIF22, KIF2C, CENPQ, CENPF, CENPE, NDC80.
GO:0007088	Regulation of mitotic nuclear division	0.0263	9	MKI67, NEK2, PRMT5, BORA, KIF20B, FBXO5, PKMYT1, RCC1, CDC25C.
GO:0000079	Regulation of cyclin-dependent protein serine/threonine kinase activity	0.0284	11	CCNE2, CDC6, CDK5R1, CDKN1A, BLM, CDKN2C, PKMYT1, CDC25C, CDKN3, CCNA2, CDC25A.

ID	Term	Bonferroni adjusted p-value*	No. genes	Genes
Biological processes – continued				
GO:0006312	Mitotic recombination	0.0403	7	RAD51C, XRCC2, RAD54B, DMC1, TOP2A, ERCC1, RAD51.
GO:0010212	Response to ionizing radiation	0.0408	12	RAD51C, XRCC3, RFWD3, XRCC2, TICRR, RRM1, H2AFX, TOPBP1, DMC1, DNMT3B, RAD54L, BRCA1.
Pathways (KEGG)				
hsa04110	Cell cycle	7.34E-26	47	E2F1, E2F2, DBF4, PKMYT1, TTK, PRKDC, CHEK1, CHEK2, PTTG1, CCNE2, CDC45, RAD21, MCM7, CDKN2C, BUB1, ORC6, CCNA2, ORC1, BUB3, TFDP1, STAG1, CDC7, CDK1, CDC6, RBL2, RBL1, SKP2, ESPL1, CDC20, MCM2, MCM3, CDC25C, MCM4, MCM5, CDK2, CDC25A, MCM6, CCNB1, CCND1, CDKN1A, CCNB2, MAD2L1, CCND3, PLK1, PCNA, BUB1B, SMC1A.
hsa03030	DNA replication	1.19E-20	25	POLA1, POLA2, RPA3, PRIM1, RPA2, MCM7, POLE2, PRIM2, FEN1, LIG1, POLE, MCM2, MCM3, RNASEH2A, MCM4, MCM5, MCM6, POLD3, RFC5, POLD4, DNA2, RFC3, RFC4, RFC2, PCNA.

ID	Term	Bonferroni adjusted p-value*	No. genes	Genes
Pathways – continued				
hsa05322	Systemic lupus erythematosus	1.25E-14	37	HLA-DQB1, HIST1H2AB, HIST2H2AA3, HLA-DRB1, HIST1H2AG, HIST1H2AE, HIST2H4A, HIST2H4B, HIST1H2BO, HIST2H2AB, HIST1H2BM, HIST1H4A, HIST1H2BL, HIST1H2BI, HIST1H2BJ, H2AFZ, H2AFX, HIST1H4C, HIST1H4D, HIST3H2BB, HIST2H3A, HIST1H2BE, HIST1H2BF, HIST1H2BG, HIST1H2BH, HIST2H2BF, HIST1H3A, HIST1H3B, SNRPB, HIST1H2AI, HIST1H3D, HIST1H2AJ, HIST1H3F, HIST1H2AM, HIST1H2AL, HIST1H3G, HIST1H3I.
hsa03460	Fanconi anemia pathway	1.39E-09	20	RAD51C, BLM, USP1, EME1, BRCA2, BRIP1, RMI1, BRCA1, RAD51, RPA3, RPA2, FANCD2, FANCI, FANCE, FANCA, UBE2T, ERCC1, FANCB, FANCC, REV3L.

ID	Term	Bonferroni adjusted p-value*	No. genes	Genes
Pathways – continued				
hsa05034	Alcoholism	1.87E-08	34	HIST1H2AB, HIST2H2AA3, HIST1H2AG, HIST1H2AE, HIST2H4A, HIST2H4B, HIST1H2BO, HIST2H2AB, HIST1H2BM, HIST1H4A, HIST1H2BL, HIST1H2BI, HIST1H2BJ, H2AFZ, H2AFX, HIST1H4C, HIST1H4D, HIST3H2BB, HIST2H3A, HIST1H2BE, HIST1H2BF, HIST1H2BG, HIST1H2BH, HIST2H2BF, HIST1H3A, HIST1H3B, HIST1H2AI, HIST1H3D, HIST1H2AJ, HIST1H3F, HIST1H2AM, HIST1H2AL, HIST1H3G, HIST1H3I.
hsa03430	Mismatch repair	6.17E-08	13	EXO1, MSH6, MSH2, LIG1, RPA3, POLD3, RFC5, RPA2, POLD4, RFC3, RFC4, RFC2, PCNA.
hsa03440	Homologous recombination	1.78E-06	13	RAD51C, XRCC3, XRCC2, BLM, EME1, BRCA2, RAD54L, RAD51, RPA3, POLD3, RPA2, POLD4, RAD54B.
hsa05203	Viral carcinogenesis	3.71E-06	33	CHEK1, HIST2H4A, HIST2H4B, HIST1H2BO, CCNE2, HIST1H2BM, HIST1H4A, GSN, HIST1H2BL, HIST1H2BI, HIST1H2BJ, RANBP1, HIST1H4C, HIST1H4D, HIST3H2BB, CCNA2, CDK1, KAT2B, RBL2, HIST1H2BE, HIST1H2BF, HIST1H2BG, HIST1H2BH, RBL1, SKP2, CDC20, CDK2, CDKN1A, CCND1, CCND3, HIST2H2BF, SCIN, RBPJ.

ID	Term	Bonferroni adjusted p-value*	No. genes	Genes
Pathways – continued				
hsa03410	Base excision repair	1.01E-05	13	HMGB1, LIG1, NEIL3, UNG, POLE, POLD3, POLD4, MPG, POLE2, PCNA, PARP3, PARP2, FEN1.
hsa00240	Pyrimidine metabolism	1.90E-04	20	POLR3G, POLE, DTYMK, POLA1, DCK, CTPS1, POLA2, PNP, TK1, PRIM1, POLD3, POLD4, TYMS, POLE2, RRM2, RRM1, PRIM2, UCK2, ENTPD1, DUT.
hsa03420	Nucleotide excision repair	7.64E-04	13	LIG1, POLE, RPA3, POLD3, RFC5, POLD4, RPA2, RFC3, RFC4, POLE2, RFC2, PCNA, ERCC1.
hsa04115	P53 signalling pathway	0.0075	14	CDK1, CHEK1, CHEK2, CDK2, GTSE1, CCNE2, CCNB1, EI24, CCND1, CDKN1A, CCNB2, CCND3, CD82, RRM2.
hsa04114	Oocyte meiosis	0.0121	18	CDK1, ADCY6, PKMYT1, AURKA, CDC20, ESPL1, PTTG1, CDC25C, CDK2, CCNB1, CCNE2, IGF1R, CCNB2, MAD2L1, PLK1, BUB1, FBXO5, SMC1A.

ID	Term	Bonferroni adjusted p-value*	No. genes	Genes
Diseases (GAD)				
	Breast cancer	1.28E-27	104	RAD51C, XRCC3, RNASEL, XRCC2, TTK, AURKA, PTTG1, AURKB, CXCL12, CDKN2C, H2AFX, ASPM, LIG1, POLE, SKP2, ESPL1, TOPBP1, TACC3, NCAPD2, MAD2L1, SPAG5, SNRPB, RAD18, NEK7, BBS4, HLA-DRB1, BLM, NEK2, ERBB2, RABGAP1L, CHEK1, CHEK2, RHOBTB2, DNMT3B, CKAP5, EME1, NUF2, BRIP1, PPFIBP2, BRCA2, ITGA2, CDC20, NDC80, RAD54L, BRCA1, CDKN1A, PLK4, DHFR, PLK1, PCNA, TUBD1, KIF23, CLSPN, CDT1, MTHFD1, KIF2C, MCM7, FANCE, RANBP1, FANCA, TOP2A, TERT, FANCB, FANCC, CDK1, KIF11, GEN1, TPX2, SPINT1, MCM2, MCM3, MCM4, MCM5, CDK2, MCM6, RAD51, CCND1, CCND3, FANCD2, BUB1B, DMC1, MED1, HLA-DQB1, CALCR, YPEL5, PRKDC, RPA3, IGF1R, TYMS, RPA2, BUB1, GPSM2, FEN1, ERCC1, BUB3, PINX1, MSH6, SHMT1, MSH2, GMNN, CENPE, CDC25C, CCNB1, BARD1.

ID	Term	Bonferroni adjusted p-value*	No. genes	Genes
Diseases – continued				
	Bladder cancer	5.42E-08	64	RAD51C, XRCC3, RNASEL, XRCC2, AURKA, H2AFX, FANCA, IFNGR2, CCNA2, TERT, FANCC, RET, LIG1, POLE, PIM1, TACC3, RAD51, RFC5, IFNAR2, CCND1, RFC3, RFC4, CCND3, FANCD2, RFC2, PSCA, REV3L, CALCR, BLM, ERBB2, UNG, PRKDC, CHEK1, CHEK2, POLA2, MYBL2, RPA3, TYMS, IGF1R, RPA2, POLE2, POLQ, ERCC1, EXO1, SHMT1, MSH6, MSH2, GGH, EPHX2, BRIP1, BRCA2, STAT1, CDC25C, RAD54L, BRCA1, CDC25A, POLD3, MPG, CDKN1A, DHFR, PLK1, PCNA, PARP3, BARD1.
	Pancreatic neoplasms	4.63E-07	18	EXO1, MSH6, MSH2, USP1, BRCA2, BRIP1, CHEK1, TOPBP1, BRCA1, RAD51, CDKN1A, MDC1, FANCD2, FANCE, RAD54B, FANCA, ABCC5, FANCC.
	Ovarian cancer	8.14E-07	49	SAT1, E2F1, RAD51C, E2F2, XRCC3, XRCC2, AURKA, PTTG1, MTHFD1, CCNE2, SPRY1, PLOD2, CDKN2C, CCNA2, TERT, H1F0, WNT10B, RBL2, RBL1, SKP2, MCM2, CDK2, RAD51, MCM6, CCND1, CCND3, HLA-DQB1, HLA-DRB1, CRLF3, ERBB2, CHEK2, TYMS, BUB1, ERCC1, TFDP1, MSH6, MKI67, MSH2, BRCA2, CDC20, STAT1, CDC25A, BRCA1, CCNB1, CDKN1A, CCNB2, ID2, PLK1, PTP4A1.

ID	Term	Bonferroni adjusted p-value*	No. genes	Genes
Diseases – continued				
	Chronic renal failure	9.06E-06	85	E2F2, XRCC3, XRCC2, CYP2S1, DBF4, E2F7, PINK1, CXCL12, TTLL12, GSTM2, SLC16A1, GSTM4, FANCE, FANCA, CCNA2, IFNGR2, CDC6, LIG1, ADGRE5, NEIL3, POLE, PBK, TACC3, MCM5, CDK2, NCAPD2, DCLRE1A, CCND1, RFC3, CCND3, SBF2, RRM1, NUCB2, RAD18, BUB1B, DMC1, REV3L, DCBLD2, CCL3, PPP2R3A, HLA-DRB1, BLM, TICRR, NEK2, ERBB2, FOXM1, DCK, CHEK1, POLA2, CHEK2, HMMR, SLC29A1, TYMS, IGF1R, FMO5, PTK2B, DNAJA1, CERK, BCAS3, POLQ, ERCC1, EXO1, MSH6, HERPUD1, MSH2, EME1, BRCA2, ITGA2, NDC80, CDC20, BIRC5, LHPP, BRCA1, CYP4B1, IKBKE, CDKN1A, PLK4, SYNE2, AOX1, PCNA, PHGDH, PARP3, RAD54B, PARP2, ABCC5.

ID	Term	Bonferroni adjusted p-value*	No. genes	Genes
Diseases – continued				
	Leukemia, Lymphocytic, Chronic, B-Cell	7.01E-05	32	HLA-DQB1, E2F2, XRCC2, HLA-DRB1, EZH2, PRKDC, AURKB, SP110, CXCL12, CDC45, RAD21, MDC1, TOP2A, EXO1, CPT1B, CDC6, RBL2, MSH2, GMNN, POLE, EPHX2, CENPF, BIRC5, CDC25C, MCM4, ESCO2, MCM5, CYP4B1, RAD51, CCND1, BUB1B, REV3L.
	Esophageal adenocarcinoma	1.12E-04	43	XRCC3, XRCC2, ERBB2, CHEK1, AURKA, CHEK2, MTHFD1, SLC29A1, TYMS, IGF1R, CASP7, FANCA, CCNA2, IFNGR2, DNMT3B, TERT, ERCC1, EXO1, MSH6, SHMT1, RET, MSH2, LIG1, RBL1, GGH, BRCA2, ITGA2, BIRC5, CDC25C, BRCA1, CDC25A, RAD51, CCNB1, IFNAR2, CCND1, CDKN1A, CCND3, RRM1, PCNA, RAD18, BUB1B, BARD1, REV3L.
	Glioma	1.37E-04	17	HLA-DQB1, PHLDB1, XRCC3, XRCC2, HLA-DRB1, GEN1, LIG1, ERBB2, EME1, BRCA2, PRKDC, RAD54B, RAD54L, BRCA1, TERT, ERCC1, RAD51.

ID	Term	Bonferroni adjusted p-value*	No. genes	Genes
Diseases – continued				
	Lung cancer	2.09E-04	54	FHIT, XRCC3, RNASEL, XRCC2, EZH2, AURKA, CASP7, IFNGR2, CCNA2, FANCA, TERT, CDK1, RET, C5AR1, LIG1, PIM1, RAD51, IFNAR2, CCND1, CCND3, RRM1, BUB1B, RAD18, HLA-DQB1, CALCR, BLM, HLA-DRB1, ERBB2, PRKDC, CHEK1, CHEK2, MYBL2, TYMS, IGF1R, DNMT3B, FEN1, ERCC1, EXO1, MSH6, MSH2, EPHX2, GGH, BRCA2, BRIP1, CDC25C, STAT1, RAD54L, BRCA1, CDC25A, CDKN1A, DHFR, PLK1, PCNA, BARD1.
	Hematologic Neoplasms	0.0142	12	RFC5, HLA-DQB1, MPG, RFC3, RFC4, HLA-DRB1, RFC2, LIG1, UNG, POLE, PCNA, FEN1.
	Colorectal Neoplasms	0.0168	18	MSH6, XRCC3, XRCC2, MSH2, LIG1, BRCA2, CHEK2, BRCA1, RAD51, TYMS, CCND1, CDKN1A, CASP8AP2, FANCD2, PCNA, RAD54B, ERCC1, BARD1.
	Cervical intraepithelial neoplasia grade 3	0.0337	12	EXO1, MSH6, XRCC3, PCNA, BRCA2, BRIP1, RAD54B, STAT1, FANCA, IFNGR2, BRCA1, TERT.

*DAVID functional annotation performed on the 06th of June 2020

Appendix 4. List of genetic and physical interactors of cell-cell junction components affected by CG7379 knockdown

Drosophila gene	Interactors in *Drosophila*	Type of interaction	Human homologue	Homology strength
Genetic interactions				
E-cadherin (shg)	PDZ-GEF	suppressible by shg	RAPGEF2	high
			RAPGEF6	high
			RASGRF2	moderate
	raw	suppressible by shg	RNASEL	low
		enhanced by shg		
	dlg1	supresses shg	DLG2	moderate
			DLG3	moderate
			DLG4	moderate
			DLG1	high
	p120-catenin	enhanced by shg	CTNND1	moderate
			PKP4	moderate
			ARVCF	moderate
			PKP3	moderate
			PKP1	moderate
			PKP2	moderate
		enhances shg	CTNND2	high
	Rho1	enhances shg	RHOC	moderate
			RHOB	moderate
			RHOD	moderate
			RHOF	moderate
			RHBDL3	moderate
			RHBDL1	moderate
			RHBDL2	moderate
		supresses shg	RHOA	high

Drosophila gene	Interactors in *Drosophila*	Type of interaction	Human homologue	Homology strength
Genetic interactions – continued				
E-cadherin (shg)	lid	suppressible by shg	KDM5B	moderate
			KDM5C	moderate
			KDM5D	moderate
			KDM5A	high
	stg	supresses shg	CDC25A	high
			CDC25B	moderate
			CDC25C	moderate
	scra	suppressible by shg	ANLN	high
	CycE	suppressible by shg	CCNE2	moderate
			CDK2	high
			CDK1	moderate
			CDK3	moderate
			CDK5	moderate
			CNTD2	moderate
			CCNF	moderate
			CCNE1	high
	lilli	supresses shg	AFF3	moderate
			AFF1	moderate
			AFF4	high
			AFF2	high
	Hrb98DE	suppressible by shg	HNRNPA1L2	moderate
			HRNPA1	moderate
			HRNPA0	moderate
			HRNPA3	moderate
			HNRNPA2B1	high

Drosophila gene	Interactors in *Drosophila*	Type of interaction	Human homologue	Homology strength
Genetic interactions – continued				
E-cadherin (shg)	AGO1	supresses shg	AGO1	moderate
			AGO3	moderate
			AGO4	moderate
		enhances shg	AGO2	high
armadillo (arm)	crol	enhanced by arm	ZNF85	moderate
		suppressible by arm	ZNF98	moderate
			ZNF256	moderate
			ZNF569	high
			ZNF254	moderate
			ZNF63O	moderate
			ZNF782	moderate
			ZNF383	moderate
			ZNF84	moderate
			ZNF492	moderate
			ZNF543	moderate
			ZNF182	moderate
			ZNF71	moderate
			ZNF678	moderate
			ZNF676	moderate
			ZNF699	moderate
			ZKSCAN1	moderate
	da	supresses arm	TCF3	High
			TCF4	High
			TCF12	high
	bsk	supresses arm	MAPK9	moderate
			MAPK8	high
			MAPK10	high

Drosophila gene	Interactors in *Drosophila*	Type of interaction	Human homologue	Homology strength
Genetic interactions – continued				
armadillo (arm)	pav	supresses arm	KIF23	high
	E2f1	suppressible by arm	E2F2	high
			E2F1	moderate
			E2F6	moderate
			E2F4	moderate
			E2F3	high
	Rbf	enhanced by arm	RBL1	high
			HNRNPA2B1	moderate
			HNRNPNA1	moderate
			HNRNPA1L2	moderate
			HNRNPA3	moderate
			HNRNPA0	moderate
			RB1	moderate
			RBL2	high
	SCAR	supresses arm	WASF3	high
			WASF1	moderate
			WASF2	moderate
	brat	enhanced by arm	TRIM3	high
			TRIM2	moderate
			NHLRC3	moderate
	tum	supresses arm	RACGAP1	high
			JAK1	high
			JAK2	high
			JAK3	moderate
			TYK2	moderate
	pbl	supresses arm	ECT2	high
			ECT2L	moderate

Drosophila gene	Interactors in *Drosophila*	Type of interaction	Human homologue	Homology strength
Genetic interactions – continued				
armadillo (arm)	CycA	enhances arm	CCNA2	high
			CCNA1	moderate
			CCNB2	moderate
			CCNB1	moderate
	Su(H)	suppressible by arm	RBPJ	high
			RBPJL	moderate
	CycE	suppressible by arm	see higher in the table	
	stg	enhances arm	see higher in the table	
	dlg1	enhances arm	see higher in the table	
	lilli	enhances arm	see higher in the table	
	p120-catenin	supresses arm	see higher in the table	
α-Catenin (αCat)	Rho1	enhanced by αCat	see higher in the table	
	p120-catenin	enhanced by αCat	see higher in the table	
	SCAR	supresses αCat	see higher in the table	
coracle (cora)	Egfr	suppressible by cora	ERBB2	moderate
			ERBB3	moderate
			ERBB4	moderate
			EGFR	high
discs large (dlg1)	CycE	suppressible by dlg1	see higher in the table	
Fasciclin III (Fas3)	-			
Physical interactions				
E-cadherin	p120-catenin	-	see higher in the table	
	Hrb98DE	-	see higher in the table	
α-Catenin	sec10	-	EXOC5	high

Drosophila gene	Interactors in *Drosophila*	Type of interaction	Human homologue	Homology strength
Physical interactions – continued				
armadillo	sec10	-	see higher in the table	
	HipK	-	HIPK3	high
			HIPK1	moderate
			HIPK2	high
			HIPK4	moderate
	NitFhit	-	FHIT	moderate
			NIT1	high
	p120-catenin	-	see higher in the table	
discs large	hts	-	ADD3	moderate
			ADD1	high
			ADD2	moderate
	Pak	-	BUB1B-PAK6	moderate
			PAK1	high
			PAK2	moderate
			PAK3	moderate
			PAK4	high
			PAK5	moderate
			PAK6	moderate
	pins	-	GPSM2	high
			GPSM1	moderate
Coracle	-			
Fasciclin III	-			

Appendix 5. Gene and interactions tables for the functionally validated network of differentially expressed genes following ING1 knockdown

			Microarray results	
Gene name	Score	Node type	p-value	FC
ARHGAP19	0.9896	query	2.10E-07	-1.9
CDK1	0.8693	query	1.92E-06	-5.6
RACGAP1	0.9423	query	9.28E-06	-3.4
LMNB1	0.9554	query	2.10E-05	-4.1
LIG1	0.9553	query	2.32E-05	-2.7
AGO1	0.9672	query	4.76E-05	-2.0
STON2	0.9793	query	5.52E-05	2.4
MYH10	0.9324	query	6.55E-05	-1.6
GPNMB	0.9925	query	7.24E-05	4.6
RBL1	0.9426	query	7.88E-05	-2.8
ECT2	0.9629	query	8.09E-05	-3.1
LGALS3	0.9549	query	0.0001	2.2
CCNA2	0.9440	query	0.0002	-4.8
EXOC5	0.9415	query	0.0004	-1.6
GPSM2	0.9726	query	0.0005	-3.1
ARHGAP21	0.9929	query	0.0006	-1.7
WASF3	0.9806	query	0.0009	1.5
PCDHB16	0.9881	query	0.0009	-1.9
KDM5B	0.9677	query	0.0009	2.4
AFF3	0.9944	query	0.0010	-1.9
E2F2	0.9530	query	0.0013	-2.1
RAPGEF2	0.9672	query	0.0014	1.7
ADD3	0.9867	query	0.0016	-2.1
ERBB2	0.8805	query	0.0016	2.2
CTNND1	0.9335	query	0.0018	1.5
DIAPH1	0.9375	query	0.0019	-1.5

			Microarray results	
Gene name	Score	Node type	p-value	FC
continued				
RHOC	0.9528	query	0.0024	1.7
AFDN	0.9379	query (AJ)	-	-
CDH1	0.9162	query (AJ)	-	-
CTNNA1	0.9321	query (AJ)	-	-
CTNNA2	0.9721	query (AJ)	-	-
CTNNA3	0.9763	query (AJ)	-	-
CTNNB1	0.8556	query (AJ)	-	-
NECTIN1	0.9881	query (AJ)	-	-
NECTIN2	0.9798	query (AJ)	-	-
NECTIN3	0.9737	query (AJ)	-	-
NECTIN4	0.9859	query (AJ)	-	-
ELF3	0.0044	result	7.18E-05	1.7
CDK2	0.0070	result	2.42E-05	-1.8
KIF23	0.0133	result	2.51E-05	-3.0
CKS1B	0.0084	result	2.69E-05	-2.6
CCNB1	0.0091	result	0.0002	-3.4
CCNB2	0.0081	result	0.0003	-4.3
PKMYT1	0.0046	result	0.0025	-1.7
EGFR	0.0068	result	-	-
EPS15	0.0049	result	-	-
TCF7L2	0.0047	result	-	-
SP1	0.0042	result	-	-
EPHB3	0.0042	result	-	-
JUP	0.0137	result	-	-
LMNA	0.0075	result	-	-
PTPRM	0.0120	result	-	-
PVR	0.0081	result	-	-

Interaction	Normalised maxim weight	Type of interaction
Genetic interactions		
ELF3 - ERBB2	0.0050	DEG
TCF7L2 - CTNNB1	0.0019	linker gene; AJ component
LMNA - JUP	3.86E-06	linker genes
CCNA2 - AFDN	2.48E-06	AJ components
EPHB3 - GPSM2	2.21E-06	DEG; linker genes
E2F2 - RHOC	2.19E-06	DEG
PVR - CCNA2	2.01E-06	DEG; linker genes
CDH1 - GPSM2	1.75E-06	DEG; AJ component
EPHB3 - DIAPH1	1.69E-06	DEG; linker genes
CCNB2 - CTNNB1	1.43E-06	DEG; AJ component
JUP - E2F2	1.41E-06	DEG; linker genes
EPS15 - GPNMB	1.39E-06	DEG; linker genes
ARHGAP19 - NECTIN1	1.37E-06	DEG; AJ component
ARHGAP21 - GPNMB	1.34E-06	DEG
JUP - CDH1	1.27E-06	linker gene; AJ component
PTRM - RHOC	1.27E-06	DEG; linker genes
CDH1 - PCDHB16	1.26E-06	DEG; AJ component
LMNB1 - RACGEF2	1.21E-06	DEG
EGFR - DIAPH1	1.19E-06	DEG; linker genes
ERBB2 - RACGAP1	1.18E-06	DEG
CTNNA1 - CCNA2	1.17E-06	DEG; AJ component
TCF7L2 - CCNB2	1.14E-06	DEG; linker genes
ADD3 - PCDHB16	1.11E-06	DEG
CTNNA3 - GPNMB	1.06E-06	DEG; AJ component
CCNB2 - CTNNA3	1.05E-06	DEG; AJ component
AFF3 - PCDHB16	1.03E-06	DEG
LMNB1 - CTNNA2	9.74E-07	DEG; AJ component
STON2 - CTNNA2	9.42E-07	DEG; AJ component

Interaction	Normalised maxim weight	Type of interaction
Genetic interactions – continued		
CCNA2 - ARHGAP21	9.24E-07	DEG
EGFR - ERBB2	8.94E-07	DEG; linker genes
CDH1 - RBL1	8.67E-07	DEG; AJ component
PTRM - DIAPH1	8.65E-07	DEG; linker genes
AGO1 - NECTIN1	8.44E-07	DEG; AJ component
KDM5B - ECT2	8.13E-07	DEG
PTRM - CCNA2	8.12E-07	DEG; linker genes
PTRM - PCDHB16	8.09E-07	DEG; linker genes
ERBB2 - CTNNB1	8.02E-07	DEG; AJ component
CDH1 - NECTIN2	7.74E-07	AJ components
RBL1 - ADD3	7.67E-07	DEG
CTNNA2 - PCDHB16	7.37E-07	DEG; AJ component
KIF23 - MYH10	7.31E-07	DEG
AFDN - ADD3	6.96E-07	DEG; AJ component
EPHB3 - KDM5B	6.94E-07	DEG; linker genes
CTNNB1 - RBL1	6.89E-07	DEG; AJ component
NECTIN2 - ADD3	6.86E-07	DEG; AJ component
EGFR - NECTIN2	6.86E-07	linker gene; AJ component
ECT2 - EXOC5	6.54E-07	DEG
RBL1 - ARHGAP21	6.35E-07	DEG
CTNNB1 - NECTIN2	6.16E-07	AJ components
KDM5B - E2F2	6.12E-07	DEG
KDM5B - EXOC5	6.11E-07	DEG
PVR - MYH10	6.05E-07	DEG; linker genes
EPS15 - NECTIN2	5.90E-07	linker gene; AJ component
CDH1 - ECT2	5.90E-07	DEG; AJ component
ELF3 - RACGEF2	5.87E-07	DEG; linker genes
AFDN - RACGEF2	5.73E-07	DEG; AJ component

Interaction	Normalised maxim weight	Type of interaction
Genetic interactions – continued		
EPHB3 - EXOC5	5.58E-07	DEG; linker genes
SP1 - CDH1	5.38E-07	linker gene; AJ component
EGFR - ECT2	5.22E-07	DEG; linker genes
MYH10 - KDM5B	5.22E-07	DEG
CTNNA2 - ARHGAP19	5.16E-07	DEG; AJ component
CTNNA1 - KDM5B	5.12E-07	DEG; AJ component
ARHGAP19 - CTNNA3	5.10E-07	DEG; AJ component
PVR - CTNNB1	5.08E-07	linker gene; AJ component
EPHB3 - CDH1	5.04E-07	linker gene; AJ component
SP1 - CTNNA1	4.99E-07	linker gene; AJ component
TCF7L2 - NECTIN2	4.88E-07	linker gene; AJ component
EGFR - KDM5B	4.88E-07	DEG; linker genes
ECT2 - AFF3	4.82E-07	DEG
EPS15 - NECTIN1	4.74E-07	linker gene; AJ component
ARHGAP21 - NECTIN1	4.56E-07	DEG; AJ component
EPHB3 - EGFR	4.46E-07	linker genes
CDH1 - E2F2	4.44E-07	DEG; AJ component
ECT2 - ARHGAP21	4.32E-07	DEG
EGFR - RACGAP1	4.14E-07	DEG; linker genes
EPHB3 - AFF3	4.12E-07	DEG; linker genes
KDM5B - RACGEF2	4.02E-07	DEG
PTRM - NECTIN1	4.01E-07	linker gene; AJ component
EGFR - E2F2	3.93E-07	DEG; linker genes
PTRM - ECT2	3.80E-07	DEG; linker genes
TCF7L2 - ECT2	3.72E-07	DEG; linker genes
PVR - CTNNA3	3.71E-07	linker gene; AJ component
EPHB3 - ARHGAP21	3.69E-07	DEG; linker genes
CTNNA2 - NECTIN1	3.65E-07	AJ components

Interaction	Normalised maxim weight	Type of interaction
Genetic interactions – continued		
E2F2 - AFF3	3.63E-07	DEG
EPS15 - RACGAP1	3.56E-07	DEG; linker genes
PTRM - KDM5B	3.55E-07	DEG; linker genes
EGFR - CDH1	3.54E-07	linker gene; AJ component
CTNNB1 - EXOC5	3.52E-07	DEG; AJ component
CTNNA1 - MYH10	3.52E-07	DEG; AJ component
SP1 - PTRM	3.46E-07	linker genes
RACGAP1 - ARHGAP21	3.43E-07	DEG
NECTIN3 - ARHGAP21	3.40E-07	DEG; AJ component
RACGEF2 - NECTIN3	3.39E-07	DEG; AJ component
EPS15 - E2F2	3.38E-07	DEG; linker genes
MYH10 - ADD3	3.35E-07	DEG
E2F2 - ARHGAP21	3.25E-07	DEG
RACGEF2 - EXOC5	3.23E-07	DEG
KDM5B - CTNNA3	3.20E-07	DEG; AJ component
CTNNB1 - CDH1	3.18E-07	AJ components
SP1 - CTNNA2	3.15E-07	linker gene; AJ component
EGFR - ADD3	3.13E-07	DEG; linker genes
EPS15 - CDH1	3.04E-07	linker gene; AJ component
PTRM - NECTIN3	2.99E-07	linker gene; AJ component
EPHB3 - CTNNA2	2.96E-07	linker gene; AJ component
EGFR - AFF3	2.89E-07	DEG; linker genes
EPS15 - MYH10	2.88E-07	DEG; linker genes
PTRM - E2F2	2.86E-07	DEG; linker genes
EPS15 - CTNNA1	2.83E-07	linker gene; AJ component
TCF7L2 - EXOC5	2.79E-07	DEG; linker genes
MYH10 - ARHGAP21	2.77E-07	DEG
CTNNA1 - ARHGAP21	2.72E-07	DEG; AJ component

Interaction	Normalised maxim weight	Type of interaction
Genetic interactions – continued		
CTNNA1 - RACGEF2	2.71E-07	DEG; AJ component
NECTIN3 - CTNNA3	2.70E-07	AJ components
EGFR - ARHGAP21	2.59E-07	DEG; linker genes
RACGEF2 - ADD3	2.58E-07	DEG
EXOC5 - CTNNA3	2.57E-07	DEG; AJ component
EPS15 - AFF3	2.49E-07	DEG; linker genes
EPS15 - CTNNB1	2.42E-07	linker gene; AJ component
ARHGAP21 - AFF3	2.40E-07	DEG
PTRM - CTNNA1	2.39E-07	linker gene; AJ component
TCF7L2 - CTNNA1	2.34E-07	linker gene; AJ component
CDH1 - CTNNA3	2.32E-07	AJ components
PTRM - EGFR	2.28E-07	linker genes
EPS15 - ARHGAP21	2.23E-07	DEG; linker genes
EPS15 - RACGEF2	2.22E-07	DEG; linker genes
MYH10 - CTNNA2	2.22E-07	DEG; AJ component
CTNNA2 - ADD3	2.08E-07	DEG; AJ component
TCF7L2 - EPS15	1.92E-07	linker genes
AFF3 - CTNNA3	1.90E-07	DEG; AJ component
PTRM - RACGEF2	1.88E-07	DEG; linker genes
TCF7L2 - RACGEF2	1.84E-07	DEG; linker genes
EPS15 - CTNNA2	1.79E-07	linker gene; AJ component
EPS15 - CTNNA3	1.77E-07	linker gene; AJ component
ARHGAP21 - CTNNA3	1.70E-07	DEG; AJ component
RACGEF2 - CTNNA3	1.69E-07	DEG; AJ component
TCF7L2 - PTRM	1.62E-07	linker genes
PTRM - CTNNA2	1.51E-07	linker gene; AJ component
PTRM - CTNNA3	1.50E-07	linker gene; AJ component
TCF7L2 - CTNNA2	1.48E-07	linker gene; AJ component

Interaction	Normalised maxim weight	Type of interaction
Genetic interactions – continued		
CTNNA2 - CTNNA3	1.36E-07	AJ components
Protein interactions		
CKS1B - CDK1	0.0045	DEG
EPS15 - STON2	0.0044	DEG; linker genes
KIF23 - RACGAP1	0.0039	DEG
EPHB3 - AFDN	0.0035	linker gene; AJ component
NECTIN3 - NECTIN2	0.0031	AJ components
PTRM - CDH1	0.0031	linker gene; AJ component
KIF23 - ECT2	0.0030	DEG
CKS1B - CDH1	0.0028	DEG; AJ component
CCNB2 - CDK2	0.0028	DEG
LMNA - LMNB1	0.0027	DEG; linker genes
EGFR - CTNND1	0.0027	DEG; linker genes
EGFR - CDH1	0.0027	linker gene; AJ component
EGFR - CDK1	0.0027	DEG; linker genes
EGFR - JUP	0.0027	linker genes
EGFR - WASF3	0.0027	DEG; linker genes
CTNNA1 - CDH1	0.0025	AJ components
CDH1 - CTNND1	0.0025	DEG; AJ component
CCNB1 - CDK1	0.0024	DEG
CCNB2 - CDK1	0.0024	DEG
SP1 - E2F2	0.0024	DEG; linker genes
RACGAP1 - ECT2	0.0021	DEG
PVR - NECTIN1	0.0021	linker gene; AJ component
TCF7L2 - CTNNB1	0.0020	linker gene; AJ component
DIAPH1 - RHOC	0.0020	DEG
CTNNB1 - CTNNA2	0.0020	AJ components
JUP - CTNNA2	0.0020	linker gene; AJ component

Interaction	Normalised maxim weight	Type of interaction
Protein interactions – continued		
PVR - NECTIN3	0.0019	linker gene; AJ component
CDK2 - LIG1	0.0017	DEG
CDK2 - CCNA2	0.0016	DEG
NECTIN4 - NECTIN1	0.0016	AJ components
CTNNB1 - CDH1	0.0014	AJ components
PKMYT1 - CDK1	0.0014	DEG
JUP - CTNNA1	0.0014	linker gene; AJ component
CDK2 - CKS1B	0.0014	DEG
CDK1 - CCNA2	0.0014	AJ components
NECTIN3 - NECTIN1	0.0013	AJ components
CTNNB1 - CTNNA1	0.0013	AJ components
NECTIN4 - NECTIN2	0.0010	AJ components
PTRM - CTNND1	9.89E-04	DEG; linker genes
CDK2 - RBL1	9.26E-04	DEG
PKMYT1 - CCNB2	7.25E-04	DEG
CCNB2 - CKS1B	6.15E-04	DEG
CTNNB1 - CTNNA3	5.53E-04	AJ components
CCNB1 - CCNB2	4.81E-04	DEG
CTNNA1 - CTNNA3	4.77E-04	AJ components
AFDN - NECTIN4	4.19E-04	AJ components
CCNB1 - CDK2	3.86E-04	DEG
JUP - CTNNA3	3.76E-04	linker gene; AJ component
ELF3 - EPS15	3.39E-04	DEG; linker genes
CCNB1 - CKS1B	3.22E-04	DEG
PKMYT1 - CCNB1	3.18E-04	DEG
AFDN - NECTIN3	3.10E-04	AJ components
AFDN - NECTIN1	2.55E-04	AJ components
CKS1B - CCNA2	2.50E-04	DEG

Interaction	Normalised maxim weight	Type of interaction
Protein interactions – continued		
TCF7L2 - JUP	2.46E-04	linker gene; AJ component
PKMYT1 - CCNA2	2.44E-04	DEG
AFDN - NECTIN2	2.25E-04	AJ components
ECT2 - GPSM2	2.13E-04	DEG
CCNA2 - RBL1	1.57E-04	DEG
CDH1 - ARHGAP21	1.49E-04	DEG; AJ component
MYH10 - LGALS3	1.28E-04	DEG
CTNNA1 - CTNND1	1.21E-04	AJ components
RBL1 - E2F2	1.15E-04	DEG
CTNNB1 - RACGEF2	1.13E-04	DEG; AJ component
CTNNA1 - AFDN	1.11E-04	AJ components
CCNB1 - CCNA2	1.06E-04	DEG
ELF3 - EGFR	1.01E-04	DEG; linker genes
CDK1 - ECT2	9.21E-05	DEG
JUP - CTNND1	9.18E-05	DEG; linker genes
CCNA2 - LMNB1	8.37E-05	DEG
CDH1 - ECT2	7.60E-05	DEG; AJ component
JUP - CTNNB1	7.27E-05	linker gene; AJ component
PTRM - CTNNB1	6.11E-05	linker gene; AJ component
CDK1 - RACGAP1	6.03E-05	AJ components
JUP - CDH1	5.93E-05	linker gene; AJ component
RACGAP1 - STON2	5.80E-05	DEG
JUP - ERBB2	5.67E-05	DEG; linker genes
CCNB1 - LMNB1	5.64E-05	DEG; linker genes
SP1 - MYH10	5.63E-05	DEG; linker genes
PVR - CDH1	5.37E-05	linker gene; AJ component
CDK1 - LMNB1	4.39E-05	AJ components
MYH10 - ARHGAP21	4.35E-05	DEG

Interaction	Normalised maxim weight	Type of interaction
Protein interactions – continued		
MYH10 - STON2	4.26E-05	DEG
EPS15 - MYH10	4.25E-05	DEG; linker genes
SP1 - ARHGAP21	4.17E-05	DEG; linker genes
SP1 - RBL1	3.77E-05	DEG; linker genes
CDK2 - LMNB1	3.68E-05	DEG
RACGAP1 - RACGEF2	3.30E-05	DEG
LMNA - CDH1	3.04E-05	linker gene; AJ component
LMNA - CDK1	2.64E-05	DEG; linker genes
EPS15 - EGFR	2.44E-05	linker genes
CTNNB1 - LMNB1	2.24E-05	DEG; AJ component
CCNB1 - CDH1	2.21E-05	DEG; AJ component
EPS15 - ERBB2	2.14E-05	DEG; linker genes
CTNNB1 - CTNND1	2.13E-05	AJ components
ERBB2 - CTNNB1	1.88E-05	DEG; AJ component
EGFR - ERBB2	1.87E-05	DEG; linker genes
SP1 - CCNA2	1.52E-05	DEG; linker genes
CTNNB1 - CCNA2	1.34E-05	DEG; AJ component
CDK2 - RHOC	1.33E-05	DEG
LMNA - CTNNB1	1.25E-05	linker gene; AJ component
JUP - MYH10	1.25E-05	DEG; linker genes
SP1 - CCNB1	1.02E-05	DEG; linker genes
EGFR - LGALS3	9.97E-06	DEG; linker genes
LMNA - RACGEF2	8.47E-06	DEG; linker genes
EGFR - CTNNB1	7.32E-06	linker gene; AJ component
SP1 - CDK1	7.13E-06	DEG; linker genes
SP1 - CDK2	6.68E-06	DEG; linker genes
CDK2 - CTNNB1	5.90E-06	DEG; AJ component
CDK2 - MYH10	4.24E-06	DEG

Interaction	Normalised maxim weight	Type of interaction
Protein interactions – continued		
SP1 - CTNNB1	4.08E-06	linker gene; AJ component
EGFR - CTNNA1	2.89E-06	linker gene; AJ component
EGFR - EXOC5	2.63E-06	DEG; linker genes
CDK2 - JUP	2.32E-06	DEG; linker genes
LMNA - CDK2	1.27E-06	DEG; linker genes
CDK2 - CDK1	1.21E-06	DEG